A VLBI POLARISATION STUDY OF 43 GHZ SIO MASERS TOWARDS VY CMA

A thesis submitted in partial fulfilment
of the requirements for the degree of

MASTERS IN SCIENCE

of

RHODES UNIVERSITY

by

LAURA RICHTER

August 2005

Abstract

This thesis reports the calibration, imaging and analysis of one epoch of VLBI observations of the $v=1$ $J=1-0$ transition of SiO towards VY CMa. Full polarisation information was recorded, allowing high resolution synthesis maps of each of the four Stokes parameters to be produced.

A total of 81 maser components were extracted from the total intensity map, each approximately 1 mas in size. The emission spans approximately 100×80 mas in right ascension and declination and is concentrated to the east. The maser component positions were fitted to a ring of radius $\sim 3.2R_*$, or 7.2×10^{14} cm for a stellar distance of 1.5 kpc. If the stellar position is assumed to be the centre of this ring then almost all of the maser components fall within the inner dust shell radius, which is at $\sim 5R_*$. All of the maser components fall between $1.5R_*$ and $6R_*$.

A velocity gradient with position angle was observed in the sparsely filled western region of the maser ring. If interpreted as evidence of shell rotation, this gradient implies a rotational velocity of $v_{rot}\ \sin i = 18$ km.s^{-1}.

The fractional circular and linear polarisations of the maser spots were derived from the Stokes parameter maps. The mean fractional circular polarisation of the masers components was $\sim 2\%$ and the median fractional linear polarisation was $\sim 6\%$, with many spots displaying over $\sim 30\%$ linear polarisation. The mean circular polarisation implies a magnetic field of ~ 4 G in the SiO maser region if the polarisation is due to Zeeman splitting.

Two maser components display a rotation of linear polarisation position angle with velocity, possibly implying a connection between the magnetic field and the velocity field variations in the region of these components.

Acknowledgements

Thanks must go to my two supervisors - to Prof Jonas for his wisdom and Dr Kemball for his patience with my many emails. It was a privilege to learn from these two people.

To my family, who have seen too little of me these last years - thank you for the support, encouragement and the food-aid. Thanks to my digsmates and friends in Grahamstown who kept me sane (or insane, perhaps). Thanks to my lab-mates for the kaif runs. Thanks to Anthony, without whom I would probably still be trying to install AIPS. I must also thank the members of the Physics Department who have always been available to answer my questions and have written me thousands of testimonials, Dr Nathanson and Dr Haggard in particular. I received help from both my supervisors, my mother and Linda with proof-reading this thesis. Its a dreary job and I would like to thank them all for the time they spent helping with this.

I gratefully acknowledge the financial assistance of Rhodes University, the NRF, the Henderson Foundation, the Ford Foundation and the Ernst and Ethel Eriksen Trust. I would also like to thank the lecturers and coordinators of the NASSP programme from whom I received an excellent six months of coursework.

Finally, thanks to the Lord, my rest.

Contents

List of Tables

List of Figures

Chapter 1

Introduction

A star leaves the main sequence when hydrogen burning in its core is exhausted. After spending the bulk of its lifetime on the main sequence, shell burning begins and the star moves ultimately to the Asymptotic Giant Branch (AGB), a region of the Hertzsprung-Russel diagram characterised by low temperature and high luminosity. Post-main sequence stellar evolution is discussed in reviews by Iben and Renzini (1983) and Habing (1996), and the evolution of massive stars ($M_* \gtrsim 9M_\odot$) is discussed by Chiosi and Maeder (1986).

Towards the end of the main sequence a star consists of a core, which is mostly helium with a hydrogen burning center, surrounded by a large hydrogen envelope, or mantle. Hydrogen shell burning takes place at the core-mantle interface. When the core hydrogen burning stops the core contracts, heating the shell burning layer and increasing the energy output, which heats up the outer layers and causes them to expand. The star is located in the Red Giant Branch (RGB) of the Hertzsprung-Russel at this stage. Subsequent evolution of the star is determined by its main sequence mass.

As the hydrogen burning stops and the core contracts, the increased density will cause a rise in temperature of the core and helium burning nuclear reactions will begin. As helium burning progresses, the same situation results with a helium burning shell around a carbon-oxygen core. Whether or not this carbon-oxygen core will ignite upon compression depends on the initial mass of the star. In low and intermediate mass stars ($M_* \lesssim 5M_\odot$) the electron gas in the core degenerates, preventing the heating required to begin further nuclear reactions. In high mass stars ($M_* \gtrsim 6M_\odot$) the core is so hot that electron degeneracy never sets in. Consequently, nuclear burning of elements of increasing atomic weight takes place in the core, each burning the product of the previous reaction and leaving an active shell around the core. This process ultimately leads to the production of iron in the core, followed by a Type II supernova (Habing, 1996). During the shell burning stages the luminosity of a massive star is so great that it is labelled a supergiant star.

During the shell burning stages the star undergoes mass-loss caused by a stellar wind. Typical supergiants may lose up to 10^{-4} $M_\odot$ of their mass in a year (Stanek et al., 1995). This mass lost by late-type stars, as well as mass lost by means of supernova, enriches the interstellar medium (ISM). Consequently, studies of Asymptotic Giant Branch (AGB) stars and supergiant stars can reveal much about the chemical content of the ISM. The heavy element content, in particular, is predominantly provided by mass-loss from massive stars. This information about the ISM provided by studies of late-type stars is required for chemical models of galaxies (Chiosi and Maeder, 1986).

The extreme mass-loss rate around late-type stars creates an envelope of ejected matter around the star. The envelope can obscure direct optical observations of the star, which is why these stars are somewhat enigmatic. Much has been learned about late-type stars from molecular line emission and dust continuum emission. Relatively recent developments in infrared interferometry have facilitated high resolution images of stellar dust shells and estimates of stellar diameters (e.g. Danchi et al., 1994; Monnier et al., 1999b; Tevousjan et al., 2004). Another excellent probe of the circumstellar environment of late-type stars is maser emission. Astronomical masers were accidentally discovered by Weaver et al. (1965) in the OH 1665 line towards a number of radio sources. Since then, masers have been observed in many molecular lines and in a range of cosmic environments. OH, H_2O and SiO masers in particular are often observed in the circumstellar envelopes of late-type stars. Excitation temperature and molecular distribution arguments predict that the OH masers lie furthest from the central star, SiO masers closest to the star and H_2O masers between them (Elitzur, 1992, pg 225).

Because of their proximity to the star, observations of SiO masers provide information about the complex near-circumstellar envelope. The compact maser features in an SiO emission region trace the kinematics of the masing region. Evidence for expanding envelopes, rotation, asymmetric acceleration and bipolar outflows can potentially be found in maps of SiO maser emission. The magnetic field in this region can also be investigated through observations of the polarisation properties of the maser emission. There are a number of open questions about the magnetic fields around late-type stars, involving their magnitudes, origins and whether they are local or global in nature.

Maser emission is produced when the population levels of the masing molecule are inverted. This results in an effective negative absorption coefficient which accounts for the amplification of incident radiation. A pumping mechanism is required to maintain the population inversion. Pumping mechanisms are generally classified as radiative or collisional, where the molecules are excited by absorption of radiation, or by collisions with other molecules in the gas. Which pumping mechanism is at work in SiO masers towards late-type stars is still uncertain.

Maser emission is, by its very nature, very intense, and it is this intensity that makes them ideal probes of the near circumstellar environment which is obscured at other wavelengths by the dusty circumstellar cloud. Masers are also excellent probes due to their compactness and ability to sample the local conditions accordingly.

Maser emission can only occur in regions of coherent velocity because significant Doppler shifting of the radiation wavelength destroys the amplification process. Consequently the maser distribution is dependent not only on the general circumstellar conditions, but on the detailed velocity field, which may be complex. This causes the masers to be located in many spatially compact features in the emission region, each taking advantage of local line-of-sight velocity coherence and having its own particular Doppler-shift relative to the line frequency (Elitzur, 1992, pg 227). This characteristic of maser emission can be used to extract information about the gas velocity in the masing region, especially in relatively simple regions such as the constant radial outflow in which 1612 MHz OH masers reside. Many single-dish spectra of OH masers towards OH/IR stars and other late-type stars are double peaked, implying radial amplification of the maser emission in an expanding gas shell. Interferometric observations have confirmed this interpretation by showing compact caps of emission over the stellar position at the the extreme velocities.

The SiO maser emission resides in a much more complex region of the envelope of the order of 10^{14} cm from the star. This region between the photosphere and the dust formation point is sometimes termed the extended atmosphere, where stellar pulsations, shocks, and localised mass ejections play a large role in the velocity field. Very Long Baseline Interferometric (VLBI) observations of a number of Mira variables display erratic, clumpy rings of maser emission around the central star which are due to the tangential amplification of these masers.

It is only with resolution provided by VLBI that spatially resolved maps of the compact SiO maser components can be obtained. The Very Large Baseline Array (VLBA) is a dedicated VLBI array with baselines between stations in the continental US, Hawaii and the US Virgin islands in the Carribean. At its longest baseline, which is over 8000 km, the VLBA has a resolution of approximately 0.2 mas at a frequency of 43 GHz (Wrobel and Ulvestad, 2004). This resolution allows the imaging of individual maser features, which are ~ 1 mas in size.

VY CMa is a supergiant and varies irregularly. It displays OH, H_2O and SiO maser emission which has been widely observed. It is a particularly strong SiO source, with a wide range of detected masing transitions, from the ground state up to high frequency transitions in the $v = 3$ and $v = 4$ states, in three isotopes (^{28}SiO, ^{29}SiO, ^{30}SiO).

A VLBI study of the VY CMa $v = 1$ $J = 1 - 0$ transition of the most abundant isotope ^{28}SiO is reported in this thesis. The SiO maser emission is mapped in full polarisation at the high resolution provided by the VLBA, with the intention of investigating the kinematic and polarisation properties of the near-circumstellar envelope. The goal of this study is to derive information about the velocity field of the circumstellar envelope near to the star, which may give information about larger-scale mass-loss asymmetries. The polarisation of the maser emission also provides potential information about the role of a magnetic field in this region. The total intensity synthesis image produced in this thesis shows an emission region of approximately 100×80 mas in right ascension and declination, concentrated in the east. The emission was examined for evidence of a projected ring distribution by fitting a ring of radius ~ 3.2 R_* to the maser spot positions. If the centre of this ring is assumed to be the stellar position, then all of the SiO maser emission falls within the inner dust shell radius. The circular polarisation of the maser emission implies a magnetic field of ~ 4 G in the inner circumstellar envelope, assuming a Zeeman interpretation of the polarisation.

Chapter 3 outlines the theory of VLBI spectropolarimetry, in preparation for Chapter 4, in which the details of the data reduction procedure are presented. Chapter 2 is a review of the literature relevant to the target source, VY CMa. Finally, Chapter 5 presents the results of the VLBI observations and Chapter 6 provides an analysis of these results.

Chapter 2

A Review of the literature

2.1 Introduction

This chapter presents review of the published literature relevant to VY CMa. The basic physical properties of the star are discussed in Section 2.2. Subsequent sections provide a description of published observations at optical, infrared and radio wavelengths. The hydroxyl and water maser emission is discussed in Sections 2.6 and 2.7. The silicon monoxide maser emission is described in detail in Section 2.8. Finally the circumstellar environment and the magnetic field are discussed in Section 2.9.

2.2 Physical properties and classification

VY Canis Majoris, or VY CMa, is situated at right ascension 07 22 58.33, declination −25 46 03.2 (J2000) (Perryman et al., 1997). It is a supergiant star located in Sharpless 310, a HII region of diameter about 5° (Moran et al., 1973). The star is embedded in a red nebula which was first observed by Perrine (1923).

VY CMa is a highly luminous, variable M-type star. Its published spectral and luminosity classification has variously been given as M4e (Joy, 1942), M5e Ia (Humphreys, 1974) and M5e Ibp (Samus et al., 2004). Hyland et al. (1969) give an infrared classification of M3-6 Ib for VY CMa. Lada and Reid (1978) determined a luminosity of $5.6 \times 10^5 L_\odot$, implying a very massive star. More recently Le Sidaner and Le Bertre (1996) found a luminosity of $\sim 9 \times 10^5 L_\odot$ by modeling the mid-infrared

Distance [pc]	Method	Reference
1500	Associated objects	1
1500 ± 500	Associated objects	2
1350 ± 150	Star-count methods	3
1900	OH phase lag	4
1400 ± 140	H_2O proper motion	5
2860	Galactic rotation	6
1500	Median	

Table 2.1: The distance to VY CMa, as determined using different techniques. The median value is given in the bottom row.

References:
1. Herbig and Zappala (1970), 2. Lada and Reid (1978), 3. Armandroff and Herbst (1981), 4. Herman and Habing (1985), 5. Marvel (1996), 6. Yuasa et al. (1999)

emission using a spherical model. Monnier et al. (1999b) derived a much smaller luminosity range of $1.7 \times 10^5 L_\odot$ to $3 \times 10^5 L_\odot$ without making assumptions about the dust shell geometry. Monnier et al. (1999b) suggest that the difference between the latter two luminosity values may be due to the spherically symmetric model used by Le Sidaner and Le Bertre (1996). Molecular-band strengths imply a surface temperature of 2500° - 3000°K (Hyland et al., 1969). This low temperature and the high luminosity of VY CMa places the star in the upper right region of the Hertzsprung-Russel diagram. The General Catalogue of Variable Stars, 3rd ed. (Kukarkin et al., 1971) designates VY CMa as an Lc variable, which is an irregular variable supergiant of late spectral type.

2.2.1 Distance

A number of estimates of the distance to VY CMa are summarised in Table 2.1. Early estimates by Herbig and Zappala (1970) and Lada and Reid (1978) base their distance of 1500 pc on the star's association with τ CMa and the cluster NGC 2362. Most other methods have given similar distances, as seen in the table. Yuasa et al. (1999) used a galactic rotation model, coupled with the radial velocity value and infrared observations, to find a rather large distance of 2860 pc.

D_* [mas]	Method	Reference
19.0	Mid-infrared interferometry	1
22.0	Mid-infrared interferometry	1
40	Luminosity	2
< 20	Near-infrared aperture masking interferometry	3
20.0	Mid-infrared interferometry	4
18.7	Near-infrared interferometry	5
20	Median	

Table 2.2: The stellar diameter D_* as determined using different techniques. The median value is given in the bottom row.

References:
1. Danchi et al. (1994), 2. Kastner and Weintraub (1998), 3. Monnier et al. (1999b), 4. Monnier et al. (2000a), 5. Monnier et al. (2004)

2.2.2 Radius

Kastner and Weintraub (1998) estimated the radius of the central star using the luminosity observed by Lada and Reid (1978), $\sim 5 \times 10^5$ $L_\odot$, and assuming a distance of 1.5 kpc. This method gives a linear radius of approximately 3×10^3 $R_\odot$, which translates to an angular radius of 20 mas. Model fits to near-infrared visibility data from the Keck I telescope imply that the diameter of the central star is smaller than 20 mas (Monnier et al., 1999b). Monnier et al. (2004) fitted uniform disks to near-infrared K band IOTA data, giving an apparent diameter of 18.7 mas in this wavelength band. This diameter is not corrected for the effect of limb darkening so it is expected to be smaller than the actual stellar diameter. Mid-infrared emission is less effected by limb darkening. The mid-infrared model produced by Monnier et al. (2000a) used a stellar radius of 10 mas. Dust shell models fitted to 11 μm visibility data indicate stellar radii of 9.5 mas and 11 mas (Danchi et al., 1994). The model does not produce good fits to IRAS spectra. This is probably because the model assumes the shell is spherically symmetric, which is too simple an approximation for the complex features in the dust cloud around VY CMa. A number of VY CMa diameter estimates are shown in Table 2.2. A nominal diameter of 20 mas is consistent with most of these values.

2.2.3 Systematic and expansion velocities

The VY CMa stellar velocity and circumstellar expansion velocities have been measured by numerous authors using a variety of spectral lines. A list of some observed values is given in Table 2.3. The different molecular transitions may sample different radii from the star and thus may give different estimates of expansion velocity. The systemic velocities should be similar unless there are asymmetries in the circumstellar envelope, which there very possibly are.

One method of finding these velocity values is to fit a parabola to the thermal SiO emission spectrum. If the emission is assumed to originate in a uniformly expanding envelope, the stellar velocity is the central velocity of the symmetric spectral profile, and the expansion velocity is derived from the profile width. The velocities derived from several thermal SiO lines are shown in Table 2.3. Snyder et al. (1986) used the weak SiO maser pedestal to estimate a stellar velocity of approximately 21 km.s^{-1}. They do not derive an expansion velocity from the pedestal because its velocity range is much less than twice the expansion velocity determined by other methods (Snyder et al., 1986).

Another method makes use of the double-peaked OH maser spectrum described in Section 2.6. The mean velocity of the outer peaks of the OH maser emission is a good measure of the stellar velocity. The expansion velocity is derived from the OH maser spectra by taking half of the total velocity width of the spectrum. Bowers et al. (1983) used OH measurements to find a stellar velocity of 21.1 km.s^{-1} and an expansion velocity of 38.9 km.s^{-1}.

Richards et al. (1998) derive an outer velocity limit from VLBI observations of H_2O masers. They use velocity features most distant from the star to find a value of 35.5 km.s^{-1}. They also determine a proper motion expansion velocity of 31.7 km.s^{-1} by performing a least squares fit of the increase in distance of a maser feature from the star between the two epochs of observations, versus the initial distance of that feature from the star.

Spectra of other molecular lines in the circumstellar envelope can also be used to find the stellar and expansion velocities. Several CO spectra have been used to this end (Stanek et al., 1995; Zuckerman and Dyck, 1986; Nyman et al., 1992) as well as the HCN(1-0) spectrum (Nercessian et al., 1989). Sub-millimeter observations of SO

v_* [km.s^{-1}]	v_e [km.s^{-1}]	Method	Reference
17.6 ± 1.5	36.7 ± 2.0	Thermal SiO $v=0$ $J=2-1$	1
22.3 ± 2.3	32.3 ± 2.4	Thermal SiO $v=0$ $J=2-1$	2
17.9 ± 2.1	33.2 ± 2.1	Thermal SiO $v=0$ $J=3-2$	2
21.1	38.9	OH masers single dish	3
21		SiO maser pedestal	4
18.7	35.9	CO(2-1) emission	5
16.0	32	HCN(1-0) emission	6
19.5	43	Millimeter SO	7
	38.3	Thermal SiO $v=0$ $J=5-4$	7
24.2	30.8	CO(1-0) emission	8
17.6	32.6	CO(3-2) emission	9
	35.5 ± 3.0	H_2O masers, VLBI	10
	31.7 ± 2.5	H_2O masers, VLBI proper motion	10
20	25	Near-infrared H_2O	11
25	20	Millimeter H_2O	12
19.75	32.9	Median	

Table 2.3: Published stellar velocities, v_*, and expansion velocities, v_e, determined from different transitions. The median values are given in the bottom row.

References:

1. Reid and Dickinson (1976), 2. Wolff and Carlson (1982), 3. Bowers et al. (1983), 4. Snyder et al. (1986), 5. Zuckerman and Dyck (1986), 6. Nercessian et al. (1989), 7. Sahai and Wannier (1992), 8. Nyman et al. (1992), 9. Stanek et al. (1995), 10. Richards et al. (1998), 11. Neufeld et al. (1999), 12. Harwit and Bergin (2002)

provide a stellar velocity of 19.5 km.s^{-1} and an expansion velocity of 43 km.s^{-1} (Sahai and Wannier, 1992). The far-infrared H_2O lines observed by Neufeld et al. (1999) have central velocities ranging from 18 to 22 km.s^{-1} and are best fit with an outflow velocity of 25 km.s^{-1}. This outflow velocity is significantly lower than the values obtained by other methods, which range from about 30 to 40 km.s^{-1} Millimeter observations of ortho-water are centred on a velocity of 25 km.s^{-1}, and models of this data give an outflow velocity of 20 km.s^{-1} (Harwit and Bergin, 2002), also low compared to the majority of the values in Table 2.3.

2.2.4 Mass-loss rate

The mass-loss rate of VY CMa is high, typical of a supergiant star. When stars reach the AGB their mass-loss rates increase by several orders of magnitude. A number of methods have been employed to find the mass-loss rate of VY CMa. Some published values of the mass-loss rate are shown in Table 2.4.

The mass-loss can be estimated from model fits of the infrared observations, assuming the velocity and mass-loss rate to be constant and spherically symmetric (Jura and Kleinmann, 1990; Danchi et al., 1994). Marshall et al. (1992) find a mass-loss rate of 62×10^{-6} $M_{\odot}$ yr^{-1} by combining mid- and far-infrared data, though their model does not fit the data well. The infrared continuum spectrum was used by Harwit et al. (2001) to estimate the mass-loss rate. The mass-loss rate can also be derived from the OH maser shell radius (Bowers et al., 1983). This estimate is not very accurate because of the large uncertainty in the value of the shell radius, and because the VY CMa circumstellar cloud does not appear to be spherically symmetric (Bowers et al., 1983). The deviation from spherical symmetry is also a problem for submillimeter derivations of the mass-loss rate (Jura and Kleinmann, 1990). Optical and mid-infrared observations of the nebula by Smith et al. (2001) yield a mass-loss rate of approximately 3×10^{-4} $M_{\odot}$ yr^{-1}.

Zuckerman and Dyck (1986) and Stanek et al. (1995) estimated the mass-loss rate from a model of the CO(2-1) and CO(3-2) emission respectively. They both used distances of 1.5 kpc to VY CMa. Models of the CO(1-0) line (Loup et al., 1993) give a low mass-loss rate of 4.4×10^{-6} $M_{\odot}$ yr^{-1}, assuming a distance of 600 pc. Zuckerman and Dyck (1986), Stanek et al. (1995) and Loup et al. (1993) base their calculations on the models of Knapp and Morris (1985). The significant differences in their results are due to the different distances used, as well as to modifications made to the model by Loup et al. (1993) to use a different CO envelope size to that used in the original model. Knapp and Morris (1985) note the large uncertainties in mass-loss values calculated in this manner, which may be uncertain by a factor of ten. Even taking this into account, the value reported by Loup et al. (1993) is well below the median.

Humphreys et al. (2005) have suggested that the high observed mass-loss rate for VY CMa is actually due to the combined effect of multiple localised high mass-loss events, evidenced by arcs and loops in the envelope, combined with gas escaping from

$\dot{\mathcal{M}}$ $[10^{-4}\ \mathrm{M}_\odot\ \mathrm{yr}^{-1}]$	Wavelength band	Reference
2.3	OH masers	1
1	CO(2-1)	2
1	Infrared	3
0.62	Submillimeter	4
0.044	CO(1-0)	5
3.1	Infrared	6
3.5	CO(3-2)	7
4	Infrared spectrum	8
3	Optical and mid-infrared	9
1.65	Median	

Table 2.4: Mass-loss $\dot{\mathcal{M}}$ determined in a number of ways. The median value is given in the bottom row.

References:
1. Bowers et al. (1983), 2. Zuckerman and Dyck (1986), 3. Jura and Kleinmann (1990), 4. Marshall et al. (1992), 5. Loup et al. (1993), 6. Danchi et al. (1994), 7. Stanek et al. (1995), 8. Harwit et al. (2001), 9. Smith et al. (2001)

low density regions of the envelope.

2.2.5 Inner dust shell radius

Several estimates of the inner dust shell radius have been published, based on mid-infrared models. Le Sidaner and Le Bertre (1996) estimate an inner dust shell radius of approximately 1200×10^{-6} pc, or $\sim$ 160 mas at a distance of 1.5 kpc. They note that their VY CMa model fit is not particularly satisfactory. Monnier et al. (2000a) find a value of 50 mas and Danchi et al. (1994) a value of 40 to 50 mas for optical minimum and maximum, which correspond to stellar radii of 9.5 and 10 R_* respectively. Monnier et al. (2004) produced a dust shell model of K-band data, for which they use an inner dust shell radius of 65 mas. Table 2.5 lists these estimates of the inner dust shell radius.

R_{dust} [mas]	Reference
40-50	1
160	2
50	3
65	4
50	Median

Table 2.5: Published estimates of the inner dust shell radius R_{dust}. The median value is given in the bottom row.

References:
1. Danchi et al. (1994), 2. Le Sidaner and Le Bertre (1996), 3. Monnier et al. (2000a), 4. Monnier et al. (2004)

2.2.6 Evolutionary status

Although VY CMa is currently accepted to be a late-type star, some early observers identified it as a protostar. Herbig and Zappala (1970) noted that VY CMa is embedded in the same nebula that contains τ CMa and the cluster NGC 2362, which they interpreted as evidence that VY CMa is a young star.

However, the 1612 MHz OH line present in the spectrum points to VY CMa being an evolved star, as similar emission lines are associated with Mira-type variables. The vibration-rotation bands of CO present in the infrared spectrum of VY CMa are also characteristic of a late M-type supergiant (Hyland et al., 1972). The position of VY CMa on the Hertzsprung-Russel diagram is that of a $\sim$ 10 $M_\odot$ star which has evolved off the main sequence (Hyland et al., 1969). Other estimates of the stellar mass have been derived from positions on the Hertzsprung-Russel diagram. de Jager (1980, pg 293) estimate a mass of 20 $M_\odot$, and Wittkowski et al. (1998) find a mass of between 30 and 40 $M_\odot$. The high luminosity and mass-loss rate displayed by the star support its classification as a supergiant.

The exact evolutionary state of the late-type star VY CMa is still a matter of research. VY CMa could be beginning to expel its envelope, or it could be creating a thick cocoon of dust and gas, similar to those observed around optically obscured carbon and M-star near the top of the AGB (Smith et al., 2001). Chiosi and Maeder (1986) proposed that red supergiants with initial mass of between 20 $M_\odot$ and 60 $M_\odot$

develop into Wolf-Rayet stars through mass-loss. VY CMa may be in the process of evolving from its red supergiant stage to become a Wolf-Rayet star. This possibility is supported by the high mass-loss rate of VY CMa (Wittkowski et al., 1998). It has also been suggested that VY CMa may be the progenitor of a star such as IRC +10420 (Smith et al., 2001; Fransson et al., 2002), which is thought to be transitioning between the red supergiant and Wolf-Rayet stages (Fransson et al., 2002). If the envelope of VY CMa is disk-like, this could be the basis for bipolar outflows in later stages of evolution, such as are observed around IRC +10420. Type IIn supernovas are probably the end point of stars like VY CMa and IRC +10420 (Fransson et al., 2002).

2.3 Optical observations

Less than 1% of the measured luminosity from VY CMa is emitted in the optical region (Hyland et al., 1969). The striking optical nebula surrounding VY CMa is about 8 × 12 arcseconds in size with a tail extending to the east (Perrine, 1923). Early optical observations reported a pair of bright central stars in the reflection nebula, and a number of other variable bright features in the nebula, which may have been stars or knots (Wallerstein, 1958). Later optical evidence indicated that the bright features were condensations in the nebulosity (Feast, 1970; Worley, 1972). Observations by Herbig (1972) in the 6500Å region showed the nebula to be highly radially polarised. The knots in the nebula displayed the same radial polarisation as the background nebula, implying that they were not stars. The close companion which had put VY CMa in binary star catalogues was not visible. Wallerstein (1978) also argued that the potential binary companion is not a star, based on the unreasonably high mass implied by the supposed binary period, and synchronous variations in luminosity of the companions. Herbig (1972) tabulated the positions of six bright features he observed, labelling them A through F, where A is the central star.

Hubble Space Telescope (HST) images by Kastner and Weintraub (1998) at 3460Å and 5500Å show a bright core near to the eastern edge of the large reflection nebula. The nebula is clumpy, asymmetric and elongated. The optical light received from the core is due to scattering rather than direct emission from the stellar photosphere. The radius of the core region is approximately 100 mas. Kastner and Weintraub (1998) suggested that VY CMa itself lies to the northeast of the core, obscured by a dusty envelope. Smith et al. (2001) used the HST to obtain images of VY CMa at different wavelengths to Kastner and Weintraub (1998), 4090.1Å, 5476.3Å, 6563.7Å and 10183.5Å. These images are also complex, and do not show any clear axisymmetry. The brightest nebulosity is located southwest of the star. The Smith et al. (2001) images feature reflection arcs, bright condensations and knots. Compact knots, of the order of 0.07 arcseconds, and thin filamentary structures are also visible around the star (Smith et al., 2001).

The optical spectrum of VY CMa displays emission lines of TiO, ScO, the resonance lines of NaI, KI, RbI and the intercombination line of CaI at 6572Å (Wallerstein, 1978). In later observations by Wallerstein (1986) the optical spectrum had undergone some changes. Absorption lines that had been measurable in the 1960s and 70s between 5200Å and 5500Å region were depressed, the molecular emission was raised and new neutral line emission was observed.

Wright et al. (1990) note that the inferred optical position of VY CMa is not in good agreement with the SiO, OH and H_2O maser positions. They suggest that this may be due to confusion between knots or extinction in the nebula. Using the table of Herbig (1972), if the optical position is associated with component A, the masers would be close to component F, 1.1 arcseconds removed from the optical position (Wright et al., 1990).

At visible wavelengths the amplitude of VY CMa varies irregularly. It can range from a few tenths of a magnitude to three magnitudes on the timescale of months (Martinez et al., 1988). A possible explanation of this is a patchy dust cloud closely surrounding the central star. This inner dust cloud allows beams of light from the star to illuminate an outer cloud through the holes. This would account for the irregular optical variations (Wallerstein, 1978). Long-term AAVSO observations show a clear periodicity of approximately 1500 days (Sudol et al., 1999; Pardo et al., 2004).

VY CMa displays 18.3, 15.0 and 12.2% linear polarisation in the U, B and V bands respectively (Serkowski, 1969) and up to 30% linear polarisation in the 0.36 - 0.94 μm range (Shawl, 1969). The degree of linear polarisation is strongly dependant on the wavelength of the observation, with increasing polarisation at longer wavelengths

(Serkowski, 1969; Shawl, 1969). Dyck et al. (1971) observed a 14.3 ± 0.8% linear polarisation towards VY CMa, averaging the B and V band data. Serkowski (1969) argued that the polarisation is due to scattering by circumstellar dust.

2.4 Infrared observations

In the late stages of stellar evolution the mass-loss process plays a large role in the development of a star, creating an envelope of dust and gas. Infrared emission is observed in the form of molecular lines and continuum emission from dust in the envelopes of such stars (Stanek et al., 1995).

VY CMa was found to be an exceptionally bright 2μ source on the Caltech 2μ Sky Survey (Neugebauer and Leighton, 1969). More than 75% of its measured luminosity is at wavelengths longer than 3μm. It is one of the brightest sources in the sky at wavelengths longer then 5μm (Hyland et al., 1969). The infrared energy distribution of VY CMa is non-Plankian, and displays radiation excess over the infrared region beyond 2-3μm (Gehrz, 1972). This excess is caused by the thermal emission from the circumstellar dust which is heated by the star (Herbig and Zappala, 1970).

VY CMa was included in a mid-infrared spectral variability study performed by Monnier et al. (1998) and found to show no significant changes over the four year period of the observations.

Gehrels (1972) detected a small degree of circular polarisation in the infrared emission towards VY CMa. Forbes (1971) observed linear polarisation in the J, H, K and L bands, where the highest polarisation of over 4% was observed in the H band. The star was observed daily for five days, and the polarisation from the nebula found to be constant, while the position angle of the polarisation varied. Forbes (1971) proposed that this is due to changing particle orientation. Hashimoto et al. (1970) also observed greater linear polarisation in the H band than the K band. The infrared polarisation may be caused by scattering, by dust particles aligned by a magnetic field or by non-spherical dust particles aligned by outflow (Hashimoto et al., 1970).

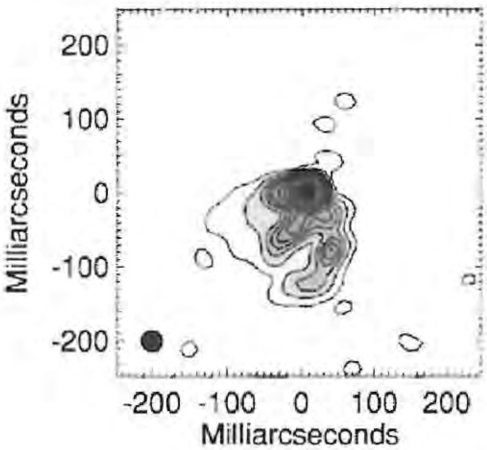

Figure 2.1: Image of VY CMa observed at 1.65 μm in December 1997 by Monnier et al. (1999b).

2.4.1 Infrared continuum images

Diffraction-limited speckle-masking interferometry of VY CMa was performed by Wittkowski et al. (1998) at near-infrared wavelengths. Their images show a non-spherical envelope around VY CMa. Gaussian fits to the circumstellar envelope were performed, with FWHM of 60 x 83 mas, 80 x 116 mas and 138 x 205 mas at 0.8 μm, 1.28 μm and 2.17 μm. These images have resolutions of 46 mas, 73 mas and 124 mas respectively.

The higher resolution Keck near-infrared aperture masking interferometry maps of Monnier et al. (1999b) show definite one sided emission at 1.65 μm, 2.26 μm and 3.08 μm. Figure 2.1 is a 1.65 μm map that shows the emission extending south of the core, while the north and northeast is almost devoid of emission. This pattern is present in the 2.26 μm and 3.08 μm images too. The polarisation angles give a possible 170° axis of symmetry for the near-infrared emission. The images all show a bright knot of emission at a position angle of 155°, about 65 mas from the core (Monnier et al., 1999b). Monnier et al. (2004) published K-band images of VY CMa using Keck aperture masking and the Infrared-Optical Telescope Array (IOTA). The addition of the IOTA data provides a resolution of approximately 20 mas, even higher than that of the original Keck images. These images also show the dust shell to be

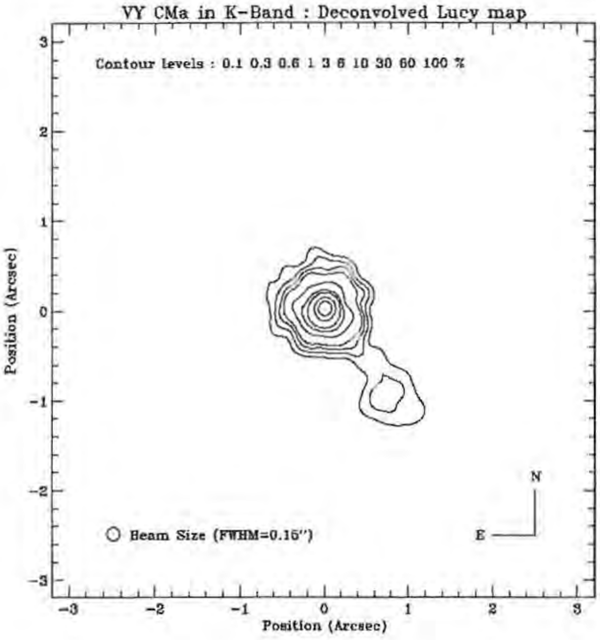

Figure 2.2: Image of VY CMa in the K-band, taken from Cruzalebes et al. (1998).

highly asymmetric, with something of an arc to the south of the star.

Cruzalebes et al. (1998) used the European Southern Observatory 3.6 m telescope at 2.2 μm to detect a clump of emission approximately 1.3 arcseconds southwest of the star, at position angle of 216°. An adaptive optics system was used to obtain the image, which is shown in Figure 2.2. The southwestern feature has a diameter of approximately 0.9 arcseconds. Monnier et al. (1999b) confirm the detection of this feature at 1.25 μm with the same telescope, using both the SHARPII+ and COMIC cameras. They report that the structure is almost two orders of magnitude brighter than other circumstellar features.

Spatial heterodyne interferometric data at 11.106 μm were fitted to a circular model of uniform brightness to yield a diameter of 600 mas (Sutton et al., 1977). The fit was not good however, and Sutton et al. (1977) rejected the circular model as an explanation of the observations. Monnier et al. (2000a) also fitted a spherically symmetric model to mid-infrared interferometric images of VY CMa at 11.15 μm. The model is considered to be a rough approximation to the true dust distribution, which may be asymmetric or time variable. An inner radius of 50 mas was found for the mid-infrared emission region (Monnier et al., 2000a). Mid-infrared images at 4.7 μm, 8.4 μm and 9.7 μm produced by Smith et al. (2001) show the dust distribution to be elongated in a roughly east-west direction.

2.4.2 Molecular infrared emission

A number of molecules have been detected towards VY CMa in the infrared. Kemper et al. (2003) observed CO(2-1), CO(3-2), CO(6-5), and CO(7-6) lines towards VY CMa. Out of a sample of approximately twenty asymptotic giant branch stars and red supergiants, they found that only in VY CMa do the CO line strengths increase for higher rotational transitions. The profiles of the higher transitions lines are significantly different to the lower transition lines.

The strength of the H_2O band indicates that VY CMa is an oxygen rich star (Hyland et al., 1972). Neufeld et al. (1999) used the Infrared Space Observatory to detect many far-infrared water vapour rotational transitions towards VY CMa. They also detected an OH absorption feature, which probably arises in a shell around the central star where the outflowing H_2O is photodissociated by interstellar radiation. The H_2O lines appear to originate in a region where the outflow has almost reached the terminal velocity.

Ammonia absorption lines have also been observed towards VY CMa (McLaren and Betz, 1980). The velocity range of the ammonia features is almost the same as the blueshifted 1612 MHz OH line. Interferometric studies of ammonia around VY CMa were made by Monnier et al. (2000b).

Detections of HCN $J = 1 - 0$ and $H^{13}CN$ $J = 1 - 0$ have been reported towards VY CMa, which is unusual for an oxygen-rich circumstellar envelope (Nercessian et al., 1989).

Gillett et al. (1970) observed a broad absorption feature between $\lambda \approx 7.7\mu$m and $\lambda \approx 9\mu$m. They attribute this feature to SiO molecules in the extended atmosphere of VY CMa. Further infrared observations, however, indicate that this depression is too deep to be due to SiO absorption. The depression observed has a depth of about 30%, whereas a silicon absorption band should only depress the continuum by about 5% (Geballe et al., 1979). The silicate emission feature at 9.7μm observed by

Merrill and Stein (1976) is nearly flat in more recent spectra observed by Monnier et al. (1998). Monnier et al. (1999a) suggest that the long-term variability of this feature may be due to changing chemical abundances in the envelope. Geballe et al. (1979) observed a number of ^{28}SiO, ^{29}SiO and ^{30}SiO infrared lines towards VY CMa. The observations show the infrared SiO emission to be located about 150 mas from the star.

2.5 Radio and sub-mm observations

The radio continuum emission catalogue of Wendker (1995) includes observations of VY CMa in the 1449 MHz to 394 GHz range, with a maximum flux of almost 3 Jy for the 394 GHz observation. Knapp et al. (1995) performed 3.6 cm interferometric observations of the continuum emission towards VY CMa at a level too weak to be due to an HII region and too strong to be thermal emission from the stellar photosphere. They suggest that this emission may be due to dust, or a partially ionized photosphere. Shinnaga et al. (2004) report Submillimeter Array (SMA) interferometric measurements of the continuum radiation at 216 GHz to be 270 ± 40 mJy, at 301 GHz, 340 ± 10 mJy, and at 658 GHz to be 7.8 ± 2.6 Jy. They claim that this continuum emission is from dust, with a fraction contributed by the star (Shinnaga et al., 2004).

Many thermal radio and sub-millimeter lines have been observed towards VY CMa and are summarised in Table 2.6. The $v=0$ $J=1-0$ SiO line was imaged with the VLA and appears to have a bipolar structure (Shinnaga et al., 2003). The emission displayed high linear polarisation aligned with the proposed northeast - southwest polar axis, which may imply that the linear polarisation is linked to the outflow (Shinnaga et al., 2003).

VY CMa is a strong OH, H_2O and SiO maser source. The relative sizes and distributions of the emission regions for each of these species is shown in Figure 2.3. The published observations of each of these masing species are discussed in the following sections.

Radio line	Reference
SO $2_2 - 1_1$	1
SO $6_5 - 5_4$	2
SO $8_8 - 7_7$	2
SO_2 $3_{1,3} - 2_{0,2}$	1
SO_2 $10_{1,9} - 10_{0,10}$	1
SO_2 $10_{0,10} - 10_{1,9}$	1
CO(1-0)	3
CO(2-1)	4
CO(3-2)	5
SiO $v=0$ $J=1-0$	6
SiO $v=0$ $J=2-1$	7
SiO $v=0$ $J=3-2$	7
SiO $v=0$ $J=5-4$	2
^{29}SiO $v=0$ $J=8-7$	8
CS(5-4)	9
CN(2-1)	10
H_2O^+	11
H_2S $1_{1,0} - 1_{0,1}$	1

Table 2.6: Thermal radio and sub-millimeter lines observed towards VY CMa.

References:
1. Omont et al. (1993), 2. Sahai and Wannier (1992), 3. Nyman et al. (1992), 4. Zuckerman and Dyck (1986), 5. Stanek et al. (1995), 6. Shinnaga et al. (2003), 7. Wolff and Carlson (1982), 8. (Gonzalez-Alfonso et al., 1996), 9. Bujarrabal et al. (1994), 10. Bachiller et al. (1997), 11. Phillips et al. (1992)

2.6 OH masers

VY CMa has been classified as a type IIb OH source (Turner, 1970). Type IIb sources are characterised by the 1667 MHz and 1665 MHz OH main lines and the 1612 MHz satellite line found in emission, and the 1720 MHz satellite line in absorption. The 1612 MHz line is the strongest of the emission lines. This class of OH source is generally associated with IR stars.

2.6.1 OH masers at 1612 MHz

Single-dish spectra of OH 1612 MHz satellite line masers towards VY CMa display the double peaked profile typical of late-type stars. The two peaks are indicative of an

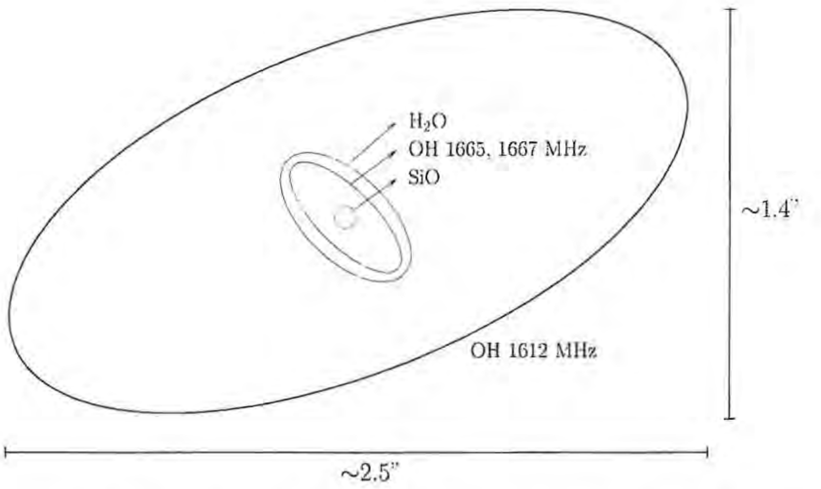

Figure 2.3: Sketch of the OH, H_2O and SiO maser distributions, based on observations discussed in Sections 2.6, 2.7 and 2.8.

expanding envelope. They are created by maser emission from the near and far sides of the stellar envelope, where the velocity coherence is greatest (Cohen, 1987). The 1612 MHz OH spectra also show a great deal of fine structure. They undergo large flux changes on the time scale of days, but show hardly any long term variation. The dramatic short term variations are probably caused by small maser hotspots which are not fully saturated (Herman and Habing, 1985). Fourier analysis of the strongest feature in the 1612 MHz spectrum observed by Herman and Habing (1985) displays a main period of about 1000 days, an intermediate time scale of about 180 days, and short term variations on a scale of less than two days.

Early interferometric studies by Masheder et al. (1974) show the 1612 MHz masing region to extend 2.2×1.4 arcseconds with a major axis at 158°. Interferometric maps by Moran et al. (1977) show an emission region of 2.5 arcseconds across, with maser spots of approximately 0.06 arcseconds in size. The general features of this map match those of Masheder et al. (1974), but the details of individual maser spots do not match well. Both Masheder et al. (1974) and Moran et al. (1977) assumed a single component model for each channel of their observations. This assumption is in fact not true for the 1612 MHz line of VY CMa, which displays a very complex spectrum (Reid and Muhleman, 1978). Reid and Muhleman (1978) used a method of

Fourier inversion and cleaning to avoid this assumption. They produced VLBI maps which were also slightly elongated and have a diameter of approximately 2 arcseconds. Most of the maser components were unresolved or partially resolved by the baseline lengths used, putting an upper limit of 0.03 arcseconds on the maser spot size. Reid and Muhleman (1978) note that their map would match the Masheder et al. (1974) 1612 MHz maser map well if the right ascension and declination axes were reversed, which they attribute to a sign error in the Masheder et al. (1974) data. Reid et al. (1981) observed the OH maser emission with the VLA. He found the diameter of the 1612 MHz maser region to be about 1.6 arcseconds. Bowers et al. (1981) found the angular size of the 1612 MHz emission region to be about 2.5 × 1.4 arcseconds across, using the VLA. The geometry of these maps is discussed in Bowers et al. (1983), where it is noted that the maser distribution displays a north-south elongation, and shows a spatial offset between the extreme blueshifted and redshifted maser clusters. The maps also show evidence of symmetry between low and high velocity emission, equidistant from the stellar velocity.

2.6.2 Main line OH masers

Single dish spectra of the 1667 MHz line display a wide emission plateau with maser lines superimposed on the blue side of the spectrum (Morris and Bowers, 1980). The plateau emission changes very little with time and resembles the non-masing SiO ground state emission. This indicates that the 1667 MHz OH emission plateau may arise in the same region as the non-masing SiO emission, which is in the extended region where the gas around the star is at terminal velocity. The 1667 MHz plateau stayed constant over three observations separated by about six months (Morris and Bowers, 1980). The spectrum contains an intense, conspicuous feature at -2.1 km.s^{-1}. This component has varied from 80% right hand circular polarisation in 1969, to 100% left hand circular in 1976, remaining entirely left hand circular throughout the observing periods of Benson and Mutel (1982). The 1665 MHz emission displays a more irregular and compact plateau, where the most intense maser lines are again blueshifted (Morris and Bowers, 1980).

Reid and Muhleman (1978) produced VLBI maps of the 1665 MHz and 1667 MHz OH emission. The 1667 MHz map had a diameter of approximately 250 mas and the

1665 MHz map has a diameter of approximately 350 mas and both maser distributions are elongated with a position angle of roughly 60°. High resolution VLBI images of the 1665 MHz and 1667 MHz OH transitions display clouds of masers of about the same size as the Reid and Muhleman (1978) images (Benson and Mutel, 1982). The 1665 MHz maser region is approximately 300 × 200 mas in right ascension and declination, extending in a northeast - southwest direction. The emission is concentrated to the southwest of this region in a 200 × 100 mas area. None of the components in this map were completely unresolved, giving a minimum size of 5 mas for an individual maser component. The 1667 MHz maser region is approximately the same size as that of the Reid and Muhleman (1978) map. It is elongated along a position angle of about 85°, which differs somewhat from the direction of elongation of the Reid and Muhleman (1978) map.

2.7 H_2O masers

The first observations of H_2O masers towards VY CMa were made by Knowles et al. (1969) of the 6_{16} - 5_{23} rotational transition of ortho-H_2O, which has a rest frequency in the 22 GHz band. Single dish spectra of these H_2O masers typically consist of a strong central component, flanked by two weaker components.

The H_2O 22 GHz masers around late-type stars are generally thought to be collisionally pumped (Deguchi, 1977; Cooke and Elitzur, 1985). They appear to be located in a thick accelerating shell (Richards et al., 1998).

2.7.1 Interferometric observations

The H_2O masers require higher excitation temperatures than OH masers, and are consequently located closer to the star (Moran et al., 1979). VLBI observations made by Rosen et al. (1978) yield a diameter of 200 mas for the H_2O masing region, which is approximately one tenth of the diameter of the OH maser region. The H_2O maser emission consists of individual masing components of around 2.5 mas in size. Bowers et al. (1993) performed 22 GHz VLA observations of VY CMa. Emission was detected throughout the 0.6 - 41.7 km.s^{-1} velocity range of the observations. This velocity range does not cover the entire range of previously observed velocities. Their map is complex, with over three hundred individual maser features detected. The most extreme blueshifted spots are clustered in one region, while the extreme redshifted spots are clustered in two separate regions, about 150 mas apart. The entire H_2O maser region covered about 600×500 mas in right ascension and declination. MERLIN observations by Yates and Cohen (1994) also show a masing region of approximately 400 mas. The emission shows a decrease in intensity with distance from the star.

Marvel (1996) observed the H_2O masers with the VLA and VLBA. His images show emission over nearly 600 mas, elongated in a northeast - southwest direction.

Further observations by Richards et al. (1998) were made using the upgraded MERLIN array. The maser region covers 700 × 400 mas in right ascension and declination. Emission close to the stellar velocity is spread throughout this region. The most extreme redshifted and blueshifted emission is much more compact and weaker, and is located close to the centre of the maps (Richards et al., 1998). A map of the location of their Gaussian fitted maser spots is shown in Figure 2.4.

The central location of the extreme velocity emission was also observed by Marvel (1996). The most redshifted and blueshifted maser regions in the maps of Richards et al. (1998) are offset from each other by about 100 mas. This could be due to a deviation from spherical symmetry, or to the true back and front of the maser shell not being observed. Richards et al. (1998) used images separated by nine years to derive the proper motions of the maser components. Only 9 of the 36 clearly matched maser features did not move away from the assumed stellar position. Richards et al. (1998) propose that the 22 GHz H_2O emission is located in areas of greater density than the surrounding envelope.

2.7.2 Variability

Gomez Balboa and Lepine (1986) examined the variability of the H_2O masers, using data acquired from 1969 to 1976. Cox and Parker (1979) considered the maser variability over the shorter period of 1974 to 1977. The data of both Gomez Balboa and Lepine (1986) and Cox and Parker (1979) show correlated short-term variability in three separate features at different velocities. This may indicate a common pump source for most of the H_2O masers. Wu Zheng et al. (1998) observed short term variations of the water masers with a period of 10.3 days in both of the strongest maser

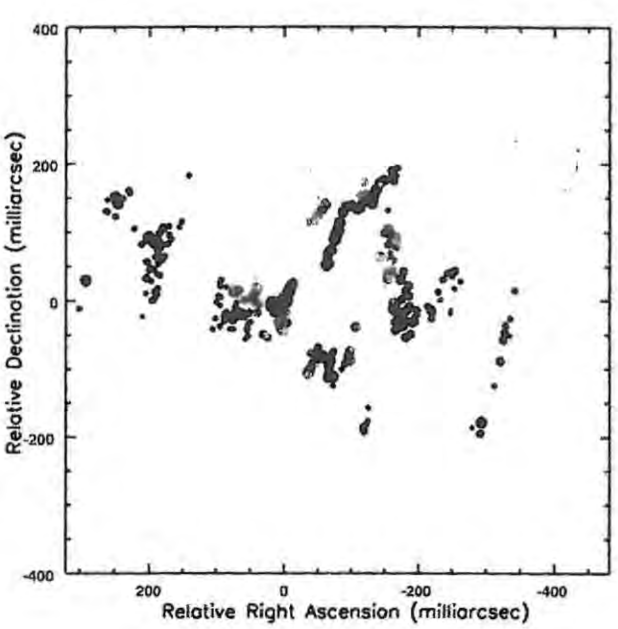

Figure 2.4: The location of H_2O maser spots observed with MERLIN, from Richards et al. (1998). They grey scale of the spots represents their velocity, where the dark spots are redshifted and the light spots blueshifted. The size of each spot is proportional to its flux density.

peaks at 14 km.s^{-1} and 20 km.s^{-1}. They propose periodic shocks as the cause of these variations. Fourier analysis by Cox and Parker (1979) of the light curve indicated a period of 350 days present in all three velocity features. This period is possibly related to an infrared pumping mechanism. The Fourier analysis also revealed periods of several years, which may be due to rotation of clouds in a disk. This period is of the same order as the ~ 1500 day period observed in the optical and ~ 1000 day period observed in the OH maser emission, perhaps implying similar origins. Over the long term some of the velocity components vary independently. The intensity of the 22 GHz H_2O spectrum decreased steadily over the duration of the Cox and Parker (1979) observations, but this decrease is not seen in the later Gomez Balboa and Lepine (1986) observations.

Imai et al. (1997) used a 1300 km baseline between two telescopes of the NRO in Japan to observe water masers towards a number of late-type stars. They observed each source on two occasions separated by a six month period, and note that the maser emission towards VY CMa is much more stable than that around the semi-regular variables in their sample.

2.7.3 Polarisation

Observations of the 22 GHz H_2O masers performed by Knowles and Batchelor (1978) in 1976 display 3% linear polarisation in the velocity range +16 to +23 km.s^{-1}. A feature at -5 km.s^{-1} and the strong feature at +14 km.s^{-1} were not polarised, implying that the H_2O masers are not radiatively pumped (Barvainis and Deguchi, 1989). High resolution VLBI maps of the H_2O maser region show circular polarisation in seven of the ten brightest maser features (Vlemmings et al., 2002a). The shape and line widths of maser components in the total power spectra of Vlemmings et al. (2002a) show the masers to be at most marginally saturated.

2.7.4 High frequency water masers

A number of emission lines from vibrationally excited water have been detected towards VY CMa. The 232 GHz v_2 $5_{50} \rightarrow 6_{43}$ transition and the 96 GHz v_2 $4_{40} \rightarrow 5_{33}$ transitions were detected by Menten and Melnick (1989). The v_2 excited water emission probably arises closer to the star than the 22 GHz emission, possibly from the same region as the SiO emission. These two spectra have their strongest peaks at the same velocity as the strongest peak in the SiO spectrum. Similar densities are required for the excitation of SiO and H_2O v_2 masers (Menten and Melnick, 1991).

The 321 GHz transition of ortho-H_2O also displays strong maser action (Menten and Melnick, 1991; Yates et al., 1995). Its spectrum is much more complex than the 22 GHz spectrum, and its velocity range smaller. This is consistent with the population inversion models of Yates et al. (1997), in which the 321 GHz transition is strongly inverted in a much more restricted set of physical conditions than the 22 GHz transition. The 321 GHz masers probably arise in a warmer and denser region, closer to the star than the 22 GHz masers. The 325 GHz line profile of para-H_2O also displays strong emission and broad emission wings. It shows a similar profile to the 22 GHz masers. This fact, coupled with the similar excitation temperatures of these two transitions, indicate that they possibly arise in the same regions and are generated by the same inversion mechanism (Yates et al., 1995). The 557 GHz $1_{10} \rightarrow 1_{01}$ line of ortho-H_2O has also been detected (Harwit and Bergin, 2002). Menten and Young (1995) observed the 658 GHz line of vibrationally excited water towards VY CMa. The emission profile is broad and centred on the stellar velocity. The photon luminosity of the 658 GHz line is three times the photon luminosity of the 22 GHz line, and comparisons of this line with the $v=1$ and $v=2$ $J=1-0$ SiO masers observed by Martinez et al. (1988) shows that the 658 GHz line is always more luminous than these SiO lines. Menten and Young (1995) propose that the distinct difference between SiO and 22 GHz H_2O lines, and the 658 GHz H_2O lines is due to the 658 GHz line being heavily saturated.

2.8 SiO masers

Because SiO masers are the object of this dissertation, the literature surrounding this topic will be discussed in greater detail. SiO is a non-paramagnetic simple rotor, so radiative transitions are limited by the $\Delta J = \pm 1$ selection rule. Vibrational transitions are most significant for $\Delta v = \pm 1$ transitions. Higher Δv transitions are much weaker, with strengths decreasing about two orders of magnitude for every Δv unit (Elitzur, 1992, pg 280). The first few vibration-rotation levels of SiO are shown in Figure 2.5.

SiO maser spectra from evolved stars usually display several narrow velocity components of very high flux densities. The high flux density and narrow line-widths indicate that these masers are produced within a few stellar diameters of the star (Moran et al., 1979). VLBI observations of Mira variables indicate that the $v=1$ $J=1-0$ masers are formed between the photosphere and the dust-formation point, and are distributed in a sparsely filled ring around the central star (e.g. Diamond et al., 1994). Further away from the star, the silicon forms part of the dust grains in the shell. Unlike the OH and H_2O masers, SiO masers are not situated in the stellar wind (Lockett and Elitzur, 1992).

For SiO masers to occur, the molecular density must be between 10^9 and 10^{10} cm^{-3}

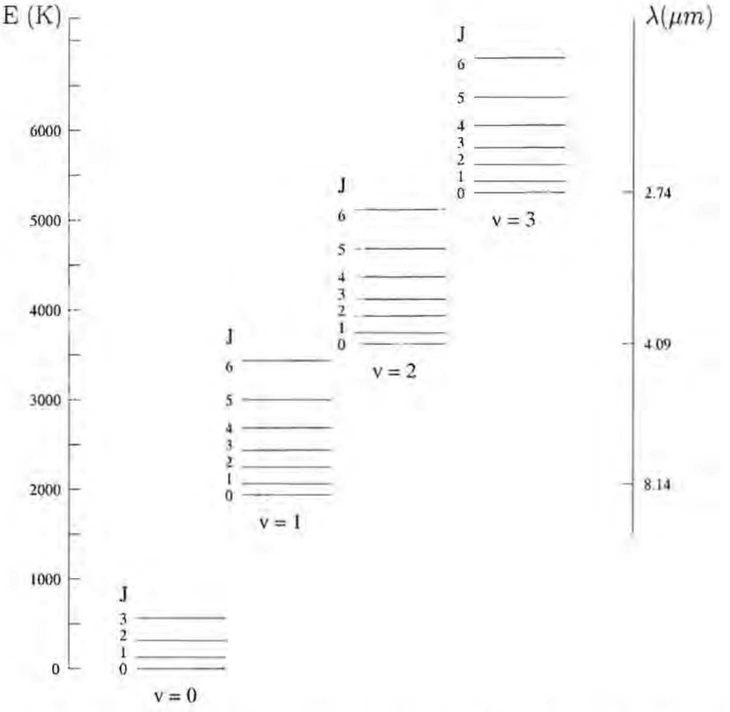

Figure 2.5: Vibration-rotation levels of SiO (Elitzur, 1992, Figure 3.3)

(Lockett and Elitzur, 1992) and Bujarrabal et al. (1994) estimated a fractional abundance of SiO in the circumstellar envelope of 5.4×10^{-5} relative to hydrogen.

2.8.1 Observed SiO maser lines in single-dish studies

VY CMa was among the first sources detected in SiO maser emission. The first detection of SiO towards VY CMa was the $v=1$ $J=2-1$ line, obtained by Buhl et al. (1974). Many other SiO maser lines have since been observed towards this star, which is one of the most intense known SiO emitters and is detected in an extensive set of SiO maser transitions. A list of SiO maser lines observed to date towards VY CMa is given in Table 2.7. The rest frequencies of the maser lines are included where available, from the "NIST Recommended Rest Frequencies for Observed Interstellar Molecular Microwave Transitions" (Lovas, 2004). The SiO maser position is right ascension 07 22 58.334 ± 0.15, declination −25 46 02.99 ± 0.25 (J2000) (Wright et al., 1990). It is offset from the optical position of VY CMa, as mentioned in Section 2.3.

In searching for $v=0$ $J=2-1$ masers, Buhl et al. (1975) found that of the observed sources, only VY CMa displayed evidence of non-thermal maser emission in this line. The velocity at which the possible $v=0$ $J=2-1$ maser peak is located coincides with a minimum in the vibrationally excited masers. The ground state $J=2-1$ line is about twenty times weaker than the $v=1$ $J=2-1$ maser line (Bujarrabal et al., 1994). The high polarisation of some of the bright $v=0$ $J=2-1$ and $v=0$ $J=1-0$ lines is also indicative of maser emission (Shinnaga et al., 1999, 2003).

The maser lines in the first and second vibrational levels are of similar intensities, except for the $v=2$ $J=2-1$ and $J=6-5$ lines, which are much weaker. The $v=2$ $J=2-1$ maser emission is unusually weak, even beyond that expected for a higher rotational transition, most likely due to a line overlap. Masers in higher vibrational states are much weaker than the $v=1$ and $v=2$ masers. The $v=3$ lines are about 35 times weaker and the $v=4$ are at least 20 times weaker than the $v=3$ (Alcolea et al., 1989; Lockett and Elitzur, 1992). The weakness of these masers is due to their requirement of much larger column densities (Lockett and Elitzur, 1992).

For the low frequency lines, the spectra of different vibrational states of the same rotational transition are similar. This may indicate that these transitions occupy the same volume of gas. Barvainis and Predmore (1985) compared the polarisations of $v=1$ and $v=2$ SiO velocity feature pairs. The similarity in polarisation of these pairs provides further evidence that the $v=1$ and $v=2$ masers, for the same rotational transition, are located in the same region. The $v=1$ velocity pairs for $J=1-0$ and $J=2-1$ rotational transitions, on the other hand, were not similarly polarised.

A large number of high frequency maser lines have been observed towards VY CMa, as shown in Table 2.7. The spectra from these lines do not have common features (Humphreys et al., 1997). The $v=1$ and 2 $J=8-7$ detections reported by Humphreys et al. (1997) are weaker and broader than the low frequency lines, and may in fact be thermal in nature.

In addition to ^{28}SiO, the isotopes ^{29}SiO and ^{30}SiO are present around VY CMa in roughly terrestrial ratios (Geballe et al., 1979). Maser emission from low J transitions of these SiO isotopes was observed by Deguchi et al. (1983) and Barcia et al. (1989). The strength of the $v=0$ $J=1-0$ ^{28}SiO is similar to that of the ^{30}SiO emission, and much less than the ^{29}SiO emission in the same transition (Barcia et al., 1989; Alcolea and Bujarrabal, 1992). Observations of $v = 0$ $J = 1 - 0$ ^{29}SiO and ^{30}SiO emission towards VY CMa are highly variable compared to $J = 1, 2$ ^{28}SiO emission, indicating that these masers are not saturated. The $v = 0$ $J = 1 - 0$ ^{29}SiO emission consists of one narrow peak corresponding in velocity to the strongest peak in the $v = 1, 2$ lines (Alcolea and Bujarrabal, 1992).

2.8.2 Interferometric observations

A number of interferometric observations of SiO maser transtitions around VY CMa have been made. The transitions that have been interferometrically imaged are indicated with an asterisk in Table 2.7.

Early KNIFE VLBI observations of the $J = 1 - 0$ $v = 1$ and $v = 2$ masers show the maser components for these two transitions to be almost spatially coincident (Miyoshi et al., 1994). Higher resolution VLBA images also show the distribution of the $v = 1$ $J = 1 - 0$ and $v = 2$ $J = 1 - 0$ maser components to be much the same (Miyoshi, 2003). VLBA observations of TX Cam and IRC+10011, on the other hand, show that the $v = 1$ and $v = 2$ $J = 1 - 0$ masers in these two stars are not coincident (Desmurs et al., 2000). Soria-Ruiz et al. (2004) find that the $v = 2$ $J = 1 - 0$ masers in IRC+10011 lie slightly closer to the star than the $v = 1$ $J = 1 - 0$ masers, and the χ Cyg $v = 1$ $J = 1 - 0$ and $v = 2$ $J = 1 - 0$ masers, while similar in total extent, have different spatial distributions. In spite of contrary observations towards other stars, the high resolution maps of Miyoshi (2003) do show that most strong maser features in their $v = 1$ $J = 1 - 0$ map of VY CMa can be aligned within 0.2 mas with the same velocity components in the $v = 2$ $J = 1 - 0$ map. The coincidence, or lack or coincidence, of the emission regions in these lines has implications for the maser pumping model.

The KNIFE and VLBA maps show SiO maser emission extending over approximately 80×80 mas in right ascension and declination towards VY CMa. The emission is mostly concentrated to the east of the maps.

VLBI maps of the $v = 1$ $J = 2 - 1$ maser emission extend over about 100×80 mas is right ascension and declination respectively (Shibata et al., 2004). Shibata et al. (2004) fitted a ring to this maser emission by eye, placing the masers at a radius of 2 - 4 R_* concentrated in the southwest region of the ring.

The Submillimeter Array was used to observe the $v=1$ $J=5-4$ SiO transition (Shinnaga et al., 2004). Seven maser components were identified. Five of these components could be located about 50 mas from the star, in the circumstellar envelope. The other two were offset by 1300 mas and 500 mas in declination, which may place these components significantly outside of the stellar envelope.

2.8.3 Variability

The SiO masers are hghly variable. Martinez et al. (1988) observed the $v=1$ $J=1-0$ and $v=2$ $J=1-0$ lines for two and a half years, at twenty to thirty day intervals. The profiles displayed some variability, but the observing period was too short to study the possible periodicity of the variations. Pardo et al. (2004) monitored the same SiO lines towards a number of late type stars for eleven years. They found that the SiO variability of supergiants is much more complex than it is in Mira-type variables. In VY CMa, the SiO variability is at odds with both the optical variability and the 1612 MHz OH variability. The main features in these SiO spectra persisted over the eleven year observing period. In particular, the intense peak at 22.5 $\mathrm{km.s^{-1}}$ is visible over the entire period. Weak peaks at 33 $\mathrm{km.s^{-1}}$ and 39 $\mathrm{km.s^{-1}}$ appear for some of the observation. Pijpers et al. (1994) undertook daily observations of the $v=1$ $J=1-0$ SiO line for about a month, during which time the profile remained constant.

Glenn et al. (2003) undertook eight single dish observations of the $v=1$ $J=2-1$ SiO line towards VY CMa over a period of 2.5 years. Two of these spectra are shwon in Figure The characteristic lifetime of a single component in the maser profile was determined to be 645 days.

A number of high frequency SiO lines have been observed by Humphreys et al. (1997) and Gray et al. (1999). Comparisons of these spectra show some slight but significant changes in the $v=1$ $J=8-7$ line over a two month period, and the $v=2$ $J=7-6$ line over a nine month period between the observations (Gray et al., 1999).

2.8.4 Line overlaps

Line overlaps are caused by the frequency overlapping of two nearly coincident transitions, from the same or different molecules, due to thermal broadening of the lines or due to the macroscopic velocity of the material producing the masers (Bujarrabal and Nguyen-Q-Rieu, 1981). Line overlaps have been invoked to explain a number of ^{28}SiO, ^{29}SiO and ^{30}SiO maser line strengths. Traditional collisional and radiative pumping mechanisms do not predict the strong contrasts observed between some rotational transitions in the same vibrational state. Line overlaps provide a means to explain many anomalous line strengths.

Line overlaps have several effects. They will increase the opacity at the frequency of the overlap. The more abundant of the species involved in the overlap will absorb most of the radiation from the central star, leading to less radiation being seen by the second species. The more abundant species may also emit radiation which may be absorbed by the second species (Cernicharo and Bujarrabal, 1992).

There are a large number of overlaps between various lines of ^{28}SiO, ^{29}SiO and ^{30}SiO. This will have a significant effect in the formation of masers (Cernicharo and Bujarrabal, 1992). Gonzalez-Alfonso et al. (1996) and Gonzalez-Alfonso and Cernicharo (1997) developed a non-local radiative transfer model incorporating many of these line overlaps. Their model explains the presence of many high frequency lines as well as the contrasting emission profiles of adjacent rotational lines. The high frequency $v=4$ $J=5{-}4$ ^{28}SiO line and the ^{29}SiO $v=2$ $J=4{-}3$ and $v=3$ $J=8{-}7$ lines are attributed to overlaps between ^{29}SiO and ^{28}SiO infrared lines. Gonzalez-Alfonso et al. (1996) both predicted and obtained the first detection of the $v=3$ $J=8-7$ ^{29}SiO line.

Line overlaps with other molecules can also have an effect on the maser emission. The frequency of the SiO infrared transition $v=1$ $J=0$ $-$ $v=2$ $J=1$ coincides almost exactly with the $v_2=012_{75}-v_2=111_{66}$ transition of H_2O. If this line is seen in emission by the SiO, as assumed by Olofsson et al. (1981), then the photons will populate the SiO $v=2$ $J=1$ level. This will strengthen the $v=2$ $J=1{-}0$ maser, while weakening the $v=2$ $J=2-1$ transition. This serves as a possible explanation of the anomalously weak $v=2$ $J=2-1$ maser line (Olofsson et al., 1981). If the excitation temperature of H_2O is less than the excitation temperature of the stellar radiation, then the same mechanism would strengthen the $v=2$ $J=2-1$ line. Such a situation could occur in collapsing layers of the star's atmosphere (Bujarrabal et al., 1996). Other infrared SiO lines, such as $v=2\,J=2-v=3\,J=1$, which either depopulate the

SiO $v=2$ $J=2$ level or populate the SiO $v=2$ $J=1$ level, could also be responsible for the weakness of this maser line (Olofsson et al., 1985).

2.8.5 Polarisation

Simultaneous SMA polarisation observations of the $v=0$ and $v=1$ $J=2-1$ masers were made by Shinnaga et al. (1999). The $v=0$ maser displayed linear polarisation of 23% and 45% at 15.5 km.s^{-1} and 18.5 km.s^{-1} respectively. The high degree of linear polarisation shown by this line is evidence of its maser nature. The $v=1$ line showed much lower linear polarisation.

McIntosh et al. (1994) performed single-dish observations of the $v=1$ $J=1-0$ and $J=2-1$ SiO maser lines towards VY CMa. They found that for both lines the fractional circular polarisation was less than 5%, and the fractional linear polarisation was less than 10%. The fractional circular polarisation of the $v=1$ $J=2-1$ line was significantly less than that of the $v=1$ $J=1-0$ line.

The 2.5 year span of single-dish observations of the $v=1$ $J=2-1$ line performed by Glenn et al. (2003) included polarisation information. The average line-integrated linear polarisation was 4.5% with a position angle of 43°. These values are lower limits on the polarisation of the maser emission because spatial blending of maser spots will decrease the observed polarisation. Neither the average line-integrated linear polarisation nor the position angle varied significantly over the observing period.

The $v=1$ $J=5-4$ masers interferometrically imaged by Shinnaga et al. (2004) displayed linear polarisation of between 10% and 60%. The polarisation angles of five of the seven observed maser spots were similar, $\sim 70°$.

2.8.6 SiO maser pumping mechanisms

Maser action requires a pumping mechanism to maintain the population inversion. In the same year as the discovery of the first SiO maser (Snyder and Buhl, 1974), Geballe and Townes (1974) suggested two different maser pumping mechanisms for this masing species. The first utilises different SiO infrared transitions of almost the same frequency. The second utilises infrared emission from hot SiO molecules, which is reabsorbed in cooler parts of the stellar envelope.

SiO masers have since been observed in many transitions (Table 2.7). Pumping mechanisms that depend on the properties of one state cannot explain all of the observations, so the frequency coincidence pumping mechanism is not viable. The second proposed pumping mechanism requires the hot and cool clouds to have the same radial velocity, which is not reasonable in the envelope of a late-type star which is expanding with increasing velocity (Deguchi and Iguchi, 1976). The pumping mechanisms proposed by Geballe and Townes (1974) were followed by a radiative pumping mechanism proposed by Kwan and Scoville (1974).

Two types of pumping mechanisms are being considered today, collisional pumping and radiative pumping, where the population inversion is caused by collisional or radiative excitation respectively. A fair amount of research has gone into determining which of these two processes is at work in various sources. The question of which pumping mechanism is driving the VY CMa SiO masers, and SiO masers in general, is still open. Theoretical models have been developed which lean in both directions, and observational tests of the models are still being undertaken.

Radiative Pumping

Radiative pumping of masers will only occur for radiative excitations where maser levels exchange population with more than one state (Elitzur, 1992, pg 291). Two fundamentally different population inversion mechanisms which fulfill this requirement have been proposed.

The first method of radiative pumping produces inversion in a vibrational state, v, by pumping level $v+1$ and relying on the subsequent cascade to the v level (Elitzur, 1980). Kwan and Scoville (1974) used this method to model SiO maser emission pumped by radiation from a central star. They considered the $v=1$ maser, assuming that radiative de-excitation of the $v=1$ to the $v=0$ states is more rapid than collisional de-excitation, and that the $v=0-1$ vibrational transition is optically thick. The pumping method is an indirect one, with $\Delta v = 2$ (Lockett and Elitzur, 1992). The collisional cross-section of the vibrational transition used by Kwan and Scoville (1974) is too high by a few orders of magnitude (Deguchi and Iguchi, 1976). The radiative pumping they describe is not viable for a more accurate value of the collisional cross-section.

The second method of radiative pumping was proposed by Deguchi and Iguchi (1976). Their model produces the necessary population inversion by anisotropic trapping of radiation. This is a $\Delta v = 1$ pump. The large velocity gradient in the gas results in different optical depths in the radial and tangential directions, which leads to the population inversion (Lockett and Elitzur, 1992). Any situation which results in such an optical depth difference will allow the pumping effect of Deguchi and Iguchi (1976). The same conditions could be met by a disk-shaped clump aligned with the star (Lockett and Elitzur, 1992).

The $\Delta v = 1$ pump rates will be much greater than $\Delta v = 2$ pump rates, so the Deguchi and Iguchi model is the more efficient of the two (Lockett and Elitzur, 1992).

Bujarrabal (1994) produced a non-local radiative transfer model which showed that SiO masers are primarily radiatively pumped, and found that different masing conditions are required for transitions in different vibrational states. However, Doel et al. (1995) points out that the zero velocity gradient assumption used in this model is physically unrealistic.

Rausch et al. (1996) found that the inclusion of a photospheric line spectrum in radiative pumping models changes the pump conditions, making radiative pumping much more efficient.

Collisional Pumping

Elitzur (1980) proposed a collisional pumping mechanism for SiO masers, motivated by the fact that these masers are produced close to the star where vibrational transitions will be largely produced by collisions.

Comparison of the the radiative pump rate described by Elitzur (1980) and the approximate collisional pump rate described by Watson et al. (1980), taking H_2 collisions into consideration, shows that collisional pumping dominates, especially for higher v (Elitzur, 1980).

For collisions to produce maser emission, the density of the gas must not be so great that collisional excitation followed immediately by collisional de-excitation, which will simply thermalise the gas. Collisional excitations must be followed by radiative de-excitations. For collisions with H_2, the density must be $\lesssim 10^{12}$ cm^{-3} for optically thin vibrational transitions (Elitzur, 1980).

The calculations of Bieniek and Green (1983) give collisional cross-sections which are much larger than had been assumed in early models. Lockett and Elitzur (1992) constructed a model, making a large velocity gradient (LVG) assumption, which incorporated these new cross-sections. Collisional pumping models tend to greatly underestimate the pumping rate because of the necessity to model a finite number of rotational levels per vibrational level. The Lockett and Elitzur (1992) model makes corrections for this effect. The LVG models developed by Lockett and Elitzur (1992) and Doel et al. (1995) imply that collisional pumping will dominate over radiative. The Doel et al. (1995) model predicts coupling of transitions involving $J=0,1,2$ of different vibrational states.

Comparison of pumping mechanisms

Lockett and Elitzur (1992) found that collisional pumping should theoretically produce the strongest masers, followed by a combination of radiative and collisional pumping. Purely radiative pumping should produce the weakest intensities. While both pumping mechanisms are possible, the collisional mechanism is less dependant on specific physical conditions. Given the wide range of SiO maser observations in late-type stars, it seems that the general pumping method may be collisional (Elitzur, 1992, pg 294). SiO maser models which include the pumping mechanism of Doel et al. (1995) in conjunction with a model for the circumstellar envelope kinematics accurately reproduce a number of physical properties of observations of SiO maser emission towards late-type stars (Humphreys et al., 1996, 2002).

As mentioned in Section 2.8.2, Desmurs et al. (2000) found that the $v=1$ and $v=2$ $J=1$–0 masers of TX Cam and IRC+10011 were not coincident in their VLBA maps, and Soria-Ruiz et al. (2004) found that while their SiO $v=1$ $J=1$–0 and $J=2$–1 VLBI images of IRC+10011 and χ Cyg show comparable emission regions, but none of the maps show spots coincident in all transitions. However, the $v=1$ and $v=2$ $J=1-0$ lines observed by Miyoshi et al. in KNIFE images in 1994 and VLBA images in 2003 do appear to be spatially coincident. Emission from rotation transitions in different vibrational states is expected to occur under different conditions, because higher vibrational states have higher excitation energies. It is more difficult to explain the coincidence of such emission regions in a radiative pumping model then in a collisional model (Soria-Ruiz et al., 2004), so the observed coincidence of the emission regions argues for collisional pumping of these masers around VY CMa.

2.9 Circumstellar environment

The earliest models of the circumstellar envelope of VY CMa make use of a thick, spherically symmetric, expanding shell (Hyland et al., 1969). Observational evidence in every wavelength regime shows the envelope to be asymmetric, so more complex models must be used for the circumstellar envelope. A contending early model is a thin expanding disk, viewed nearly edge-on (Herbig and Zappala, 1970). The disk theme reoccurs in many subsequent observations of VY CMa.

The circumstellar environment of the star will be discussed in this section. The physical properties of the star will be assumed to be the median of the literature values reported in Section 2.2, that is 10 mas for the stellar radius, 50 mas for the inner dust shell radius and 1.5 kpc for the distance to the star.

2.9.1 Near circumstellar shell

The smallest scale structure observable in the circumstellar environment is delineated by SiO masers, which are located only a few stellar radii from the star. Van Blerkom and Auer (1976) have claimed that the triple structure of the single-dish $v=1$ $J=1-0$ SiO spectrum can be explained by a rotating disk viewed almost edge-on. Zhou and Kaifu (1984) further considered a rotating, expanding disk model for the $v=1,2$ $J=1-0$ lines, making use of an updated terminal velocity. They find that a three-peaked profile is only obtained when free-fall or decelerating motion is included in the model. Free-fall motion gives a slightly redshifted central peak, and deceleration a slightly blueshifted one, which fits the spectrum of VY CMa better. The most reasonable scenario produced by this model is of a rotating, edge on disk, with a decelerating region near the photosphere, and an accelerating region outside of it. The Zhou and Kaifu (1984) model predicts SiO maser emission at a radius of about 2.5 R_*.

Several interferometric observations of SiO maser emission around the star have been made. Interferometric maps have the potential to give more direct information

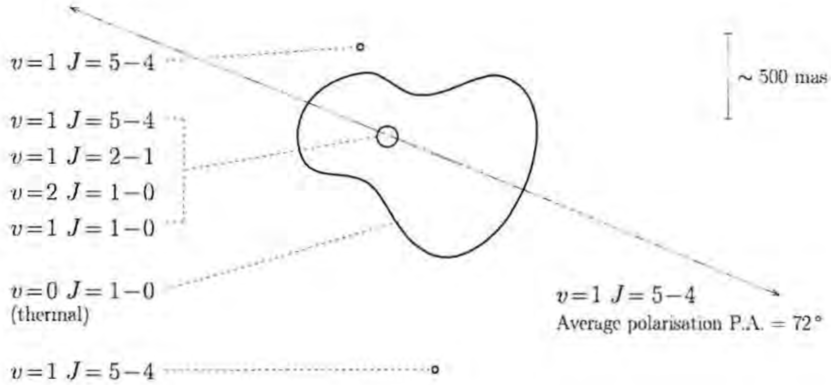

Figure 2.6: Sketch of the interferometric images of SiO thermal and maser emission discussed in the text. The $v=1$ $J=1-0$, $v=2$ $J=1-0$ and $v=1$ $J=2-1$ and the core of the $v=1$ $J=5-4$ maser emission is assumed to be located in the central region, within the dust formation radius.

about the inner envelope structure than single-dish spectra. As reported in Section 2.8.2, maps of the $v=1$ $J=1-0$ and $v=2$ $J=1-0$ emission span approximately 80 × 80 mas (Miyoshi et al., 1994; Miyoshi, 2003), the $v=1$ $J=2-1$ emission spans 100 × 80 mas (Shibata et al., 2004) and the majority of the $v=1$ $J=5-4$ maser features are within 50 mas of the star. Shibata et al. (2004) suggested that their $v=1$ $J=2-1$ VLBI images show a ring-like distribution of maser components, where only the southern section of the ring is visible. This would situate these masers at a radius of 2 - 4 R_*. The inner dust shell radius is approximately 50 mas, or 5 R_*, which places the maser regions imaged with VLBI inside the inner dust shell radius, except for two of the $v=1$ $J=5-4$ features. Shinnaga et al. (2004) suggest that these features may be located in a bipolar outflow, where shock excitation could produce the required conditions for these masers. The average position angle of the linear polarisation of these masers is 72°±4°, which is roughly aligned with the bipolar distribution of thermal $v=0$ $J=1-0$ SiO emission mapped by Shinnaga et al. (2003). This may indicate a correlation between the structure of the near circumstellar shell, where the SiO masers are located, and the extended outflow mapped by the thermal SiO emission (Shinnaga et al., 2004). The $v=0$ $J=1-0$ map also displays some bright components whose linear polarisation is aligned with the assumed outflow axis

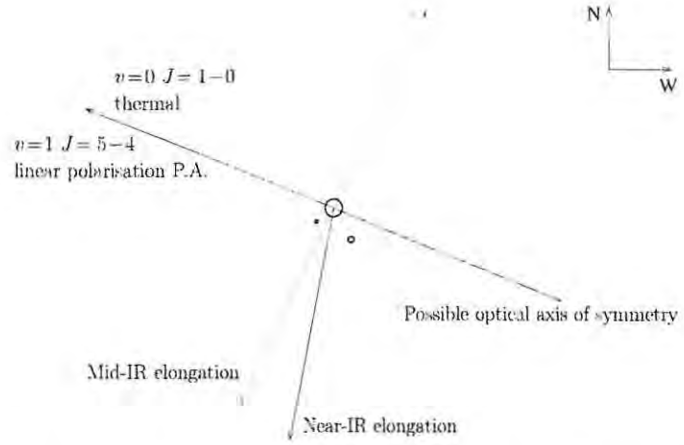

Figure 2.7: Dominant axes in the infrared and SiO emission images. The central ring represents the SiO maser region. The southeastern and southwestern spots are the bright emission observed in the near-infrared by Monnier et al. (1999b) and Cruzalebes et al. (1998) respectively. The SiO and optical emission provide generally northeast - southwest axes, while the elongation of the infrared emission is in the northwest - southeast direction.

(Shinnaga et al., 2003). A sketch of the various SiO maser and thermal emission regions is shown in Figure 2.6.

2.9.2 Inner dust shell

The temperature of the circumstellar cloud at the dust formation radius is approximately 1400 to 1500 K and the dust shell extends to a radius of about 2.5 arcseconds (Danchi et al., 1994).

Monnier et al. (2000a) compare a number of observations of mid-infrared emission and find that the emission distribution is effectively the same in all of them, which they argue implies that continuous condensation of dust has been occurring in the envelope. The bright emission observed by Monnier et al. (1999b) at about 65 mas southeast of the star, visible in Figures 2.1 and 2.8, is near the inner dust shell radius, and they suggest that it could be a recently formed dust clump.

The near-infrared speckle interferometry maps produced by Wittkowski et al. (1998) extend over roughly 100 mas, 10 R_*, and are asymmetric, elongated along a

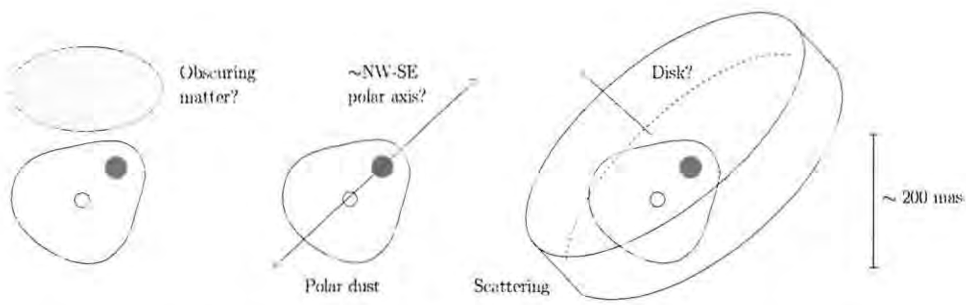

Figure 2.8: Sketches of the three environments of the near-infrared emission region proposed by Monnier et al. (1999b). The near-infrared emission in each sketch is represented by the dark circle, smaller unfilled circle to the southeast and the larger outlined southeastern region, after the maps of Monnier et al. (1999b) (See Figure 2.1). The three geometries are discussed in the text.

position angle of approximately 160°. They suggest several reasons for the asymmetry: a bipolar outflow, a close binary, erratic mass-loss mechanisms, or a disk-like envelope. The polarisation position angle of the near-infrared emission suggests that the emission also extends in the southeast direction, towards 170° (Monnier et al., 1999b). These infrared axes, along with the axes observed in the SiO thermal and maser emission, are shown in Figure 2.7.

Monnier et al. (1999b) propose several explanations of the clumpy, highly asymmetric near-infrared emission they observed towards VY CMa. One possibility is that there is simply less dust, or cooler dust, to the north of the star in an optically thin envelope. However, they consider this possibility unlikely. What is more likely is that the northern region of the nebula is obscured. This scenario is supported by the H_2O maser emission to the north and east of the star which implies high dust densities in these regions (Monnier et al., 1999b). A second scenario proposed by Monnier et al. (1999b) is of a high opacity inner dust shell, where the material to the north of the star has the highest optical depth. This situation could arise if the star is surrounded by an equatorial disk of high density. The warm dust at the poles would be the source of the near-infrared emission (Monnier et al., 1999b). The final possibility put forward by Monnier et al. (1999b) is that the near-infrared emission is created by forward scattering from an equatorial disk, which is tilted towards us in the southwest. Smith et al. (2001) also suggest that the asymmetry could be explained by high extinction to the northwest of the star, as well as the effects of forward and back scattering. Efstathiou and Rowan-Robinson (1990) developed an axisymmetric flared disk dust shell model which fitted the spectral energy distribution very well for a viewing angle just inside the disk. These three geometries proposed by Monnier et al. (1999b) and other authors are depicted in Figure 2.8. Monnier et al. (1999b) comments that the small-scale near-infrared images seem to be at odds with the general larger-scale model, possibly because the emission observed at this resolution is due to chaotic dust formation and doesn't reflect the larger scale dust shell structure.

Geballe et al. (1979) observed infrared SiO lines towards VY CMa, which they argue are formed at about 150 mas, 15 R_*, from the star, in an accelerating and expanding region where most of the silicon is incorporated into dust grains. The circumstellar cloud has a temperature of about 600 K in this region (Geballe et al., 1979). Observations by Monnier et al. (2000b) in the mid-infrared imply a molecule formation radius of greater than 40 R_*, which is approximately the outer radius of the H_2O emission mapped by Richards et al. (1998). Mid-infrared interferometry of the ammonia spectral lines indicates that there is turbulence in the inner stellar envelope around the 40 R_* region (Monnier et al., 2000b).

2.9.3 OH and H_2O maser emission regions

Both OH and H_2O maser regions appear to fall outside the dust formation region. VLBI observations of H_2O masers show an emission region with an inner radius close to the inner dust shell radius and an outer radius of $\sim$ 450 mas.

The early VLBI maps of H_2O masers produced by Rosen et al. (1978) oppose a rotating disk model for this envelope region, because emission near the stellar velocity does not fall between the locations of the more extreme velocity emission. Rosen et al. (1978) instead propose that emission near the stellar velocity arises in a shell close to the star, while the low and high velocity features are formed in shells further out, in areas of greater acceleration. MERLIN maps of H_2O masers around VY CMa display a possible disk structure, with what may be material ejected along the polar axis of a jet in the northeast - southwest direction (Yates and Cohen, 1994), consistent with the bipolar signature in the observed thermal SiO emission (Shinnaga et al., 2003). Yates and Cohen (1994) fit a uniformly expanding thin shell model to their H_2O map, with an inner boundary of 35 mas and outer boundary of 400 mas. Their radial distance versus velocity plots show inner and outer elliptical boundaries for the emission, with an inner boundary velocity of 7 km.s^{-1}, and an outer boundary velocity of 27 km.s^{-1}. The expansion velocity at the inner elliptical boundary is less than the escape velocity (Yates and Cohen, 1994).

Further MERLIN observations by Richards et al. (1998) show a possible thick expanding shell. The extreme redshifted and blueshifted emission is weaker and more compact than the central emission, as reported in Section 2.7. This indicates that it is possibly located in the caps of an expanding envelope. The maps were modelled by a simple spherical, expanding shell with an inner radius of 75 mas and an inner velocity of 7.8 km.s^{-1} (Richards et al., 1998). The emission region extends to a radius of 440 mas with an outer velocity of 35.5 km.s^{-1}. This model fails to predict the lack of emission along the line of sight to the expected stellar position, and the extended emission to the southwest and northeast. Marvel (1996) and Richards et al. (1998) find that the proper motions of most of the maser spots are away from the assumed stellar position, implying the H_2O maser region is expanding. The proper motion model gives an outer velocity of 31.7 km.s^{-1} at an outer boundary of 360 mas (Richards et al., 1998). Marvel (1996) determined a mean expansion velocity of 12.8 km.s^{-1} from the proper motion observations, assuming a distance of 1.5 kpc. Richards et al. (1998) found that the mean expansion velocity in the plane of the sky increased as a linear function of the angular separation of the components from the assumed stellar position. This is evidence for acceleration in this region, which is consistent with the tangential beaming of the H_2O masers (Richards et al., 1998). The H_2O emission region is elongated northeast - southwest (Marvel, 1996; Richards et al., 1998), which can be seen in Figures 2.4 and 2.9. Figure 2.9 is a sketch of the circumstellar envelope around the H_2O maser region. Richards et al. (1998) suggest that the H_2O masers are situated in an equatorial belt, perpendicular to a polar outflow.

The 1667 MHz OH emission plateau observed by Morris and Bowers (1980) cannot be produced by a spherically symmetric envelope. An axially symmetric model with outflow towards the equator, viewed far out of the mid-plane, was invoked to explain the plateau emission. This model is essentially an expanding equatorial disk. The

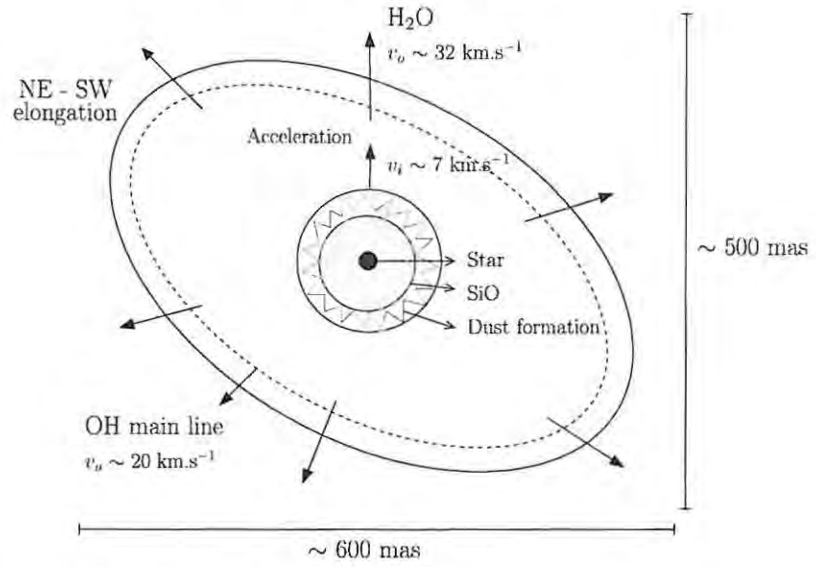

Figure 2.9: Sketch of the OH main line, H_2O and SiO maser emission regions. The inner dust shell radius is represented by the jagged line which separates the SiO emission region from the H_2O and OH main line emission regions. The OH main line emission region lies inside the H_2O emission region, represented by the dashed ellipse.

SiO and H_2O masers would also fall within this disk. Main line OH masers are located about 5×10^{15} cm to 10^{16} cm from the star, $\sim$20 R_*, in a region which is expanding at a rate of about 20 km.s^{-1} (Morris and Bowers, 1980). The OH main line maser region is also shown in Figure 2.9.

The 1612 MHz OH VLA maps produced by Bowers et al. (1983) show an elongated distribution. The spatial offset between the extreme velocity maser clusters suggests a tilted expanding disk-like model for the envelope (Bowers et al., 1983). The mean position of the maser components is close to the optical position of the star. The projected polar axis of the disk model has a position angle of 49°, and the intersection of the disk with the plane of the sky will form a line at approximately 140°. Bowers et al. (1983) propose velocity gradients and the effect of close O type stars to explain the complexity of the maps.

2.9.4 Extended emission

Larger-scale images of VY CMa in the infrared show emission extending a few arcseconds, or about 150 R_*, concentrated to the south and southwest of the core (Monnier et al., 1999b). High resolution HST optical observations show a dusty, axisymmetric circumstellar envelope (Kastner and Weintraub, 1998). These images imply that VY CMa is surrounded by a flattened envelope or the massive circumstellar disk suggested by Herbig and Zappala (1970). The disk, or envelope, obscures the central star. The composite color HST images of Smith et al. (2001) and the images of Kastner and Weintraub (1998) suggest a northeast - southwest axis of symmetry. Kastner and Weintraub (1998) interpret the nebula extending in the direction west-southwest to be a forward-facing polar lobe. A rear lobe is not visible however, possibly because the large envelope conceals it. The envelope around VY CMa may consist of the remnants of a pre-main sequence disk (Kastner and Weintraub, 1998). Thermal SiO maps also show a possible bipolar structure extending over about 1 arcsecond, where the southwestern blue lobe of the emission is brighter than the north-eastern red lobe (Shinnaga et al., 2003).

The bright knot first observed by Cruzalebes et al. (1998), ~ 1.3 arcseconds from the star, is embedded in the extended southwestern emission. Cruzalebes et al. (1998) suggest that the knot may be gas accreted by a companion star. Monnier et al. (1999b) extrapolate the location of the possible binary companion discussed by Wallerstein (1978), component B in the table of Herbig (1972). They find that the southwestern knot falls along the extrapolated path, and may therefore be the component B reported by Wallerstein (1978) and other early observers. Wallerstein (1978) described this emission in terms of light escaping through holes in a dusty cloud, as mentioned in Section 2.3. This explanation yields rotation rates that are too large for an isolated supergiant star, so it may be that VY CMa does have a companion, or that it is not an evolved object (Monnier et al., 1999b).

The Smith et al. (2001) HST images also show clumps of small bright knots around the star. The two most prominent clumps are located to the south and southwest of the star. Both of these clumps are close to the position of component B in the table of Herbig (1972).

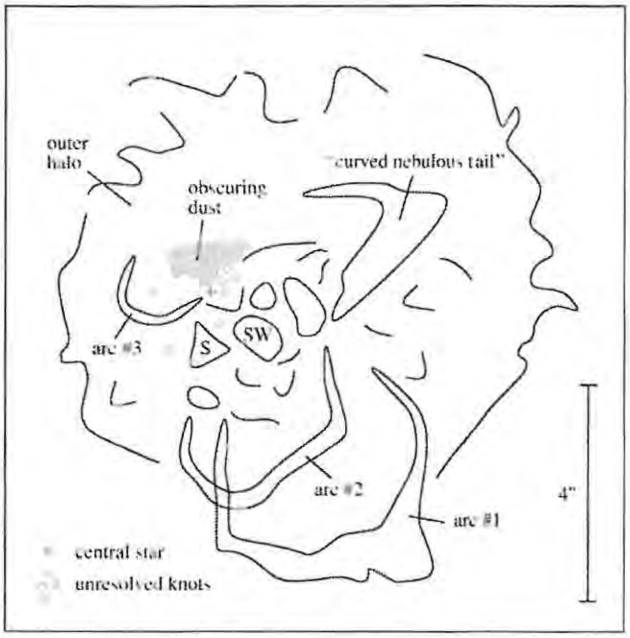

Figure 2.10: Sketch of the optical and near-infrared features observed in the large scale structure around VY CMa, from Smith et al. (2001).

2.9.5 Large scale structures

The optical nebula surrounding VY CMa is asymmetric with a number of features including reflection arcs, bright condensations and knots, which are mentioned in Section 2.3. Figure 2.10 is a sketch by Smith et al. (2001) of the large scale structure.

Images of the optical and near-infrared nebulosity produced by Smith et al. (2001) show emission concentrated south and west of the star. Three reflection arcs are visible, two of which were also observed in the near-infrared by Monnier et al. (1999b). What Monnier et al. (1999b) calls a curved nebulous tail can be seen at the higher resolution of the HST to be another reflection arc, which discounts the plume model put forward by Monnier et al. (1999b) (Smith et al., 2001). The arcs have also been observed by Humphreys et al. (2005) and Smith (2004) in high-resolution optical spectra.

The features observed in the extended nebula suggest that the star is undergoing many asymmetric local mass-loss events (Smith et al., 2001; Smith, 2004; Humphreys et al., 2005). Long-slit spectroscopy by Humphreys et al. (2005) shows that the dust and gas in the nebula surrounding VY CMa has much the same velocity as the central star, a fact which conflicts with the known high mass-loss rate of VY CMa. They observe three arcs in the nebula. One of these is the large north-western arc labeled by Smith et al. (2001) as a nebulous tail. The north-western arc appears to have been ejected 400 years ago, and the other two arcs between 800 and 1000 years ago (Humphreys et al., 2005).

2.9.6 Magnetic field

At the end of its lifetime, an AGB star is thought to develop a superwind which causes a period of very high mass-loss. This wind is caused primarily by radiation pressure on dust in the circumstellar envelope, and also by molecular acceleration (Soker, 1998). The radiation pressure on the dust, which is itself created by stellar pulsations, results in dense equatorial mass-loss. A weak magnetic field can create cool spots on the photosphere of the giant star that are expected to be primarily located in the equatorial regions. Dust formation is increased above the cool spots, which will enhance the equatorial mass-loss of the star (Soker and Clayton, 1999). Chapman and Cohen (1986) considered the configuration of the magnetic field around VX Sgr, which they derive from OH maser observations. Their calculated magnetic field will have an energy density large enough to influence the outflow of material from the star. García-Segura et al. (2003) show that a toroidal magnetic field can lead to fast winds from AGB stars. This mass-loss takes the form of local structures such as filaments and arcs, as well as a general increase in mass-loss from the equatorial regions (Soker, 2000).

The big question is how this magnetic field is generated. Dynamos in AGB stars provide a possible explanation. In this phase of evolution, the contracted core will rotate much faster than the expanded envelope. This differential rotation can create a dynamo between the core of the star and the outer layers (Blackman et al., 2001). Such a dynamo could create magnetic fields of the order of 400 G at the surface of a star. Magnetic energy could cause coronal emission and enhance particle acceleration (Blackman et al., 2001).

Dorch (2004) performed numerical magneto-hydrodynamical simulations of dynamo action in a late-type supergiant star. These simulations show only a few large-scale convective cells on the stellar surface and the magnetic field concentrated in long structures with widths much less than those of the convective cells. In this model, small local dynamos create a global magnetic field. Magnetic fields produced by this method will have maximums of around 500 G at the stellar surface (Dorch, 2004).

The polarisation of maser emission provides a probe of the magnetic field around a late-type star. The magnetic field introduces a quantisation axis, which differentiates magnetic sublevels according to their magnetic quantum number. This differentiation will take place when the gyrorate exceeds other quantum rates. The energies of the magnetic sublevels are shifted by the Zeeman effect, by a distance proportional to the magnetic field strength (Elitzur, 1996). The relationship between maser polarisation and the magnetic field is discussed in Section 6.4.1.

The polarisation of the H_2O masers around VY CMa implies a magnetic field of around 200 mG for the H_2O masers observed by Vlemmings et al. (2002a), which they place at a radius of approximately 150 mas, based on the extent of the H_2O maser region observed by Diamond et al. (1987). Benson and Mutel (1982) observed the development of a Zeeman doublet in the 1665 MHz OH emission. The Zeeman splitting implies a longitudinal magnetic field of about 1 mG in the OH emission region, which remained constant for at least two years. Vlemmings et al. (2002a) places this magnetic field observation at 1.6 arcseconds from the star, the diameter of the 1612 MHz emission region observed by Reid et al. (1981) with the VLA.

ν [MHz]	v	J'	J''	Ref
^{28}Si^{16}O				
43423.864	0	1	0	7*
86847.010	0	2	1	1
43122.079	1	1	0	3,4*
86243.440	1	2	1	2,3,6,9*
129363.366	1	3	2	3,6
172481.140	1	4	3	3
215596.05	1	5	4	2,3,8*
258707.36	1	6	5	2
301814.37	1	7	6	5
344916.36	1	8	7	5
42820.582	2	1	0	3,4*
128458.875	2	3	2	1
171275.150	2	4	3	3
214088.56	2	5	4	3
256898.37	2	6	5	3
299703.88	2	7	6	5
342504.35	2	8	7	5
42519.373	3	1	0	3
170070.31	3	4	3	3
211077.90	4	5	4	3

References:
1. Buhl et al. (1975)
2. Jewell et al. (1987)
3. Cernicharo et al. (1993)
4. Miyoshi et al. (1994)*
5. Humphreys et al. (1997)
6. Cho et al. (1998)
7. Shinnaga et al. (2003)*
8. Shinnaga et al. (2004)*
9. Shibata et al. (2004)*

* Interferometric observations

ν [MHz]	v	J'	J''	Ref
^{29}Si^{16}O				
42879.922	0	1	0	3
85759.144	0	2	1	2
214385.62	0	5	4	2
127748.594	1	3	2	1
170328.194	1	4	3	1
255478.30	1	6	5	2
84575.208	2	2	1	2
253703.23	2	6	5	2
	3	8	7	4
^{30}Si^{16}O				
42373.365	0	1	0	5
84746.047	0	2	1	2,5
211853.17	0	5	4	2
168323.089	1	4	3	2
167160.642	2	4	3	2

References:
1. Cernicharo et al. (1991)
2. Cernicharo and Bujarrabal (1992)
3. Cho et al. (1996)
4. Gonzalez-Alfonso et al. (1996)
5. Cho and Ukita (1998)

Table 2.7: Tables showing the observed SiO maser lines for the isotopes ^{28}Si^{16}O (left), ^{29}Si^{16}O and ^{30}Si^{16}O (right). The first column shows the corresponding frequencies, where available. The second column is the vibrational level v of the maser transition, between rotational levels J' and J''. The reference for the observation is in the last column of each table.

Chapter 3

Observing technique

3.1 Introduction

The angular resolution of a radio antenna is inversely proportional to the antenna diameter, expressed in wavelengths. For this reason individual radio telescopes have much lower resolving power than optical telescopes, which operate at much higher frequencies. Within the radio wavelength regime, higher observing frequencies or physically larger radio antenna must be used to provide better resolving power.

Fortunately, increases in resolving power can also be achieved by using more than one radio telescope in the form of an interferometer. In a two-element interferometer, the resolution is proportional to the distance between the two antennas. Consequently, higher resolutions can be achieved simply by increasing the distance between antennas rather than building ever larger single antennas, a process that would be both expensive and impractical. The primary motivation for the development and use of large interferometric arrays is then to address scientific questions which require high angular resolution.

This thesis in paricular concerns an imaging study of individual SiO maser components in the atmosphere of the late-type star, VY CMa. The individual maser components have typical sizes of the order of milliarcseconds (e.g. Greenhill et al., 1995) and VLBI angular resolution is essential for their study.

3.2 Radio interferometry

Modern radio interferometers consist of arrays of multiple radio antennas. Each pair of antennas in these arrays can be treated as a single two-element interferometer. This pair of antennas observes a cosmic source, with each antenna receiving signals from the source. Because the source dimensions and the distance between the antennas are small compared to the source distance, the complex degree of coherence between the two received signals is related to the brightness distribution of the source by a Fourier transform. This is a result of the van Cittert-Zernike Theorem, which is derived in Born and Wolf (1999, pg 547). A mathematical expression of the relationship between the complex degree of coherence and the brightness distribution of the source spread over area Ω is:

$$j_{12} \propto \iint_{\Omega} I(l,m) e^{-j2\pi(lu+mv)} dl\, dm \tag{3.1}$$

where j_{12} is the complex degree of coherence and $I(l,m)$ is the source brightness distribution in the frame shown in Figure 3.1. The (u,v) coordinates are the antenna separation in units of wavelength, projected onto a plane perpendicular to the source direction.

The signals are captured at each individual antenna in the form of voltages. Before reception by the antennas, the electric field radiated by the source has already been affected by the Earth's atmosphere and ionosphere. The signal is captured at the antenna by imperfectly polarised feeds that also distort the signal. The signals pass through receiving systems, where they are amplified and mixed to intermediate frequency with a local oscillator signal. The propagation through the receiver system further affects the signal. If the reference point for the incident electromagnetic radiation from the source $\vec{E}$ is set at the point above the Earth's atmosphere, then the induced voltage at each antenna is:

$$V = \vec{h}.\vec{E} \tag{3.2}$$

where $\vec{h}$ is the instrumental response, including all atmospheric, ionospheric and instrumental effects. These voltages are sampled digitally and then cross-correlated to estimate the spatial coherence as the cross-correlation.

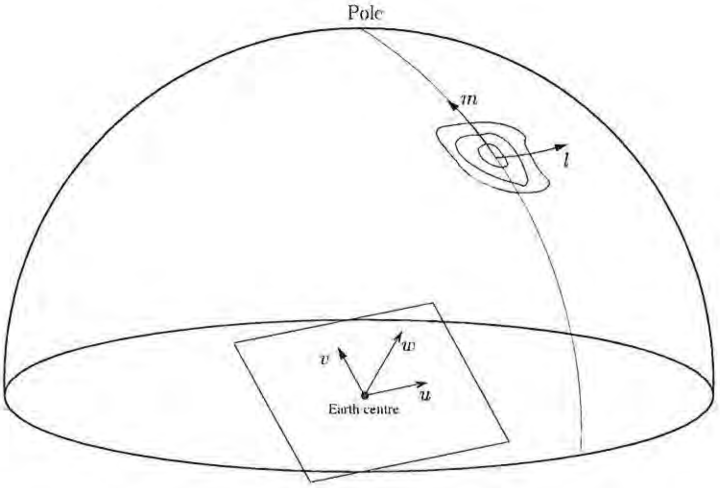

Figure 3.1: The coordinate systems used in Equation 3.1 and 3.3. The (u, v, w) coordinate system is the spatial coordinate system of the antenna baselines, measured in units of wavelength. The mutually orthogonal components u, v and w are measured in the east, north and source direction respectively. The (u, v) vectors are the basis vectors for the plane orthogonal to the source direction, w. The (l, m) vectors describe the position of the source on the sky. They are direction cosines measured with respect to the u and v axes respectively. (Thompson, 1989; Thomson et al., 2001, pg 70).

During correlation the signal must be corrected for geometric propagation effects. A wavefront from the source will not reach all the antennas simultaneously, as shown in Figure 3.2. This delay in the signal reception between two antennas is referred to as the differential geometric delay τ_g. Additional delays are also introduced by signal propagation effects through the atmosphere, telescope, electronics and cables. The total delay is compensated for in the correlator system by adding an offset delay to the signal in a chosen reference frame. In practice, the delay correction used in correlation may not model all effects exactly, and remaining residual delays may need to be determined and removed in post-processing. The geometric delay correction must continually be adjusted to account for the rotation of the Earth (Thomson et al., 2001, pg 81). A delay in the intermediate frequency stage of the receiving system adds phase terms of the form $2\pi\nu_{LO}\tau$ to the signal. Such phase terms are removed by an appropriate phase rotation, a practice referred to as fringe stopping (Thomson et al., 2001, pg 174).

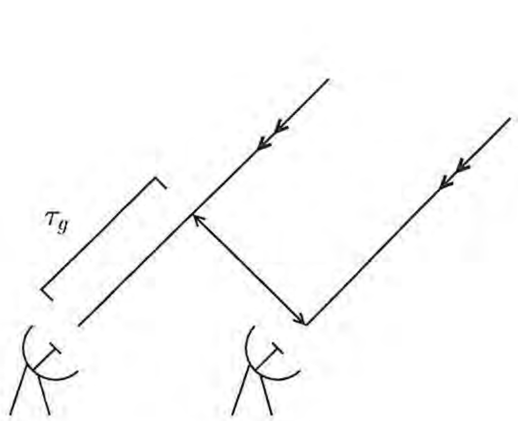

Figure 3.2: A single wavefront will reach each antenna at a different time. The time difference in receiving the signal at different antennas is the geometric delay, τ_g. These time differences are accounted for in the correlator.

The correlator output x is the cross-correlation of the two voltage signals which have been corrected for geometrical effects:

$$x_{mn}(u, v, \tau) =< V_m(t + \tau_m)V_n^*(t + \tau_n - \tau) > \tag{3.3}$$

for antenna pair (m, n) (D'Addario, 1986). The delays τ_m and τ_n are offset delays added by the correlator to place each antenna in a geocentric reference frame. The τ is the variable lag offset by which the voltage V_n is delayed with respect to V_m within the correlator. The cross-correlation can also be represented by $V_m(t) \star V_n(t)$ and is conventionally referred to as the visibility function (Thomson et al., 2001, pg 81).

Lag spectral correlators, or XF correlators, measure the cross-correlation for a range of time lags τ between the two voltage signals. This method is used to produce spectral output in the form of N visibility values for N frequency values, or channels, across a bandwidth $\Delta\nu$. The Fourier transform of the cross-correlation, as a function of delay, gives the cross power spectrum of the signals as a function of frequency:

$$r_{mn}(u, v, \nu) = \int_{-\infty}^{\infty} x_{mn}(u, v, \tau)e^{-j2\pi\nu\tau}d\tau \tag{3.4}$$

(D'Addario, 1986). Therefore the output of the correlator is the cross power spectrum

$r_{mn}(u, v, \nu)$ as is required for spectral line observations. Another type of correlator used by some arrays is the FX correlator. In these correlators the visibility data are first Fourier transformed from the time domain to the frequency domain. It is then cross multiplied with data from other antennas. The FX correlator output will then also be in the form of a cross power spectrum (Thomson et al., 2001, pg 290).

3.3 Very Long Baseline Interferometry

Conventional radio interferometers consist of arrays of antennas that are directly connected using one of several signal transport mechanisms, including transmission waveguides, radio links and fibre-optic cables. These links distribute a standard local oscillator reference to the antennas and transmit received signals to a correlator, enabling real-time correlation of the data. These arrays are known as connected-element interferometers. The Very Large Array (VLA) is an example of a connected-element interferometer that uses waveguide to transmit signals to a correlator. The antennas of the MERLIN array are connected by radio links, that are currently being upgraded to fibre-optic cable.

Signal transport in connected-element arrays becomes increasingly difficult over longer baselines. Long baselines are desirable, however, because of the greater angular resolution they can provide. This motivated the development of VLBI, a technique that uses baselines of up to thousands of kilometers. The Very Large Baseline Array (VLBA)[1] is a dedicated VLBI array of ten twenty-five meter radio telescopes spread across the United States of America.

The antennas in VLBI arrays cannot currently be routinely directly connected, a fact which has two significant consequences. Firstly, independent local oscillators must be used at each antenna station. Secondly, the data cannot be directly correlated on-line. Instead, the data are converted to base-band, sampled, and written to high-density magnetic tape. The tapes are sent to a central correlator for subsequent off-line processing. Correlators synchronize the tapes from each station in time, taking into account clock offsets, delay offsets and differing Doppler shifts at each antenna due to the rotation of the Earth. The data are correlated and written to commodity

---

[1] http://www.aoc.nrao.edu/vlba/html/

magnetic tape to await further data processing. Current experiments are under way to connect VLBI antennas using high-speed network connections. This signal transport mechanism will likely be used for future VLBI arrays.

The final stages of data processing are the calibration and imaging of the visibility data. The calibration process accounts for the propagation effects encompassed in the instrumental response $\vec{h}$. Imaging is the process of Fourier transforming and deconvolving the visibility data to give the brightness distribution of the source.

3.4 VLBI spectropolarimetry

Techniques for VLBI observations in full polarisation have been developed over the past twenty years. Cotton et al. (1984) and Roberts et al. (1984) describe the continuum VLBI polarimetry techniques they used to image various radio sources. In both cases, each antenna of the VLBI array recorded both left circular polarisation (LCP) and right circular polarisation (RCP) signals, allowing the polarisation of the source radiation to be determined by their full cross-correlation. Early experiments in VLBI spectral line polarimetry are described by Garcia-Barreto et al. (1988), Kemball (1992) and Kemball et al. (1995). The discussion here is based on the description of Kemball (1992) and Kemball et al. (1995).

VLBI polarimetry is possible if some, or all, antennas in the array have feeds that receive both orthogonally polarised signals. The complete spatial coherence of the electric field is then described by the correlations of these orthogonally polarised signals. If the antenna feeds measure left and right circular polarisations, then these correlations are LL, LR, RL and RR, where L and R represent the left and right circularly polarised signals respectively (Fomalont and Perley, 1989).

The voltage induced in the antenna feed is the product of the response of the antenna feeds and the incident electric field vector of the electromagnetic radiation emitted by the source. In practice, the two ortho-mode transducers or other polarizers in the feeds are imperfect. Each polarised feed admits some fraction of the orthogonally polarised radiation, as discussed by Morris et al. (1964) and Conway and Kronberg (1969), an effect known as instrumental polarisation. Conway and Kronberg (1969) modelled the instrumental polarisation response by the use of two leakage terms, which are complex numbers describing the response of the feed to its orthogonal polarisation. The leakage terms have come to be known as D-terms. They are usually small, and assumed to be independent of time, frequency and direction in VLBI observations (Kemball et al., 1995). Garcia-Barreto et al. (1988) calculated D-terms of less than 10% for their observations of W3(OH) with a VLBI array consisting of five antennas in the United States of America and one at Dwingeloo Observatory in the Netherlands.

At frequency ω and polarisation p, the voltage detected by the feed is given by:

$$(\vec{h}^p.\vec{E}) = \frac{1}{\sqrt{1+D^{p*}D^p}} V^p e^{j(\omega t+\epsilon+\gamma^p)} \tag{3.5}$$

$$\begin{aligned} V^R &= E^R e^{-j\alpha(t)} + D^R E^L e^{j(\alpha(t)+\gamma^{L-R})} \\ V^L &= E^L e^{-j\alpha(t)} + D^L E^R e^{j(\alpha(t)+\gamma^{R-L})} \end{aligned} \tag{3.6}$$

where ϵ and γ^p are phase terms added by propagation through the non-dispersive neutral atmosphere and dispersive ionosphere respectively. The argument γ^{R-L} is shorthand for $\gamma^R - \gamma^L$. The parallactic angle $\alpha(t)$ is the angle between the feed axis and the source meridian which changes over the course of the observations for alt-azimuth antennas. Following Kemball (1992), the D-terms are D^L for the LCP signal and D^R for the RCP signal.

The passage of this signal through the receiving system affects the gain and phase of the signal. The response of the system at an antenna m can be summarised by two factors: the time variable gain $G_m(t)$ and the normalised complex bandpass response $B_m(\omega)$. In each sampled orthogonal polarisation, $p \in \{R, L\}$, the signal V becomes:

$$V_m^{p'}(t) = V_m^p(t)\ G_m^p(t)\ B_m^p(\omega) \tag{3.7}$$

The cross power spectrum produced by cross-correlation and Fourier transform of the voltages V' at two antennas m and n is:

$$r_{mn}^{pq}(u,v,\omega) = (G_m^p G_n^{*q})(B_m^p B_n^{*q}) \times \int\int_\Omega < V_m^p(\omega) V_n^{q*}(\omega) > e^{-j2\pi(lu+mv)} dl dm \tag{3.8}$$

where the polarisation reception $(p, q) \epsilon \{R, L\}$.

The polarisation state of the radiation from the source is fully described by the four Stokes parameters, I, Q, U and V. The parameter I is the total intensity of the radiation, Q and U describe the linear polarisation and V describes the circular polarisation. The correlation of the signal from two circularly polarised feeds, LL, LR, RL and RR, can be expressed as:

$$
\begin{aligned}
< E^L E^{L*} > \; &= \; LL \; = \; I(u,v) + V(u,v) \\
< E^R E^{R*} > \; &= \; RR \; = \; I(u,v) - V(u,v) \\
< E^R E^{L*} > \; &= \; RL \; = \; Q(u,v) + jU(u,v) \\
< E^L E^{R*} > \; &= \; LR \; = \; Q(u,v) - jU(u,v)
\end{aligned}
$$

(Conway and Kronberg, 1969). The Stokes parameters in the visibility plane are the Fourier transform of the image plane Stokes parameters:

$$I(u,v) \;\Rightarrow\; \mathcal{I}(l,m) = \frac{1}{2}[\mathcal{LL} + \mathcal{RR}] \tag{3.9}$$

$$V(u,v) \;\Rightarrow\; \mathcal{V}(l,m) = \frac{1}{2}[\mathcal{LL} - \mathcal{RR}] \tag{3.10}$$

$$Q(u,v) \;\Rightarrow\; \mathcal{Q}(l,m) = \frac{1}{2}[\mathcal{RL} + \mathcal{LR}] \tag{3.11}$$

$$U(u,v) \;\Rightarrow\; \mathcal{U}(l,m) = \frac{j}{2}[\mathcal{LR} + \mathcal{RL}] \tag{3.12}$$

where $\mathcal{LL}, \mathcal{RR}, \mathcal{RL}$ and $\mathcal{LR}$ are the visibility counterparts of LL, RR, RL and LR, in units of correlated flux density and $\Rightarrow$ denotes a Fourier transform relationship (Kemball et al., 1995).

The cross power spectrum described by Equation 3.8 can be written in terms of the visibility counterparts of the Stokes parameters. Using Equation 3.6 in Equation 3.8:

$$
\begin{aligned}
r_{mn}^{RR}(u,v,\omega) \; = \; & (G_m^R G_n^{*R})(B_m^R B_n^{*R}) \, [\, (\mathcal{RR}) e^{-j(\alpha_m - \alpha_n)} \\
& + (\mathcal{RL}) D_n^{R*} e^{-j(\alpha_m + \alpha_n)} e^{j\gamma_n^{R-L}} \\
& + (\mathcal{LR}) D_m^{R} e^{j(\alpha_m + \alpha_n)} e^{j\gamma_m^{L-R}} \\
& + (\mathcal{LL}) D_m^{R} D_n^{R*} e^{j(\alpha_m - \alpha_n)} e^{j\gamma_m^{L-R} - \gamma_n^{L-R}}]
\end{aligned}
$$

$$\begin{aligned}
r_{mn}^{LL}(u,v,\omega) &= (G_m^L G_n^{*L})(B_m^L B_n^{*L})\,[\,(\mathcal{L}\mathcal{L})e^{j(\alpha_m-\alpha_n)} \\
&\quad + (\mathcal{L}\mathcal{R})D_n^{L*}e^{j(\alpha_m+\alpha_n)}e^{j\gamma_n^{L-R}} \\
&\quad + (\mathcal{R}\mathcal{L})D_m^{L}e^{-j(\alpha_m+\alpha_n)}e^{j\gamma_m^{R-L}} \\
&\quad + (\mathcal{R}\mathcal{R})D_m^{L}D_n^{L*}e^{-j(\alpha_m-\alpha_n)}e^{j\gamma_m^{R-L}-\gamma_n^{R-L}}\,] \\[2ex]
r_{mn}^{RL}(u,v,\omega) &= (G_m^R G_n^{*L})(B_m^R B_n^{*L})\,[\,(\mathcal{R}\mathcal{L})e^{-j(\alpha_m+\alpha_n)} \\
&\quad + (\mathcal{R}\mathcal{R})D_n^{L*}e^{-j(\alpha_m-\alpha_n)}e^{j\gamma_n^{L-R}} \\
&\quad + (\mathcal{L}\mathcal{L})D_m^{R}e^{j(\alpha_m-\alpha_n)}e^{j\gamma_m^{L-R}} \\
&\quad + (\mathcal{L}\mathcal{R})D_m^{R}D_n^{L*}e^{j(\alpha_m+\alpha_n)}e^{j\gamma_m^{L-R}-\gamma_n^{R-L}}\,] \\[2ex]
r_{mn}^{LR}(u,v,\omega) &= (G_m^L G_n^{*R})(B_m^L B_n^{*R})\,[\,(\mathcal{L}\mathcal{R})e^{j(\alpha_m+\alpha_n)} \\
&\quad + (\mathcal{L}\mathcal{L})D_n^{R*}e^{j(\alpha_m-\alpha_n)}e^{j\gamma_n^{R-L}} \\
&\quad + (\mathcal{R}\mathcal{R})D_m^{L}e^{-j(\alpha_m-\alpha_n)}e^{j\gamma_m^{R-R}} \\
&\quad + (\mathcal{R}\mathcal{L})D_m^{L}D_n^{R*}e^{-j(\alpha_m+\alpha_n)}e^{j\gamma_m^{R-L}-\gamma_n^{L-R}}\,]
\end{aligned} \tag{3.13}$$

(Kemball et al., 1995). For nearly perfect antenna feeds, the second order terms in Equation 3.13 are small. So terms of order O($D.\mathcal{R}\mathcal{L}$), O($D.\mathcal{L}\mathcal{R}$) or O(D^2) can be neglected (Roberts et al., 1984), which linearises the equations:

$$\begin{aligned}
r_{mn}^{RR}(u,v,\omega) &= (G_m^R G_n^{*R})(B_m^R B_n^{*R})(\mathcal{R}\mathcal{R})e^{-j(\alpha_m-\alpha_n)} \\[2ex]
r_{mn}^{LL}(u,v,\omega) &= (G_m^L G_n^{*L})(B_m^L B_n^{*L})(\mathcal{L}\mathcal{L})e^{-j(\alpha_m-\alpha_n)} \\[2ex]
r_{mn}^{RL}(u,v,\omega) &= (G_m^R G_n^{*L})(B_m^R B_n^{*L})\,[\,(\mathcal{R}\mathcal{L})e^{-j(\alpha_m-\alpha_n)} \\
&\quad + (\mathcal{R}\mathcal{R})D_n^{L*}e^{-j(\alpha_m+\alpha_n)}e^{j\gamma_n^{L-R}} \\
&\quad + (\mathcal{L}\mathcal{L})D_m^{R}e^{j(\alpha_m-\alpha_n)}e^{j\gamma_m^{L-R}}\,] \\[2ex]
r_{mn}^{LR}(u,v,\omega) &= (G_m^L G_n^{*R})(B_m^L B_n^{*R})\,[\,(\mathcal{L}\mathcal{R})e^{j(\alpha_m+\alpha_n)}
\end{aligned}$$

$$
\begin{aligned}
&+ (\mathcal{LL}) D_n^{R*} e^{j(\alpha_m - \alpha_n)} e^{j\gamma_n^{R-L}} \\
&+ (\mathcal{RR}) D_m^{L} e^{-j(\alpha_m - \alpha_n)} e^{j\gamma_m^{R-L}}]
\end{aligned}
\tag{3.14}
$$

3.5 Calibration

The cross power spectra described by Equations 3.13 and 3.14 cannot be directly transformed into a brightness distribution, because the observations are influenced by propagation and instrumental effects. Calibration is the process of removing these effects to estimate the true visibilities, $\mathcal{RR}$, $\mathcal{LL}$, $\mathcal{RL}$ and $\mathcal{LR}$ from the observed cross power spectra $r_{mn}^{pq}(u, v, \omega)$. The calibration technique used in this thesis follows the technique used by Kemball et al. (1995).

Polarisation observations require additional calibration steps to those needed for standard spectroscopy:

- The different receivers and electronics at each antenna for each polarisation have phase and delay offsets between the orthogonally polarised signals. These offsets could be caused by differing cable length, filters or receiving electronics, and must be determined and removed.
- The D-terms must be determined and used to correct the r_{mn}^{RL} and r_{mn}^{LR} data.

The calibration method is outlined here, in preparation for Chapter 4, where the data reduction procedure used for the VY CMa data is discussed in detail. The major calibration steps deal with the bandpass response B_m^p and the amplitude and phase parts of the gain term term G_m^p:

$$
G_m^p = g_m^p \, e^{j\phi_m^p} \tag{3.15}
$$

where g_m^p describes the amplitude gain and ϕ_m^p the phase gain at antenna m for polarisation p. In spectral line VLBI, observations of the target source are interleaved with observations of a continuum source. The continuum source data are used in a number of calibration steps.

3.5.1 Bandpass calibration

The antenna-based bandpass frequency responses are determined using the parallel-hand cross power spectra of a point source continuum calibrator. Residual delays, which introduce phase slopes in the frequency domain, are removed from the calibrator data and the data are averaged over time before the bandpass fit is attempted. The bandpass fit is performed for each channel in the parallel-hand spectrum simultaneously by varying the bandpass response for each antenna and polarisation to minimize the χ^2 error:

$$\chi^2 = \sum_{m=1}^{N_a} \sum_{n=m+1}^{N_a} \sum_{l=1}^{N_c} ||r^{pp}_{mn}(\omega_l) - B^p_m(\omega_l) B^{p*}_n(\omega_l)|| \tag{3.16}$$

where N_a is the number of antennas, N_c is the number of channels, and $r^{pp}_{mn}(\omega_l)$ is the pre-averaged calibrator spectrum for antenna pair (m, n), at channel frequency ω_l. The complex bandpass responses $B^p_m(\omega_l)$ found by this method describe the frequency response of antenna m for polarisation p. A reference antenna is chosen, and the phase response of the bandpass of that antenna is set to zero. The phase components of the other bandpasses are adjusted to be relative to the reference antenna. This is necessary because the full set of equations for the phase response is under-determined as the cross-correlation data contains information about the phase difference between antennas only. The bandpass responses are smoothed and used to correct the source autocorrelation and cross-correlation data as follows:

$$r^{pp'}_{mm} = \frac{r^{pp}_{mm} - B^p_m(\omega)}{B^p_m(\omega)} \tag{3.17}$$

$$r^{pq'}_{mn} = \frac{r^{pq}_{mn}(\omega)}{\sqrt{B^p_m(\omega) B^{q*}_n(\omega)}} \tag{3.18}$$

(Kemball et al., 1995).

3.5.2 Amplitude calibration

The goal of the amplitude calibration process is to convert the uncalibrated cross-correlation spectra to units of correlated flux density, in Jy. To do this, the cross-correlation spectra are scaled by the geometric mean of the system equivalent flux densities (SEFD) of the antenna pair involved. The SEFD for antenna m is the product of the effective system temperature T_{sys} and the point source sensitivity PSS of the antenna, SEFD $= T_{sys} \times$ PSS. So the amplitude calibration to be applied to the continuum cross-correlation data is:

$$r_{mn}^{pq'} = b\,\sqrt{\mathrm{SEFD}_m\ \mathrm{SEFD}_n}\, r_{mn}^{pq} \tag{3.19}$$

where the factor b accounts for digitisation and sampling losses (Reid, 1995). The point source sensitivity of an antenna is directly proportional to its effective collecting area. This relationship is described by the gain curve of the antenna, which is the point source sensitivity as a function of elevation angle. By determining the point source sensitivity from the known antenna gain curve and using system temperatures obtained by noise diode measurements, the system equivalent flux density can be found and used to perform the amplitude gain calibration. The result will a calibrated cross-correlation spectra in units of Jy (Moran and Dhawan, 1995).

The amplitude calibration factors for the spectral line data for the target source, VY CMa, can be determined more accurately using a template-fitting method (Reid et al., 1980). In this method the elevation-dependent gain factors are determined by fitting each autocorrelation spectrum to a calibrated template spectrum $r^p(\omega)$ selected from the data for its high signal-to-noise ratio. Every other spectrum is compared to this template spectrum in a least squares sense. The differences are used to estimate a single multiplicative quality factor Q_m, for each antenna and each solution interval, which will scale the spectrum to fit the template spectrum. The quality factor is defined by:

$$r_{mm}^{pp}(\omega) = Q_m\, r^p(\omega) \tag{3.20}$$

where $r_{mm}^{pp}(\omega)$ is the autocorrelation spectrum for antenna m and polarisation p. The quality factors are determined by minimizing the sum of squares of $r_{mm}^{pp}(\omega) - Q_m r(\omega)$ for each antenna and polarisation in each solution interval.

For full polarisation observations, the gains determined by the amplitude calibration procedure suffer from a R/L amplitude offset caused by the unknown absolute calibration of the LL template spectrum relative to the RR template spectrum. Several methods are used to solve for the differential polarisation gain gain, g_0^{R-L}. Amplitude self-calibration of a continuum calibrator source with zero circular polarisation will give the residual RR and LL amplitude gains. The ratio of these values is the polarisation offset sought (Kemball, 1999). Kemball et al. (1995) find g_0^{R-L} directly from the r_{mn}^{RR} and r_{mn}^{LL} continuum calibrator data. The data reduction method used in this thesis fits the RCP template spectrum to the LCP template spectrum applying the Reid et al. (1980) technique discussed above to perform the fit. The offset between the LCP and RCP template spectra is the differential polarisation gain desired, assuming integrated Stokes V is small, as is true for these data. This technique was used by Diamond and Kemball (2003) for the reduction of VLBA SiO maser data.

3.5.3 Phase calibration

Phase calibration deals with the phase gain term in Equation 3.15. All known instrumental and propagation effects are removed a priori, leaving a residual phase error from clock errors, errors in the correlator model, propagation through the receiving system and atmospheric fluctuations. The residual phase can be approximated by a linear slope over time and frequency:

$$\phi_m^p(\omega, t) = (\omega - \omega_0)(\tau_m^p - \tau_0^p) + (\dot{\phi}_m^p - \dot{\phi}_0^p)(t - t_0) + (\phi_m^p - \phi_0^p) \qquad (3.21)$$

where τ_m^p is the residual group delay, $\dot{\phi}_m^p$ is the residual fringe rate, ϕ_m^p is the residual phase at antenna m for polarisation p and $m = 0$ at the reference antenna. The other two subscript zero values are the frequency edge of the band ω_0 and a reference time t_0 (Kemball et al., 1995). The residual group delay is $\tau_m^p = \frac{\partial \phi_m^p}{\partial \omega}$ and the residual fringe rate is $\dot{\theta}_m^p = \frac{\partial \phi_m^p}{\partial t}$. These gradients effectively approximate the phase error by linear slopes in time and frequency over short time intervals, with an offset of the residual phase.

Fringe fitting

The optimum delay and rate residuals are determined by searching the delay and fringe rate space for a pair of values that maximizes the correlation function. This process is known as fringe fitting. For spectral line sources the search is best done in the fringe rate and frequency domain as the signal is sharper in each of these domains than in their Fourier conjugates, time and delay (Reid, 1995).

One cause of residual delays is the differing local oscillator signals at each antenna. The local clocks may have an offsets and slow drifts. Residual delay errors are primarily caused by these clock offsets and residual propagation and electronic group delays in the signal path. Errors in the position of the antennas or source, or frequency offsets in the local oscillator may cause the residual fringe rate (Thomson et al., 2001, pg 326). The residual delay and rate errors originate largely in individual antennas and can consequently be treated in an antenna-based manner. For an array of N antennas, data from $N(N-1)/2$ baselines is available to find the N antenna-based rates and delays. A reference antenna is required for the phase calibration in the same way that it was for the bandpass calibration and because baseline-based data are used to estimate antenna-based gains the residual delay and rate at the reference antenna are set to zero. The delays and rates of other antennas are measured relative to those of the reference antenna. This method of fringe fitting is termed global fringe fitting, a technique developed by Schwab and Cotton (1983).

In the case of spectral line VLBI, the residual delays for each antenna are found by fringe fitting the continuum calibrator data. For maser observations in particular, the residual rate can be found by using a frequency channel in the target source data exhibiting a strong maser peak as a phase reference, as described by Reid et al. (1980). A fringe fit of this channel is performed using a point source model, with a residual delay of zero. The rate determined by this fringe fit can then be applied to all of the channels.

As implied by Equation 3.21, the phase gain is not independent of polarisation. The phase gain at each antenna will be referenced to a single chosen antenna but there will be a phase offset between the LCP and RCP phase gain at this reference antenna. Corrections for these polarisation offsets are discussed below.

Self-calibration

With the residual delays and rates removed, the visibility data still include a phase offset ϕ^p_m. The iterative process of self-calibration is used to find the residual phase. A review of this technique is given by Pearson and Readhead (1984).

Both the residual gain and source structure are estimated by a least-squares fit of the visibility data to the Fourier transform of a trial source model $\hat{r}_{mn}(u_k, v_k)$, to minimize:

$$\chi^2 = \sum_k \sum_{m=1}^{N_a} \sum_{n=m+1}^{N_a} a_{mn}(t_k)[r_{mn}(u_k, v_k, \omega_c) - d_m(t_k)d^*_n(t_k)\hat{r}_{mn}(u_k, v_k)]^2 \qquad (3.22)$$

where a_{mn} are weights, d_m are the residual gains to be determined and ω_c is the reference channel frequency (Pearson and Readhead, 1984; Kemball, 1992). The residual gain solutions provided by fitting Equation 3.22 are applied to the correlation function data. The corrected correlation functions are Fourier transformed to give a new source map. The method used to Fourier transform the data to give a source map is outlined in Section 3.6. The map is used as a new trial map in a second iteration of the self-calibration procedure. The initial trial source model is only a rough approximation to the true source structure, so this iterative procedure is required to find the correct residual phase gains (Thomson et al., 2001, pg 441).

The residual phase is not assumed to vary with frequency across the observed spectral line bandwidth, so for maser observations a self-calibration can be performed on a single frequency channel and the gain solution applied to all channels. The emission in the channel chosen for use in the self-calibration must be strong enough to allow high signal-to-noise ratio phase solutions and must not be too complex.

Polarisation offsets

Differences in the LCP and RCP phase calibration arises because the signal in each polarisation passes through different electronics in the receiver system (Roberts et al., 1994).

If the phase gains for the RCP and LCP data, $\phi^R_m(\omega, t)$ and $\phi^L_m(\omega, t)$, are determined in independent self-calibration, then there will be a positional offset between the two data sets, if the source is sufficiently circularly polarised (Kemball et al., 1995). For this reason the phase gain is initially solved for in one polarisation only, say LCP, relative to a reference antenna. The polarisation offset between the LCP and RCP phase gain at the reference antenna is then determined and added to the LCP gain to find the RCP phase gain, without losing the positional coincidence.

The polarisation offset consists of delay and phase residual offsets. There is no significant residual fringe rate offset in VLBI observations over the time intervals required for Equation 3.21 to hold (Kemball et al., 1995).

The residual delay and phase offsets at the reference antenna are given by:

$$\begin{aligned}\delta\tau_0^{R-L} &= \tau_0^R - \tau_0^L \\ \delta\phi_0^{R-L} &= \phi_0^R - \phi_0^L\end{aligned}$$

These polarisation corrections are added to Equation 3.21. If LCP is taken as the reference polarisation, then the final phase gains are:

$$\begin{aligned}\phi_m^L &= (\tau_m^L - \tau_0^L)(\omega - \omega_0) + (\dot{\theta}_m^L - \dot{\theta}_0^L)(t - t_0) + (\theta_m^L - \theta_0^L) \\ \phi_m^R &= (\tau_m^R - \tau_0^R + \delta\tau_0^{R-L})(\omega - \omega_0) + (\dot{\theta}_m^L - \dot{\theta}_0^L + \delta\dot{\theta}_m^{R-L})(t - t_0) \\ &\quad + (\theta_m^L - \theta_0^L + \delta\theta_m^{R-L})\end{aligned} \tag{3.23}$$

The delay offsets at a particular antenna are found from the cross-hand delays, τ_{mn}^{pq}, and parallel-hand delays, τ_{mn}^{pp} for baseline (m, n) of the continuum calibrator:

$$\begin{aligned}\delta\tau_m^{R-L} &= \tau_{mn}^{RL} - \tau_{mn}^{LL} = \tau_{mn}^{RR} - \tau_{mn}^{LR} \\ \delta\tau_n^{R-L} &= \tau_{mn}^{RL} - \tau_{mn}^{RR} = \tau_{mn}^{LL} - \tau_{mn}^{LR}\end{aligned}$$

So the delay offsets at a single antenna can be found from every baseline to that antenna. The delay offset at the reference antenna is found in this manner and applied according to Equation 3.23. This technique for finding the delay offsets was developed by Brown et al. (1989).

The residual phase polarisation offset at the reference antenna is also found from the continuum calibrator, which is assumed to have negligible circular polarisation.

Following the method used in Kemball et al. (1995), the phase offset can be determined from the parallel-hand baseline-based phases, Φ^{pp}_{mn}, by:

$$\Phi^{RR}_{mn} - \Phi^{LL}_{mn} = \delta\phi^{R-L}_{n} - \delta\varphi^{R-L}_{m} \tag{3.24}$$

where the baseline-base phase differences are found by dividing the RR by the LL data, which gives a phase which is the desired $\Phi^{RR}_{mn} - \Phi^{LL}_{mn}$. The set of Equations 3.24 for each antenna pair can be solved for the phase offsets up to an additive constant at the reference antenna.

After correction of all relative $R - L$ phase and delay offsets at the reference antenna, the absolute $R-L$ phase remains unknown. This is equivalent to uncertainty in the absolute electric vector position angle on the sky (Kemball et al., 1995). To find the absolute electric vector position angle, a calibrator source of known polarisation angle must be observed in conjunction with the target source (Cotton, 1993). The calibrator source data are calibrated and imaged and the relative polarisation position angle of the calibrator found. A polarisation position angle offset is determined by comparing the relative polarisation position angle of the calibrator with its known polarisation position angle. This offset can then be applied to the source data.

3.5.4 Antenna feed calibration

The final stage of VLBI spectral line polarisation calibration is solving for the D-terms discussed in Section 3.4. There are several methods used to find the D-terms, depending on the type of continuum calibrator used. Kemball and Diamond (1997) use a method which finds the D-terms from the target source, rather than a calibrator. It is a modification of the similarity method developed by Cotton (1993) for continuum observations. Cotton (1993) makes the assumption that the linear polarisation is a scaled version of the total intensity. This is adapted to the spectral line case by assuming that the linear polarisation in each channel is a scaled version of the total intensity in that channel, channel i:

$$Q(\omega_i) + jU(\omega_i) = \beta_i I(\omega_i) \tag{3.25}$$

where the linear polarisation is $Q(\omega_i) + jU(\omega_i)$ and β_i is the scaling factor. The β_i scaling factors for each channel are solved for in conjunction with the D-terms (Kemball and Diamond, 1997).

When the D-terms are known, the calibrated visibilities $\mathcal{RR}, \mathcal{LL}, \mathcal{RL}$ and $\mathcal{LR}$ can be derived from Equation 3.14.

3.6 Imaging

Once the data are calibrated, all that remains is to Fourier transform the data to give the source brightness distribution:

$$I(l,m) = \int\int \mathcal{V}(u,v)e^{j2\pi(lu+mv)}du\,dv \tag{3.26}$$

where $\mathcal{V}(u,v)$ is the visibility derived from the calibrated correlation function. This imaging process is discussed by Cornwell (1995). Unfortunately, the task is complicated by the fact that the visibility data are sparsely sampled in the (u,v) plane. The effect of the sampling is expressed as a sampling function $S(u,v)$ which is multiplied by the visibility to give what is called the dirty image I^D:

$$I^D(l,m) = \int\int S(u,v)\mathcal{V}(u,v)e^{j2\pi(lu+mv)}du\,dv \tag{3.27}$$

The dirty image is the convolution of the true image I and the Fourier transform of the sampling function, which is known as the dirty beam B, $I = B * I^D$. A deconvolution algorithm is required to extract the true source brightness distribution from the dirty image. The CLEAN algorithm devised by Högbom (1974) can be used for this purpose. The CLEAN process consists of subtracting a fraction of the dirty beam shape from the dirty map, where the dirty beam is centered at the point of maximum intensity on the dirty map. The fraction of the beam that is subtracted is called the loop gain. The subtraction is repeated with the new residual dirty map, where the subtracted dirty beam shape is now centered at the maximum intensity of the new dirty map. The subtractions are repeated until the maximum intensity of the final dirty map is comparable to the noise level of the map. At this stage the components subtracted from the original map are returned to the map, but in the form of clean beams, rather than dirty beams. The clean beam is the dirty beam without sidelobes. Clark (1980) developed a computationally efficient adaption of the original CLEAN algorithm known as the Clark CLEAN algorithm.

The goal of imaging polarisation data is to produce maps of all four Stokes parameters, I, Q, U and V. The visibility Stokes parameters, $\mathcal{I}$, $\mathcal{V}$, $\mathcal{U}$ and $\mathcal{Q}$ are derived from the visibility data using Equations 3.14. Equations 3.9 and 3.10 show that the Stokes I and V maps depend to first order on the parallel-hand $\mathcal{LL}$ and $\mathcal{RR}$ only. The Stokes Q and U maps depend to first order on the cross-hand $\mathcal{LR}$ and $\mathcal{RL}$, shown by Equations 3.11 and 3.12. Each image is independently deconvolved using the CLEAN algorithm.

The following chapter describes the reduction of the VY CMa SiO data in detail. The theory outlined in this chapter is applied in the process of calibrating and imaging the VLBI data.

Chapter 4

Data reduction

4.1 Introduction

The calibration of the VY CMa visibility data was undertaken within the Astronomical Image Processing System (AIPS)[1] environment. This software package is routinely used for the reduction and analysis of radio-interferometric data. It was developed, and is maintained, by the National Radio Astronomy Observatory (NRAO)[2]. A users' guide is available in the form of the AIPS Cookbook (Greisen, 2004). AIPS is the primary data reduction package for the VLBA.

The AIPS calibration model stores the results of calibration steps in tables attached to the visibility data files. The raw visibility data is not corrected by the program until the information in the tables is deliberately applied to the data (Diamond, 1995).

This chapter describes the calibration steps applied to the VY CMa data and the imaging of the calibrated data. Within AIPS, the steps are performed by individual independent programs called tasks, which are launched from the main program. The primary calibration steps consist of finding the bandpass response, amplitude calibration, phase calibration and polarisation calibration. Observations were made of both the target source VY CMa and continuum calibrators in the schedule. A summary of the sequence of tasks used in the full calibration is shown in Figure 4.14. Calibrations

---

[1] http://www.aoc.nrao.edu/aips

[2] http://www.nrao.edu

are built up incrementally in the associated tables. The final calibration tables contain the full calibration parameters. Each step in the calibration and imaging process is described in further detail below.

4.2 Observations

These data formed part of the VLBA project BK18 on 2 December 1994, spanning 06:17:08 to 10:59:51 UT. The locations of the ten VLBA antennas are shown in Table 4.2, along with the station code abbreviations used in figures produced by AIPS. The cartesian components of the VLBA station position are cited from the Goddard VLBI global solution 2004b[3].

Observations of VY CMa were interposed with observations of a continuum calibrator, the quasar 0420-014. The continuum source was used as a bandpass, phase and polarisation calibrator. Five scans were scheduled of both VY CMa and 0420-014, each scan of approximately twelve minutes in length. The VY CMa (u, v)-coverage is shown in Figure 4.1. The parameters u and v are the projected baseline lengths in the plane orthogonal to the source direction, in units of observing wavelength. Each arc in the figure is produced by one antenna pair. The gaps in the arcs at times when the antennas were observing sources other than VY CMa.

Both left-circular and right-circular polarised signals were recorded at each antenna and the data were cross-correlated in full polarisation. The observing band was centred at a LSR velocity of 19 km.s^{-1}, with a bandwidth of 4 MHz. The 4 MHz band was correlated over 128 spectral channels of nominal width 31.25 kHz (0.217 km.s^{-1}).

The data recorded at each antenna were written to magnetic tape and shipped to the VLBA correlator in Socorro. This correlator has an FX architecture. The correlated visibility data were written to DAT tape in FITS format for further processing.

---

[3] http://gemini.gsfc.nasa.gov/solutions/2004b/

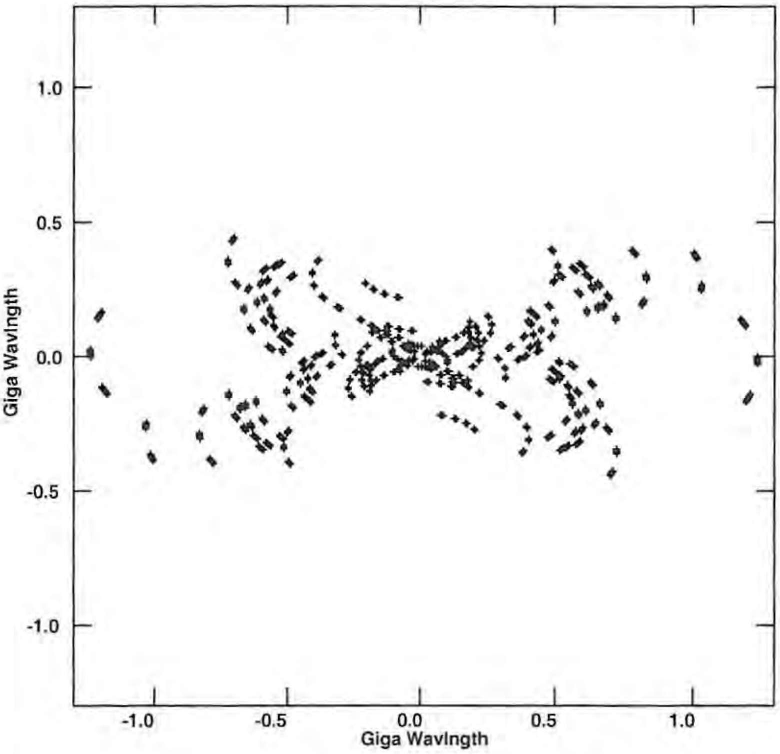

Figure 4.1: The (u, v)-coverage for the VY CMa observations. u and v are scaled in units of $10^9\lambda$.

4.3 Data loading

The data from these tapes were read into AIPS by the task FITLD. No data were excluded based on weight threshold at this stage. The data were recorded with one-bit (two-level) quantisation. FITLD corrected for quantisation effects.

4.4 Initial flagging

The first step in the data reduction process is the identification and removal of bad visibility data. Four initial flagging steps were performed on both the VY CMa and calibrator data.

The first flags applied were those generated by the on-line observing software,

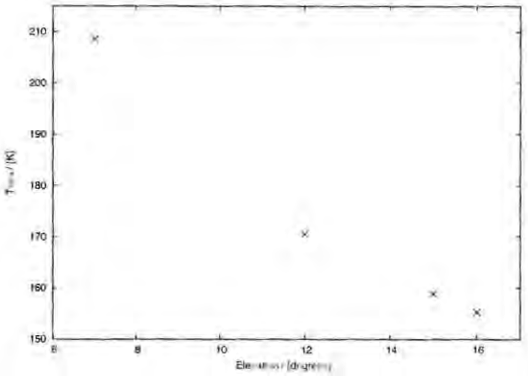

Figure 4.2: Plot of RCP system noise temperature versus elevation angle at the Brewster antenna for four VY CMa scans. The Brewster antenna was down for the first scan. Each point denotes the average system temperature and average elevation per scan.

which removes all data known to be bad at the time of observation. The next step was flagging observations made below an elevation threshold of 10°. The removal of this data is required because of the rising system temperature due to the increasing atmospheric noise contribution at low elevation. The brightness temperature of the atmosphere T_B as a function of elevation angle θ is:

$$T_B = T_{at}(1 - e^{-\tau_0 \sec(\pi/2-\theta)}) \tag{4.1}$$

where T_{at} is the temperature of the atmosphere and τ_0 is the zenith opacity. Equation 4.1 describes an exponential decrease in system temperature with increasing elevation angle, which is visible in Figure 4.2, a plot of system temperature versus elevation for the Brewster antenna scans. The rise in noise temperature with elevation is clear in this plot. In the second Brewster scan the average elevation angle was less than 10°, so this scan was flagged, along with all scans from other antennas meeting this criterion. The third set of flags was determined from the operator logs accompanying the data. These logs note problems recorded by the operator during the observing run. These first three flagging steps were performed using the AIPS task UVFLG.

The final step was flagging by correlator weight. The correlation completeness weight is a measure of the fraction of valid data present in each correlation integration interval. Data may be lost due to tape playback synchronisation errors. Figure 4.3 displays graphs of weight versus time for the VY CMa autocorrelation data. Most of the data has a constant correlator weight, as expected. Regions of lower weight were excluded by choosing appropriate weight cutoffs. The weight cutoff determined from the VY CMa autocorrelation data weight plot was 0.16130. The same cutoff was used for the VY CMa cross-correlation data. A cutoff of 0.32016 was used for the calibrator autocorrelation and cross-correlation data. This step was performed using the task UVCOP. Figure 4.4 displays the weight versus time graphs with the weight flagging applied.

4.5 Calibrator autocorrelation data

The continuum calibrator 0420-014 was used to determine the autocorrelation bandpass response. The technique used to solve for the autocorrelation bandpass is outlined in Section 3.5.1.

4.5.1 Calibrator autocorrelation editing

Before solving for the autocorrelation bandpass response, a final interactive flagging step was undertaken on the 0420-014 autocorrelation data with the AIPS task IBLED. IBLED displays the visibility plot for a single baseline, averaged over multiple spectral channels, on a graphics device. Outlier points are interactively identified and flagged. All of the Owens Valley data were flagged in the autocorrelation data of the calibration source at this stage. This was done because the IBLED plots of the left circular polarisation Owens Valley data showed much higher values than the other antennas, indicating a left circular polarisation problem at this antenna.

4.5.2 Autocorrelation bandpass

After final interactive flagging, the task CPASS was used to determine the antenna-based autocorrelation bandpass responses. This task models the bandpass profile as a Chebyshev polynomial expansion. The algorithm uses least-squares minimisation so it is sensitive to outliers and requires the previous flagging steps to achieve the

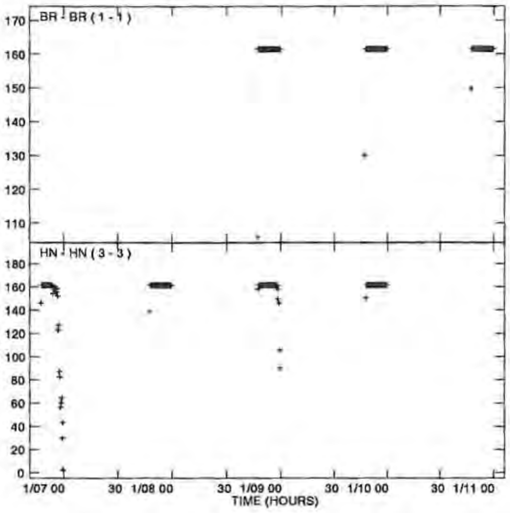

Figure 4.3: VY CMa autocorrelation plots of correlator weight vs time for antennas Brewster and Hancock for the RR data. The on-line, elevation and operator log flagging has been applied. Note the regions of low weight below the threshold of 0.1613.

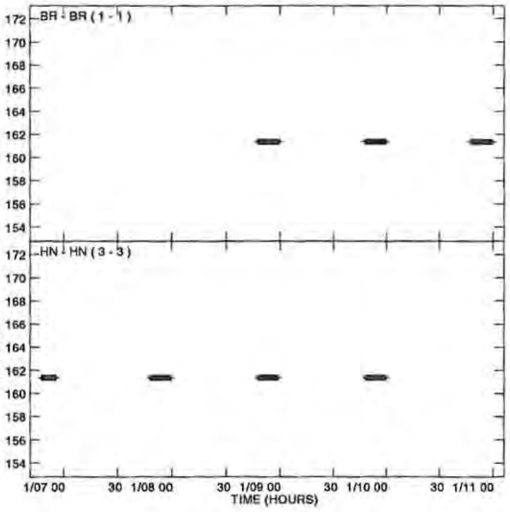

Figure 4.4: VY CMa autocorrelation plots of correlator weight vs time for antennas Brewster and Hancock for the RR data. The on-line, elevation and operator log and correlator weight flagging has been applied.

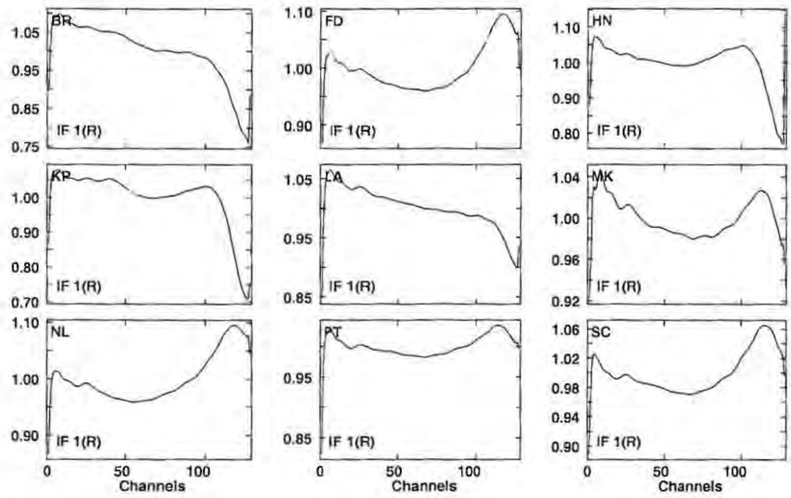

Figure 4.5: Normalised RCP autocorrelation bandpass responses for each antenna. The axes are normalised amplitude versus channel number. The antenna station code is in the top left corner of each figure. The text at the bottom left indicates the intermediate frequency band used for the bandpass solutions, IF 1, and the polarisation in brackets.

best solution. The bandpass profiles produced were examined, any further flagging performed as necessary, and CPASS rerun. The normalised RCP autocorrelation bandpass profile for each antenna is shown in Figure 4.5.

4.6 VY CMa autocorrelation data

The antenna-based bandpass responses determined using the continuum calibrator data were applied to the VY CMa spectral line autocorrelation data. The VY CMa autocorrelation data were then used to derive the amplitude calibration described in Section 3.5.2. Final interactive flagging of the VY CMa autocorrelation data was performed using IBLED, in a similar manner to the calibrator autocorrelation data.

4.6.1 Velocity shifting

The VLBA does not make any real-time Doppler frequency correction, beyond a mean correction for the centre of the run set in the observing file, so the spectral profile will

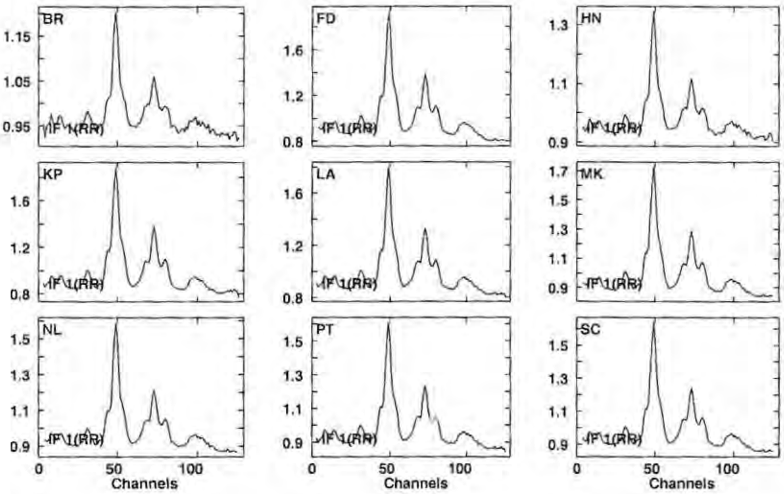

Figure 4.6: Doppler-shifted VY CMa autocorrelation spectra in RR, averaged over the full observing run. The ordinate is amplitude, in uncalibrated units, and the abscissa is channel number.

move in the observing band over time. The VLBA correlator places the spectra in a geocentric frame, but further velocity shifts are required to transform the spectra to the local standard of rest reference frame. These shifts are necessary because of time variable Doppler shifts due to the velocity of the sun with respect to the local standard of rest, the velocity of the earth-moon barycenter with respect to the sun, and the velocity of the earth's center with respect to the earth-moon barycenter.

The local standard of rest velocity of the band centre used during the observing is not preserved in the data flow through the correlator, and needs to be set explicitly with the task SETJY. The velocity shifting was then applied by the task CVEL, which shifts each autocorrelation spectrum to correct for the time varying residual Doppler shift, to place the spectra in the local standard of rest reference frame. The calibrator autocorrelation bandpasses determined by CPASS were also applied during this step.

The VY CMa autocorrelation spectra after the Doppler shift corrections were made are shown in Figure 4.6. The correction is small, with the spectra being shifted by only a fraction of a channel, as expected.

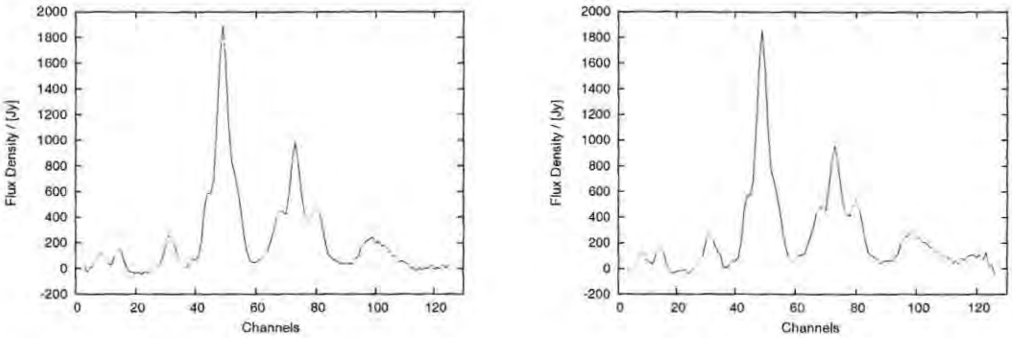

Figure 4.7: The template spectra at Los Alamos. The ordinates are amplitude, in units of Jy, and the abscissas are channel number. The left figure is the RR template spectrum and the right figure is the LL template spectrum.

4.6.2 Amplitude calibration

The template-fitting method developed by Reid et al. (1980) was used to perform the amplitude calibration of the autocorrelation data. The template scan required by this technique needs to have a high signal-to-noise ratio. The fourth scan, from 09:47 to 09:59, at the Los Alamos antenna, was chosen to be the most suitable. The right and left circular polarised autocorrelation spectra of this scan are shown in Figure 4.7.

The mean system temperatures for the template scans in each polarisation were determined from the calibration files accompanying the data to be 161.1 K for RCP and 160.9 K for LCP.

The average elevation angle of Los Alamos during the template scan was 28.4°. The correponding zenith angle of 61.6° was used to calculate the point source sensitivity PSS of the antenna during this scan, using the expression:

$$\mathrm{PSS} = \frac{1}{G_0(a + b\,z + c\,z^2 + d\,z^3)} \tag{4.2}$$

where z is the zenith angle. The zenith angle polynomial expression must be scaled by a gain factor, G_0, and inverted to yield the point source sensitivity. The coefficients a, b, c and d are measured periodically for the receivers at each VLBA antenna, and are provided to observers by VLBA Operations. The gain factor and coefficients

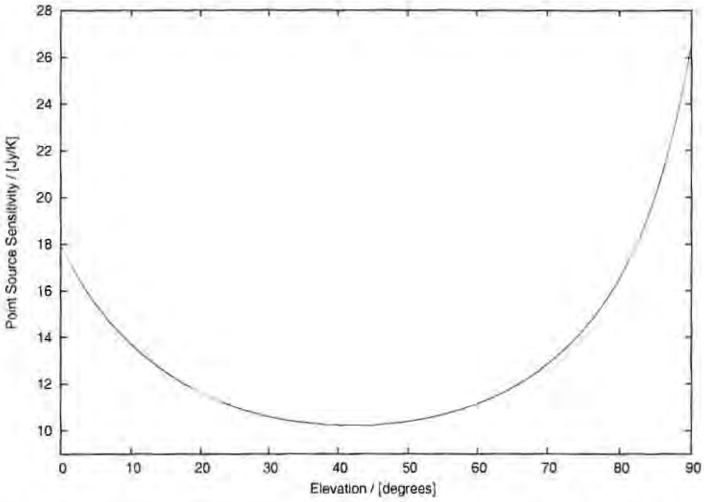

Figure 4.8: The point source sensitivity a function of elevation angle for the Los Alamos antenna at 7 mm.

provided for Los Alamos during this observation were:

$$
\begin{aligned}
G_0 &= 0.097 \\
a &= 0.574 \\
b &= 2.011\, e^{-2} \\
c &= -2.193\, e^{-4} \\
d &= -3.024\, e^{-7}
\end{aligned}
$$

These values were taken from VLBA gain calibration text files. The same value of G_0 was used for both the RCP and LCP data. A plot of the point source sensitivity given by Equation 4.2 at Los Alamos for a range of elevation angles is shown in Figure 4.8. The resulting point source sensitivity for the template scan was 11.33 Jy/K.

The antenna-based system temperatures and point source sensitivities are required inputs to the amplitude calibration task ACFIT. This task fits the chosen template to to all autocorrelation spectra over successive solution intervals and over all frequency channels using a linear least-squares algorithm. A second degree residual quadratic spectral baseline was solved for in each solution interval, along with the relative gain

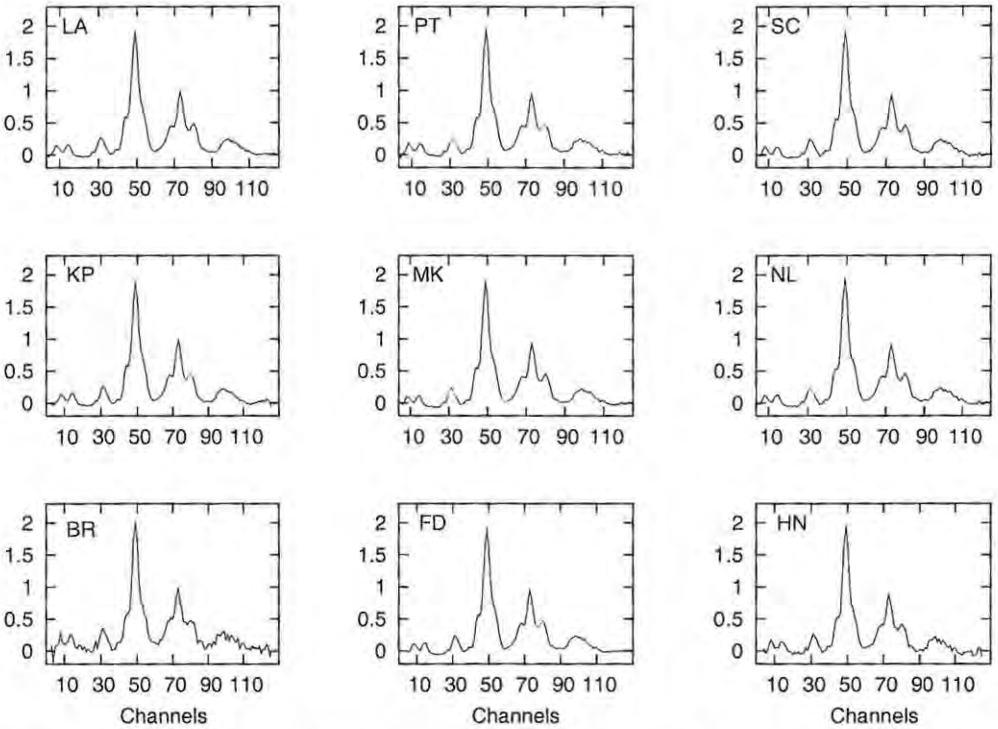

Figure 4.9: Calibrated VY CMa autocorrelation spectra in RR, averaged over the full observing run. The ordinates are amplitude, in units of kJy, and the abscissas are channel number. The amplitude calibration was performed using the template spectra shown in Figure 4.7

factor with respect to the template spectrum. The system temperature and point source sensitivity for the template scan serve to translate the relative antenna-based gains determined by ACFIT to absolute gains. The ACFIT solutions were smoothed and clipped of outliers before being applied to the data. Figure 4.9 shows the RCP VY CMa autocorrelation spectra with the ACFIT solutions applied.

4.6.3 Polarisation offset: Amplitude

The task ACFIT fits the RCP target source autocorrelation data to the RCP template spectrum shown, and the LCP target source autocorrelation data to the LCP template spectrum. This leaves an unknown amplitude offset between the two template spectra.

ACFIT was used again to find this offset by fitting the LCP template spectrum to the RCP template spectrum, following the method described in Section 3.5.2. This method relies on the assumption that the integrated Stokes V is negligible, as is the case for these data. The differential scaling factor for the template scan was found to be 0.979 for the VY CMa data.

4.7 Calibrator cross-correlation data

The continuum calibrator cross-correlation data were used to find the composite bandpass response of the system and to derive elements of the required phase calibration.

The template spectrum fitting method can only be used for spectral-line data. For the continuum calibrator data the amplitude calibration was performed using the task APCAL, that uses system temperatures measured throughout the observing period and gain information for each antenna and receiver as described in Section 3.5.2. The effect of the parallactic angle was also accounted for at this stage, using the task CLCOR.

The data was interactively flagged before solving for the cross-correlation bandpass responses, as it was for the autocorrelation bandpass responses. The cross-correlation data had to be averaged in time and frequency prior to the interactive flagging step, which requires a preliminary fringe fit to be performed to correct for the residual fringe rates and delays. Before the fringe fit, the cross-correlation continuum calibrator data was averaged in frequency over eight channels by the task AVSPC. The fringe fit was then performed using the task FRING, applying the previously determined parallactic angle and amplitude corrections prior to fringe fitting. The group delay and fringe rate solutions were applied to the data before interactive flagging using IBLED.

4.7.1 Cross-correlation bandpass

The cross-correlation bandpass response was determined using the task CPASS. The interactive flags perviously determined using IBLED were applied in advance of a second fringe fit for residual group delays and fringe rates. The final fringe fit solutions were applied in CPASS in solving for the complex antenna-based cross-correlation bandpass response. At 43 GHz the amplitude response of the autocorrelation data has

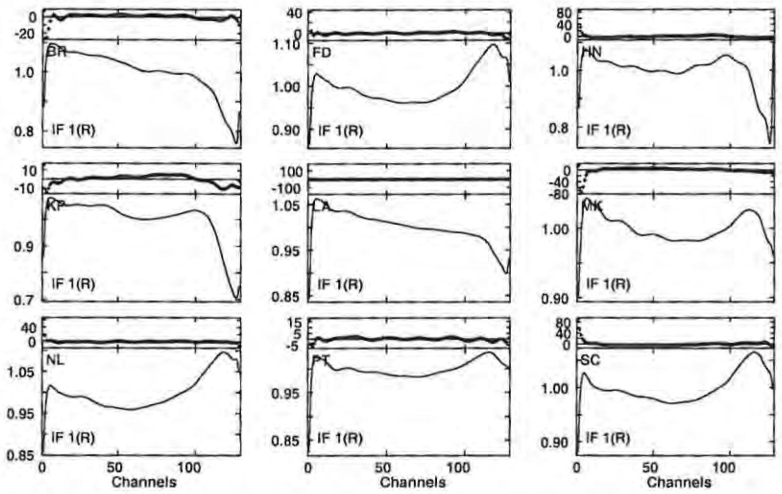

Figure 4.10: The full RCP antenna-based bandpasses for each antenna. The abscissa is channel number. The ordinate of the top frame of each figure is the phase of the bandpass response in degrees. The ordinate of the bottom frame of each figure is normalised amplitude.

much higher signal-to-noise ratio than that of the cross-correlation data. Therefore the original amplitude bandpass response determined by the autocorrelation data was used as the amplitude of the cross-correlation bandpass response, and CPASS was only used to determine the phase of the full complex bandpass response. Both amplitude and phase of the full bandpass responses are shown in Figure 4.10. The phase response is reasonably constant over the central channels, with approximately $5^\circ - 10^\circ$ variations. Los Alamos was used as a reference antenna so it's phase was set to zero and other antenna phases are relative to Los Alamos.

4.7.2 Phase calibration: Delay

The calibrator cross-correlation data were fringe fit to determine the residual delay by the process described in Section 3.5.3. The amplitude calibration and the cross-correlation bandpass response were applied to the data before the fringe fit was performed. The delay, rate and phase solutions determined by FRING were clipped to remove outliers and the delay solutions were smoothed by the task SNSMO. SNSMO applied boxcar smoothing with a smoothing interval of 3 minutes.

4.7.3 Polarisation offset: Phase

The residual delay calibration procedure described in Section 4.7.2 determines the group delays relative to R and L respectively at the reference antenna. This leaves a R-L group delay offset at the reference antenna This group delay offset between left and right polarisations at the reference antenna, Los Alamos, was found using an antenna-based method, similar to the technique of Brown et al. (1989). The rates and delays from the previous fringe fit performed in Section 4.7.2 were applied to a subset of the cross-correlation data comprising all baselines to the reference antenna, Los Alamos. The task SWPOL was used to switch the polarisation labelling, so FRING could be used to fringe fit the cross-hand polarisation data, RL and LR, rather than the usual LL and RR. This provides the residual LR and RL delays, which, after applying the parallel hand delays, are used to derive the group delay offsets. The LR and RL delay solutions were averaged to improve their signal-to-noise ratio and stored in a solution table with the task POLSN. They were also averaged in time over the length of the observations, as the R-L delay offset is expected to be constant over the entire duration of the observation. The delay offset for Los Alamos was -20.4 ± 1.9 ns, which is of the order of the delay offsets found by Roberts et al. (1994). This value was stored for application in the final calibration steps.

The phase calibration procedure described in Section 4.8.2 finds the residual phase for a single reference polarisation, here chosen to be RCP. The offset between the right circularly polarised and left circularly polarised calibration must then be determined in order to derive the phase correction for the LCP data. The phase RR-LL offset was found by averaging the calibrator cross-correlation data across all spectral channels, then dividing the RR visibility data by the LL visibility data. This division results in an amplitude which is the ratio of the RR and LL amplitudes, and a phase which is the difference between the RR and LL phases. The AIPS task DIFRL performs the division. A self-calibration was performed on these data using the task CALIB, which determines the calibration necessary to conform the data to a desired source model. The technique of self-calibration is discussed in Section 4.8.2. The model in this case was a point source at the phase centre. The left-right phase offsets remain reasonably constant at each antenna, varying by less than 8° across the course of the observing run.

These methods of finding the phase and group delay polarisation offsets are described in Section 3.5.3.

4.8 VY CMa cross-correlation data

The calibrations determined from the continuum calibrator data and the VY CMa autocorrelation data were then systematically applied to the cross-correlation VY CMa line data. Firstly, the complex bandpass response found in Section 4.7.1 was transferred to the VY CMa cross-correlation data. The cross-correlation line data, like the autocorrelation line data, were then corrected for the effect of Doppler shift by the task CVEL, having set the velocity and rest frequency of a reference channel with the task SETJY. The amplitude calibration determined for the autocorrelation line data in Section 4.6.2 was applied to the cross-correlation data. Parallactic angle corrections were applied, as they were to the calibrator data. The smoothed delay solutions from Section 4.7.2 were applied to the data, as well as the smoothed R-L delay offset from Section 4.7.3 and the differential polarisation amplitude gain from Section 4.6.3.

4.8.1 Phase calibration: Rate

The next calibration step was the determination of the residual fringe rate. The data were examined by baseline and channel to find a channel displaying an unresolved compact maser spot which was visible on both short and long baselines. Channel 72 was chosen on this basis, corresponding to a velocity of 17.479 $km.s^{-1}$.

The residual fringe rate solution was found in an iterative manner. A preliminary fringe fit was performed on channel 72 with FRING - searching only for the rate solution. The fringe fit solution was applied to the data and a further round of interactive flagging was performed with IBLED on the channel 72 cross-correlation data. The flagged data were removed and a final fringe fit performed on the reference channel. The final rate solutions were smoothed and applied to both the right and left circular polarisation data.

It was assumed that there was no offset between the left and right polarisation residual fringe rates. This assumption can be made because the origins of fringe rates in the VLBI data are not polarisation dependant. A common local oscillator drives both RCP and LCP receiving systems, giving no polarisation fringe rate offset. Propagation through the neutral atmosphere does not give a polarisation fringe rate offset, and propagation through the ionosphere will also not have a significant effect on 43 GHz observations.

4.8.2 Self-calibration

The final antenna-based phase corrections were determined through the process of self-calibration. The self-calibration was performed using the two tasks CALIB and IMAGR on the RR data only. The AIPS task CALIB compares *uv* data with visibilities derived from a source model. It solves for the antenna-based gains required to bring the data into agreement with the model. CALIB was used in the phase only mode, to determine phase but not amplitude calibrations for the selected spectral reference channel. As in Section 4.8.1, the reference channel was chosen to be channel 72. Following Reid et al. (1980), this channel is used as a phase reference source. IMAGR was used as an imaging task which applies the Clark CLEAN algorithm (Clark, 1980).

The CALIB phase gains were applied to the *uv* data and imaged with IMAGR. The image produced by IMAGR was used as the input model in the next CALIB-IMAGR iteration.

The first step of this algorithm used a point source model of unit flux density in CALIB. The calibrated *uv* data were cleaned using IMAGR until the first negative clean component was encountered. The next CALIB step used this IMAGR image as the source model. The first three iterations halted the IMAGR clean at the first negative clean component. Thereafter, the clean was halted when the maximum absolute residual in the image was less than a prescribed limiting flux which varied with iteration number. For the first three iterations the solution interval used in CALIB was held constant. The fourth and subsequent iterations linearly reduced the solution interval used in CALIB and the flux limit used in IMAGR to yield a final solution interval of approximately 20 s and a target deconvolution threshold for the

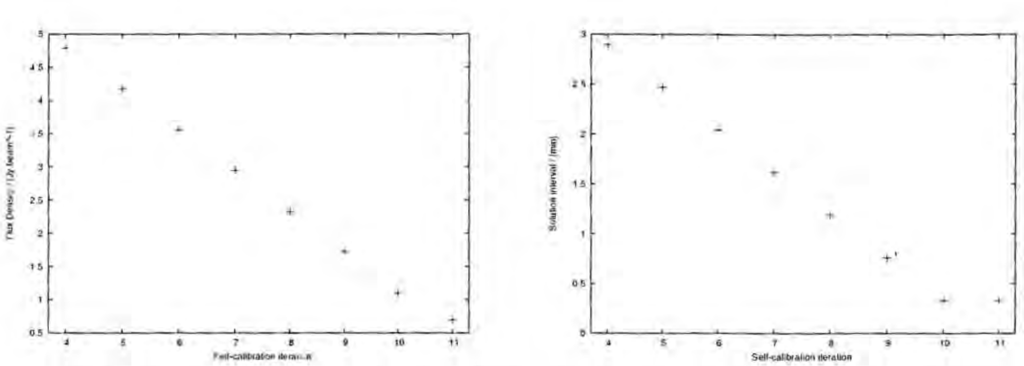

Figure 4.11: Plot of the parameters used in each self-calibration iteration. The flux limits used in IMAGR are shown on the left. The first three iterations were stopped when the first negative clean component was reached. Thereafter the flux was decreased linearly from 4.79 Jy.beam^{-1} to 1.1 Jy.beam^{-1}. The solution interval used in CALIB is shown on the right. The first three iterations used a solution interval of 3.33 minutes. Thereafter the solution interval was decreased linearly from 3.33 minutes to 20 seconds. An eleventh iteration used a solution interval of 20 seconds again, and limiting flux of 0.7 Jy.beam^{-1}.

final iteration.

The final flux should be a small multiple of the thermal noise S:

$$S = \frac{\mathrm{SEFD}}{\eta_s\sqrt{N_{vis}\delta t_{corr}\Delta\nu}} \tag{4.3}$$

where η_s is the quantisation efficiency, which is assumed to be unity, N_{vis} is the total number of visibility data points, δt_{corr} is the correlator integration time and $\Delta\nu$ is the bandwidth of the channel (Thomson et al., 2001, pg 191). A nominal zenith 7 mm SEFD of 1436 Jy was used (Wrobel and Ulvestad, 2004) with the channel width of 31.25 kHz. The total number of visibilities in the flagged data was 9918 and the correlator integration time was 4.718592 s, giving a thermal noise level of 0.04 Jy.

The cell size used in IMAGR was 0.04 mas, which was approximately 1/8 of the PSF FWHM. A field size of 4096 by 4096 cells was used, given the angular extent of the SiO emission towards VY CMa, which is approximately 80 × 80 mas (Miyoshi, 2003).

Several sets of self-calibration parameters were explored to find the optimal values.

Ultimately the combination of solution interval and final CLEAN threshold that resulted in the best final image was chosen. The images were judged according to their RMS noise, the integrated intensity of a Gaussian fitted to the main component in the channel, the CLEAN threshold the final IMAGR step could clean down to before diverging, the total cleaned flux in the image and deepest negative component in the image. The parameter values used in the final self-calibration are shown in Figure 4.11. A solution interval of 3.33 minutes was used for the first three iterations, which was linearly decreased over the next seven iterations to 20 s. The CLEAN threshold was also linearly decreased from a value of 4.79 Jy in iteration number four, to a final value of 1.1 Jy. A final iteration dropped the CLEAN threshold to 700 mJy, the lowest value IMAGR would clean to before diverging.

Figure 4.12 shows the RMS noise in the images produced in each step of this process, illustrating the successful use of self-calibration to improve the phase calibration. The RMS noise was calculated in a region which contained no emission, a corner box of size approximately (10 x 10) % of the overall map dimensions. The first map and final map, of iteration number 11, produced by IMAGR during the self-calibration are shown in Figure 4.13. A dramatic change in the noise levels is clearly visible. A dynamic range of $\sim$ 1470 was achieved for the final channel 72 image in the self-calibration.

Errors in the self-calibration and deconvolution lead to errors, such as deep negatives, in the final maps. These errors are used to derive a threshold value for real maser emission, as described in Chapter 5. The calibration and deconvolution errors scale with peak flux-density to first-order. VY CMa is a strong SiO maser emitter, so the thermal noise level was not reached because the systematic calibration errors are above the thermal noise limit.

4.8.3 Polarisation correction

The right circular polarisation phase solution found by the self-calibration process was applied to both the right and left circular polarisation data after applying the R-L offsets found from the calibrator cross-correlation data. The phase difference between the right and left circularly polarised data obtained in Section 4.7.3 was copied to a calibration table as a left-circular polarisation calibration. It was negated and applied

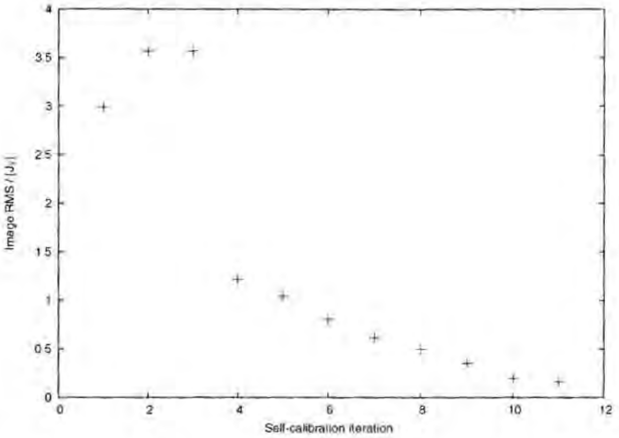

Figure 4.12: RMS noise in each of the eleven images produced by IMAGR at each iteration of the self-calibration process.

to the data to perform the final correction. This procedure was performed by several runs of the task SNCOR.

4.9 Image cubes

At this stage the results of the full calibration process were contained in tables attached to the VY CMa cross-correlation data. The final imaging step applied these tables to all of the visibility data, and imaged the full data cube. Channels 10 to 118 were imaged with IMAGR using uniform gridding weighting. In order to avoid edge effects, the channels 1 to 9 and 119 to 128 were not imaged. The channels were individually imaged to form an image cube containing 109 images, one for each channel, of 4096 by 4096 cells each. The Stokes I and V image cubes were created from the LL and RR parallel-hand polarisation data only, as described in Section 3.6. For the total intensity, Stokes I, image cube IMAGR used a restoring beam of 1.087×0.370 mas in half-power with a position angle of $-8.7°$. The restoring beam used for the Stokes V image cube was 1.274×0.401 mas in half-power with a position angle of $-12.4°$.

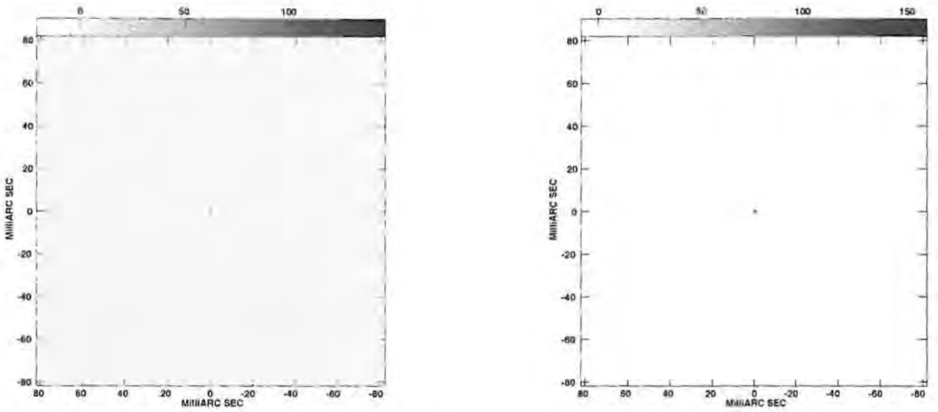

Figure 4.13: The initial (left) and final (right) channel 72 images produced in the self-calibration process.

4.9.1 Feed calibration

Imaging of the Stokes Q and U parameters require a correction for instrumental polarisation. The AIPS task SPCAL was used to determine the D-terms. This task assumes that the linear polarisation in each channel is a scaled version of the corresponding total intensity, as described in Section 3.5.4. The amplitude and phase of the D-terms are listed in Table 4.1. These D-terms were applied to the data, and Stokes Q and U images cubes were created with IMAGR from the LR and RL data. IMAGR used a restoring beam of 1.274 × 0.401 mas in half-power with a position angle of $-12.4°$ for the Stokes Q and U image cubes.

Antenna	D_R		D_L	
	Amplitude	Phase [deg]	Amplitude	Phase [deg]
BR	0.13796	149.59	0.06100	47.35
FR	0.02503	-113.29	0.04908	-68.62
HN	0.09580	-45.50	0.00993	-90.60
KP	0.03218	-59.80	0.01520	25.66
LA	0.00103	-58.67	0.03290	-30.80
MK	0.15598	28.01	0.09729	-96.67
NL	0.04066	-129.20	0.02195	-77.49
PT	0.04781	113.51	0.01809	-39.48
SC	0.01554	-93.83	0.03816	-172.28

Table 4.1: The D-term amplitude and phase for the left and right circularly polarised feeds at each antenna. The D-terms are complex numbers which describe the instrumental feed cross-polarisation contamination.

Antenna	Abbreviation	Cartesian component	Value [mm]	Uncertainty [mm]
St. Croix	SC	X	2607848521.82	0.489
		Y	-5488069685.59	0.989
		Z	1932739539.62	0.548
Hancock	HN	X	1446375115.36	0.254
		Y	-4447939653.94	0.590
		Z	4322306122.76	0.599
N. Liberty	NL	X	-130872253.82	0.210
		Y	-4762317114.15	0.486
		Z	4226851039.05	0.514
Fort Davis	FD	X	-1324009126.11	0.242
		Y	-5332181964.79	0.511
		Z	3231962473.17	0.513
Los Alamos	LA	X	-1449752358.72	0.230
		Y	-4975298588.23	0.461
		Y	3709123927.82	0.504
Pie Town	PT	X	-2732333293.10	18.036
		Y	-4217634736.49	27.010
		Z	3914491294.78	25.474
Kitt Peak	KP	X	-1995678626.36	0.267
		Y	-5037317712.98	0.527
		Z	3357328129.97	0.540
Owens Valley	OV	X	-2409150112.48	0.281
		Y	-4478573229.62	0.507
		Z	3838617399.97	0.557
Brewster	BR	X	-2112064976.18	0.258
		Y	-3705356515.65	0.460
		Z	4726813799.25	0.566
Mauna Kea	MK	X	-5464074960.17	0.730
		Y	-2495249115.62	0.581
		Z	2148296844.62	0.630

Table 4.2: Cartesian components of the VLBA station position vectors, from the Goddard VLBI global solution 2004b

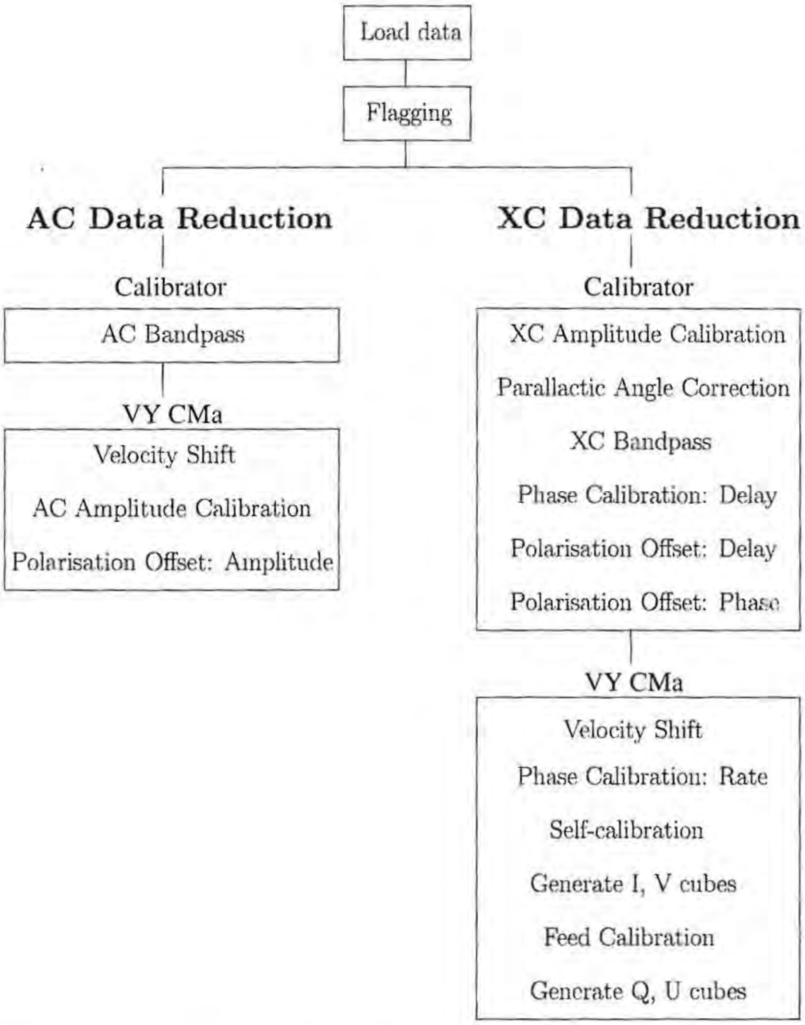

Figure 4.14: Flowchart outlining the data reduction and imaging steps.

Chapter 5

Results

5.1 Introduction

The imaging process described in Chapter 4 resulted in an image cube for each of the four Stokes parameters, I, Q, U and V. Each cube consists of 109 individual maps for each of the channels imaged. Maps of the Stokes I total intensity in each channel and the linear polarisation in each channel are shown in Appendix A and Appendix B respectively. Maps of each channel of the Stokes Q, U and V data cubes are shown in Appendix C, D and E of the electronic version of this thesis. Composite maps of the emission averaged over all frequency channels in the image cubes are shown in Figures 5.3 to 5.6. A similar composite map of the linearly polarised intensity in each channel is shown in Figure 5.7.

The total-power spectrum of the SiO emission observed is shown in Figure 5.1. Figure 5.2 shown the total flux in the final Stokes I map, Figure 5.3, summed over each pixel. There is a substantial amount of missing flux due to emission that is too resolved to be detected with VLBI. The flux recovered in the synthesis image is $\sim 40\%$ of the total flux shown in Figure 5.1. The spatial distribution of this missing flux is unknown.

In order to analyse the maser maps the properties of individual maser components must be extracted. This chapter describes the identification of maser components in the total intensity data cube and the derivation of the polarisation properties of the components.

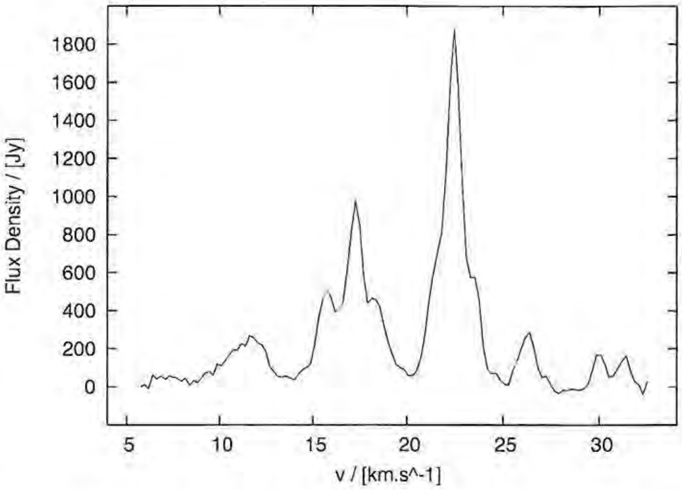

Figure 5.1: The total power spectrum at the Los Alamos antenna, averaged over the full observing period. The ordinate is Flux Density, in units of Jy.

5.2 Identifying maser components

The individual channels in the Stokes I, Q, U and V cubes are subject to a non-Gaussian noise distribution resulting from the calibration and imaging processes. Error propagation in these processes adds a non-Gaussian tail to the noise distribution (Kemball, 1992). A threshold level must be chosen, above which the map pixels are considered to represent real maser emission, and below which they are considered noise. This threshold was chosen by applying the technique of Kemball (1992).

The off-source RMS in the channel maps is an underestimate of systematic calibration and imaging errors, which vary across the map in practice. Negative values in the maps provide a measure of these systematic errors, as negative values should not occur in total intensity maps. Kemball (1992) broadened the off-source noise variance so that the deepest negative occurs with probability of $1/(4096 \times 4096)$, assuming a Gaussian noise distribution, for a map of 4096×4096 pixels.

The deepest negative value in each Stokes I image was found with the AIPS verb IMSTAT. These values were used to determine a broadened noise variance of $\sigma_I \sim |I_{neg}|/5.294$ for the Stokes I maps. The noise variance was calculated for each channel map and threshold was chosen to be ten times this value. The necessity to

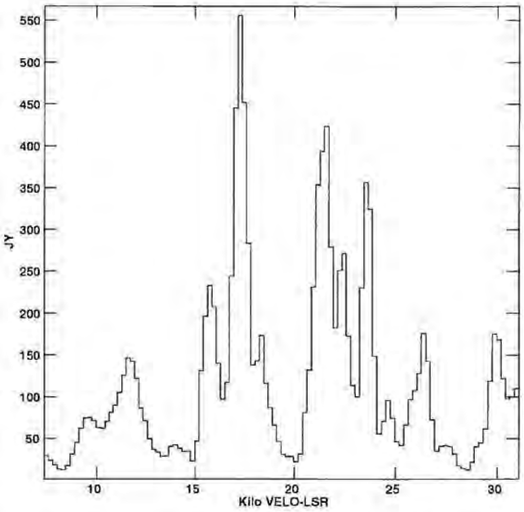

Figure 5.2: The flux density spectrum obtained from the final total intensity map, Figure 5.3, by summing the intensity over all pixels in the map. The ordinate is Flux Density, in units of Jy.

have individual channel cutoffs is highlighted by Figures A.5 and A.6 in Appendix A. The maps of velocities 22 through 22.9 km.s^{-1} have the highest flux densities of the cube and consequently greater deconvolution errors. This is seen in the high number of features in the maps of these velocities in Appendix A. The use of higher cutoffs for these maps ensures that only statistically significant features are retained.

The AIPS task SAD was used to automatically find and fit two-dimensional Gaussians to individual maser components in channels of the Stokes I image cube. SAD found regions of intensity above the specified threshold and merged these regions into islands of emission. A least squares algorithm was used to fit a two-dimensional Gaussian to each peak in this island region. The Gaussians were subtracted from the original images to form residual images. The residual images were examined for any emission greater than the cutoff intensity. A number of such regions were found. Two-dimensional Gaussians were manually fitted to these regions with the task JMFIT. A total of 322 Gaussian components were fitted in the channel maps.

The Doppler width of an SiO line in the circumstellar environment will span several of the 0.217 km.s^{-1} velocity channels used in the observations. The $v = 1$

$J = 2$–1 SiO masers observed around VX Sgr by Doeleman et al. (1998), for example, had line widths of the order of 0.5 km.s^{-1}. Consequently real maser features should be present in a number of adjacent channel maps, colocated within the clean beam size. The Gaussian fitted components were grouped with components in adjacent channels which met this coincidence requirement. Components which were only present in one channel were rejected. This resulted in a total of 81 groups, which were taken as individual maser components. Each component is about 1 mas in size.

Full component details are shown in Table 5.1. The full width at half maximum Δv was derived from one-dimensional Gaussian fits to the component groups over frequency. This field is blank where a reliable fit was not possible. The right ascension and declination values were taken to be the peak position of the original two-dimensional Gaussian which had the highest intensity of the group. These positions are relative to the phase center of the map, located at the maser feature used as a phase reference in the self-calibration process. Errors in the component positions were found by the method of Condon (1997), which deals with errors in elliptical Gaussian fits. Kogan (1996) put these errors into a convenient form for right ascension α and declination δ measurements,

$$\begin{aligned}\sigma_\alpha^2 &= \frac{2}{\rho^2}\frac{1}{8\ln(2)}\left(\theta_M^2 \sin^2\phi + \theta_m^2 \cos^2\phi\right)\\ \sigma_\delta^2 &= \frac{2}{\rho^2}\frac{1}{8\ln(2)}\left(\theta_m^2 \sin^2\phi + \theta_M^2 \cos^2\phi\right)\end{aligned}$$

where θ_M and θ_m are the major and minor axis of the fitted Gaussian respectively, and ϕ is the position angle of the major axis. The parameter ρ is a measure of the overall signal-to-noise ratio of the Gaussian fit. In the case of partially resolved source, where the beam size is similar to the source size, the factor $\frac{2}{\rho^2}$ is equal to $\frac{\sigma_I^2}{I^2}$, the ratio of the squares of the broadened noise variance and the intensity (Kogan, 1996).

5.3 Polarisation

While the Stokes parameters fully describe the polarisation of the source, the polarisation information is more useful in the form of the fractional circular polarisation m_c and the fractional linear polarisation m_l. These values are derived from the Stokes parameters:

$$m_c = \frac{V}{I} \tag{5.1}$$

$$m_l = \frac{P}{I} \tag{5.2}$$

where $P = \sqrt{Q^2 + U^2}$. In order to compare the four Stokes parameter image cubes, parameter values were extracted from the maps at the peak position of the original two-dimensional Gaussian fit which had the largest Stokes I value of each group. The values of each of the Stokes parameters at this pixel position were found with IMVAL and the fractional polarisations calculated using Equations 5.1 and 5.2.

The noise distributions of the polarisation parameters are not Gaussian. The detection limit for each of these values is consequently found using the method suggested by Kemball (1992). The measured off-peak RMS noise in each image, $\sigma_I^0(\omega)$, $\sigma_V^0(\omega)$, $\sigma_Q^0(\omega)$ and $\sigma_U^0(\omega)$, was found in an off-source box in the corner of the image, using the task IMSTAT. These values were broadened using the assumed Stokes I noise variance σ_I to give $\sigma_V = \beta\sigma_V^0$, $\sigma_Q = \beta\sigma_Q^0$, $\sigma_U = \beta\sigma_U^0$, where β is given by $\beta = \frac{|I_{neg}|}{5.294 \times \sigma_I^0(\omega)}$. The thresholds used were:

$$u_c \sim \frac{1.96\sigma_V}{I} \tag{5.3}$$

$$u_l \sim \frac{1.65}{\sqrt{2}} [\frac{P + \sigma_P}{I - \sigma_I} - \frac{P - \sigma_P}{I + \sigma_I}] \tag{5.4}$$

where $\sigma_P = \frac{\sqrt{Q^2 {\sigma_Q}^2 + U^2 {\sigma_U}^2}}{P}$.

The fractional linear polarisation has a Rice probability distribution so a corrected version m_l' of this value must be used so as not to overestimate the linear polarisation (Wardle and Kronberg, 1974):

$$m_l' = \frac{\sqrt{Q^2 + U^2 - \sigma_{QU}}}{I} \tag{5.5}$$

where $\sigma_{QU} = \sqrt{\sigma_Q \sigma_U}$ assuming $\sigma_Q \backsim \sigma_U$ (Kemball, 1992). The linear polarisation angle is given by:

$$\chi = \frac{1}{2} \arctan(\frac{U}{Q}) \tag{5.6}$$

The error in the linear polarisation angle has a symmetric probability distribution with zero mean and consequently does not need to be corrected for statistical bias (Wardle and Kronberg, 1974).

As described in Section 3.5.3, the absolute electric vector position angle is unknown. The absolute position angle was determined through VLA observations of the continuum calibrator source, 0420-014, and a source of known polarisation position angle, 3C286. The electric vector position angle was transferred from the 3C286 VLA data to the VY CMa VLA data, and finally applied to the VY CMa VLBA data used in this thesis. The VLA observations took place on 12 November 1994, shortly before the VLBA observations. These observations were also used by Kemball et al. (1996), who found a final position angle offset of −7.8°, assuming an absolute polarisation position angle of 33° for 3C286. The relative position angles calculated from the Stokes Q and U data cubes were translated into absolute electric vector position angles by rotating the χ values obtained by Equation 5.6 clockwise by 7.8°. The linear polarisation vectors displayed in Figure 5.7 and Appendix B have been rotated to show the absolute polarisation position angles.

The Stokes parameter values and broadened noise variances for the identified components are displayed in Table 5.1, along with the non-zero fractional circular polarisations, fractional linear polarisations and the absolute polarisation position angles for components displaying linear polarisation. The uncertainties in m_c, m_l' and χ quoted in the table are calculated from the corresponding Stokes parameter uncertainties following Boboltz (1997):

$$\sigma_c = \frac{1}{I}\sqrt{\sigma_V^2 + \frac{V}{I}\sigma_I^2} \tag{5.7}$$

$$\sigma_l = \frac{1}{I}\sqrt{\sigma_P^2 + \frac{P}{I}\sigma_I^2} \tag{5.8}$$

$$\sigma_\chi = \frac{1}{2P^2}\sqrt{Q^2\sigma_U^2 + U^2\sigma_Q^2} \tag{5.9}$$

The following chapter describes the analysis of the VY CMa SiO maser data summarised in Table 5.1.

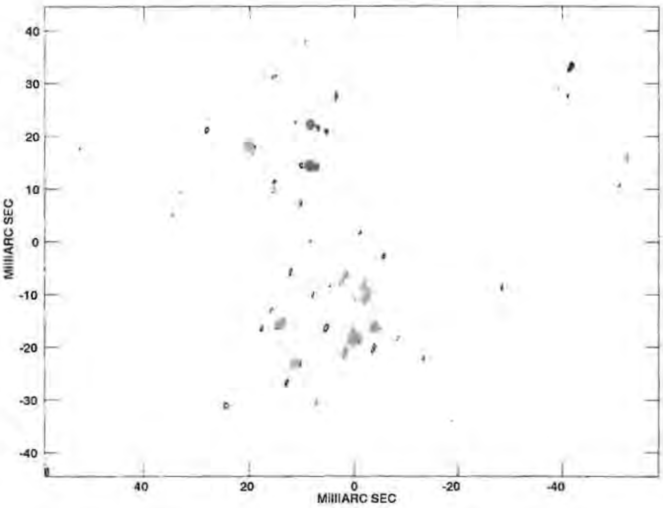

Figure 5.3: A contour plot of the total intensity (Stokes I) maser emission towards VY CMa, averaged over frequency. The contour levels are -100, -80, -60, -40, -20, -10, -5, 5, 10, 20, 40, 60, 80 and 100% of the peak brightness in the Stokes I cube, 148.93 Jy/beam. The velocity of the emission is represented by the colour of the contours, where the red features are the most redshifted and blue features are the most blueshifted. The synthesised beam is displayed in the bottom left corner, and is 1.087 × 0.370 mas in half-power with a position angle of $-8.7°$.

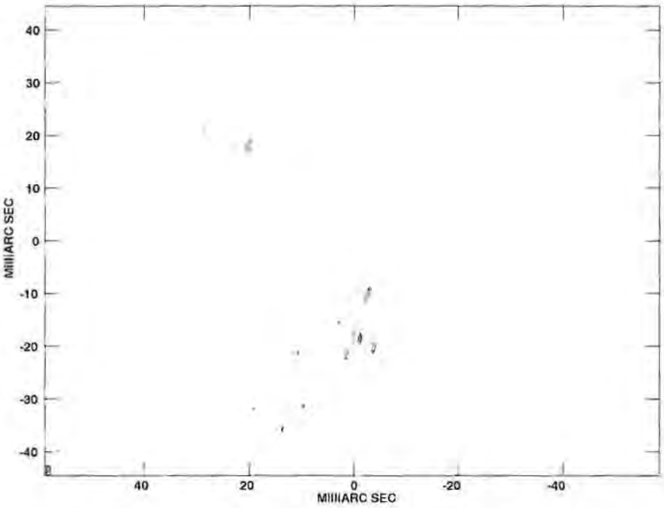

Figure 5.4: A contour plot of the Stokes V maser emission towards VY CMa, averaged over frequency. The contour levels are -100, -80, -60, -40, -20, -10, 10, 20, 40, 60, 80 and 100% of the peak brightness in the Stokes V cube, 10.694 Jy/beam. The velocity of the emission is represented by the colour of the contours, as for Figure 5.3. The synthesised beam is displayed in the bottom left corner, and is 1.274 × 0.401 mas in half-power with a position angle of $-12.4°$.

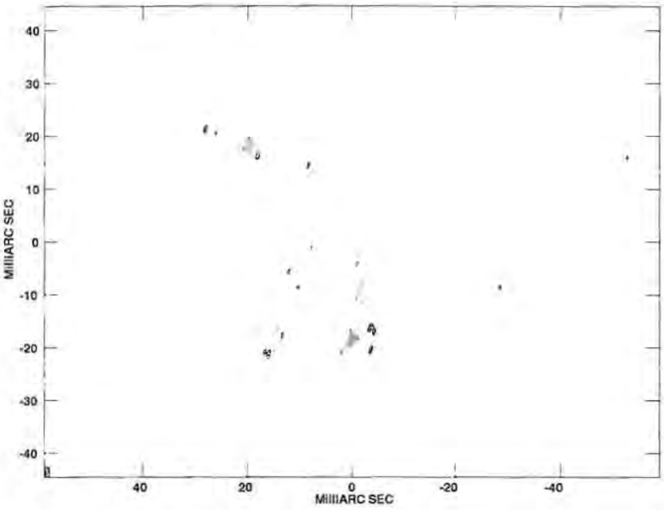

Figure 5.5: A contour plot of the Stokes Q maser emission towards VY CMa, averaged over frequency. The contour levels are -100, -80, -60, -40, -20, -10, -5, 5, 10, 20, 40, 60, 80 and 100% of the absolute value of the peak brightness in the Stokes Q cube, -42.891 Jy/beam. The velocity of the emission is represented by the colour of the contours, as for Figure 5.3. The synthesised beam is displayed in the bottom left corner, and is 1.274 × 0.401 mas in half-power with a position angle of $-12.4°$.

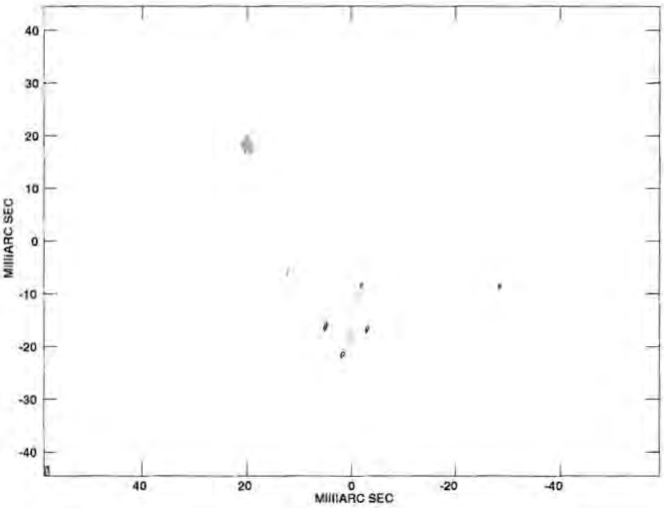

Figure 5.6: A contour plot of the Stokes U maser emission towards VY CMa, averaged over frequency. The contour levels are -100, -80, -60, -40, -20, -10, -5, 5, 10, 20, 40, 60, 80 and 100% of the peak brightness in the Stokes U cube, 75.699 Jy/beam. The velocity of the emission is represented by the colour of the contours, as for Figure 5.3. The synthesised beam is displayed in the bottom left corner, and is 1.274 × 0.401 mas in half-power with a position angle of $-12.4°$.

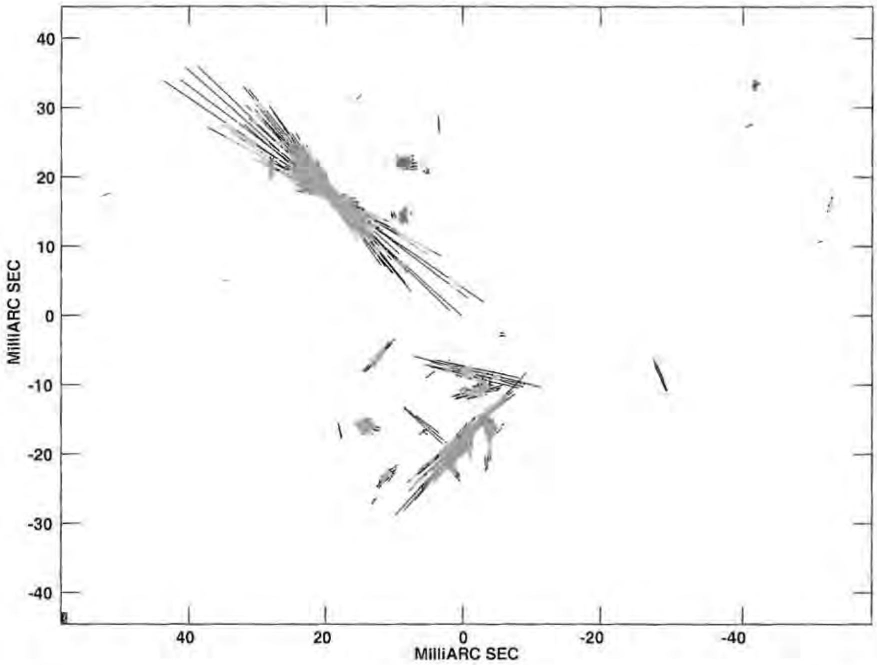

Figure 5.7: Linear polarization vectors for regions of intensity greater than 5% of the peak intensity in the Stokes I image cube, 148.93 Jy/beam. The fractional linear polarisation m_l is represented by the length of the vectors, where 1 mas = 1.25 Jy/beam. The absolute polarisation position angle χ is represented by the orientation of the vector in the image. The velocity of the emission is represented by the colour of the contours, as for Figure 5.3. The synthesised beam is displayed in the bottom left corner, and is 1.274 × 0.401 mas in half-power with a position angle of $-12.4°$.

Table 5.1: List of maser components. See text for explanation of column headings.

v [km.s^{-1}]	Δv [km.s^{-1}]	α [mas]	σ_α [mas]	δ [mas]	σ_δ [mas]	I [Jy]	σ_I [Jy]	V [Jy]	σ_V [Jy]	Q [Jy]	σ_Q [Jy]	U [Jy]	σ_U [Jy]	m_c %	σ_c %	m_l %	σ_l %	χ [deg]	σ_χ [deg]
30.949		3.372	0.007	45.936	0.017	20.799	0.671	-0.196	0.576	2.085	0.814	1.289	0.593			11.3	3.7	8.1	7.7
30.949		7.008	0.006	32.472	0.010	32.582	0.671	-0.648	0.576	0.349	0.814	0.057	0.593						
30.732		6.792	0.024	43.468	0.041	5.000	0.401	-0.276	0.374	-0.724	0.457	-0.684	0.360						
30.515	0.381	-28.648	0.004	9.788	0.012	15.463	0.365	-0.715	0.322	2.777	0.365	5.090	0.362	-4.6	2.1	37.4	2.5	22.9	1.8
29.863	0.389	8.556	0.002	32.752	0.004	65.083	0.485	-2.474	0.358	0.937	0.466	-0.872	0.403	-3.8	0.6	1.9	0.7	-29.3	9.7
29.863		15.108	0.015	29.740	0.024	10.081	0.485	0.126	0.358	0.039	0.466	-0.323	0.403						
29.428	0.507	9.576	0.008	32.864	0.012	12.530	0.309	0.269	0.189	0.166	0.320	0.584	0.257						
27.908	0.294	4.548	0.013	9.976	0.018	8.006	0.270	-0.125	0.221	0.062	0.347	-2.132	0.255			26.4	3.3	-52.0	4.7
27.690	0.256	10.984	0.012	46.564	0.022	5.647	0.225	-0.576	0.241	0.546	0.280	-0.205	0.226	-10.2	4.3				
27.473		15.596	0.015	5.820	0.021	7.405	0.250	-0.304	0.249	0.087	0.284	-0.075	0.284						
27.256		19.380	0.038	28.292	0.049	3.239	0.313	0.055	0.381	-1.201	0.357	0.450	0.364			38.0	11.7	71.9	8.1
27.256		15.732	0.016	5.392	0.022	8.843	0.313	-0.347	0.381	0.121	0.357	0.135	0.364						
26.821		13.000	0.025	48.480	0.032	5.599	0.343	0.366	0.300	0.484	0.415	-0.840	0.365						
26.387	0.302	13.712	0.004	2.872	0.005	46.502	0.497	-2.369	0.405	-3.840	0.500	0.781	0.426	-5.1	0.9	8.4	1.1	76.4	3.1
26.387	0.351	14.564	0.006	2.608	0.010	23.837	0.497	-1.533	0.405	-0.256	0.500	1.136	0.426	-6.4	1.7	4.5	1.8	43.5	12.2
25.735		14.800	0.022	49.880	0.034	8.144	0.551	-0.620	0.474	0.545	0.656	-1.330	0.557						
25.518	0.482	-37.256	0.006	22.224	0.014	6.718	0.174	-0.369	0.143	-0.987	0.218	0.192	0.186	-5.5	2.1	14.7	3.3	76.7	5.3
25.518	0.401	15.328	0.012	49.664	0.011	7.849	0.174	-0.699	0.143	-0.459	0.218	-0.430	0.186	-8.9	1.8	7.6	2.6	-76.2	9.2
25.083		16.140	0.013	1.636	0.026	4.908	0.249	-0.514	0.172	-0.009	0.230	-0.145	0.217	-10.5	3.5				
24.866		-5.592	0.033	1.800	0.062	2.084	0.173	0.049	0.113	0.244	0.150	-0.318	0.147						
24.649	0.305	-3.918	0.003	-1.956	0.005	20.562	0.186	2.086	0.132	4.972	0.195	-0.458	0.165	10.2	0.6	24.3	1.0	-10.4	0.9
24.649	0.283	17.564	0.003	1.916	0.006	14.508	0.186	-0.147	0.132	2.129	0.195	1.699	0.165			18.7	1.3	11.5	1.9
24.431	0.537	-51.052	0.004	29.096	0.011	9.474	0.197	-0.210	0.147	-0.593	0.211	-0.613	0.186			8.8	2.1	-74.8	6.7
23.562	0.314	-2.536	0.002	7.892	0.002	97.705	0.368	3.317	0.376	-3.857	0.406	-5.321	0.391	3.4	0.4	6.7	0.4	-70.8	1.7
23.562		-5.048	0.023	12.384	0.050	3.997	0.368	0.172	0.376	-0.006	0.406	0.060	0.391						
23.562	0.265	10.168	0.012	-0.328	0.029	6.322	0.368	0.148	0.376	-0.078	0.406	-0.111	0.391						
22.693	0.328	11.276	0.020	-4.760	0.026	58.046	2.990	-0.905	1.829	0.604	2.090	-2.191	1.814						
22.259		-2.080	0.009	10.104	0.015	62.634	1.948	-0.600	1.362	-27.071	1.525	5.638	1.393			44.1	2.8	76.3	1.4
21.824		19.656	0.006	36.276	0.014	33.477	0.864	1.251	0.813	-8.994	1.009	0.365	0.853			26.7	3.1	81.0	2.7
21.824		-52.756	0.004	34.396	0.011	36.813	0.864	0.021	0.813	2.722	1.009	-0.364	0.853			7.0	2.7	-11.6	8.9
21.824		10.168	0.012	25.676	0.026	15.925	0.864	0.189	0.813	-0.062	1.009	0.114	0.853						
21.824		19.200	0.004	35.720	0.009	47.656	0.864	-0.274	0.813	-20.757	1.009	22.829	0.853			64.7	2.3	58.3	0.9
21.390	0.398	32.916	0.018	27.748	0.032	7.973	0.564	0.033	0.491	-0.634	0.600	3.028	0.506			38.2	7.0	43.1	5.5
21.390	0.409	20.044	0.001	36.568	0.002	137.827	0.564	9.387	0.491	-39.759	0.600	65.455	0.506	6.8	0.4	55.6	0.4	52.8	0.2
21.173		30.560	0.014	16.188	0.031	6.092	0.415	-0.016	0.357	-0.010	0.411	0.416	0.349						
20.955		-53.516	0.018	35.304	0.044	4.073	0.390	0.182	0.321	0.208	0.417	-0.059	0.379						
20.738		21.312	0.021	37.772	0.041	2.497	0.234	-0.079	0.177	0.019	0.254	0.642	0.217						
20.521		19.828	0.005	37.240	0.005	21.964	0.228	1.279	0.189	4.206	0.253	10.527	0.193	5.8	0.9	51.6	1.1	26.3	0.6
19.869		24.680	0.023	38.368	0.033	3.193	0.203	-0.071	0.156	1.906	0.193	2.487	0.183			98.0	8.6	18.5	1.7
19.869		25.172	0.030	48.620	0.048	2.183	0.203	-0.070	0.156	0.314	0.193	0.266	0.183						
19.652	0.297	-54.568	0.009	36.256	0.022	5.932	0.250	-0.048	0.189	-0.091	0.229	-0.563	0.245						
19.435	0.336	18.548	0.013	38.104	0.029	4.173	0.244	-0.342	0.180	-0.065	0.203	-0.413	0.211						
19.000		50.872	0.025	35.716	0.037	6.051	0.404	-0.140	0.431	-1.182	0.466	-0.210	0.480						

Continued on the next page

v [km.s^{-1}]	Δv [km.s^{-1}]	α [mas]	σ_α [mas]	δ [mas]	σ_δ [mas]	I [Jy]	σ_I [Jy]	V [Jy]	σ_V [Jy]	Q [Jy]	σ_Q [Jy]	U [Jy]	σ_U [Jy]	m_c %	σ_c %	m_l %	σ_l %	χ [deg]	σ_χ [deg]
19.000	0.257	51.624	0.014	36.056	0.027	8.532	0.464	-0.018	0.431	-0.662	0.466	-1.263	0.480			15.8	5.7	-66.6	9.4
18.348	0.285	1.584	0.004	-2.840	0.006	43.862	0.486	-1.227	0.386	1.321	0.417	5.983	0.464	-2.8	0.9	13.9	1.1	31.0	2.0
18.131		27.188	0.015	39.464	0.035	7.072	0.478	-0.348	0.365	1.275	0.442	1.643	0.433			28.7	6.5	18.3	6.0
17.696		27.992	0.011	39.536	0.019	20.056	0.766	-0.743	0.765	4.434	0.811	0.932	0.730			22.3	4.1	-1.9	4.0
17.479	0.308	0.024	0.003	0.068	0.005	146.590	1.245	-0.456	1.219	11.712	1.410	-34.545	1.185	-4.4	0.8	24.9	0.9	-43.4	1.1
17.262		0.224	0.001	0.900	0.003	110.714	0.649	-0.941	0.611	1.534	0.643	-21.104	0.589			19.1	0.5	-50.7	0.9
17.262		12.720	0.020	-8.304	0.041	10.310	0.649	-0.546	0.611	0.924	0.643	-0.312	0.589						
16.827	0.389	-1.116	0.005	-0.156	0.008	48.244	0.773	2.369	0.674	4.964	0.838	2.297	0.794	4.9	1.4	11.2	1.7	4.6	4.2
16.610	0.396	1.328	0.009	12.012	0.016	20.255	0.569	-0.470	0.473	-0.241	0.683	0.125	0.589						
16.176	0.295	-4.948	0.009	1.764	0.020	13.511	0.588	0.512	0.488	0.569	0.595	-2.601	0.535			19.3	4.1	-46.6	6.4
15.958		1.904	0.010	11.150	0.026	12.594	0.504	-1.339	0.468	-0.414	0.549	0.076	0.502	-10.6	3.7				
15.741	0.382	-4.003	0.006	2.224	0.008	41.537	0.601	-0.451	0.552	3.368	0.644	0.156	0.548			8.0	1.6	-6.5	4.7
15.741	0.320	2.716	0.017	10.376	0.034	8.872	0.601	-0.429	0.552	-0.046	0.644	0.115	0.548						
15.307	0.279	12.044	0.006	12.656	0.017	20.708	0.681	-0.054	0.600	2.795	0.641	-8.689	0.624			44.0	3.4	-43.9	2.0
14.872		19.504	0.029	62.068	0.035	3.148	0.223	-0.117	0.192	-0.150	0.240	0.135	0.217						
14.655	0.304	11.160	0.008	41.040	0.015	8.774	0.255	0.768	0.204	-1.112	0.232	0.779	0.225	8.8	2.3	15.3	2.7	64.7	4.8
14.438	0.442	-10.632	0.009	60.172	0.021	5.169	0.222	-0.421	0.179	0.040	0.191	-0.013	0.207	-8.2	3.5				
14.003	0.256	-0.228	0.004	7.556	0.007	11.831	0.152	-0.049	0.097	-0.409	0.135	-1.970	0.129			17.0	1.1	-58.7	1.9
13.351	0.649	-41.192	0.003	46.068	0.007	10.148	0.131	-0.438	0.093	-0.513	0.101	-1.307	0.119	-4.3	0.9	13.8	1.2	-63.5	2.1
13.351		-34.924	0.011	34.004	0.028	2.307	0.131	-0.084	0.093	-0.360	0.101	0.007	0.119			14.9	4.5	81.6	9.4
13.134		-34.400	0.012	34.116	0.027	2.611	0.133	-0.204	0.057	-0.659	0.121	0.021	0.131	-7.8	3.4	24.8	4.8	81.3	5.7
12.699	0.313	10.864	0.013	43.044	0.026	5.283	0.267	0.267	0.193	-0.196	0.246	0.548	0.250						
12.048	0.552	8.716	0.004	40.736	0.007	24.372	0.365	-0.859	0.309	-1.258	0.339	0.663	0.290	-3.5	1.3	5.7	1.4	68.3	6.1
11.613	0.540	8.107	0.001	40.358	0.002	51.272	0.240	-1.422	0.202	-3.092	0.233	-1.830	0.192	-2.8	0.4	7.0	0.4	-82.5	1.6
10.961	0.540	6.788	0.007	39.832	0.014	11.255	0.316	-0.725	0.268	-0.900	0.352	-0.769	0.257	-6.4	2.4	10.2	2.8	-77.6	7.3
10.527	0.743	-39.380	0.006	47.688	0.015	8.037	0.236	-0.545	0.228	0.573	0.252	-0.369	0.211	-6.8	2.8	8.0	3.0	-24.2	9.4
10.527	0.520	5.116	0.004	39.168	0.009	13.242	0.236	-0.605	0.228	-0.251	0.252	1.060	0.211	-4.6	1.7	8.0	1.6	43.9	6.6
10.310		5.208	0.014	41.764	0.037	2.964	0.223	-0.267	0.207	-0.097	0.206	0.235	0.213						
10.092	0.682	-40.740	0.029	51.604	0.034	3.592	0.221	-0.226	0.244	-0.014	0.239	-0.038	0.239						
10.092	0.303	-42.052	0.008	51.836	0.011	10.690	0.221	-0.242	0.244	-0.169	0.239	-0.389	0.239						
9.658	0.561	-41.848	0.001	51.764	0.003	22.782	0.128	-0.339	0.108	-0.326	0.134	-1.018	0.142	-1.5	0.5	4.7	0.6	-61.7	3.6
9.441		-39.584	0.018	46.968	0.046	1.460	0.143	-0.032	0.130	-0.068	0.150	-0.076	0.156						
9.223		-41.688	0.002	51.448	0.005	17.545	0.135	-0.207	0.107	0.154	0.137	-0.776	0.147			4.4	0.8	-47.2	5.0
9.223	0.413	-41.488	0.003	51.376	0.007	14.124	0.135	-0.468	0.107	0.231	0.137	-0.363	0.147	-3.3	0.8	2.9	1.0	-36.6	9.3
9.006	0.671	-4.872	0.016	13.816	0.024	2.689	0.109	0.044	0.090	-0.402	0.104	0.326	0.107			20.7	4.0	64.6	5.4
9.006		-5.856	0.017	13.260	0.046	1.641	0.109	-0.030	0.090	-0.302	0.104	0.180	0.107			25.5	6.6	69.9	7.1
7.920	0.816	-6.880	0.011	14.420	0.023	2.286	0.091	0.069	0.067	0.064	0.067	0.002	0.052						
7.485	0.557	-5.864	0.002	15.608	0.004	12.007	0.103	-0.944	0.086	-0.752	0.080	-0.181	0.077	-7.9	0.7	6.4	0.7	-91.0	2.9

Chapter 6

Analysis

6.1 Introduction

The SiO maser emission observed towards late-type stars originates in a complex, dynamic region of the circumstellar envelope. Published VLBI maps of these regions show the masers to lie within a few stellar radii of the star, in the extended atmosphere. The circumstellar material in these regions is influenced by stellar pulsations, shocks, mass loss and turbulence.

Diamond and Kemball (2003) recently published a time-lapse image sequence of the $v = 1$ $J = 1-0$ SiO masers towards TX Cam which consisted of 44 individual synthesis maps captured over a two year observing period. Although TX Cam is a Mira-variable and displays a more regular SiO maser distribution than VY CMa, the variability of the maser emission during the "movie", the local infall and outflow superimposed on a global expansion of the shell, and the general asymmetry of the SiO emission give some indication of the typical complexity of the near-circumstellar envelopes around late-type stars. Single-dish spectra of $v=1$ $J=1-0$ SiO emission towards late-type stars generally show high time variability, also reflecting the complexity of the maser region (Pardo et al., 2004). The dynamic nature of the SiO maser emission means that any analysis of a single synthesis image must be done with care. A brief description of synthesis images of SiO maser emission towards late-type stars is given in Section 6.2.

This chapter presents an astrophysical analysis of the images produced in this thesis. The total intensity maser emission is sparse, with an irregular distribution concentrated in the east. The possibility of a ring structure is investigated in Section 6.3.1. The next section, Section 6.3.2, looks for evidence of a bipolar flow in the SiO emission, followed by an examination of velocity gradients in the masers in Section 6.3.3. The observed polarisation of the maser features is considered in Section 6.4, particularly with reference to the magnetic field in the maser shell region.

It should be noted that the VLBA observations do not cover the entire velocity range of the $v = 1$ $J = 1 - 0$ emission towards VY CMa. The single-dish spectra observed by Spencer et al. (1981), for example, show emission over a velocity range of almost 40 km.s^{-1}, while the VLBA data used in this thesis only spans about 28 km.s^{-1}. The single dish monitoring performed by Pardo et al. (2004) shows emission beyond 30 km.s^{-1} around the time of the VLBA observations used in this thesis, which would have been missed by the velocity range of the VLBA observations. The redshifted emission observed by Pardo et al. (2004) is of similar strength to the weaker blueshifted emission between 9 and 14 km.s^{-1} in Figure 5.1. The missing emission may have an impact on the interpretation of the VLBA maps, but the effect of this missing emission on images at the resolution of the VLBA is unknown. VY CMa is known to be a variable SiO maser source (Pardo et al., 2004), and significant changes in the single-dish spectra do not necessarily imply major changes to the spatial morphology of VLBI images as the changes in the spectra could be due to unresolved emission, which would not be detected by VLBI observations, or changes in individual spot intensities. Possible implications of the missing emission will be mentioned in this chapter.

6.2 Observed SiO maser distributions

VLBI observations of SiO maser emission have been performed for a number of late-type stars. A selection of published synthesis images of SiO maser emission towards these objects are summarized in Table 6.1. These maps generally show sparse, irregular rings of clumpy emission situated between the stellar photosphere and the dust-formation point. The estimated radii of the observed rings are listed in Table 6.1.

Source Name	Classification	SiO line	Radius [R$_*$]	Ref.
U Her	Mira variable	$v=1$ $J=1-0$	$\leqslant 2$	1
TX Cam	Mira variable	$v=1$ $J=1-0$	$2-4$	1
W Hya	Semi-regular pulsating star	$v=1,2$ $J=1-0$	$1-2$	2
VY CMa	Pulsating variable star	$v=1,2$ $J=1-0$		2
VX Sgr	Semi-regular pulsating star	$v=1$ $J=1-0$	1.3	3
TX Cam	Mira variable	$v=1$ $J=1-0$		4
R Aqr	Mira variable	$v=1$ $J=1-0$	1.9	5
VX Sgr	Semi-regular pulsating star	$v=1$ $J=2-1$	< 1.5	6
o Cet	Mira variable	$v=1$ $J=2-1$		7
NML Cyg	Variable star	$v=1,2$ $J=1-0$		8
IRC +10011	Mira variable	$v=1,2$ $J=1-0$		9
χ Cyg	Mira variable	$v=1$ $J=1-0$		10
χ Cyg	Mira variable	$v=1$ $J=2-1$		10
VY CMa	Pulsating variable star	$v=1,2$ $J=1-0$		11

Table 6.1: Published synthesis maps of SiO masers towards late-type stars.

References:

1. Diamond et al. (1994), 2. Miyoshi et al. (1994) 3. Greenhill et al. (1995), 4. Humphreys et al. (1996), 5. Boboltz et al. (1997), 6. Doeleman et al. (1998), 7. Phillips and Boboltz (2000), 8. Boboltz and Marvel (2000), 9. Desmurs et al. (2000), 10. Desmurs et al. (2002), 11. Miyoshi (2003)

The quoted values are subject to uncertainties in both the stellar distance and photospheric radius. Stellar classifications were taken from the SIMBAD database[1]. The estimated radii of the o Cet and VY CMa rings are absent because these maps did not show clear evidence of a ring-like distribution of SiO maser emission in the tabulated observations. Other sources radius estimates are absent because they were not published in the referenced papers.

The $v=1$ and 2, $J=1-0$ SiO maser emission towards VY CMa has been mapped by Miyoshi et al. (1994) and Miyoshi (2003). The observation epochs were 1991 and 1998 respectively, sandwiching the observations used in this thesis, which were made in 1994. The Miyoshi maps do not show an obvious ring distribution. The early maps show a maser region elongated in the northeast - southwest direction (Miyoshi et al., 1994). The later maps show the maser region observed in the early maps, as well as

---

[1] http://simbad.u-strasbg.fr/sim-fid.pl

new extensions in the northwest (Miyoshi, 2003).

6.3 The total intensity maser distribution

As shown in Figure 5.1, the SiO maser emission towards VY CMa extends 100×80 mas in right ascension and declination, making the SiO maser region about one fifth the size of the H_2O and main line OH maser emission regions and about twenty times smaller than the OH 1612 MHz maser region.

The total intensity SiO maser map is similar to the maps of Miyoshi et al. (1994) and Miyoshi (2003), displaying the northeast - southwest region with extensions to the northwest, though the western emission is less extended than in the Miyoshi (2003) map.

The maser components show a possible sparsely filled ring structure, with the emission concentrated in the eastern region. The most extreme redshifted and blueshifted maser components lie on the inner edge of the ring, which is indicative of tangential amplification of these masers. The geometry of the maser distribution is determined by coherence in the velocity field of the masing gas. In regions of significant radial velocity gradient in a flow from a central star, the greatest coherence is found in the direction perpendicular to the radial outflow, tangential to the stellar surface. This will result in maser emission in a ring around the star (Elitzur, 1992, pg 228).

6.3.1 Shell model

A circle was fitted to the spatial distribution of maser components listed in Table 5.1 to examinine how the data can be described by a typical ring distribution. A least squares algorithm (Bucher, 1991) was used to perform the fit of the maser component positions, unweighted by flux density. The fitted circle shown in Figure 6.1 has a radius of 32 mas. If we assume the stellar radius to be 10 mas, as suggested by the median of the values in Table 2.2, this places the mean SiO maser shell radius at approximately 3 R_*, if we assume the stellar position is near the center of the fitted ring in this model. The radial distribution of maser emission extends from 15 to 60 mas from the assumed centre, or equivalently from 1.5 - 6 R_*. This range is reasonable when compared to SiO maser distributions around other late-type stars.

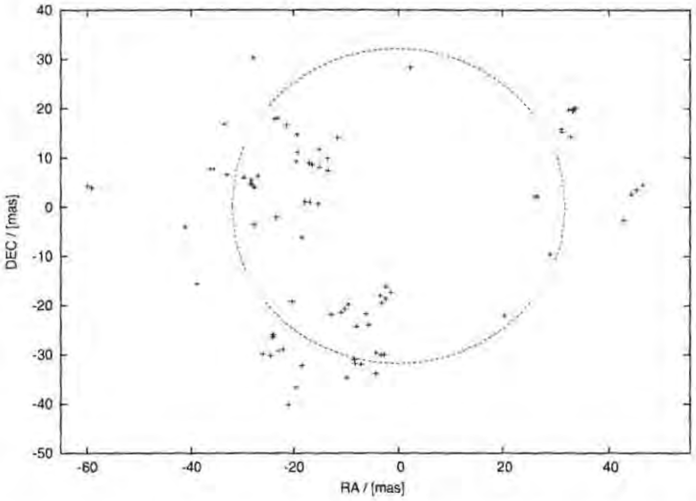

Figure 6.1: Maser components represented by crosses, with the origin at the centre of the fitted circle. The fitted circle has a radius of 32 mas.

Silicon in the circumstellar envelope is expected to condense onto dust grains at the dust formation radius, terminating the SiO maser region at this threshold. Several estimates of the dust formation radius are listed in Table 2.5, with a median value of 50 mas. Figure 6.2 is a plot of the angular distance from the stellar position versus the velocity of the maser components. The vast majority of the components fall within 50 mas of the assumed stellar position, and they all fall well within 160 mas, the largest value in Table 2.5. Similar plots to 6.2 were made assuming the stellar position at the centroid of the maser components (Figure 6.3, left) and a position between the two major regions of emission in the southeast and the northeast (Figure 6.3, right). Neither of these plots show a better fit to the expanding shell model than Figure 6.2 does, so the stellar position is assumed to be the centre of the circle fit. Astrometric observations of the 22 GHz H_2O masers towards the mira variable U Her have shown that the central star may in fact not be in the center of the H_2O maser emission (Vlemmings et al., 2002b). The H_2O maser distribution was also interpreted as a ring and the star was found to be located towards the edge of the ring. In light of this finding, VY CMa cannot be definately located near the center of the circle fitted to the SiO maser spots. If VY CMa is located towards the edge of the SiO maser

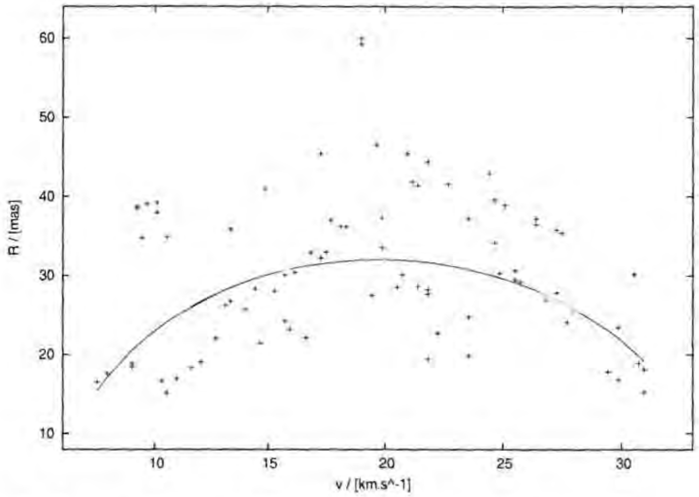

Figure 6.2: Plot of the distance of the maser components from the assumed stellar position versus the maser velocity. The crosses are observed maser components. The solid line is the standard expanding shell model described by Equation 6.1, with $d = 32$ mas, $v_* = 19.75$ km.s^{-1} and $v_e = 14$ km.s^{-1}.

ring then this would imply that the dynamics of the gas in the SiO maser region is much more complicated than the simple models which will be applied to the maser spot data. In all of the following analysis the stellar position is assumed to be the centre of the circle fit.

OH masers towards late-type stars are commonly fitted to a simple thin expanding shell model (Reid et al., 1977):

$$d(v) = R\sqrt{1 - \frac{(v - v_*)^2}{v_e^2}} \tag{6.1}$$

where d is the observed angular distance of a particular ring from the central star, R is the angular radius of the shell, v is the observed velocity of the emission from the maser components, v_* is the stellar velocity and v_e is the stellar expansion velocity. The parameters R and v_e are adjusted to fit the data. The solid line in the Figure 6.2 shows a simple expanding shell model with stellar velocity $v_* = 19.75$ km.s^{-1}, the mean value of Table 2.3, angular radius of $R = 32$ mas and expansion velocity

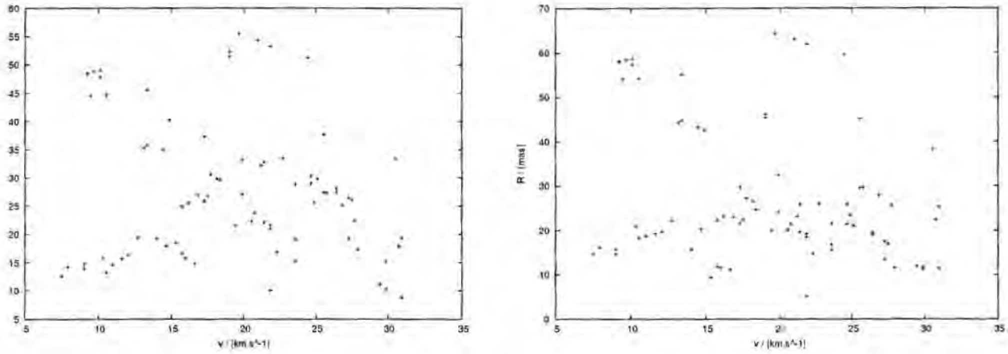

Figure 6.3: Plot of the distance of the maser components from the assumed stellar position versus the maser velocity. The left figure uses the centroid of the maser components as the stellar position, and the right figure uses a point between the two major maser regions, as described in the text.

$v_e = 14$ km.s^{-1}.

The formal reduced chi-squared of the fit to the thin shell model is 5423, assuming that the variance in the data is only due to uncertainty in angular radius which was taken to be half the size of a pixel, 0.02 mas. Other possible physical causes of variance, such as the thickness of the SiO maser shell or turbulence in the maser region, were not taken into account. The fit is not good, as seen by the hight chi-squared value, but it is not expected that SiO maser components will fit the simple expanding shell model particularly well, given current models of tangential amplication of SiO masers due to radial acceleration in the maser region. However, Figure 6.2 does suggest a general trend of emission further from the stellar velocity occurring closer to the assumed stellar position. On this basis, redshifted emission missed by these VLBA maps may be expected to be towards the inner region of the maser distribution. Interferometric observations of the $v = 0$ $J = 2 - 1$ thermal SiO emission towards a number of late-type stars suggests that the SiO generally resides in an accelerating region of the circumstellar envelope (Lucas et al., 1992). The SiO maser region is also expected to be heavily influenced by shocks and mass-loss (Humphreys et al., 2002), which results in the complex velocity distribution of maser spots.

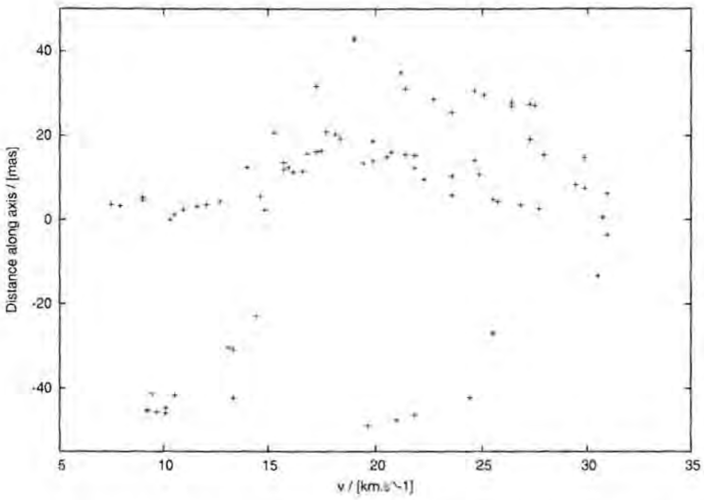

Figure 6.4: Plot of maser component distance along a 70° axis versus velocity. No linear trends are visible that would support a bipolar outflow model.

6.3.2 Bipolar flow

The recent VLA maps of the thermal $v = 0$ $J = 1 - 0$ SiO emission towards VY CMa show a possible bipolar outflow, with the outflow axis at a position angle of $\sim 70°$ (Shinnaga et al., 2003). Mid-infrared images also show a possible east-west elongation, which may be evidence of a bipolar flow (Smith et al., 2001). On the other hand, Wittkowski et al. (1998) proposed that the near-infrared elongation they observe at a position angle of about 160° is evidence of a north-south bipolar outflow that is caused by an east-west obscuring equatorial disk. Large scale optical and near-infrared images of VY CMa display a possible northeast - southwest axis of symmetry, which both Kastner and Weintraub (1998) and Monnier et al. (1999b) attribute to a possible bipolar structure. These optical observations of asymmetry are from dust emission much further from the star than the circumstellar SiO masers.

In light of these conflicting suggestions of bipolar structure, the $v = 1$ $J = 1 - 0$ maser components measured in this work were examined for any evidence of such a bipolar outflow. Zijlstra et al. (2001) considered bipolar flows from OH/IR stars by examining the OH maser maps of the stars. For bipolar flow the velocity of the maser components should be proportional to their distance along the axis of the flow (Zijlstra et al., 2001). They identify bipolar flows through a linear relationship between the velocity of maser components and their distances from the central star.

The VY CMa SiO data were examined for linear trends in velocity versus distance along potential bipolar axes with position angles ranging from -45° to 135°. None of the plots displayed evidence of linear outflow. A plot of the distance of maser components along a 70° axis versus their velocity is included as an example (Figure 6.4).

6.3.3 Velocity gradients

Velocity gradients with respect to position angle around the maser shell have been observed in the SiO maser emission of several Mira variables. VLA maps of SiO masers towards R Aqr show such a velocity gradient (Hollis et al., 2000), as do VLBA maps of TX Cam (Diamond et al., 1994). Such gradients can be interpreted in terms of the rotation of the maser shell, although they could also simply be projection effects from inclined ellipsoidal outflows. Diamond et al. (1994) use the velocity gradient to find a potential rotation velocity of v_{rot} $\sin i = 2$ km.s^{-1} for TX Cam, where i is the inclination angle of the assumed orbital axis and v_{rot} is the rotational velocity. Hollis et al. (2000) find a value of about 3.75 km.s^{-1} for R Aqr, where they have used a known inclination angle.

A plot of the velocity of each maser component against its position angle around the VY CMa maser shell is shown in Figure 6.5. Most of the maser components are concentrated to the east of the map, with positive position angles. The sparse western components show a general decrease in velocity with position angle, which may be indicative of shell rotation. It cannot be known if observations of the missing redshifted emission would also displayed this linear trend in the western region of the emission. If it was found to do so then it would confirm the presence of this velocity gradient.

If the velocity gradient between position angles of -150° and -50° is due to rotation, then the rotational period can be derived assuming a solid body model, which predicts a sinusoidal variation of velocity with position angle. Cotton et al. (2004) examined a number of stars for this velocity gradient and found that only R Aquarii and S Corona Boralis display a possible sinusoidal signature, from which they derived rotational

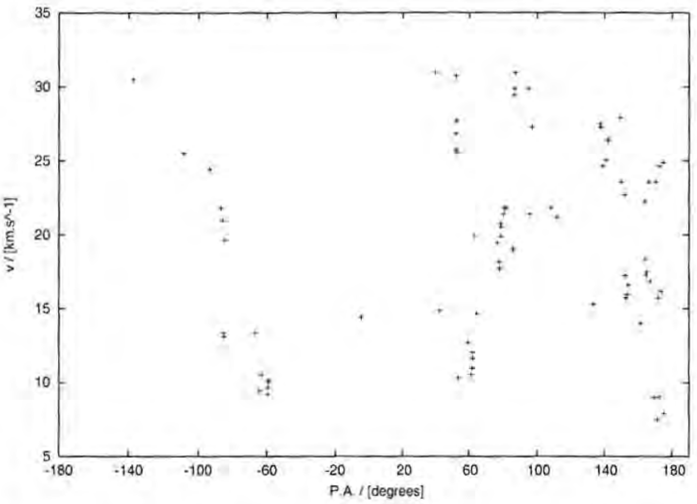

Figure 6.5: Plot of the velocity of the maser components versus the position angle of the component around the shell.

velocities in the range 3 - 4 km.s^{-1}.

Figure 6.6 shows a solid body model sinusoid fitted to the -150° and -50° region of Figure 6.5. The curve describes the expected velocity at the surface of a sphere of radius 32 mas, period 80 years, projected rotational velocity of 18 km.s^{-1} and rotation axis in the east-west direction. A stellar velocity of 19.75 km.s^{-1} was assumed, being the median value in Table 2.3.

The observed velocity v is dependant on the inclination angle i:

$$v \;=\; v_{rot}\ \sin\ i\ +\ v_* \tag{6.2}$$

The projected rotational velocity is $v_{rot}\ \sin i = 18$ km.s^{-1} and thus the actual rotational velocity of the maser shell v_{rot} is greater than 18 km.s^{-1}, making the period correspondingly less. The period is expected to be larger than the 8 - 34 year period predicted for R Aqr, for example, because VY CMa is a much larger star. A rotational velocity as large as 18 km.s^{-1} would not generally be expected at the outer region of a red supergiant envelope because the rotation of the star will decrease over the evolutionary path from the main sequence to the supergiant part of the Hertzsprung-Russel diagram, and because the presence of such a high rotational velocity requires

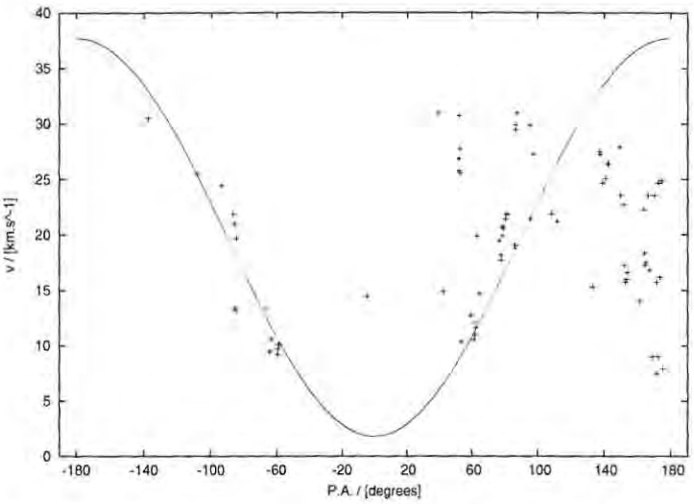

Figure 6.6: Plot of the velocity of maser the components versus the position angle of the component around the shell. The solid line in the figure is a solid body rotation model with a east-west rotation axis and a period of 80 years.

a mechanism to transport angular momentum through the extended stellar envelope (Soker and Harpaz, 1999). If the circumstellar envelope is undergoing solid body rotation then there must be some coupling between the star and envelope that causes the envelope to co-rotate with the star. Doeleman et al. (1998) observed a linear velocity gradient in VY Sgr along a chord tangent to the projected shell, which they attribute to solid body rotation. They suggest that the coupling between envelope and star could be created by magnetic field lines frozen into the circumstellar envelope.

If the velocity signature observed in Figure 6.5 is due to solid body rotation, then the eastern region of the ring may be undergoing large bulk motions which will obscure the evidence of rotational motion, as suggested by Cotton et al. (2004) for their observations of Mira variables.

While the velocity gradients with position angle can be interpreted as evidence of rotation, they could also simply be projection effects. The velocity versus position angle profile of a tilted expanding disk, for example, may appear sinusoidal. Other asymmetrical outflows can also produce velocity gradients. Figures 6.7 to 6.10 each show a plot of the projected positions of 220 maser spots (left) and a plot of the

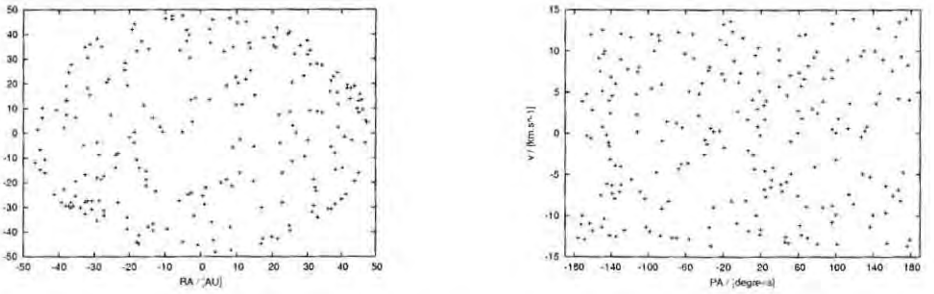

Figure 6.7: Expanding sphere: radius 48 AU, expansion velocity 14 km.s^{-1}.

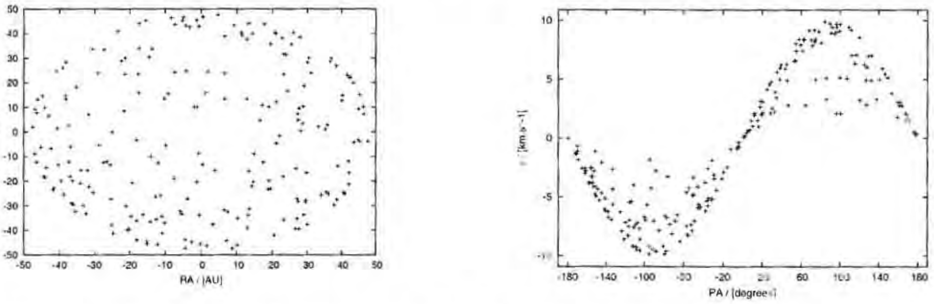

Figure 6.8: Rotating sphere: radius 48 AU, linear rotational velocity 10 km.s^{-1}.

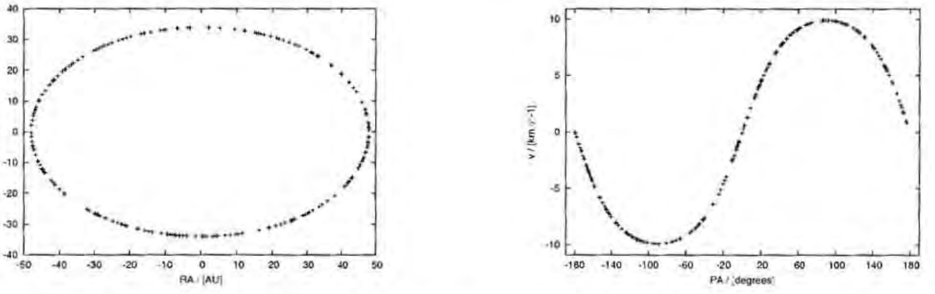

Figure 6.9: Expanding disk: radius 48 AU, expansion velocity 14 km.s^{-1}, $i = 45°$.

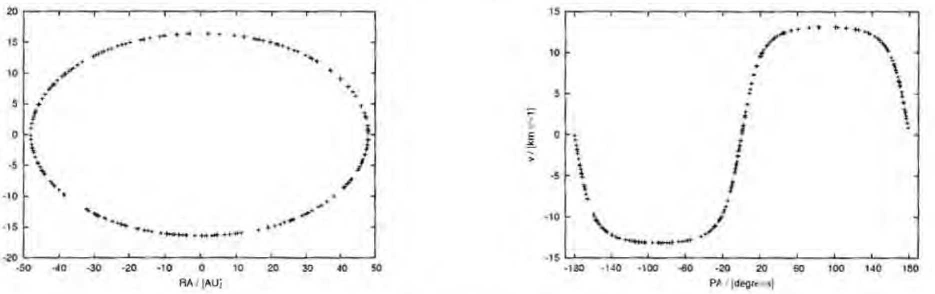

Figure 6.10: Expanding disk: radius 48 AU, expansion velocity 14 km.s^{-1}, $i = 20°$.

velocity of the components versus their position angles (right) for four geometries. Figures 6.7 and 6.8 are spheres of radius 48 AU (32 mas at 1.5 kpc), with Figure 6.7 showing a constant expansion of 14 km.s^{-1} and Figure 6.8 showing solid body rotation of 10 km.s^{-1} around an east-west axis through the centre of the sphere, with no expansion. Figures 6.9 and 6.10 are flat disks of radius 48 AU, where Figure 6.9 is at an inclination angle of 45° and Figure 6.10 is at an inclination angle of 20°. The maser spots were randomly placed in these geometries using Monte Carlo methods. No attempt was made to include the effects of velocity coherence. These plots only serve to show the velocity signatures displayed by these very simple shell geometries.

The expanding sphere does not show any velocity gradient with position angle. The position angle velocity gradient of the rotating sphere is sinusoidal. This geometry was used above to derive the 18 km.s^{-1} projected rotational velocity for the VY CMa SiO maser region. The two disk geometry figures show how projection effects can mimic rotation. These disks are not rotating, yet their velocity versus position angle plots display a similar shape to those of the rotating shell, especially for the disk inclined at 45°.

Boboltz and Marvel (2000) observed velocity gradients with radius in linear maser features towards NML Cyg. The features decreased in line of sight velocity with increasing distance from the star. They suggest that these features are due to local deceleration or turbulence.

The longest linear feature in the total intensity maps of VY CMa presented here has a radial velocity gradient, as shown in Figure 6.11. It spans ten velocity channels, or 2.172 km.s^{-1}. The feature encompasses three maser components at 30.949, 29.863 and 29.428 km.s^{-1}, with the 29.863 km.s^{-1} component located $\Delta\alpha = 8.556$ mas, $\Delta\delta = 32.752$ mas relative to the phase centre. The velocity of the feature decreases with increasing distance from the star. Such radial linear features are a property of tangential amplification.

Shibata et al. (2004) did not find any systematic velocity gradients in their VLBI $v=1$ $J=2-1$ SiO maser maps of VY CMa.

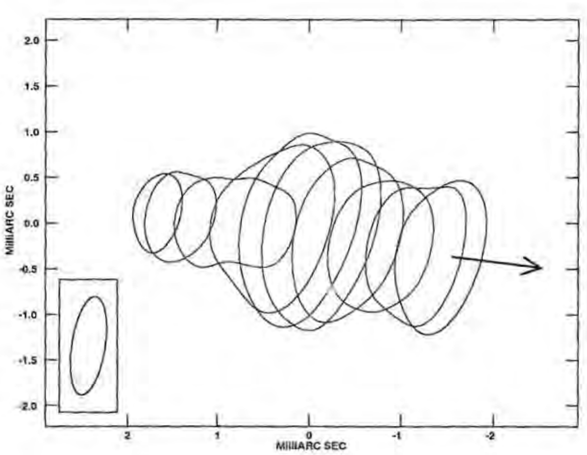

Figure 6.11: Linear velocity gradient of a maser feature over 2.172 km.s^{-1}. The velocity of the components of this feature is represented by the colour of the contours, where the red features are the most redshifted and blue features are the most blueshifted. The arrow points in the direction of the assumed stellar position. The synthesised beam is displayed in the bottom left corner, and is 1.087 × 0.370 mas in half-power with a position angle of $-8.7°$.

6.4 Polarisation

Just over half of the maser components listed in Table 5.1 display fractional linear polarisations above the detection threshold, with a median fractional linear polarisation of $\sim 6\%$. The peak value of the fractional linear polarisation is almost 100% and values of 30% and higher are not uncommon. About a third of the maser components display a fractional circular polarisation above the detection threshold. The values of circular polarisation thresholds u_c were close to the peak fractional circular polarisations for signal-to-noise reasons, so a reliable median could not be estimated with confidence. The mean of the absolute value of the fractional circular polarisation was $\sim 2\%$, with a peak fractional circular polarisation of $\sim 10\%$.

McIntosh et al. (1994) performed single-dish observations of the SiO maser polarisation towards VY CMa. The fractional circular polarisation in the $v=1$ $J=1-0$ SiO line was less than 5%, and the fractional linear polarisation was less than 10%, as discussed in Section 2.8.5. Barvainis and Predmore (1985) found a fractional linear polarisation of 3.8%. The polarisation observed in this thesis is consistent with these single-dish polarisation values measured for VY CMa, as well as with the circular polarisation measured for TX Cam (Kemball and Diamond, 1997).

6.4.1 Magnetic field

Exactly how the polarisation is related to the underlying circumstellar magnetic field is dependant upon the details of the maser polarisation theory assumed. Two different models are presently used to interpret the polarisation in terms of a magnetic field.

The first model was developed by Elitzur in a series of papers (Elitzur, 1991, 1993, 1996, 1998, 1992). The maser polarisation in these models is generated by standard Zeeman splitting. The polarisation of SiO maser emission falls into the category of overlapping Zeeman components, as it is a non-paramagnetic molecule. The Zeeman theory predicts that the fractional circular polarisation should decrease with increasing rotational quantum numbers, and consequently frequency, of the maser transition. This decrease has been observed in the $v=1$ $J=2-1$ and $v=1$ $J=1-0$ SiO lines of VY CMa (McIntosh et al., 1994), lending support to the model.

The second polarisation model proposes a non-Zeeman interpretation of the maser polarisation and is described by Western and Watson (1983), Nedoluha and Watson (1994), Wiebe and Watson (1998) and references therein. In this framework, circular polarization is generated from linear polarization due to changing optical axes along the direction of propagation. Nedoluha and Watson (1994) showed that in this framework magnetic fields as small as $10-100$ mG can produce a circular polarisation of 10%, unlike in the Zeeman model which requires magnetic fields of the order of 100 G to produce similar levels of polarisation. The fractional polarisation predicted by the non-Zeeman model is largely insensitive to magnetic field strength over several orders of magnitude.

Kemball and Diamond (1997) derived the expression:

$$B = 3.2\, m_c\, \Delta v_D \cos\theta \tag{6.3}$$

from the work of Elitzur (1996), to estimate the magnetic field strength from the fractional circular polarisation m_c. The angle θ is the unknown angle between the

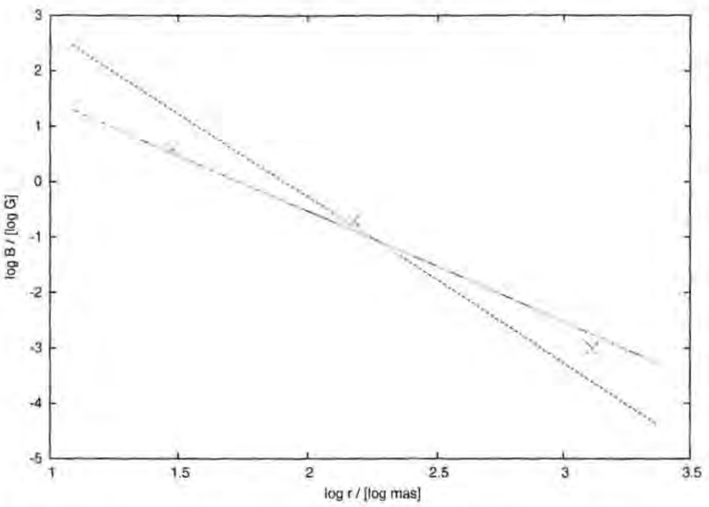

Figure 6.12: Plot of inferred magnetic field versus radial distance from VY CMa. The scales are both logarithmic. The three crosses represent magnetic field values derived from SiO maser observations (this thesis), H_2O maser observations (Vlemmings et al., 2002a) and OH maser observations (Benson and Mutel, 1982). The dotted line represents a dipole-type magnetic field relationship which best fits the three points, and the solid line is the best fitting solar-type magnetic field relationship.

magnetic field and the line of sight, and Δv_D is the Doppler line width for the SiO $v = 1$ $J = 1$–0 transition, which they take to be 0.6 km.s^{-1}. They used this relationship to find a value of $B \sec\theta \sim 5 - 10$G in the SiO maser region of TX Cam. Using the mean value of the fractional circular polarisation, $m_c \sim 2\%$, and the same Doppler linewidth, the magnetic field strength around VY CMa predicted by the Zeeman model is $B \sec\theta \sim 4$G.

The strength of a magnetic field in the circumstellar envelope, if assumed global, may reasonably be assumed to vary as a power law with radial distance. Vlemmings et al. (2002a) used a solar and dipole-type relationship to model this dependence:

$$B \propto r^{\alpha} \tag{6.4}$$

where α is -2 for solar-type magnetic fields, and -3 for dipole-type magnetic fields. Published magnetic field values derived from OH and H_2O masers, and the SiO maser

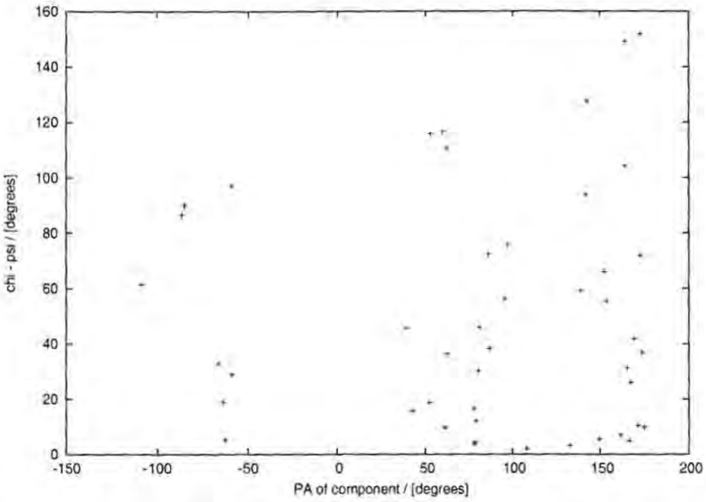

Figure 6.13: Plot of $|\chi - \psi|$, the difference between the linear polarisation vector χ of a maser component and the position angle of a tangent to the maser distribution at that point, ψ, versus the position angle of the component on the maser shell.

magnetic field value calculated in this thesis, are shown in Figure 6.12 as a function of their assumed distances from the star, following Vlemmings et al. (2002a). The OH magnetic field is ~ 1 mG at a distance of 1.6 arcseconds, and the H_2O magnetic field is ~ 200 mG at a distance of 150 mas (Section 2.9.6). The best-fitting solar and dipole-type magnetic fields are also shown in the figure. The best fitting solar-type field would give a field of 30 G at the stellar surface, and the dipole-type field a value of about 500 G. The ~ 4 G SiO magnetic field value, located at a radius of approximately 30 mas, seems consistent with the power-law relationship proposed by Vlemmings et al. (2002a), and also appears to favour the solar-type law over the dipole-type law, which they also find.

In the standard Zeeman model the position angle of the linear polarisation χ is dependent on the angle θ between the magnetic field and the line of sight to the maser feature. The vector χ is either parallel or perpendicular to the magnetic field vector γ_B projected onto the sky plane, depending on the angle θ:

$$\chi \parallel \gamma_B \qquad \theta < 55^\circ$$

$$\chi \perp \gamma_B \quad \theta > 55^\circ \tag{6.5}$$

(Elitzur, 1992, pg 184). Kemball and Diamond (1997) undertook full polarisation VLBI observations of SiO towards TX Cam. In the resultant linear polarisation maps the linear polarisation position angles of maser components show fine scale structure superimposed on generally tangential polarisation position angles relative to the maser ring. The polarisation morphology is not inconsistent with an ordered magnetic field influenced by local magnetic features. In light of Equation 6.5, a tangential pattern of polarisation angles is consistent with a radial magnetic field (Kemball and Diamond, 1997). The VY CMa polarisation position angles shown in Figure 5.7 do not display the overall tangential distribution that is observed towards TX Cam, nor do they show any obvious regularity.

R Aqr displays groups of primarily radial or primarily tangential linear polarisation vectors around certain position angles on the maser shell (Boboltz, 1997). Boboltz (1997) examined the linear polarisation angles for radial or tangential polarisation regions by considering the difference between a local tangent to the ring distribution, with position angle ψ, and the linear polarisation position angle, χ. The difference $|\chi - \psi|$ will be close to 0° for tangential polarisation, and close to 90° for radial polarisation. A similar plot of $|\chi - \psi|$ for the linearly polarised VY CMa maser components listed in Table 5.1 is shown in Figure 6.13. Unlike the plots of Boboltz (1997), Figure 6.13 does not show the clear clusters of components at 0° and 90° which would imply distinct radial or tangential polarisation regions.

A particularly interesting feature of the linear polarisation is a rotation of position angle with velocity observed in several individual maser components. Barvainis (1984) observed that the SiO linear polarisation position angle rotated with velocity towards IRc2 in the Orion KL nebula. The polarisation position angle rotated by about 60° over each of the two components in the maser profile. Since the direction of the linear polarisation is dependant on the magnetic field (Equation 6.5), a rotation of polarisation position angle implies a change in the projected direction of the magnetic field. Barvainis (1984) attribute the position angle changing with velocity to a velocity field and a magnetic field which changes with position in a rotating and expanding disk structure.

Figure 6.15 shows two maser components with rotating linear polarisation position

v [km.s^{-1}]	α [mas]	δ [mas]	Rotation [deg]	Rotation rate [deg/km.s^{-1}]	$\Delta\alpha$ [mas]	$\Delta\delta$ [mas]
26.387	13.712	2.872	17.1	26.3	0.240	0.880
21.390	20.044	36.568	36.5	28.0	0.264	0.288

Table 6.2: Rotation of the linear polarisation position angle χ of two maser components. The first three columns are centre velocity, right ascension and declination of the component from Table 5.1. The forth column is the clockwise rotation of the polarisation position angle and the fifth is the rotation divided by the velocity spread of the component. The final two columns are the difference in right ascension and declination of the spots in the first and final velocity channels of each component.

angles. The properties of these two components are shown in Table 6.2. They rotate by $\sim 5°$ each channel, which translates to a rate of $\sim$ 25 deg/km.s^{-1}. Several other components appear to rotate by lesser degrees over a smaller velocity range, but the large uncertainties in polarisation position angle calculations makes the other rotation detections very tentative.

The rotating components are located in south-east and north-east regions of the maser ring. In accordance with Barvainis (1984), the rotation may imply a changing magnetic field direction with velocity in the circumstellar matter from which the spots arise. The two spots move marginally in right ascension and declination over the frequency width of the component, so perhaps the changing properties of the medium over this length can account for the rotation. Barvainis (1984) derived global velocity field information from the rotation, which cannot be done here for two main reasons. Firstly, we are only observing this effect in two small isolated maser spots from the entire emission region. Secondly, the the movement of the spot is on a much smaller scale than that considered by Barvainis (1984) for magnetic field and velocity field changes and, in fact, the greatest rotation is observed for the component which moves the least.

Boboltz (1997) points out that in the non-Zeeman interpretation there should be some correlation between the linear and circular polarisation of the observed maser spots. Figure 6.14 is a plot of fractional circular polarisation m_c versus fractional linear polarisation m_l. The circular and linear polarisations do not show any evidence of correlation - the pairwise Pearson correlation coefficient is 0.052. There are many

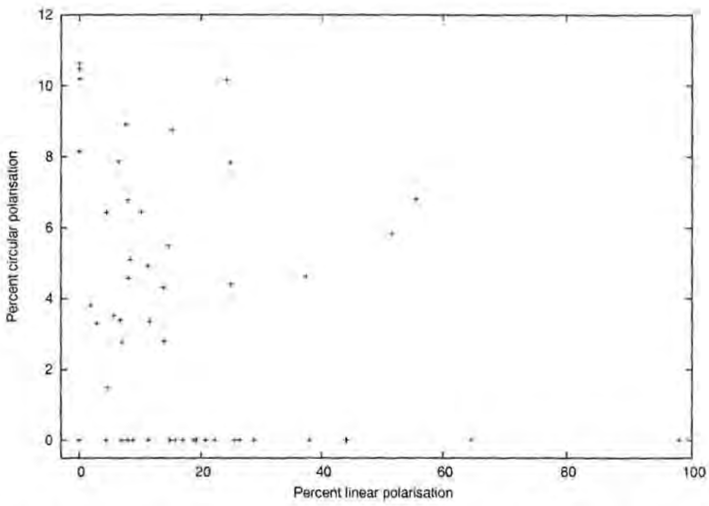

Figure 6.14: Plot of fractional circular polarisation, $|m_c|$, versus fractional linear polarisation, m_l.

linearly polarised spots that have a circular polarisation below the circular polarisation cutoff, creating the horizontal row at zero circular polarisation in the figure. Wiebe and Watson (1998) performed numerical simulations of SiO maser polarisation in late-type stellar envelopes using the non-Zeeman interpretation. They found that the correlation between circular and linear polarisation of individual maser components was destroyed by statistical variations in the velocity field and the magnetic field in the circumstellar envelope. Consequently the lack of observed correlation between the fractional circular and fractional linear polarisations of the SiO maser components towards VY CMa does not rule out the non-Zeeman interpretation of the polarisation.

6.5 Discussion

The total intensity maser map was compared to a number of theoretical distributions to investigate the underlying kinematics of the SiO maser region. The maser spots show a possible ring distribution with a radius of 32 mas. Most of the maser components fall within 50 mas from the center of this ring.

The data were fitted to a simple expanding shell model with a radius of 32 mas around the center of the fitted ring, assumed to be the stellar position. This assumption is questionable, however, given that astrometric observations of H_2O masers towards U Her show that U Her is not located in the center of the H_2O maser ring. (Vlemmings et al., 2002b). The simple expanding shell model did not fit the data well, which is not suprising as the SiO masers are located in a complex region of the stellar-envelope where the gas is accelelerating. The maser map was also unsuccessfully tested for evidence of a bipolar flow. Several authors have suggested that observations on VY CMa at different wavelengths display evidence for a bipolar flow along various axes, but the SiO maser map presented in this thesis does not verify their claims. A velocity gradient with position angle around the maser shell was observed in the total intensity maser map, and was modeled by solid body rotation of the maser shell. The model gives a projected rotational velocity of 18 $\mathrm{km.s^{-1}}$, which is higher than would be expected for a massive late-type star such as VY CMa. While Cotton et al. (2004) found that the mira variables R Aquarii and S Corona Boralis also displayed evidence of solid body rotation, the velocities were smaller and these stars are not supergiants. Consequently, the observed velocity gradient may be better interpreted as the projection effect of an asymmetric outflow in the SiO maser region, such as a tilted expanding disk. Of the three models considered, the simple expanding shell, bipolar flow and rotating shell, none showed a convincing fit to the data. In light of the significant variability of the SiO maser emission, further observations will be useful to investigate the models further.

The levels of circular and linear polarisation of the SiO maser spots are consistent with previous polarisation measurements of TX Cam (Kemball and Diamond, 1997) and single-dish observations of SiO masers towards VY CMa (Barvainis and Predmore, 1985; McIntosh et al., 1994).

A magnetic field of $B \sec\theta \sim 4$G was calculated from the mean circular polarisation, applying the Zeeman theory of maser polarisation. The magnetic field in the circumstellar envelope was be modelled by a power law decrease in strength with distance from the stellar position. The 4G magnetic field fitted well with magnetic field values derived from H_2O and OH maser emission. The fact that the magnetic field values derived from each of the three maser species fit this model implies that 4G is a reasonable estimate of the magnetic field in the SiO maser emission region. This favours the Zeeman interpretation of the SiO maser polarisation, from which the 4G magnetic field estimate was derived. The position angles of the linear polarisation are irregular and there is no correlation between the linear and circular polarisation of the maser components, giving no further information about which of the competing maser polarisation theories should be applied to the SiO masers.

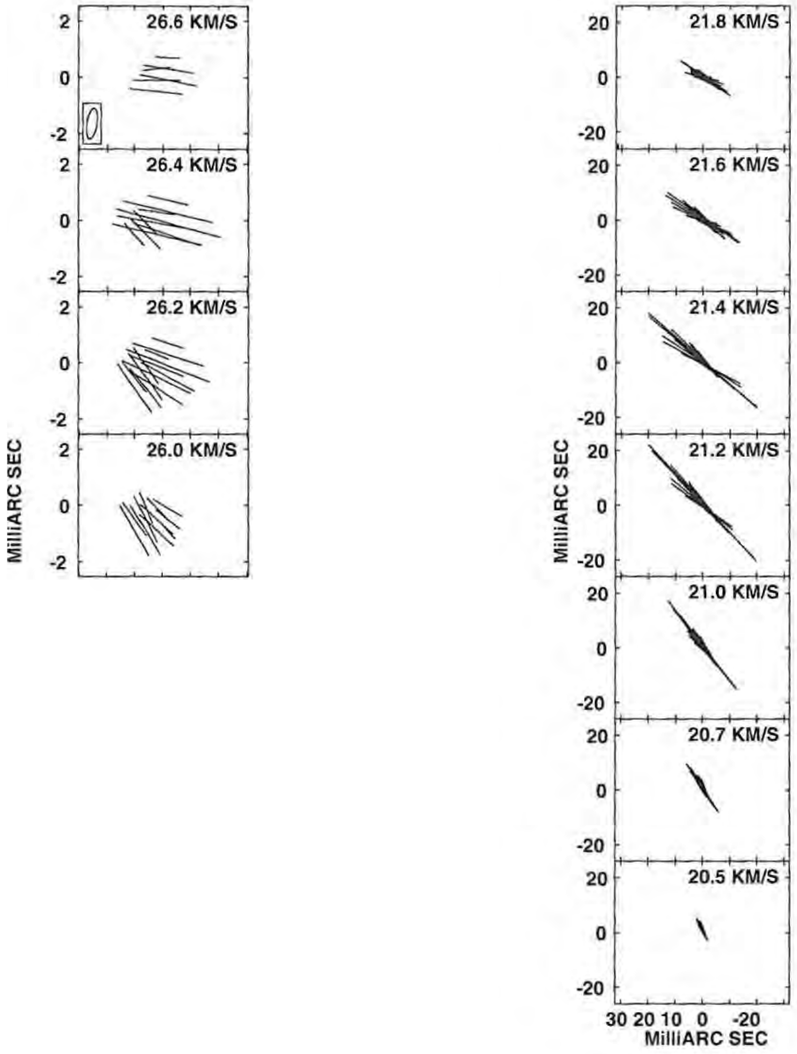

Figure 6.15: Rotation of linear polarisation position angle of maser components with velocity. The position angle of the linear polarisation of the 26.387 km.s^{-1} component rotates by 17° (left) and the linear polarisation of the 21.390 km.s^{-1} component rotates by 36° (right). The angles of the vectors in the figures are the linear polarisation position angles and the linear polarisation is represented by the length of the vectors, with 1 mas = 1.25 Jy/beam. The synthesised beam is displayed in the bottom left corner of the top panel of each figure, and is 1.274 × 0.401 mas in half-power with a position angle of −12.4°.

Chapter 7

Conclusion

7.1 Synopsis of results

This thesis reports the production and analysis of VLBI synthesis images of the SiO $v=1$ $J=1-0$ maser emission in all four Stokes parameters towards VY CMa.

The intensity map shows a number of individual maser components covering an area of 100×80 mas in right ascension and declination. Gaussian fits to the emission features yields a total of 81 distinct components over a velocity range of 7.485 to 30.949 km.s^{-1}. The individual spots are about 1 mas in size.

The maser components exhibit an irregular distribution. A circle fit to the components gives a nominal radius of 32 mas for the SiO maser emission, which converts to 7.2×10^{14} cm assuming a distance of 1.5 kpc. Assuming a stellar radius of 10 mas the maser ring has a radius of 3.2 R$_*$. If the stellar position is assumed to be at the centre of the fitted ring, almost all of the maser components are found to lie inside the inner dust shell radius, which is at approximately 5 R$_*$. The components all fall between 1.5 and 6 R$_*$.

The velocity distribution of the maser components was investigated for evidence of a bipolar flow, but none was found in these data. A systematic velocity gradient with position angle was observed in the sparsely populated western region of the maser ring. If this gradient is the result of solid body rotation of the circumstellar shell, then it implies a rotational velocity of v_{rot} $\sin i$ = 18 km.s^{-1} and a corresponding maximum rotation period of approximately 80 years assuming an east-west rotation axis. The velocity gradient could, however, be caused by projection effects from an aspherical outflow.

The linear and circular polarisation of the maser components was derived from the Stokes Q, U and V images. The median fractional linear polarisation was found to be $\sim 6\%$, with some components displaying up to almost 100%. The mean circular polarisation was found to be $\sim 2\%$, with a peak value of $\sim 10\%$. In the standard Zeeman interpretation of maser polarisation, the level of circular polarisation implies a magnetic field of ~ 4 G in the SiO maser region. This value is consistent with published H_2O and OH measurements of the magnetic field and a solar or dipole-type relationship between magnetic field magnitude and radial distance from the star, which favours the Zeeman interpretation of the SiO maser polarisation. The linear polarisation position angles do not show any systematic radial or tangential trend relative to the projected shell. No correlation was observed between the degree of linear and circular polarisation of the maser spots. Two maser spots show a rotation in polarisation position angle with velocity at a rate of ~ 25 deg/km.s^{-1}. This change in polarisation position angle may be due to change in magnetic field over the maser component.

7.2 Future work

VY CMa is a strong emitter in many SiO lines (see Table 2.7), making it an ideal object for testing maser polarisation models and maser pumping models.

Simultaneous VLBI polarimetry of the $J = 1 - 0$ and $J = 2 - 1$ SiO lines in a particular vibrational state can distinguish between the Zeeman and non-Zeeman theories of maser polarisation. The Zeeman theory predicts that circular polarisation should decrease for higher J transitions, when other properties are constant (Elitzur, 1996). Single dish observations have shown less circular polarisation in the $J = 2 - 1$ line than the $J = 1 - 0$ line (McIntosh et al., 1994). VLBI resolution observations are necessary, however, to compare the circular polarisations of individual maser features present in both lines. Such observations will ensure that spatial blending of many maser components at a given frequency does not impair the comparison.

Total intensity maps for transitions between the same rotational levels for different vibrational states can serve as a test of the competing radiative and collisional pumping models. The VLBA is capable of near simultaneous observations of the $J=1-0$ and $J=2-1$ transitions in the $v=0,1,2,3$ vibrational states, which allows direct comparison of the maser components in maps of these emission lines. Soria-Ruiz et al. (2004) recently compared VLBA maps of $v=1$ and 2 $J=1-0$ and $J=2-1$ lines towards IRC+10011 and χ Cyg with the purpose of investigating the SiO maser pumping mechanisms. A similar set of comparisons could be made for VY CMa, including lines in the $v=0$ and 3 vibrational states.

Proper motion studies of the SiO maser towards VY CMa would be valuable in studies of the circumstellar shell kinematics and in extending the results of this thesis. Globally, proper motion information would assist in differentiating between rotational models for large-scale velocity gradients and non-rotational models, such as asymmetric outflows or disk geometries. Tracking the development of smaller-scale features may help constrain models of the circumstellar environment in terms of shocks, turbulence and asymmetric mass-loss.

The recent Shinnaga et al. (2004) $v=1$ $J=5-4$ SiO map gave the appearance that these masers may be located in a bipolar outflow, where the conditions for such high frequency masers exist. In light of this result, it would be interesting to observe other high frequency SiO masers to see if they reside in similar regions of the circumstellar envelope. Many high frequency SiO maser spectra have been observed towards VY CMa, up to the $J=8-7$ transitions which have frequencies of $\sim$ 340 GHz (Table 2.7). Attempts could be made to image these masers with instruments such as the Submillimeter Array used by Shinnaga et al. (2004) and by future telescopes such as the Atacama Large Millimeter Array.

Appendix A

Total intensity channel maps

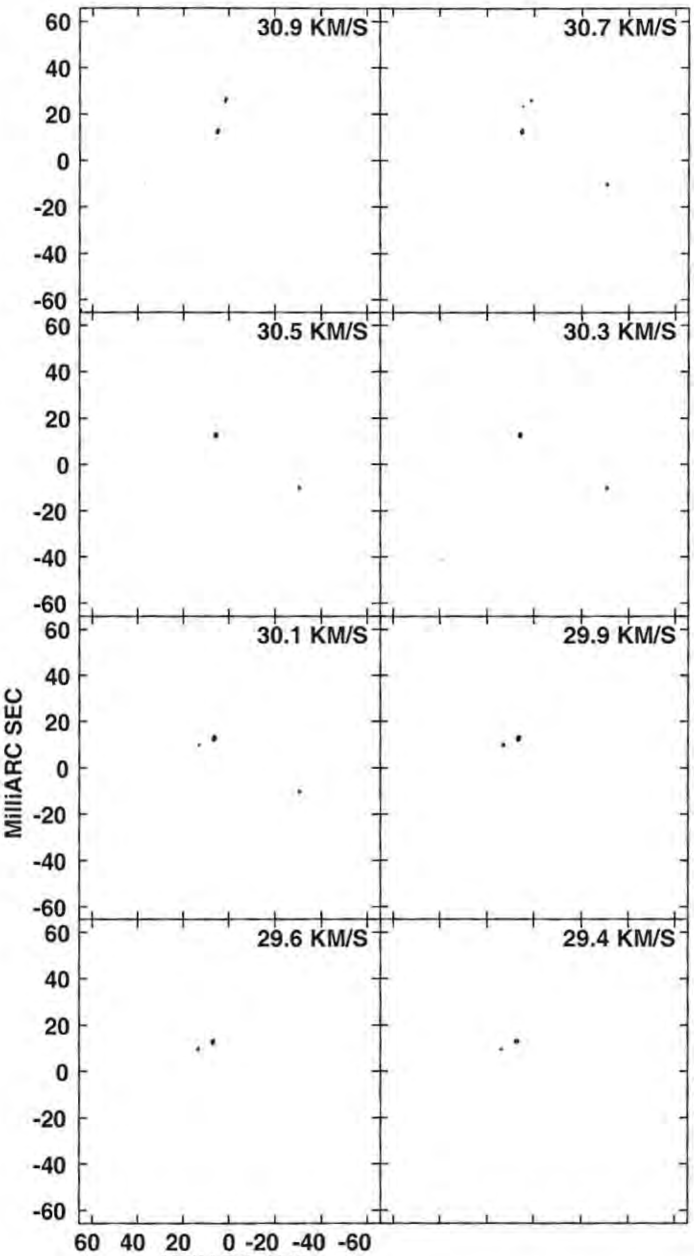

Figure A.1: A contour plot of the total intensity (Stokes I) maser emission for channel maps 29.4 - 30.9 km.s^{-1}. The contour levels are -100, -80, -60, -40, -20, -10, -5, -3, 3, 5, 10, 20, 40, 60, 80 and 100% of the peak flux density in the Stokes I cube, 148.93 Jy/beam.

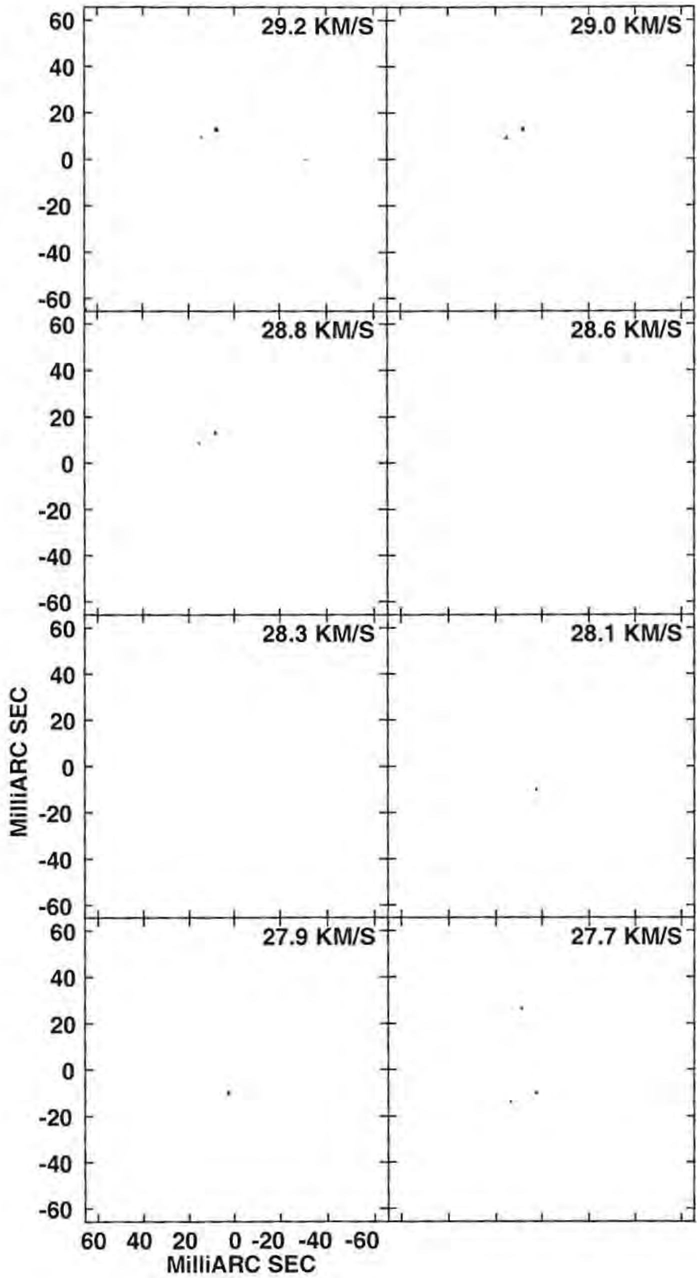

Figure A.2: A contour plot of the total intensity (Stokes I) maser emission for channel maps 27.7 - 29.2 km.s^{-1}, as for Figure A.1.

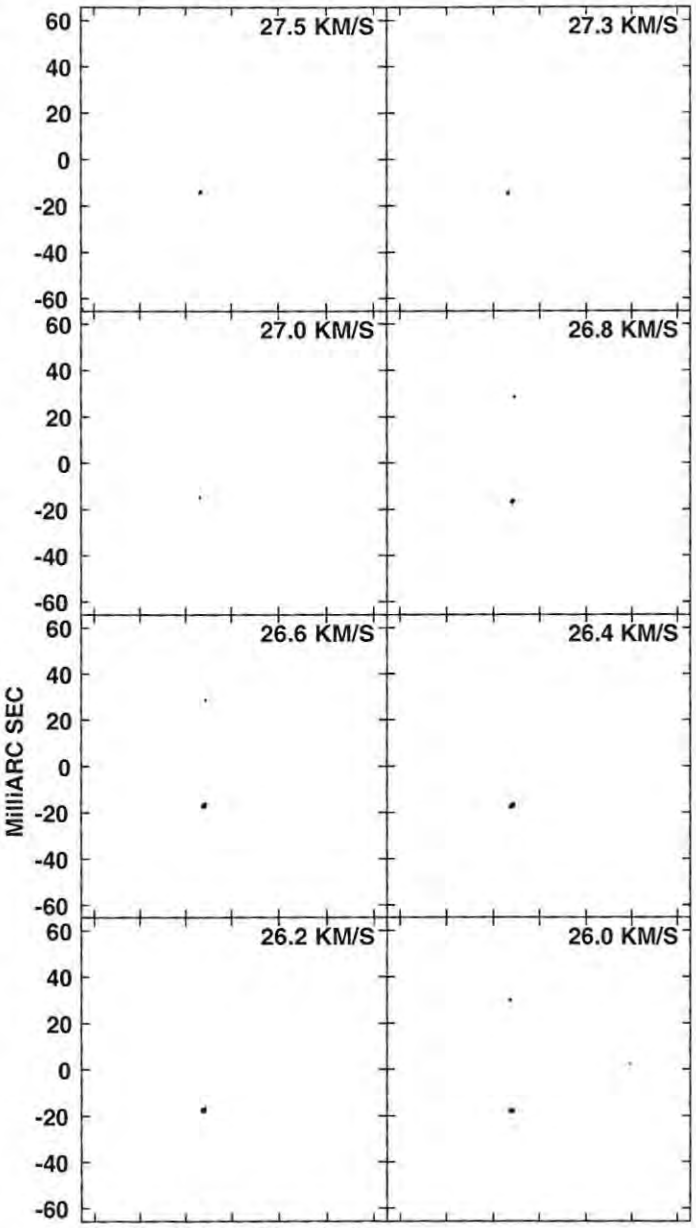

Figure A.3: A contour plot of the total intensity (Stokes I) maser emission for channel maps 26.0 - 27.5 km.s^{-1}, as for Figure A.1.

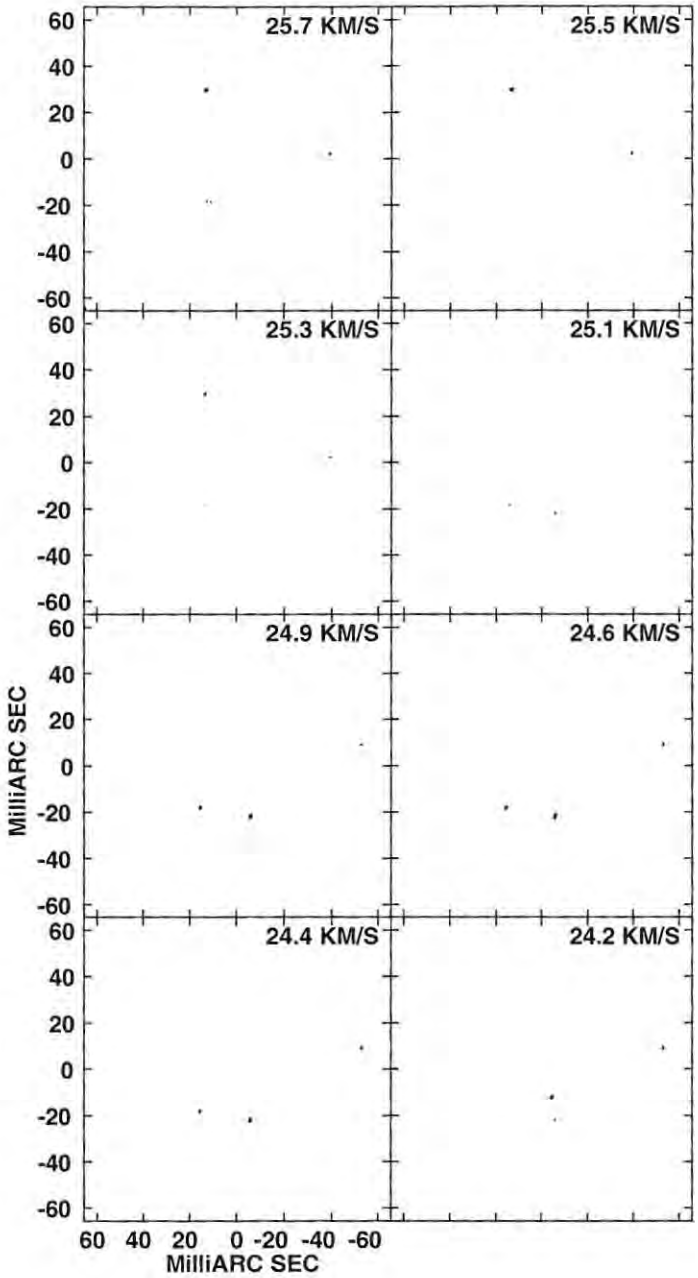

Figure A.4: A contour plot of the total intensity (Stokes I) maser emission for channel maps 24.2 - 25.7 km.s^{-1}, as for Figure A.1.

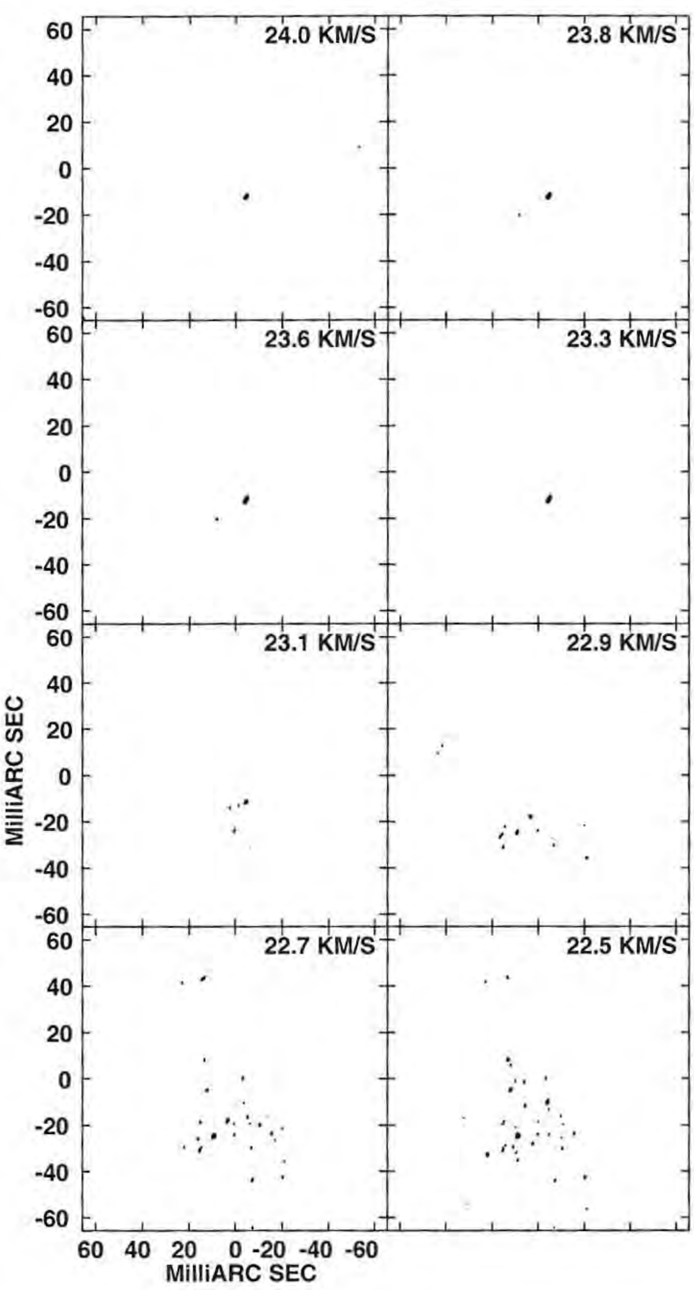

Figure A.5: A contour plot of the total intensity (Stokes I) maser emission for channel maps 22.5 - 24.0 km.s^{-1}, as for Figure A.1.

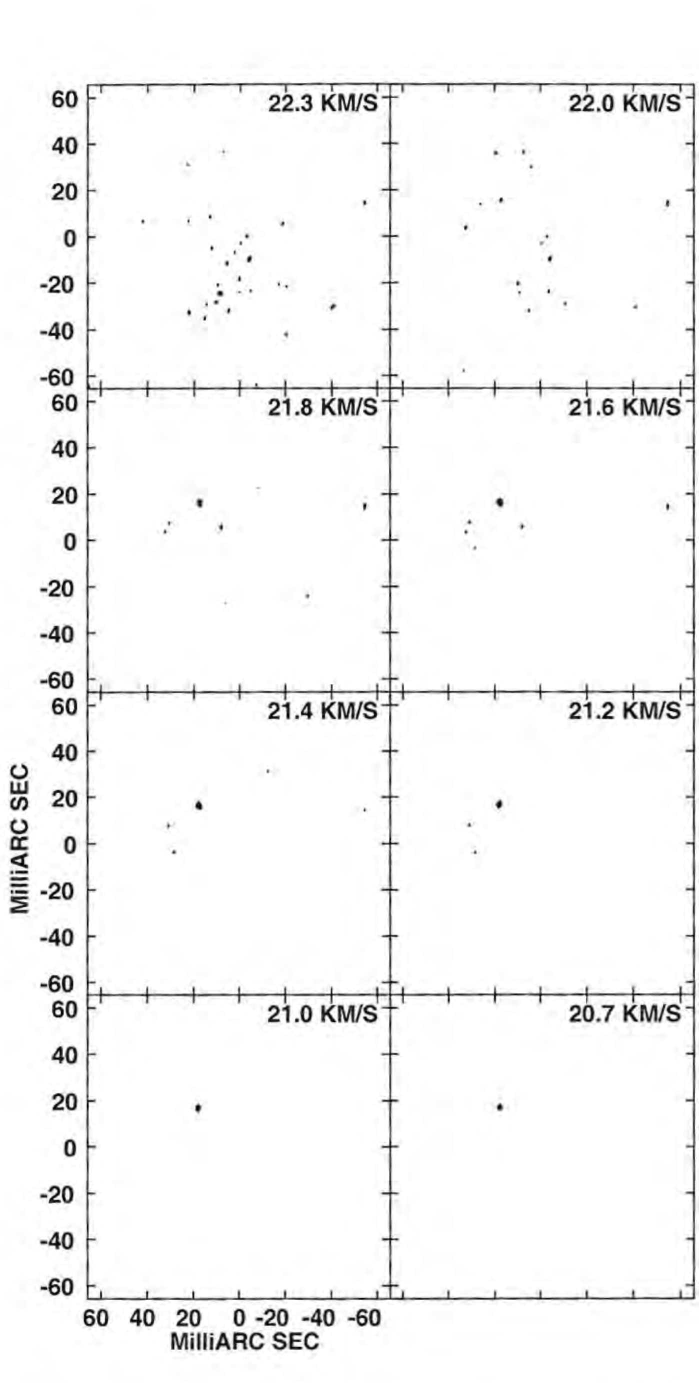

Figure A.6: A contour plot of the total intensity (Stokes I) maser emission for channel maps 20.7 - 22.3 km.s^{-1}, as for Figure A.1.

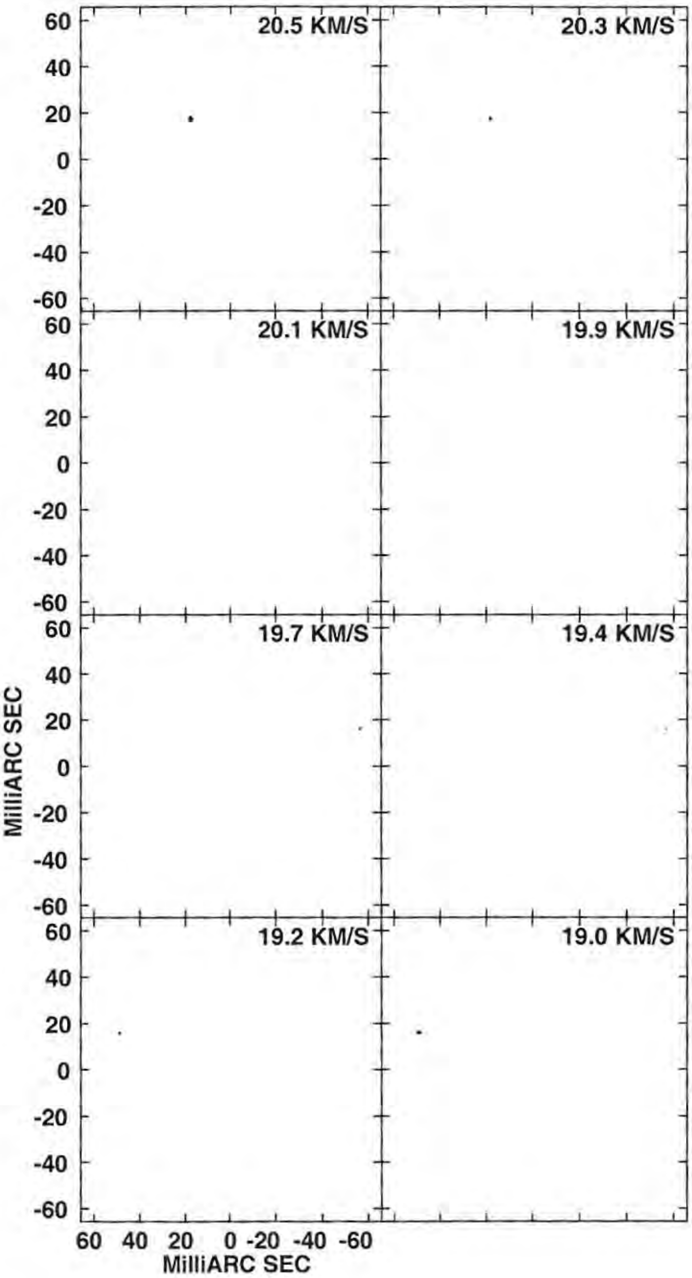

Figure A.7: A contour plot of the total intensity (Stokes I) maser emission for channel maps 19.0 - 20.5 km.s^{-1}, as for Figure A.1.

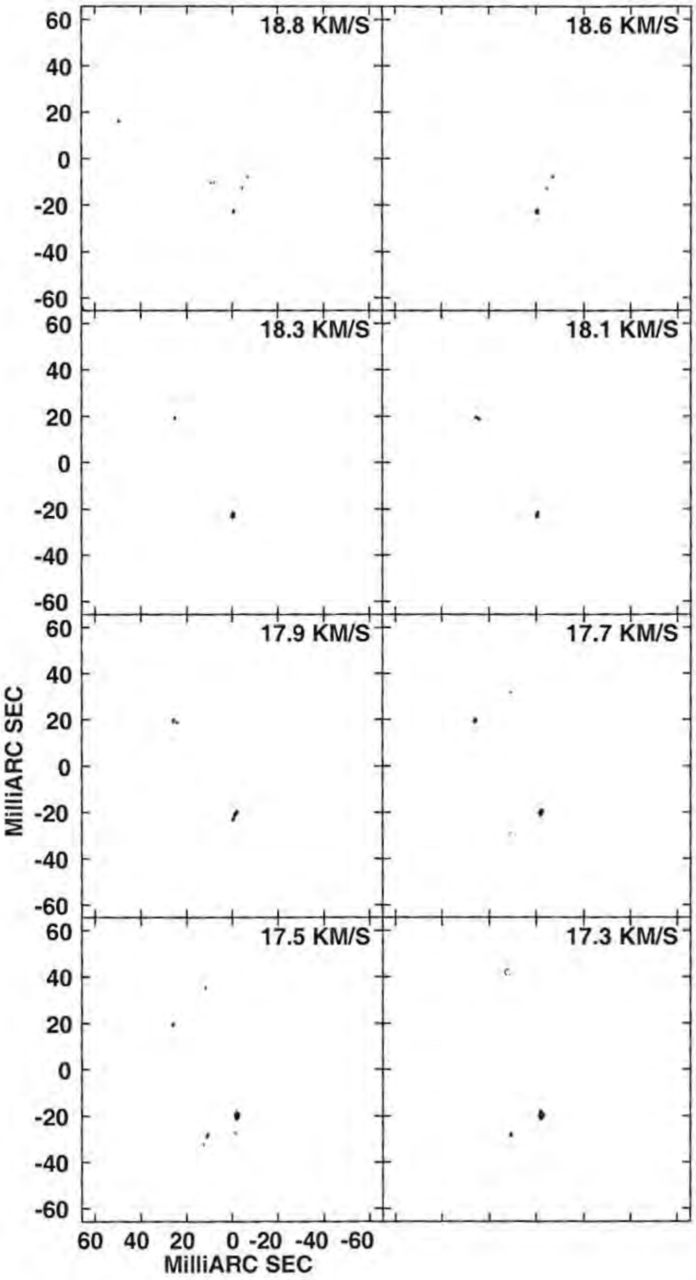

Figure A.8: A contour plot of the total intensity (Stokes I) maser emission for channel maps 17.3 - 18.8 km.s^{-1}, as for Figure A.1.

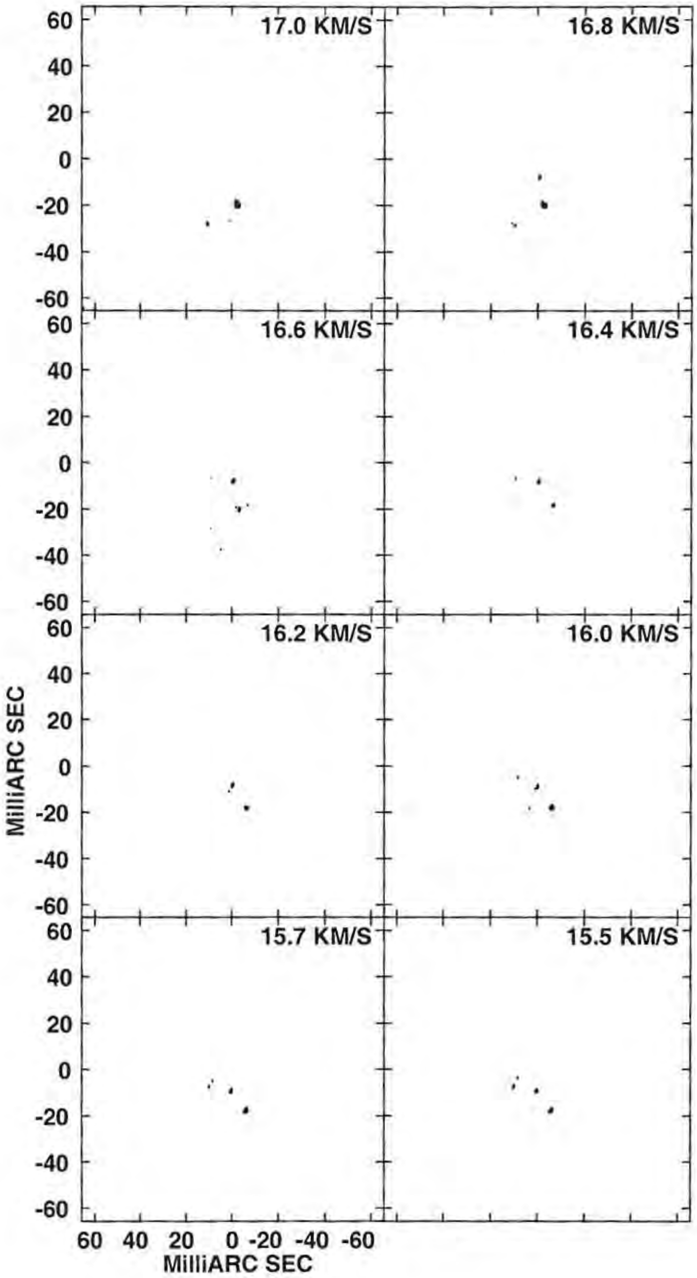

Figure A.9: A contour plot of the total intensity (Stokes I) maser emission for channel maps 15.5 - 17.0 km.s^{-1}, as for Figure A.1.

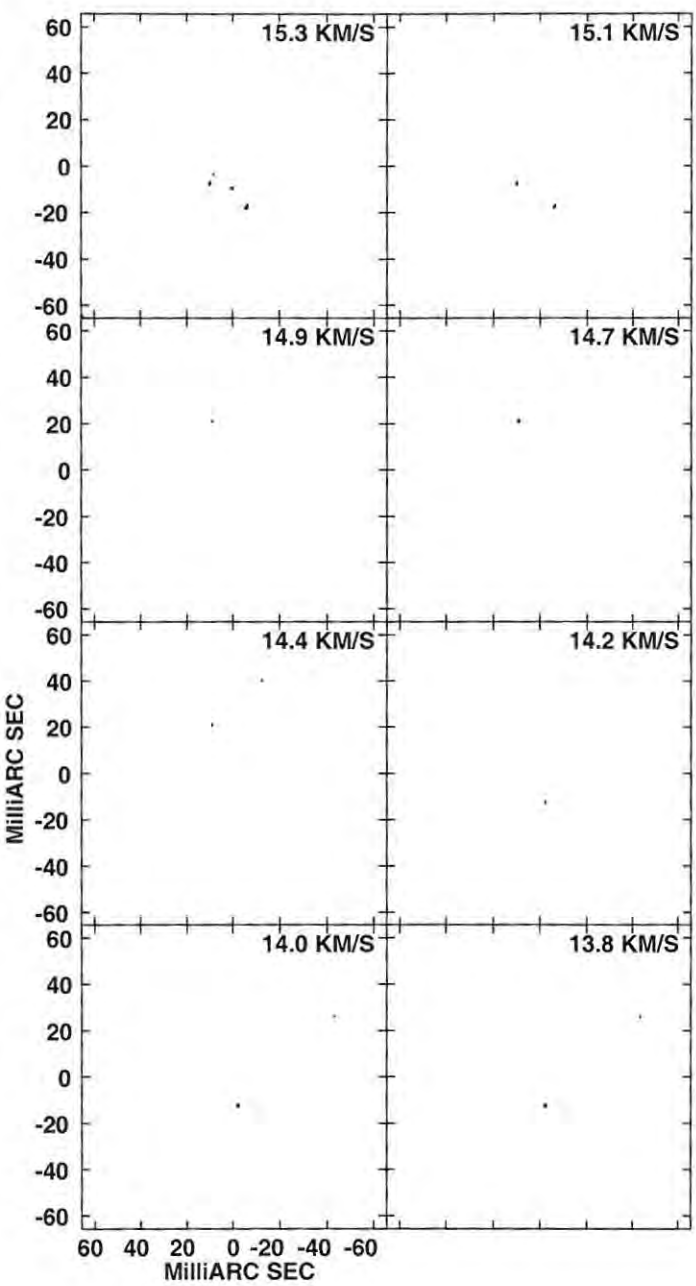

Figure A.10: A contour plot of the total intensity (Stokes I) maser emission for channel maps 13.8 - 15.3 km.s^{-1}, as for Figure A.1.

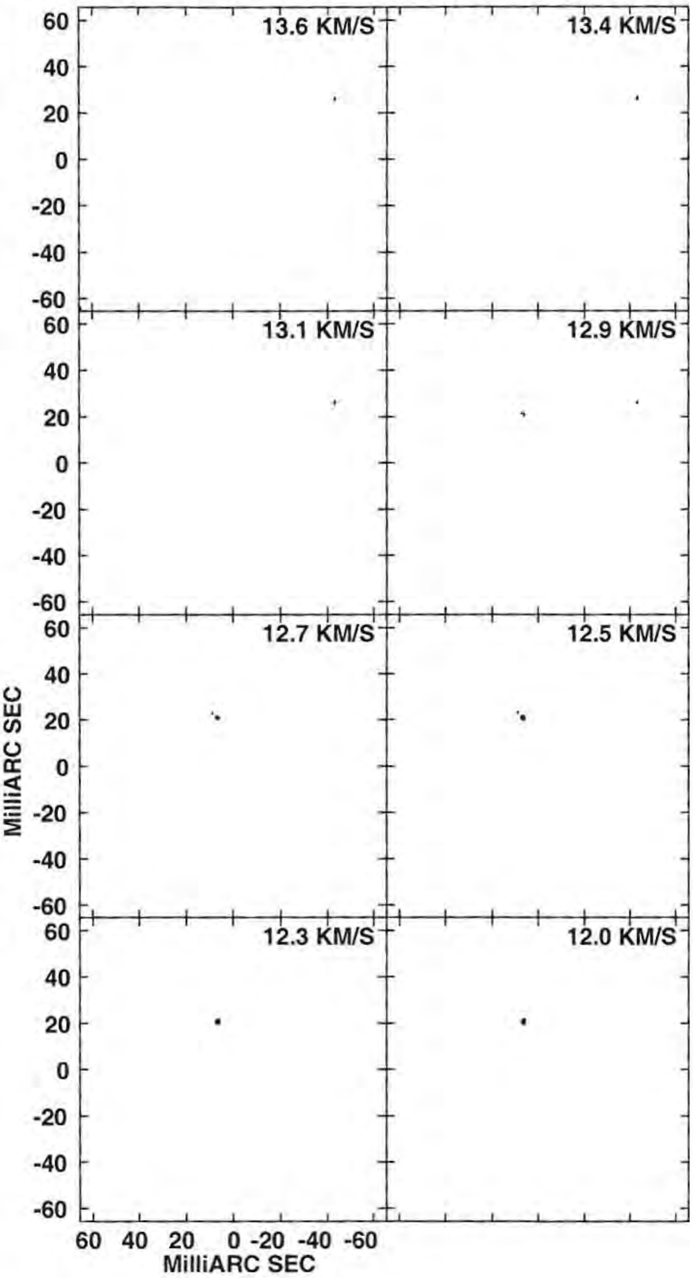

Figure A.11: A contour plot of the total intensity (Stokes I) maser emission for channel maps 12.0 - 13.6 km.s^{-1}, as for Figure A.1.

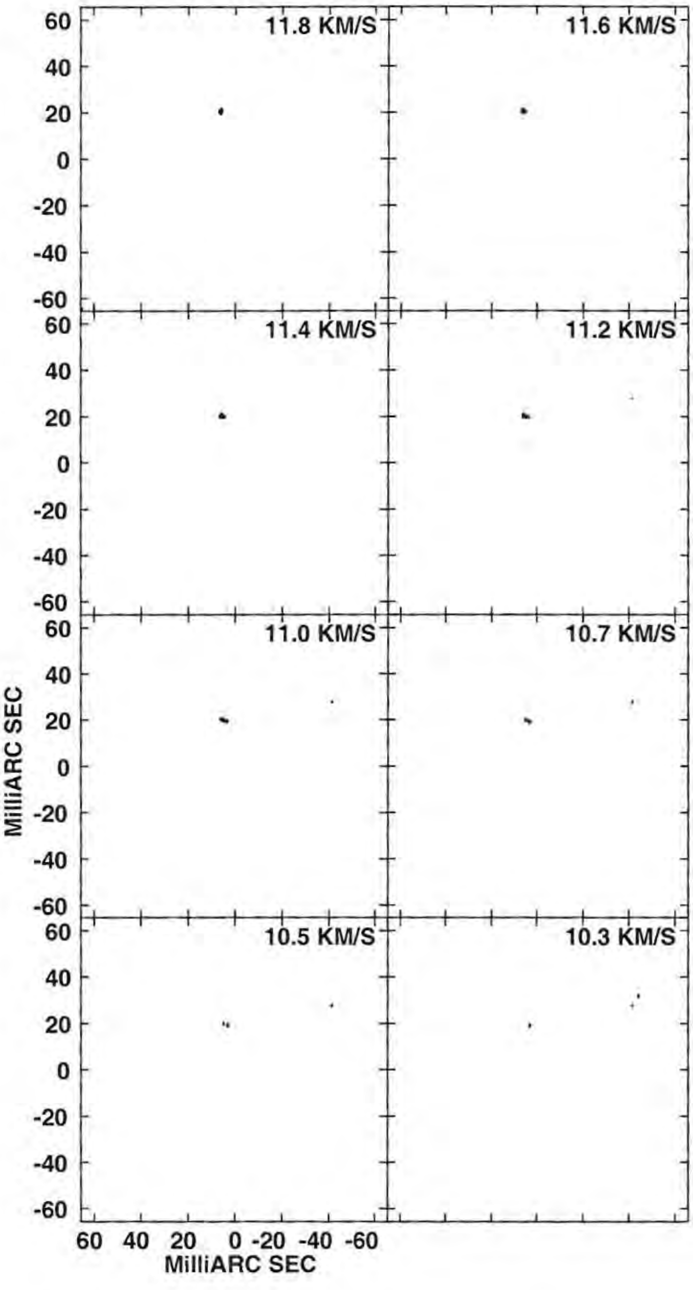

Figure A.12: A contour plot of the total intensity (Stokes I) maser emission for channel maps 10.3 - 11.8 km.s^{-1}, as for Figure A.1.

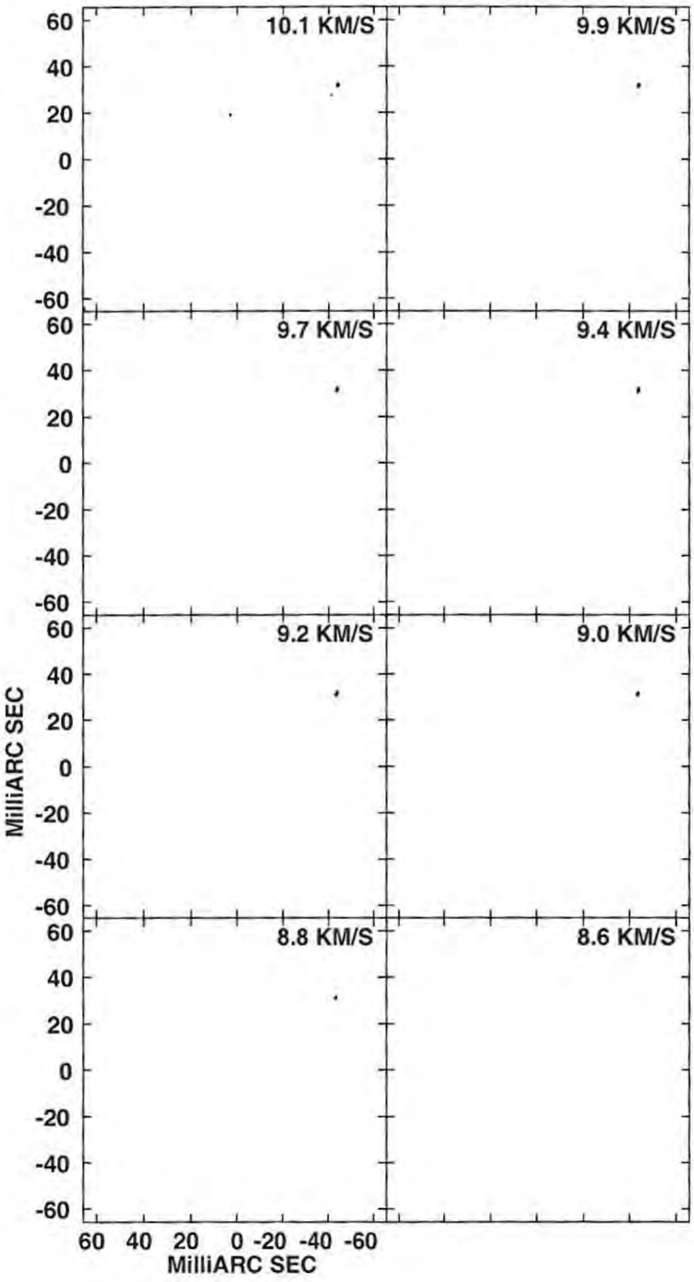

Figure A.13: A contour plot of the total intensity (Stokes I) maser emission for channel maps 8.6 - 10.1 km.s^{-1}, as for Figure A.1.

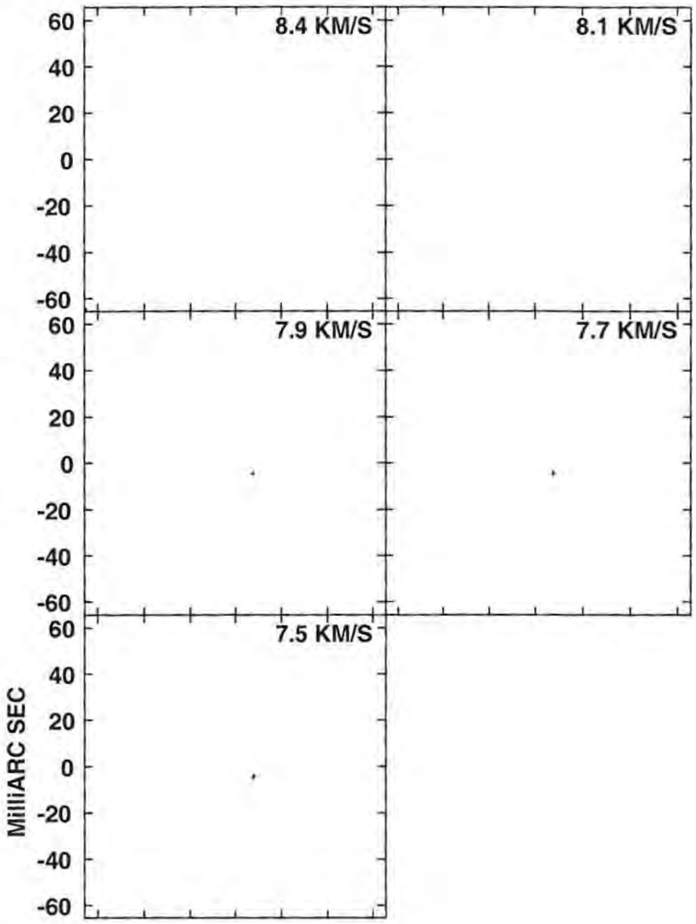

Figure A.14: A contour plot of the total intensity (Stokes I) maser emission for channel maps 7.5 - 8.4 km.s^{-1}, as for Figure A.1.

Appendix B

Linear polarisation channel maps

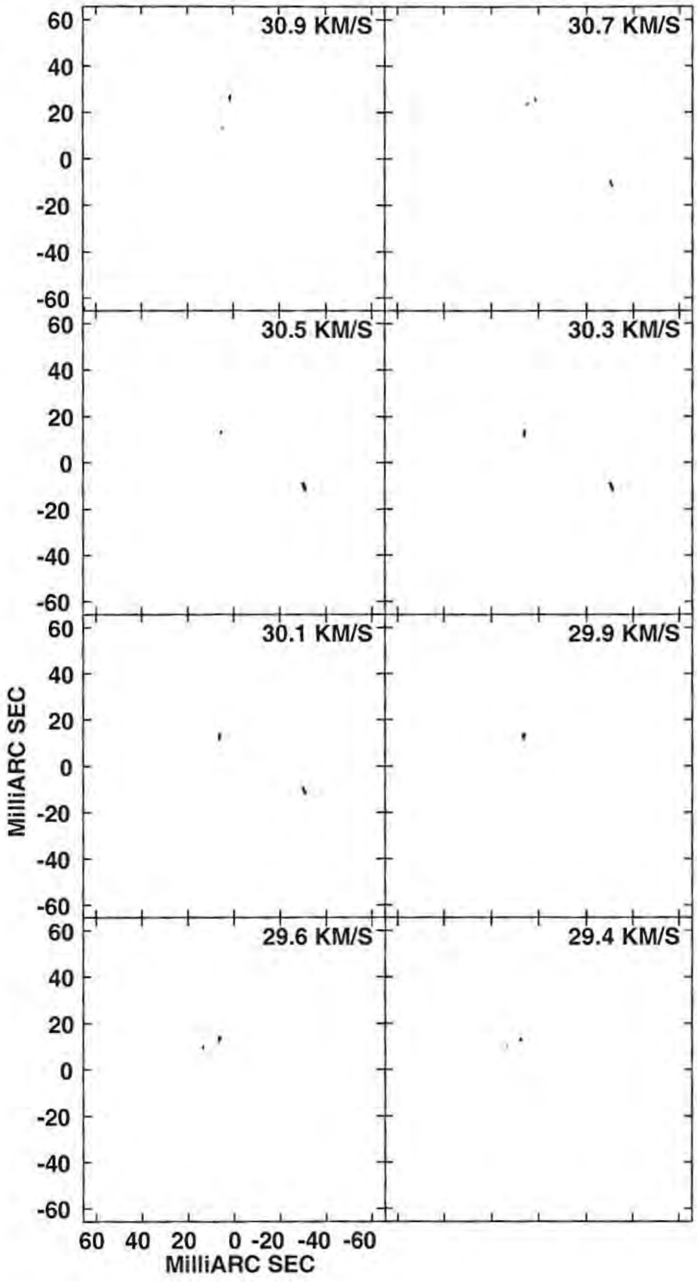

Figure B.1: Linear polarisation vectors in channels 29.4 - 30.9 km.s^{-1}, for regions of intensity greater than 3% of the peak intensity in the Stokes I image cube, 148.93 Jy/beam. The fractional linear polarisation, m_l, is represented by the length of the vectors, where 1 mas = 1.25 Jy/beam. The absolute polarisation position angle, χ, is represented by the rotation of the vector in the image.

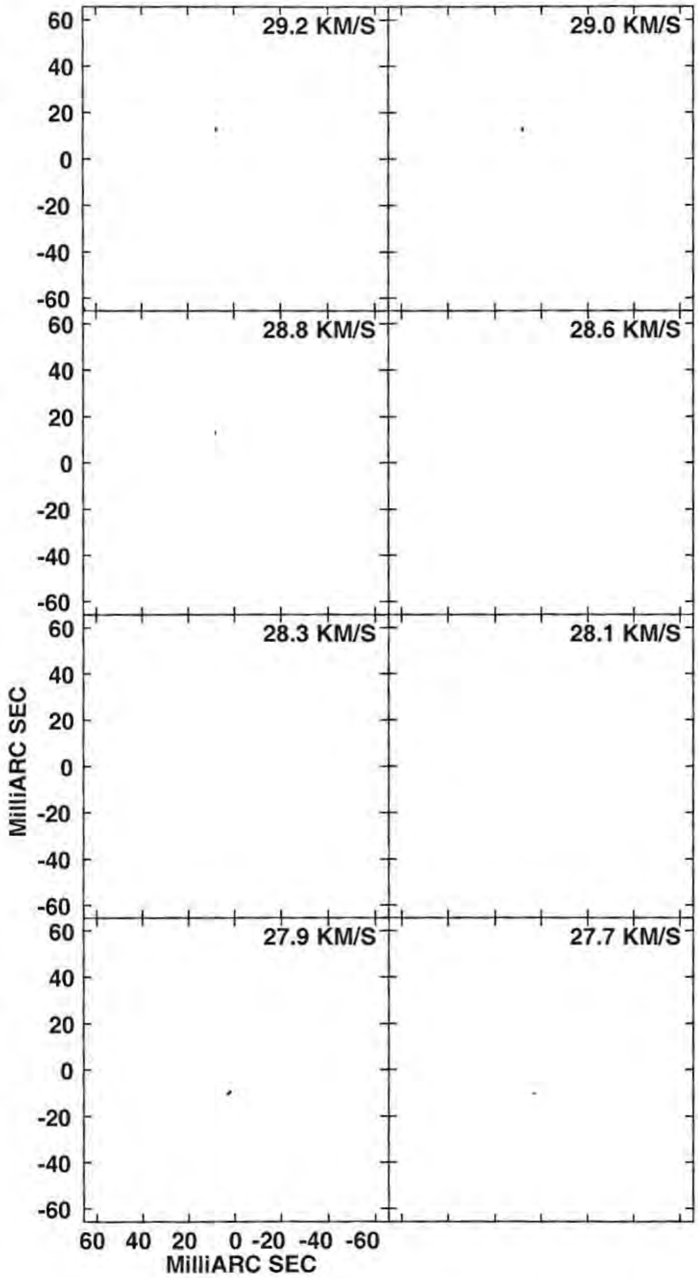

Figure B.2: Linear polarisation vectors in channels 27.7 - 29.2 km.s^{-1}, as for Figure B.1.

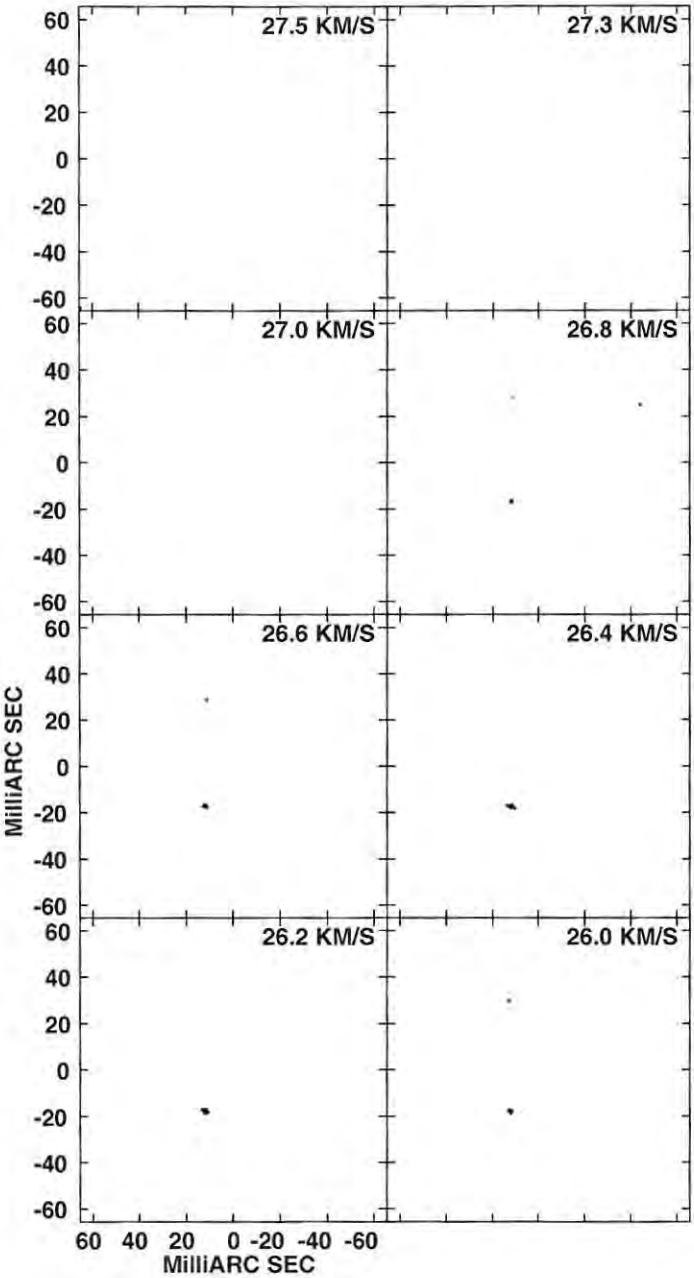

Figure B.3: Linear polarisation vectors in channels 26.0 - 27.5 km.s^{-1}, as for Figure B.1.

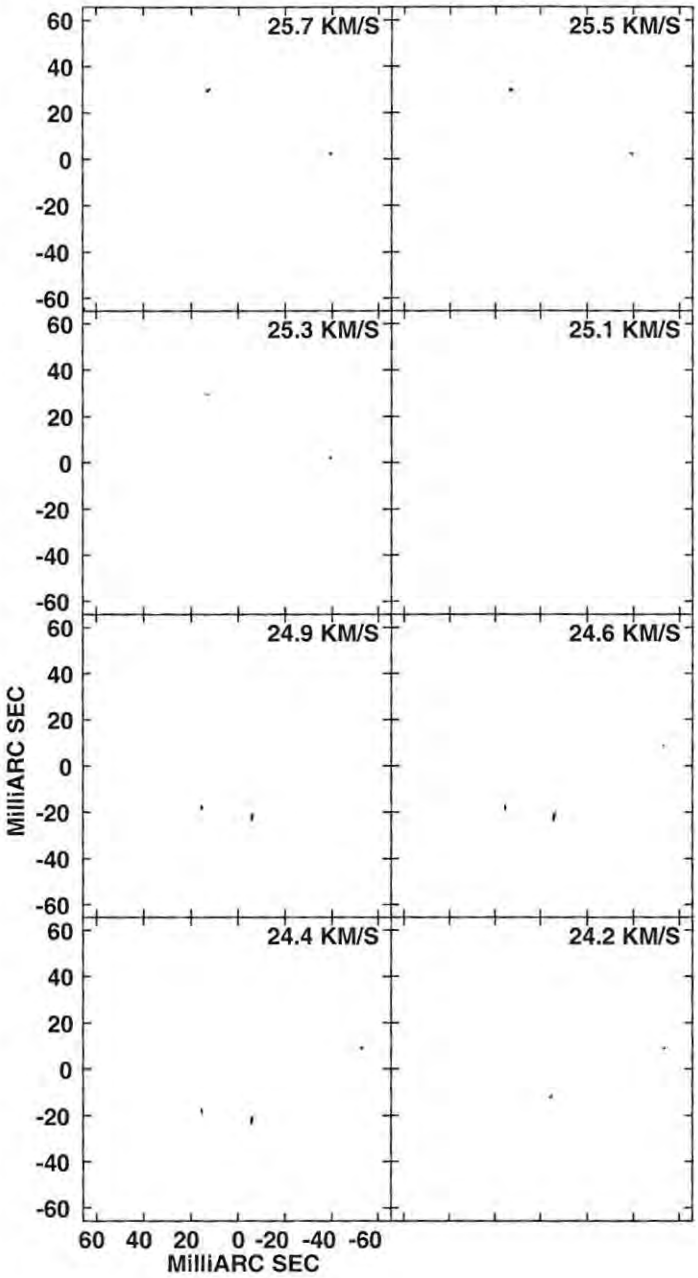

Figure B.4: Linear polarisation vectors in channels 24.2 - 25.7 km.s^{-1}, as for Figure B.1.

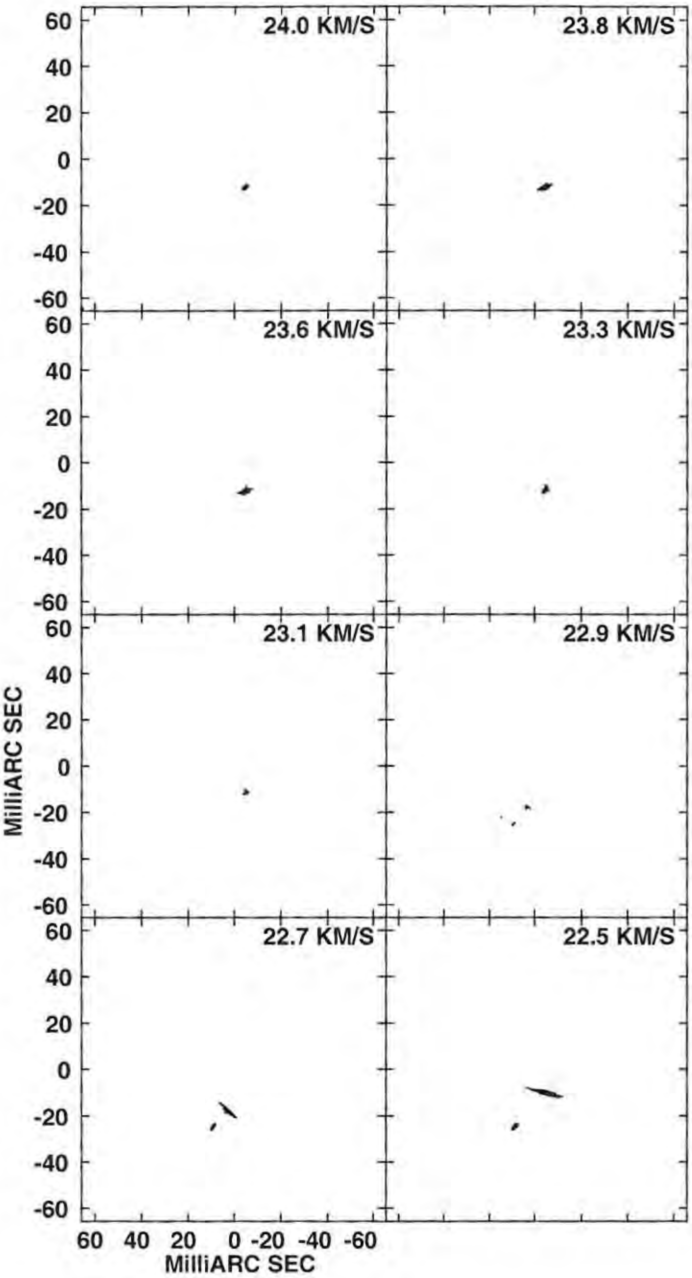

Figure B.5: Linear polarisation vectors in channels 22.5 - 24.0 km.s^{-1}, as for Figure B.1.

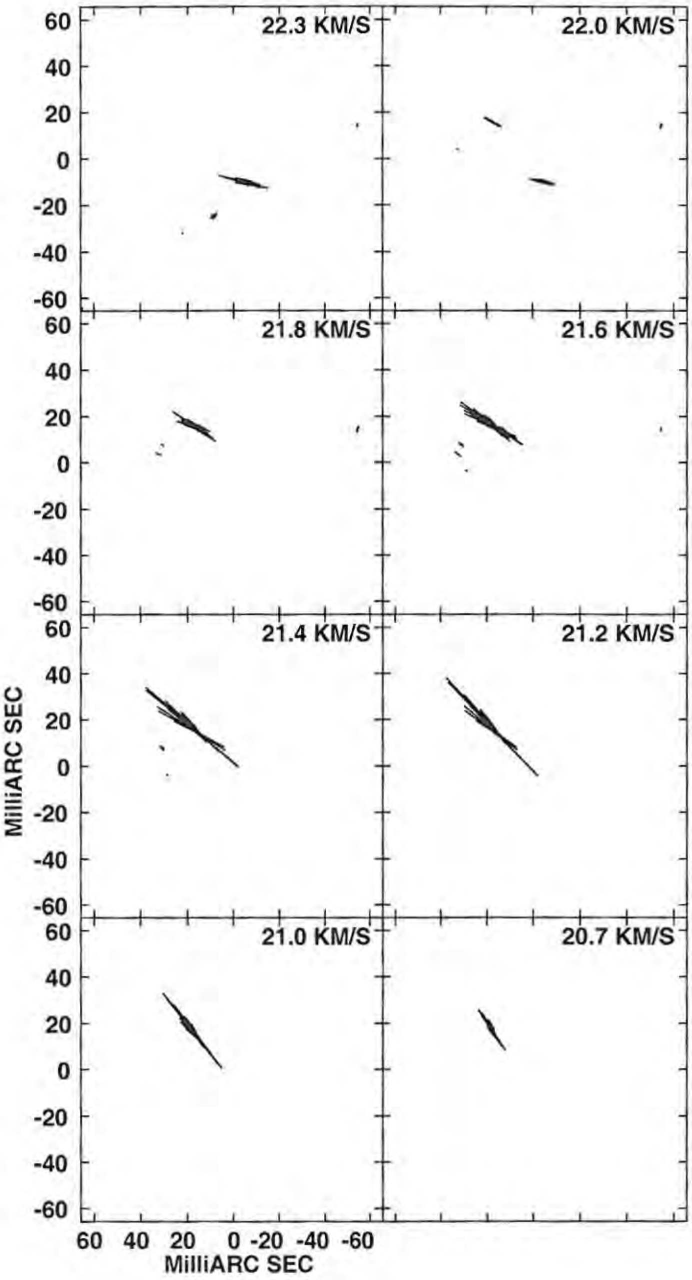

Figure B.6: Linear polarisation vectors in channels 20.7 - 22.3 km.s^{-1}, as for Figure B.1.

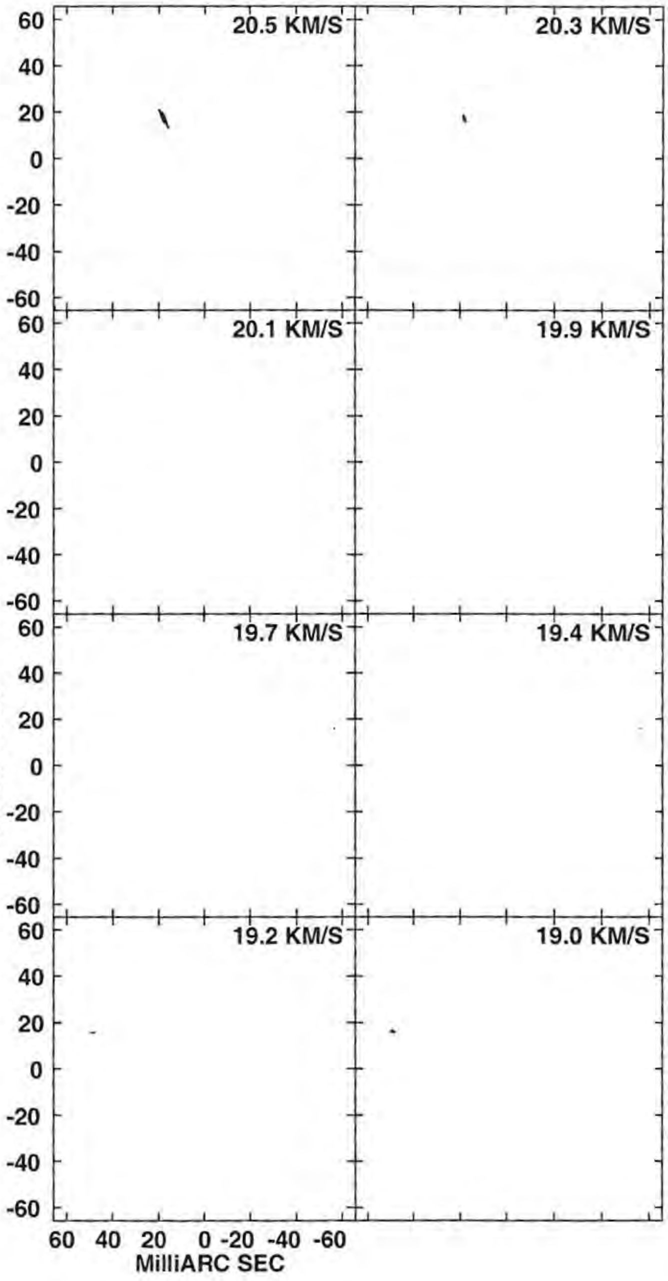

Figure B.7: Linear polarisation vectors in channels 19.0 - 20.5 km.s^{-1}, as for Figure B.1.

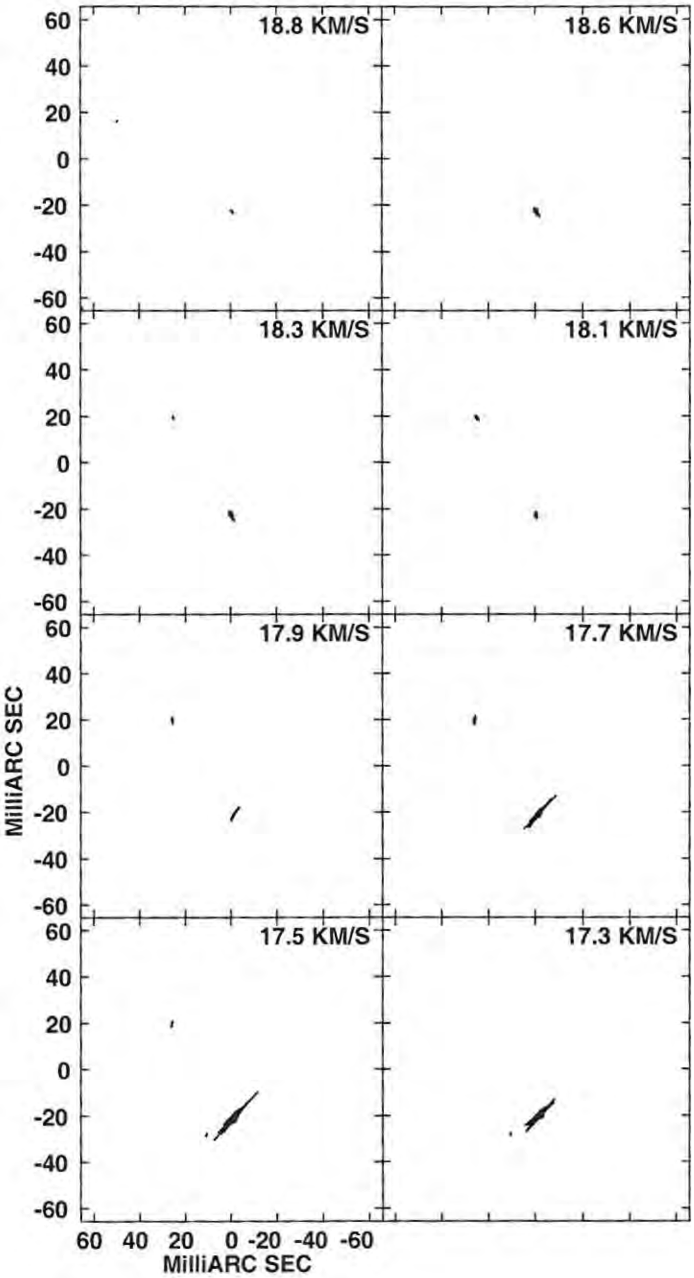

Figure B.8: Linear polarisation vectors in channels 17.3 - 18.8 km.s^{-1}, as for Figure B.1.

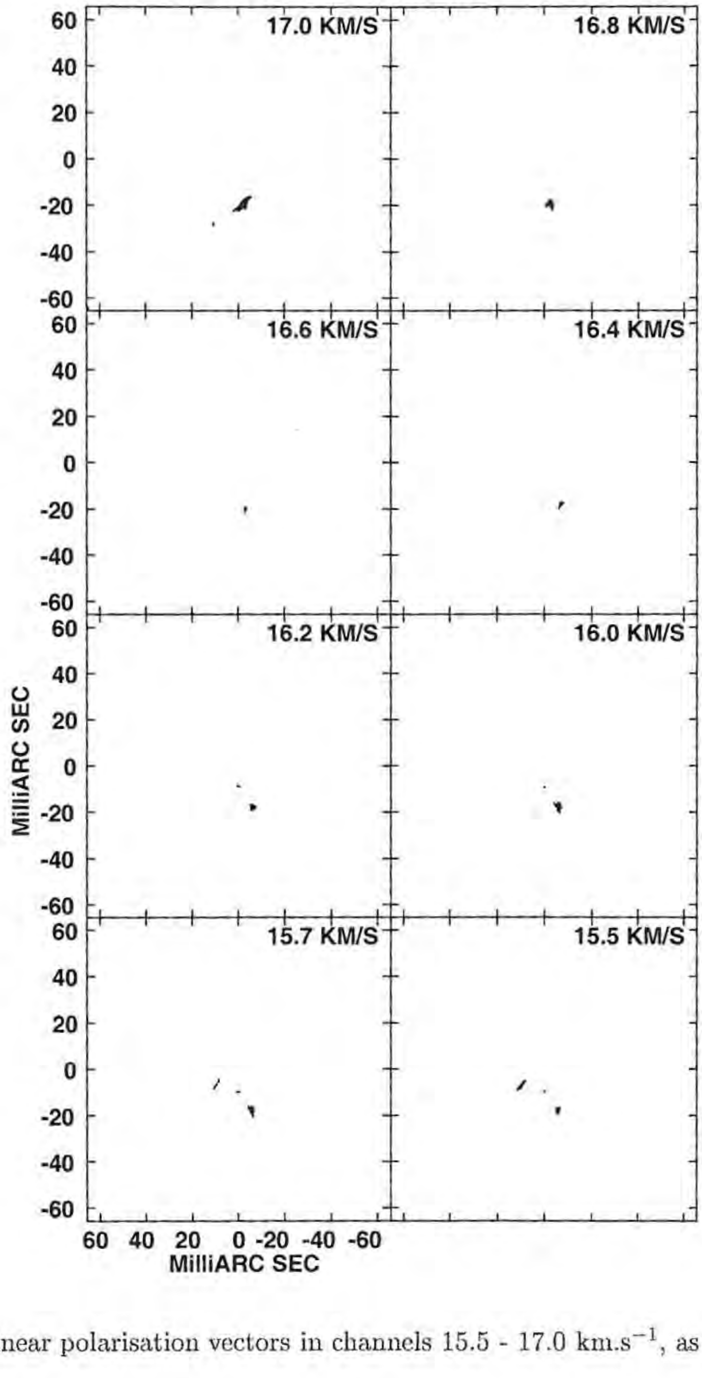

Figure B.9: Linear polarisation vectors in channels 15.5 - 17.0 km.s^{-1}, as for Figure B.1.

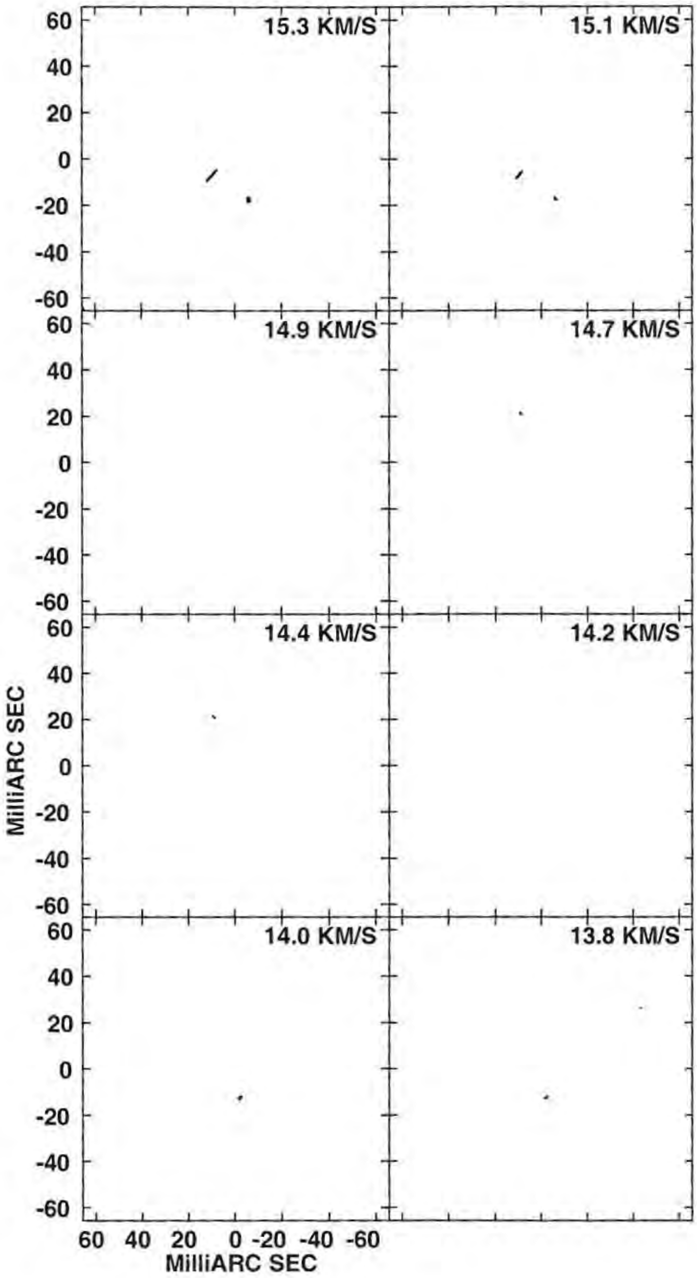

Figure B.10: Linear polarisation vectors in channels 13.8 - 15.3 km.s^{-1}, as for Figure B.1.

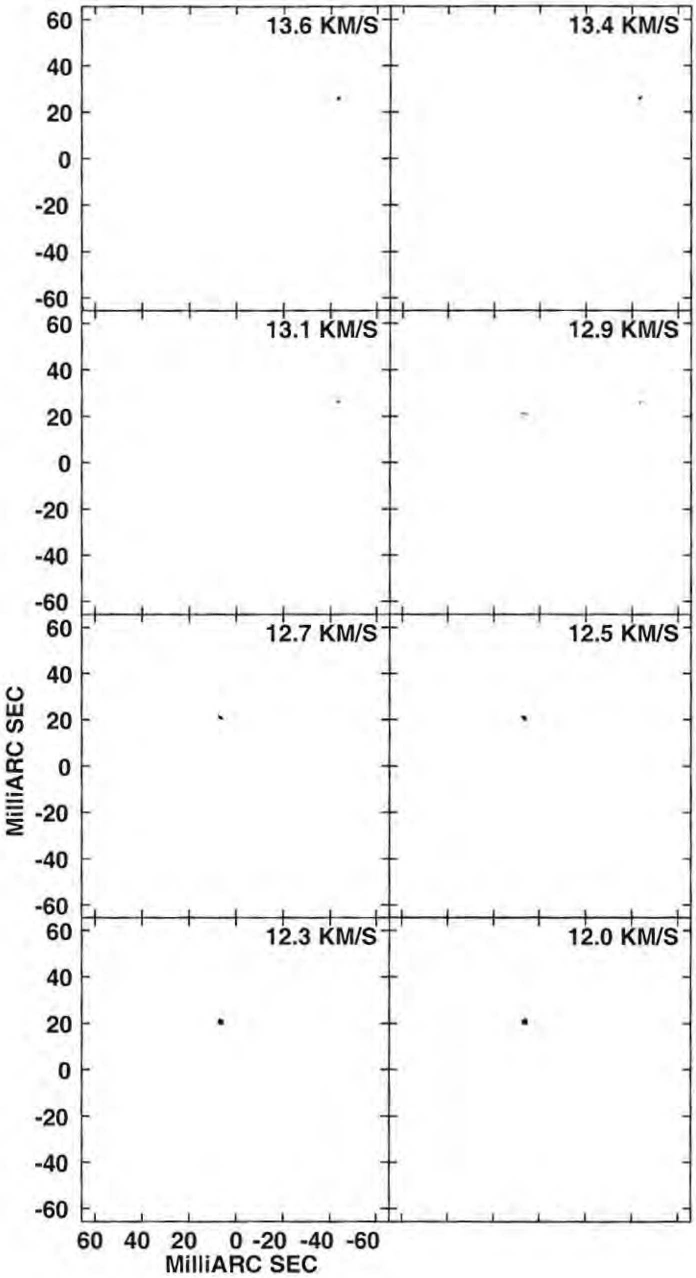

Figure B.11: Linear polarisation vectors in channels 12.0 - 13.6 km.s^{-1}, as for Figure B.1.

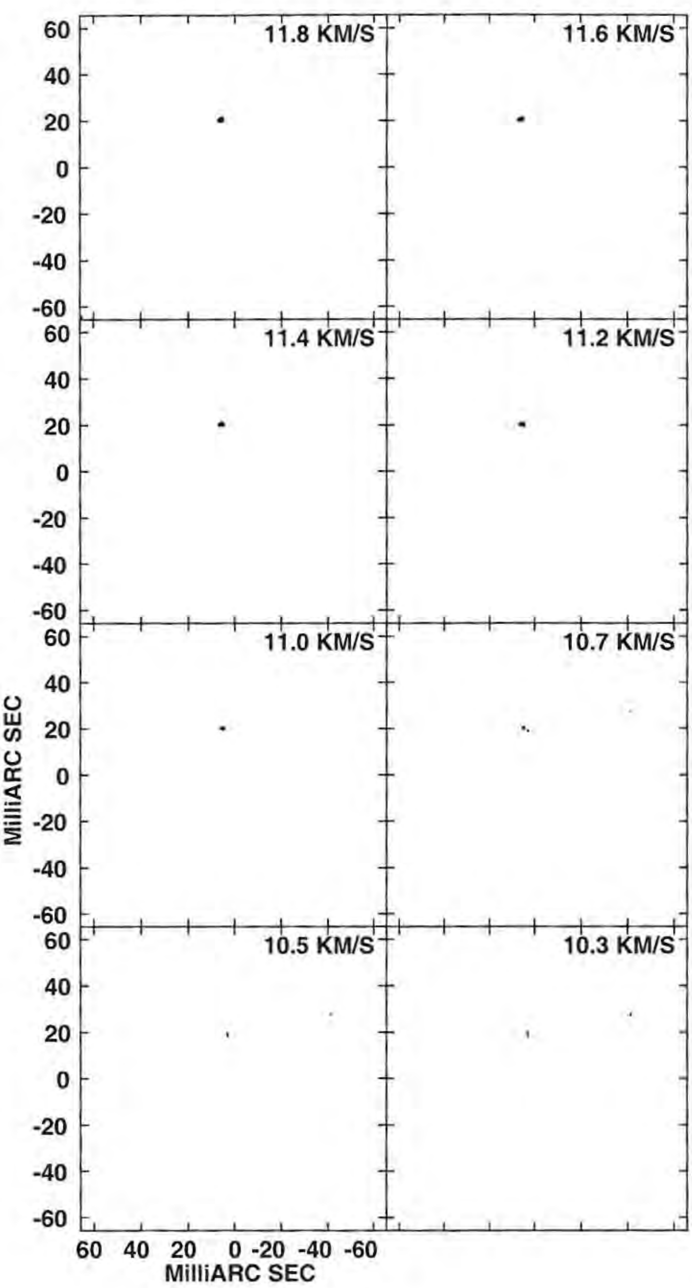

Figure B.12: Linear polarisation vectors in channels 10.3 - 11.8 km.s^{-1}, as for Figure B.1.

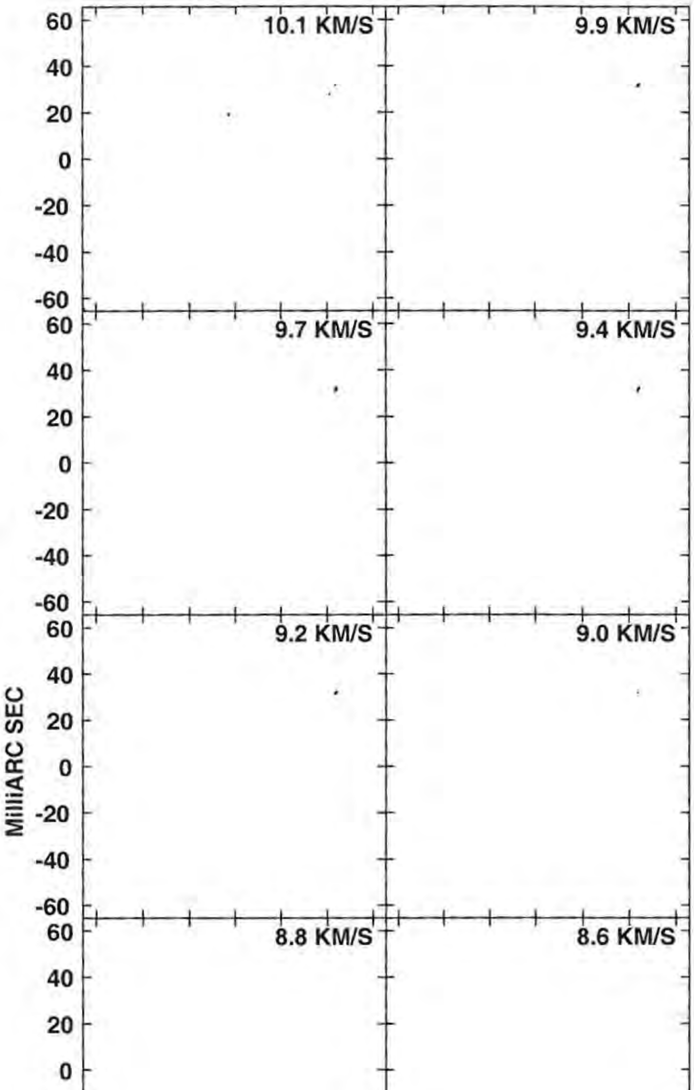

Figure B.13: Linear polarisation vectors in channels 8.6 - 10.1 km.s^{-1}, as for Figure B.1.

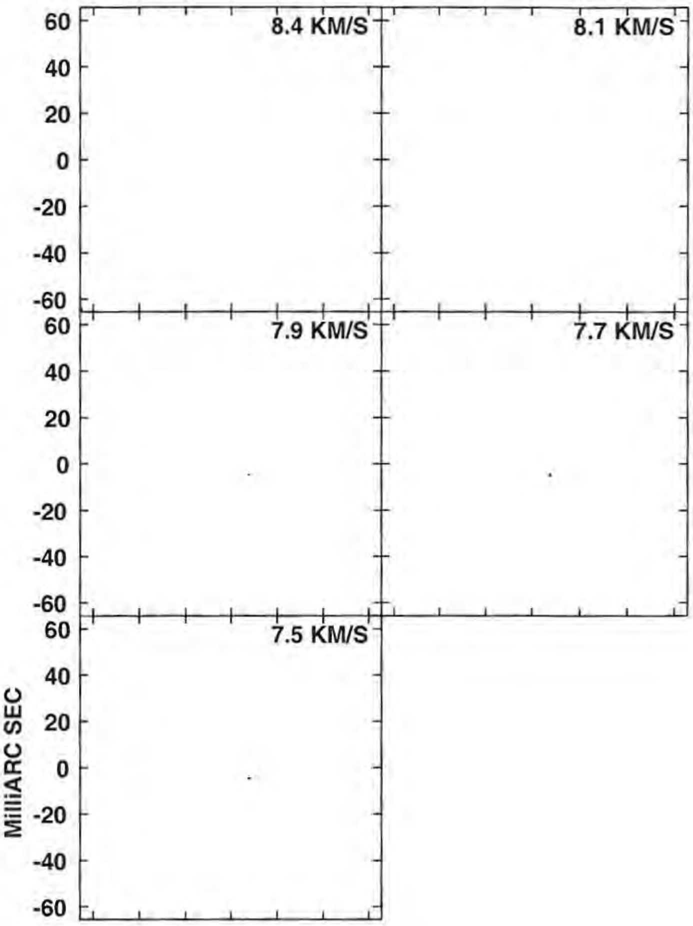

Figure B.14: Linear polarisation vectors in channels 7.5 - 8.4 km.s^{-1}, as for Figure B.1.

Appendix C

Stokes Q channel maps

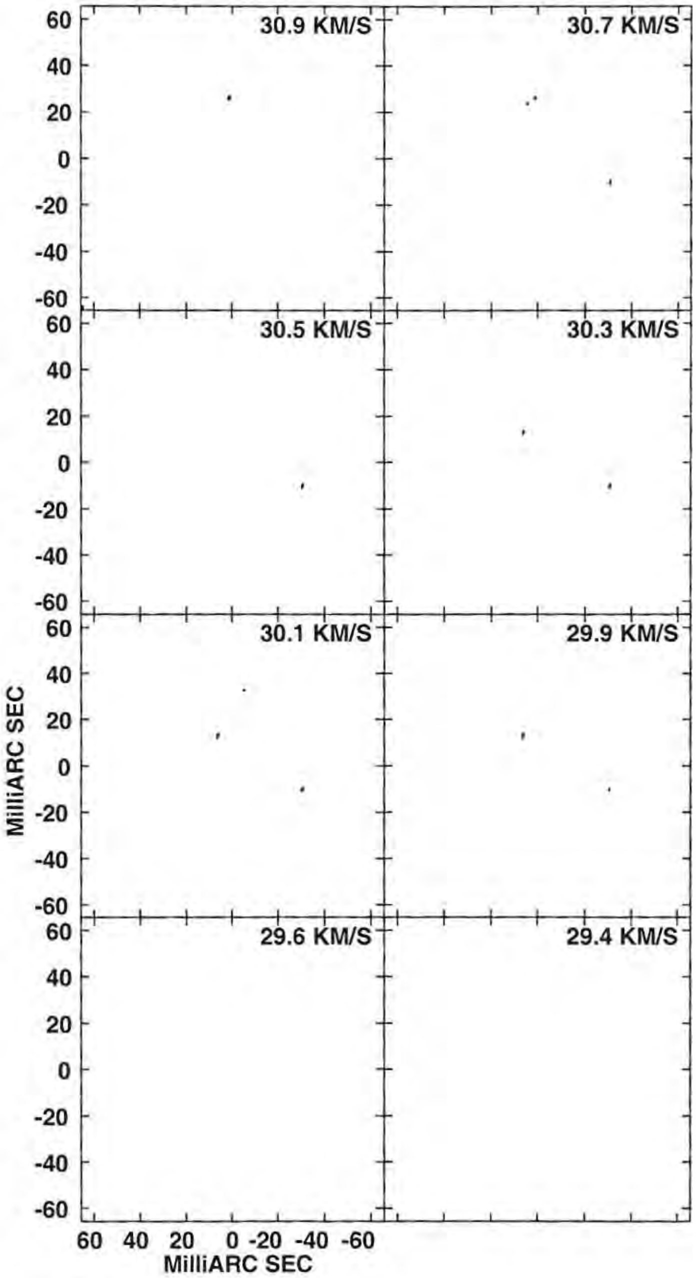

Figure C.1: A contour plot of the Stokes Q maser emission for channel maps 29.4 - 30.9 km.s^{-1}. The contour levels are -100, -80, -60, -40, -15, -5, -2, 2, 5, 15, 40, 60, 80 and 100% of the absolute value of the peak flux density in the Stokes Q cube, -42.891 Jy/beam.

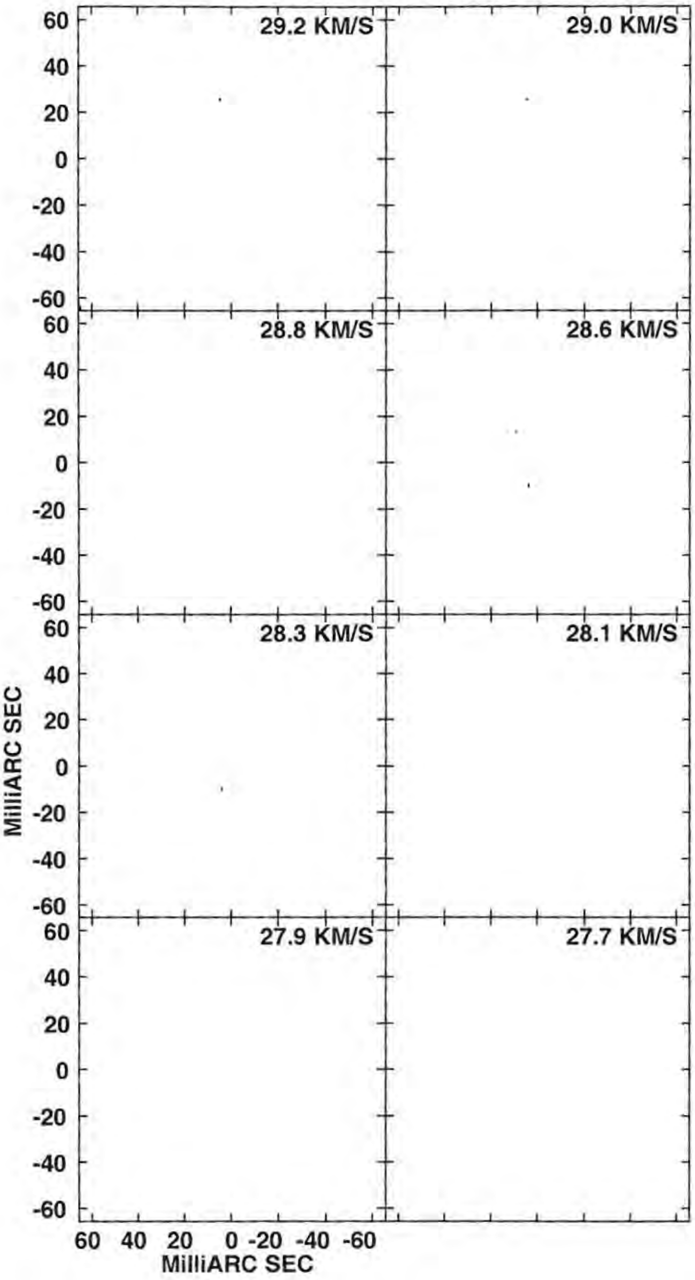

Figure C.2: A contour plot of the Stokes Q maser emission for channel maps 27.7 - 29.2 km.s^{-1}, as for Figure C.1.

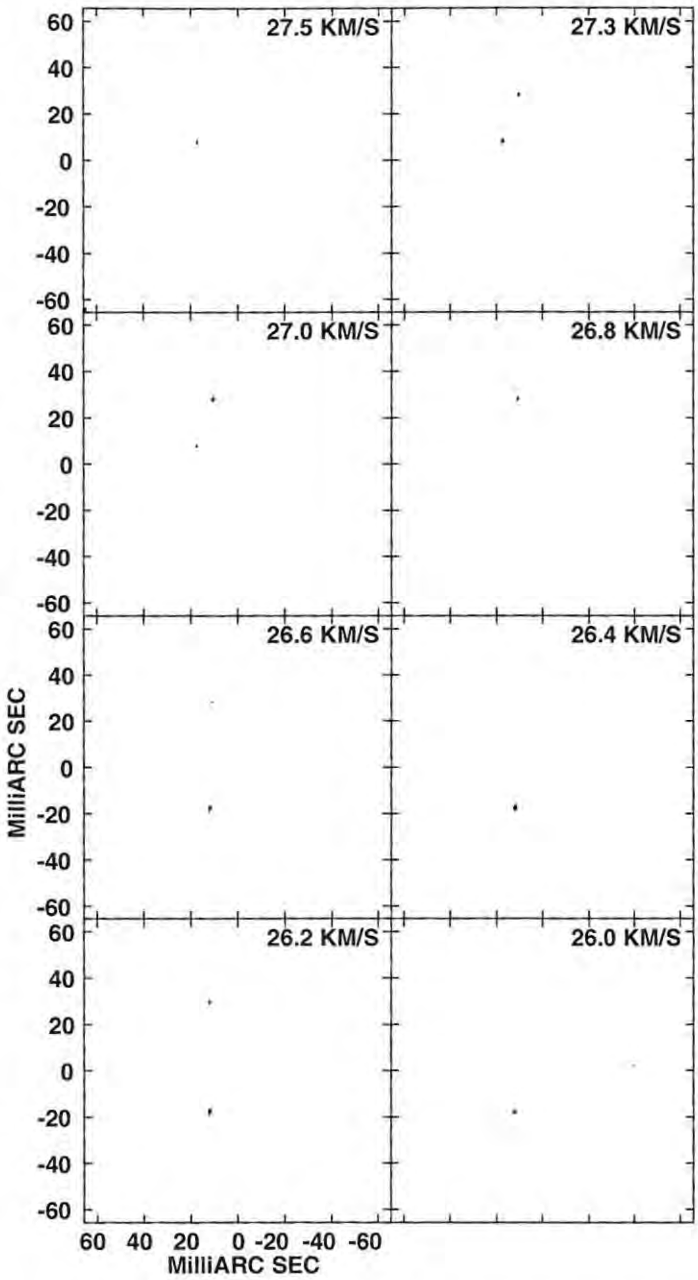

Figure C.3: A contour plot of the Stokes Q maser emission for channel maps 26.0 - 27.5 km.s^{-1}, as for Figure C.1.

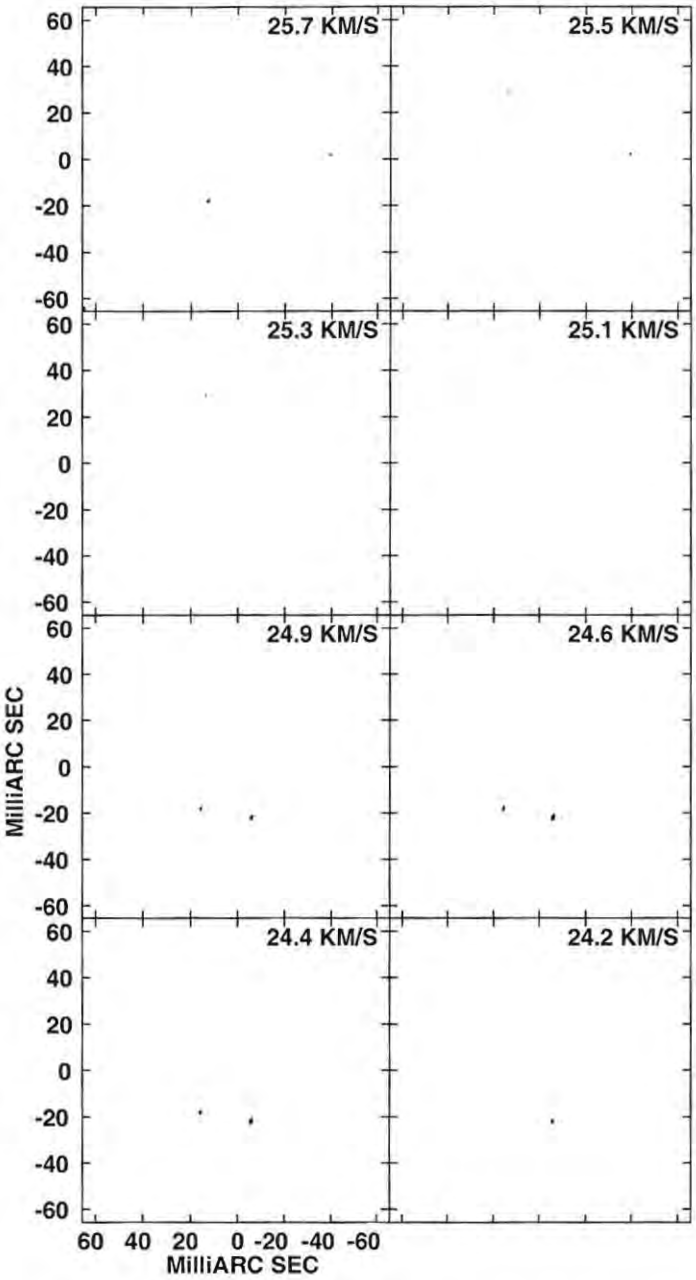

Figure C.4: A contour plot of the Stokes Q maser emission for channel maps 24.2 - 25.7 km.s^{-1}, as for Figure C.1.

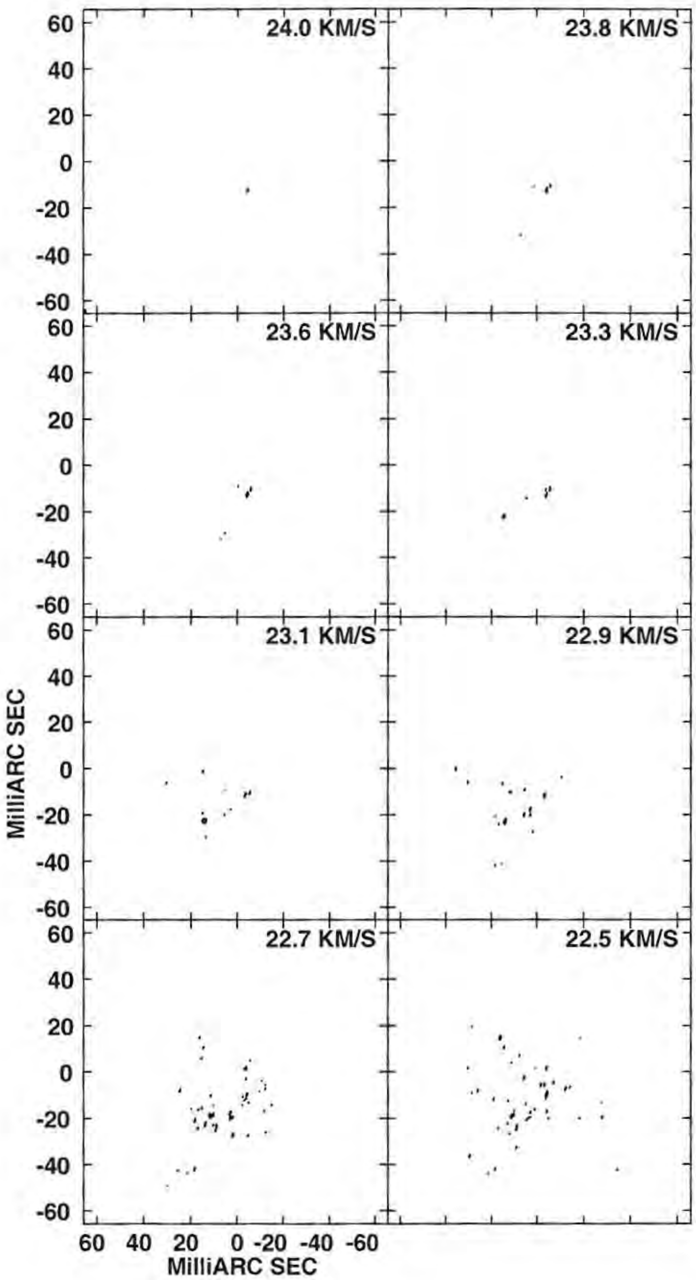

Figure C.5: A contour plot of the Stokes Q maser emission for channel maps 22.5 - 24.0 km.s^{-1}, as for Figure C.1.

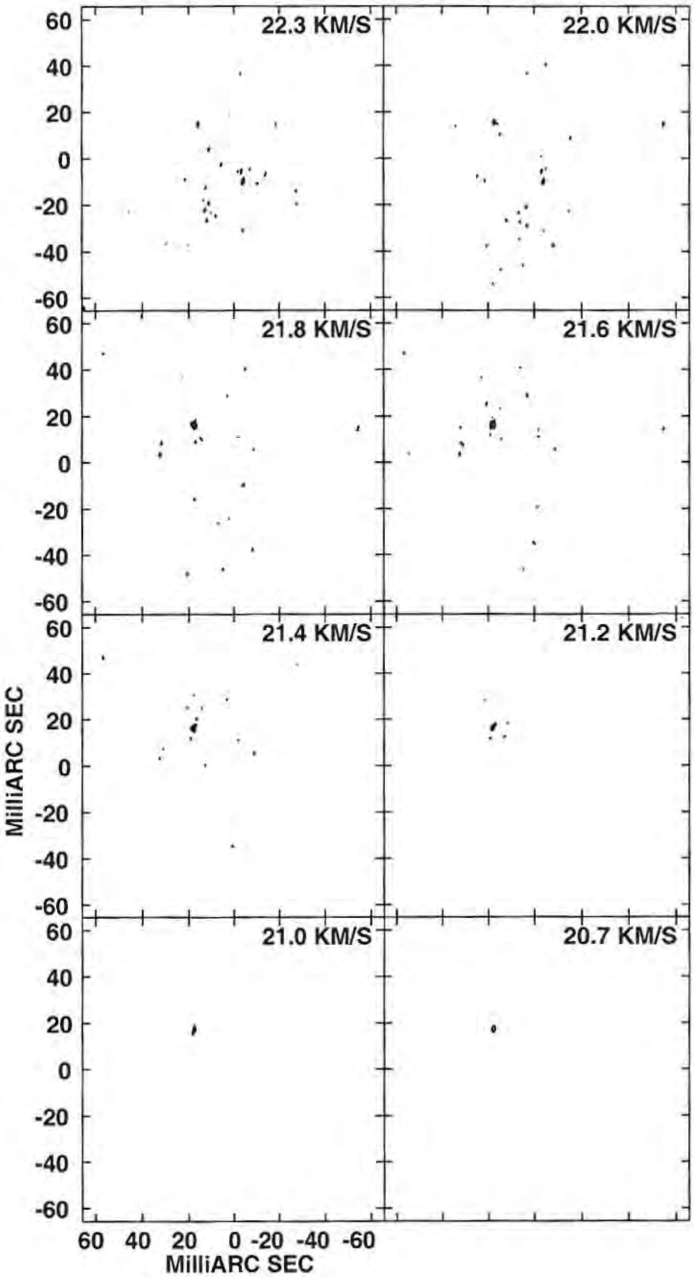

Figure C.6: A contour plot of the Stokes Q maser emission for channel maps 20.7 - 22.3 km.s^{-1}, as for Figure C.1.

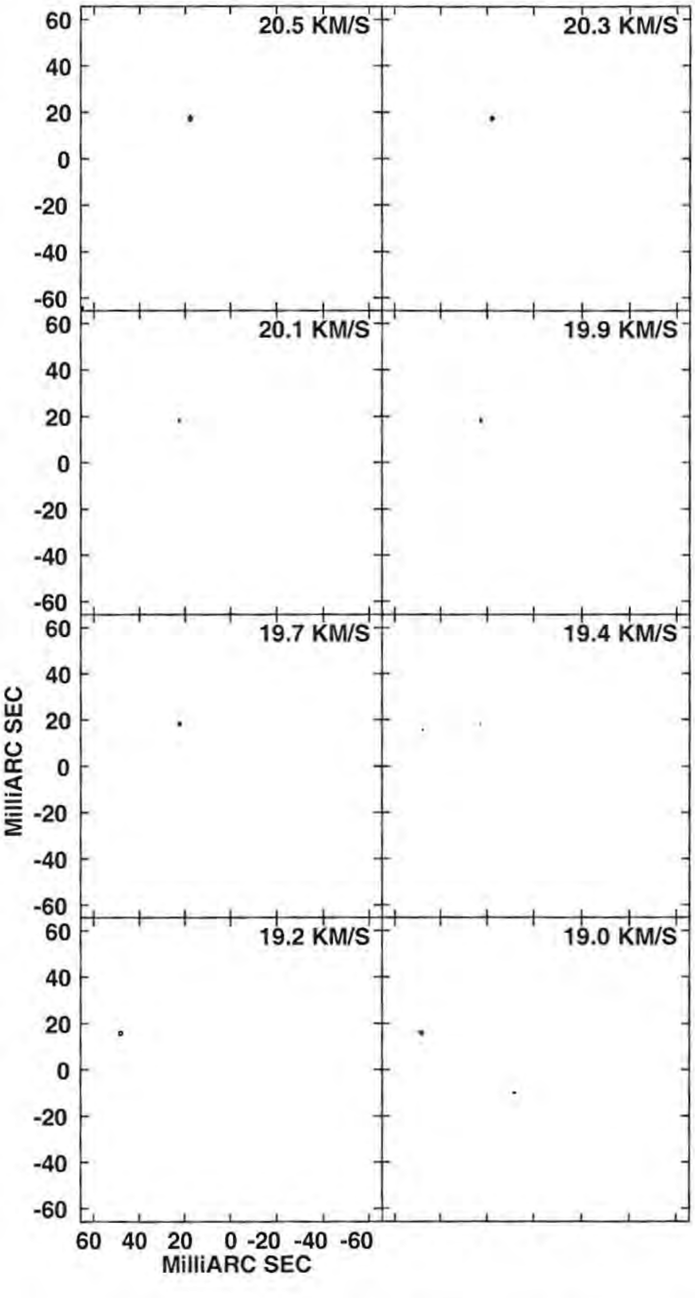

Figure C.7: A contour plot of the Stokes Q maser emission for channel maps 19.0 - 20.5 km.s^{-1}, as for Figure C.1.

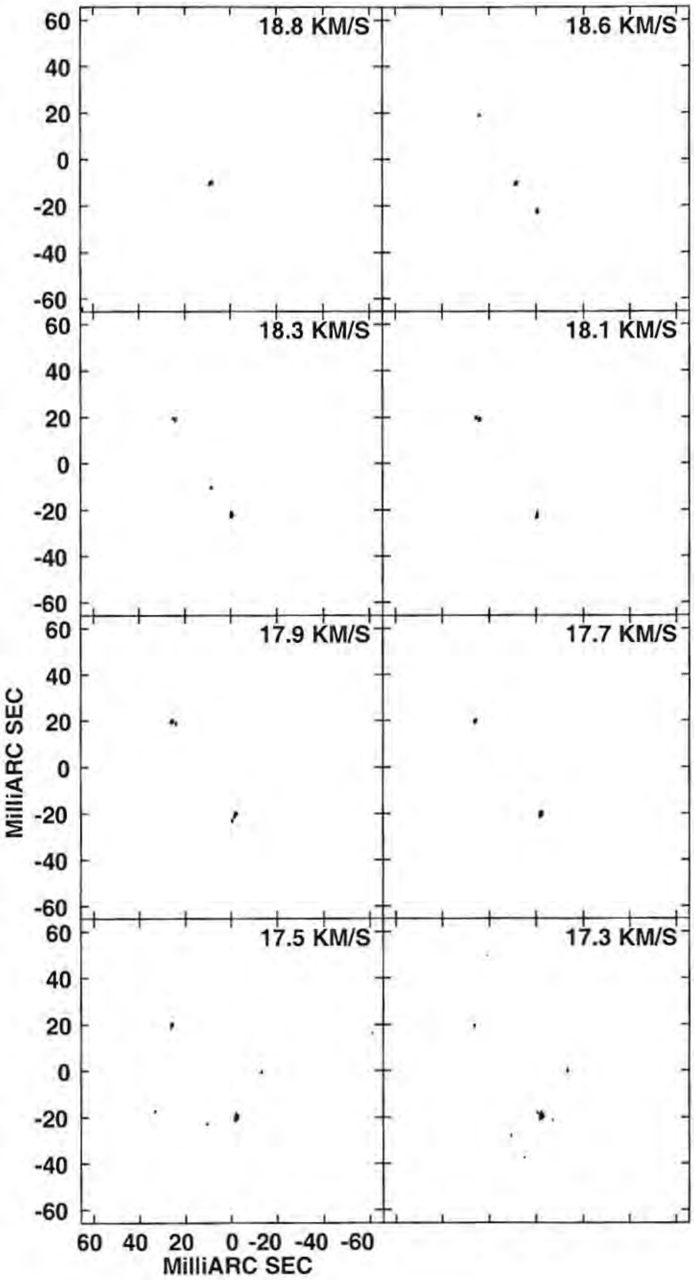

Figure C.8: A contour plot of the Stokes Q maser emission for channel maps 17.3 - 18.8 km.s^{-1}, as for Figure C.1.

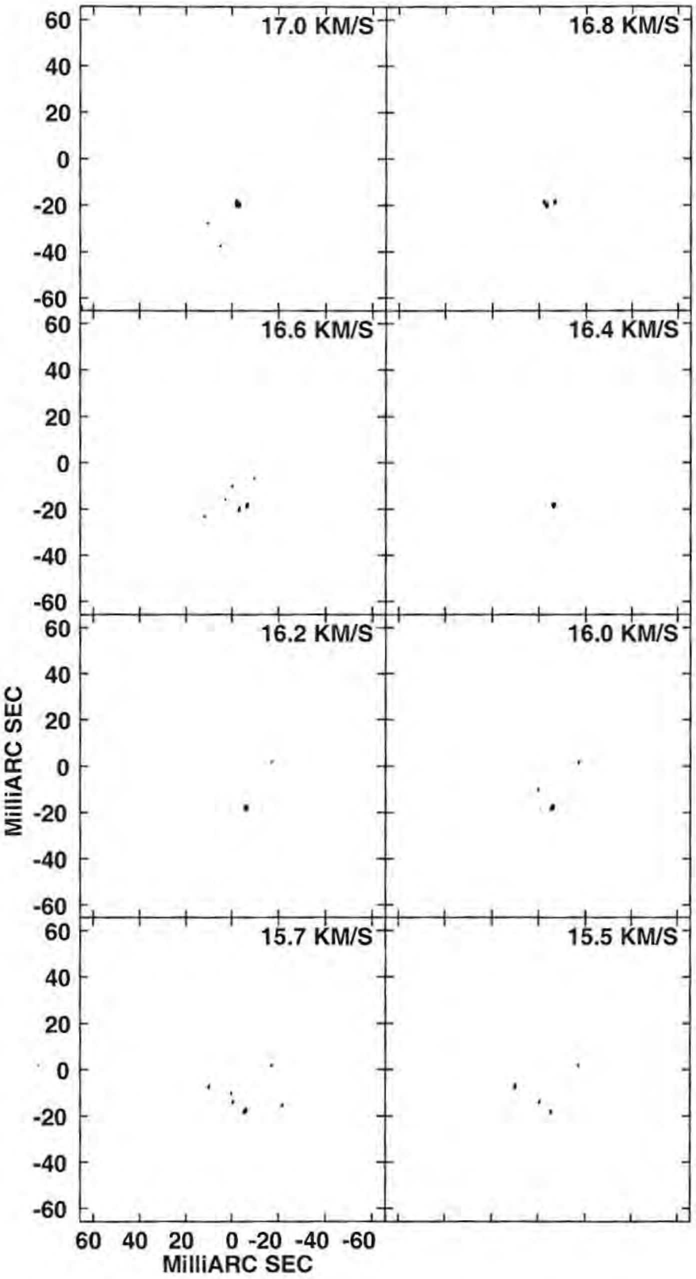

Figure C.9: A contour plot of the Stokes Q maser emission for channel maps 15.5 - 17.0 km.s^{-1}, as for Figure C.1.

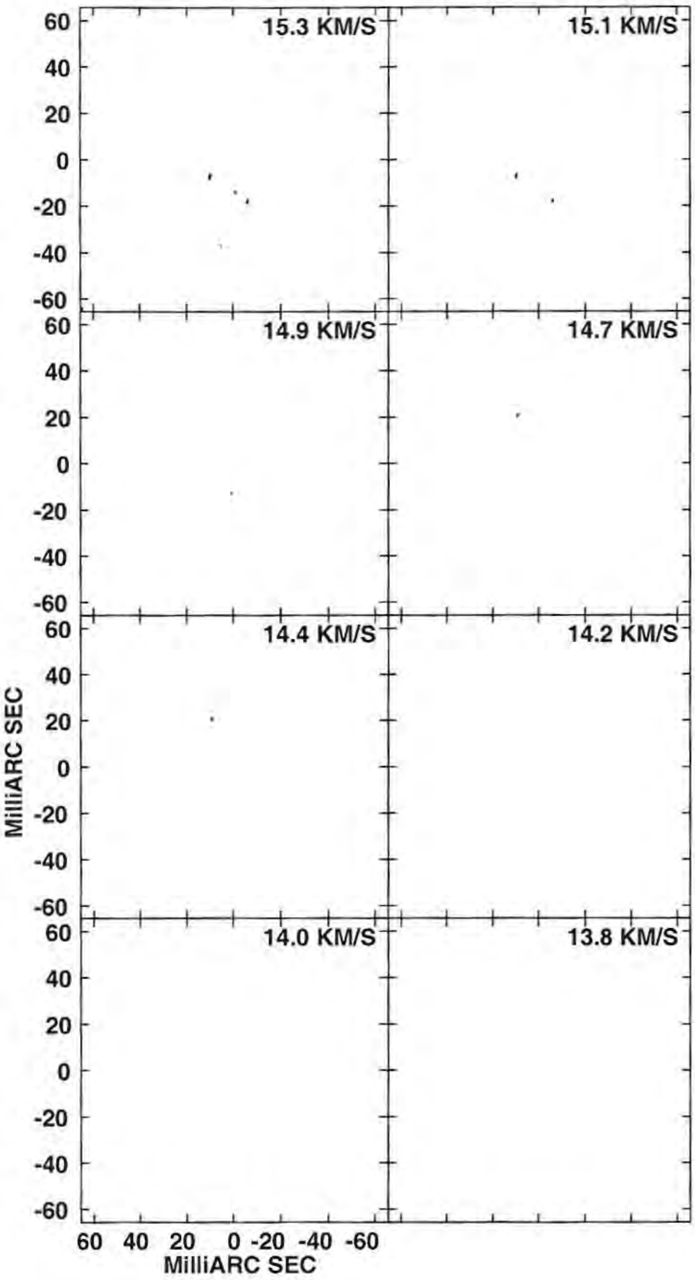

Figure C.10: A contour plot of the Stokes Q maser emission for channel maps 13.8 - 15.3 km.s^{-1}, as for Figure C.1.

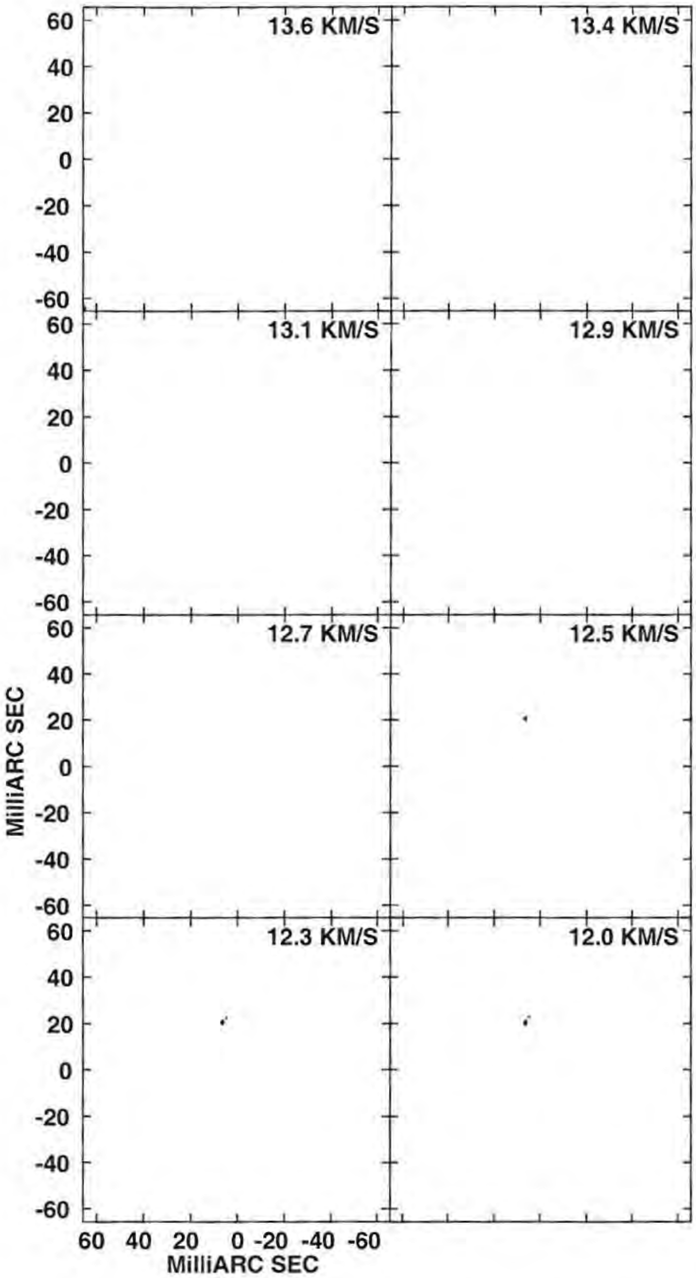

Figure C.11: A contour plot of the Stokes Q maser emission for channel maps 12.0 - 13.6 km.s^{-1}, as for Figure C.1.

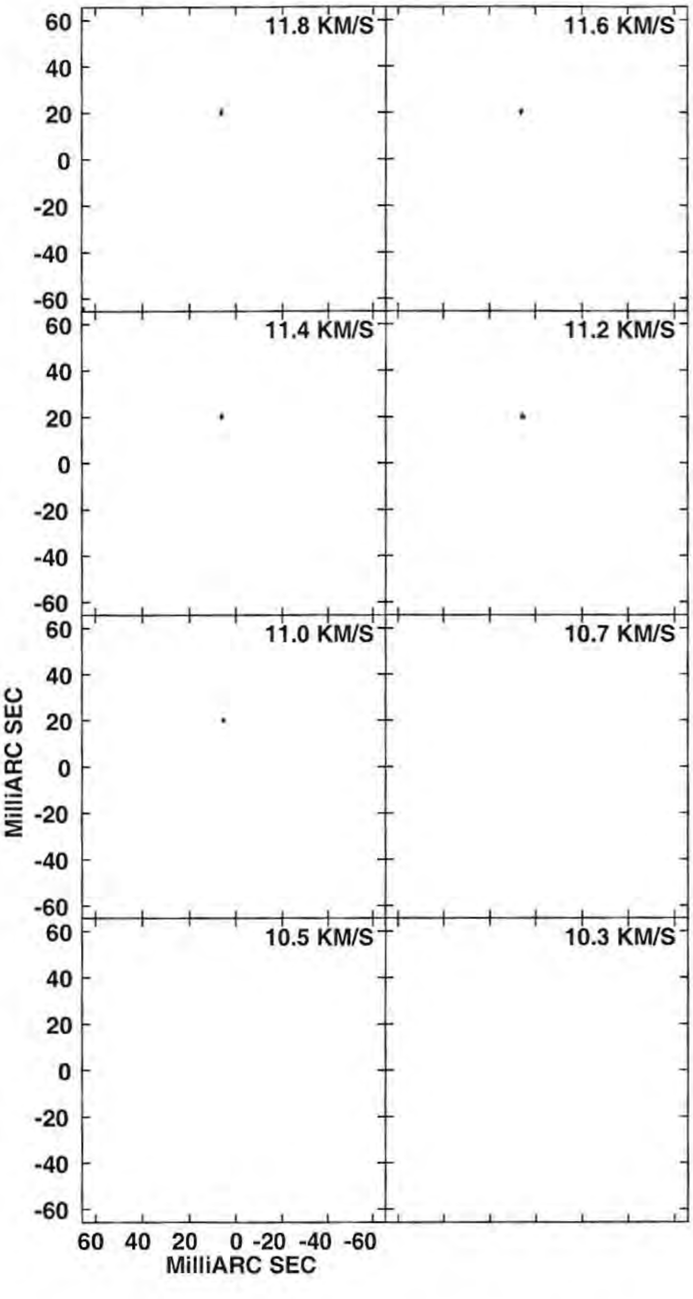

Figure C.12: A contour plot of the Stokes Q maser emission for channel maps 10.3 - 11.8 km.s^{-1}, as for Figure C.1.

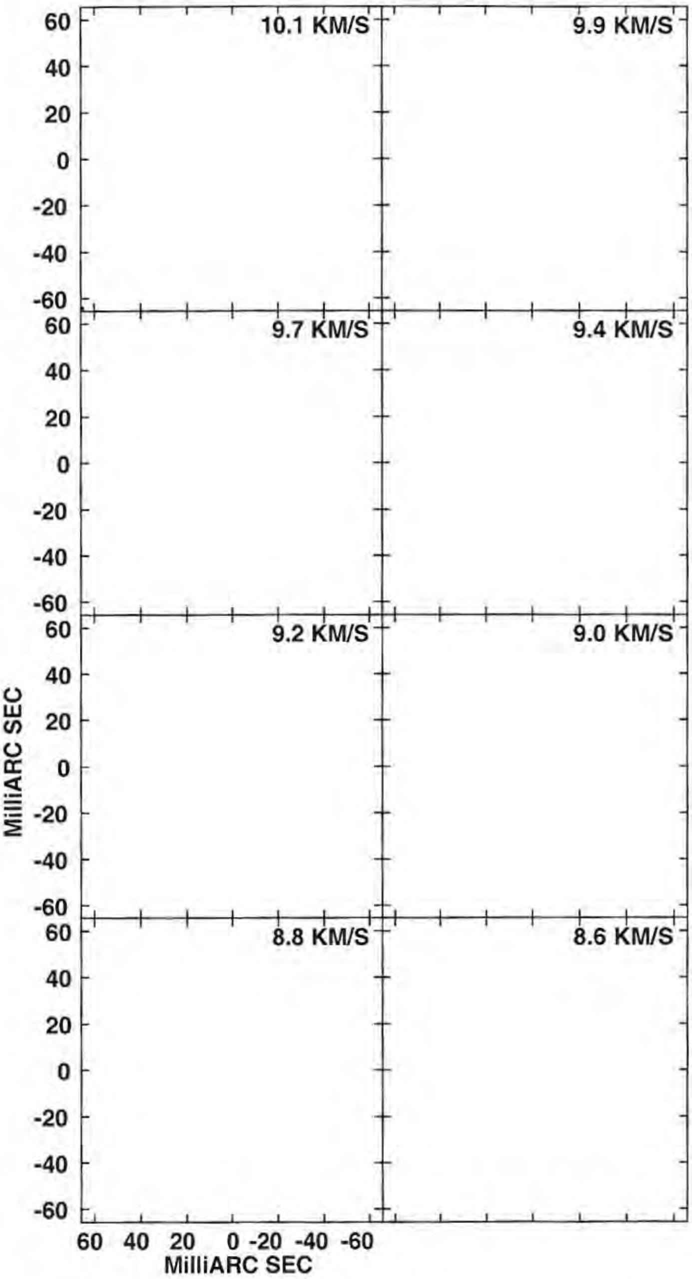

Figure C.13: A contour plot of the Stokes Q maser emission for channel maps 8.6 - 10.1 km.s^{-1}, as for Figure C.1.

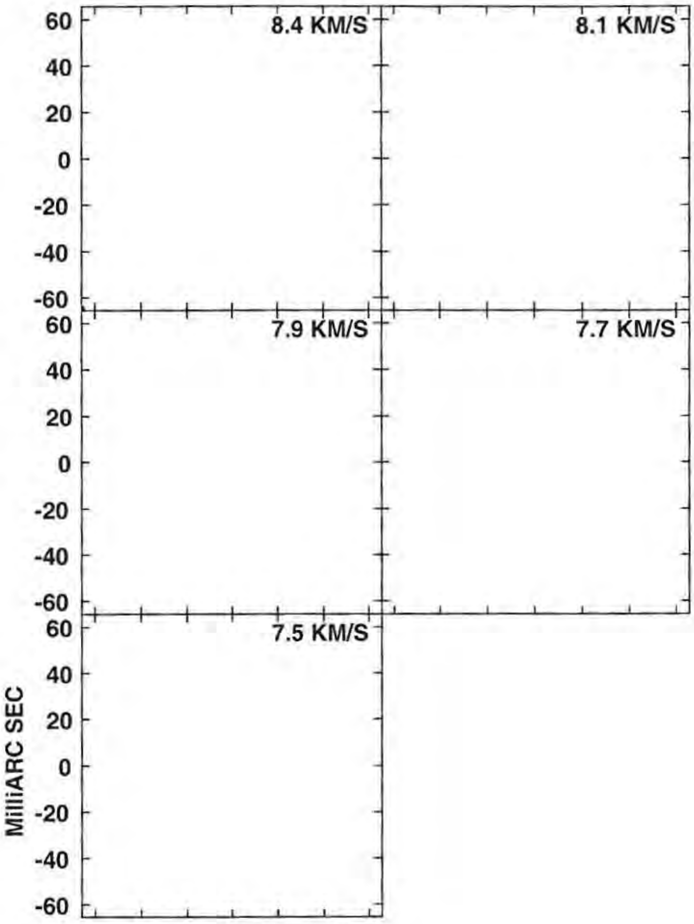

Figure C.14: A contour plot of the Stokes Q maser emission for channel maps 7.5 - 8.4 km.s^{-1}, as for Figure C.1.

Appendix D

Stokes U channel maps

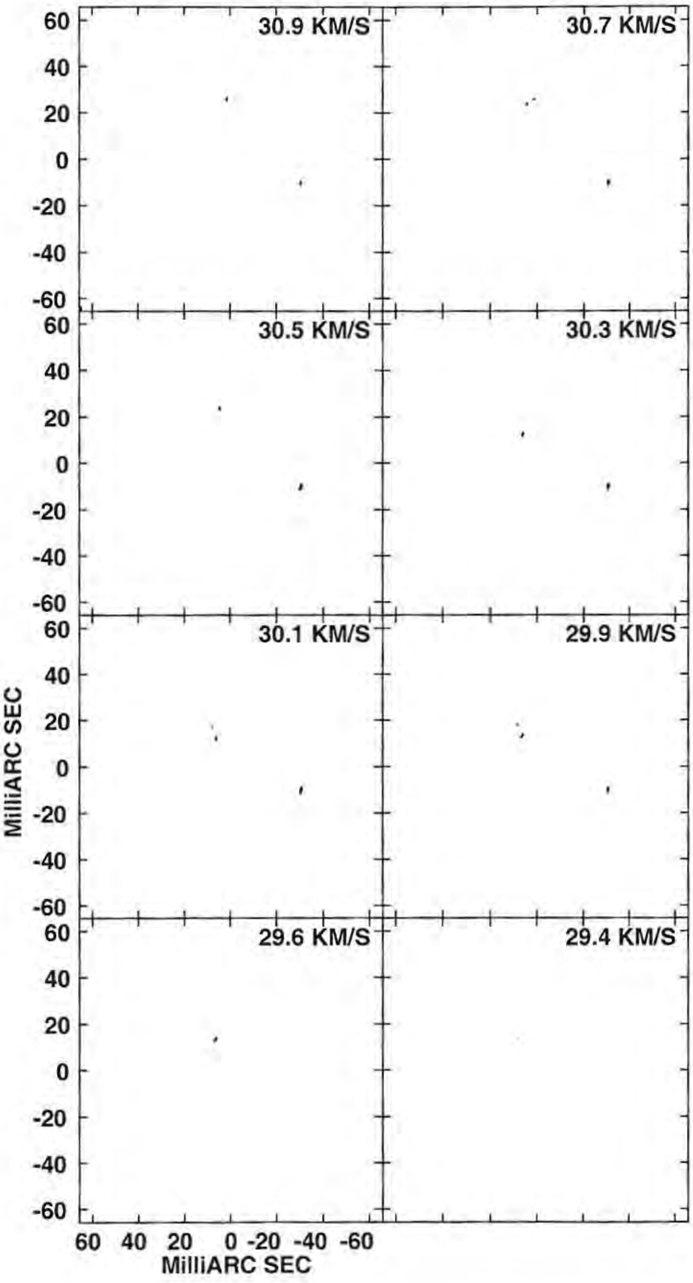

Figure D.1: A contour plot of the Stokes U maser emission for channel maps 29.4 - 30.9 km.s^{-1}. The contour levels are -100, -80, -60, -40, -15, -5, -1, 1, 5, 15, 40, 60, 80 and 100% of the absolute value of the peak flux density in the Stokes U cube, 75.699 Jy/beam.

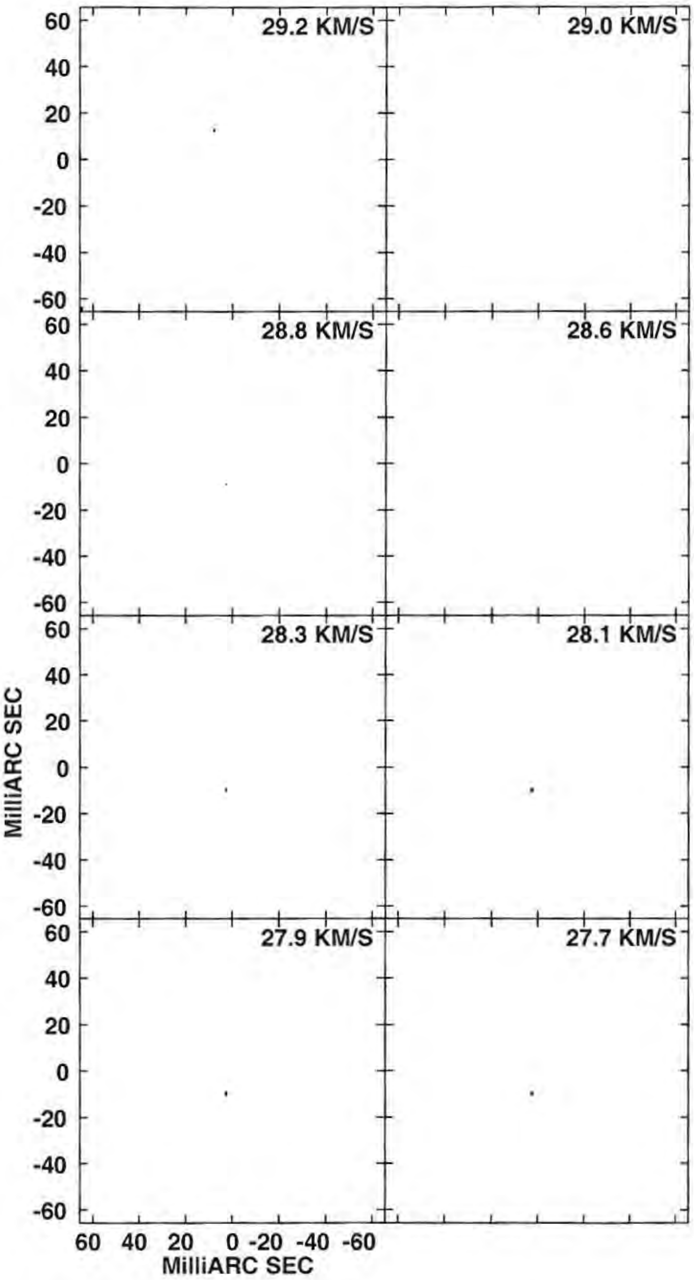

Figure D.2: A contour plot of the Stokes U maser emission for channel maps 27.7 - 29.2 km.s^{-1}, as for Figure D.1.

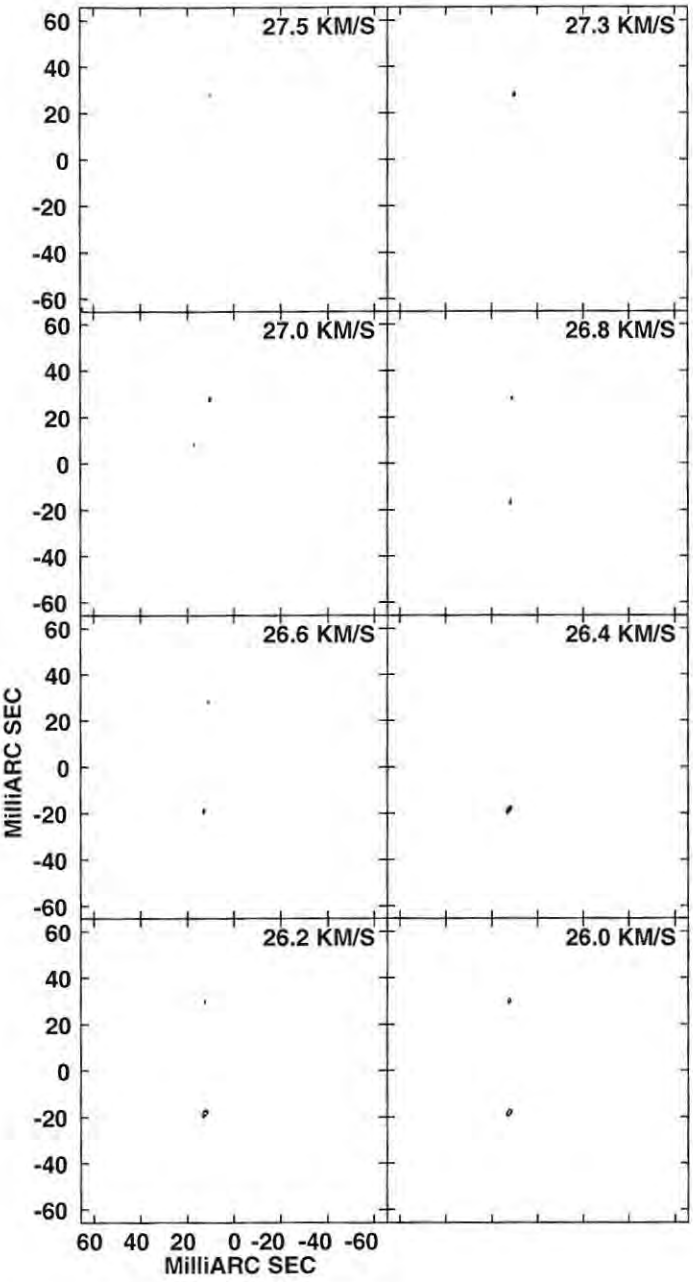

Figure D.3: A contour plot of the Stokes U maser emission for channel maps 26.0 - 27.5 km.s^{-1}, as for Figure D.1.

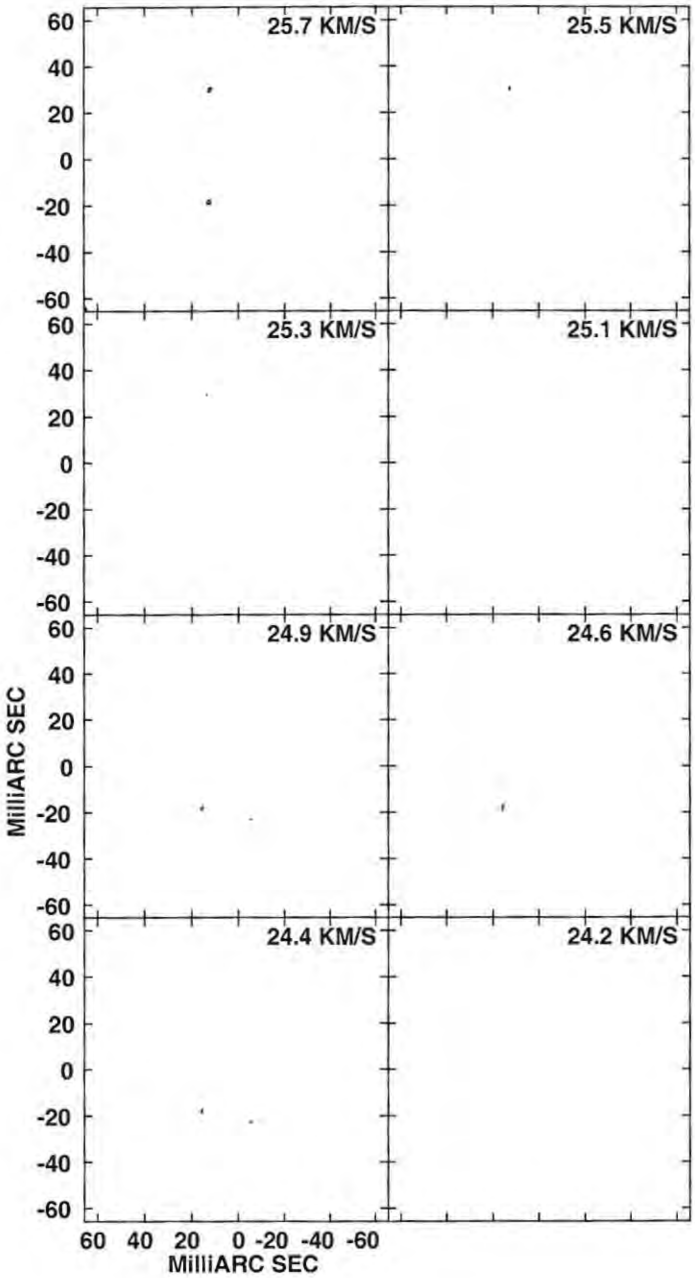

Figure D.4: A contour plot of the Stokes U maser emission for channel maps 24.2 - 25.7 km.s^{-1}, as for Figure D.1.

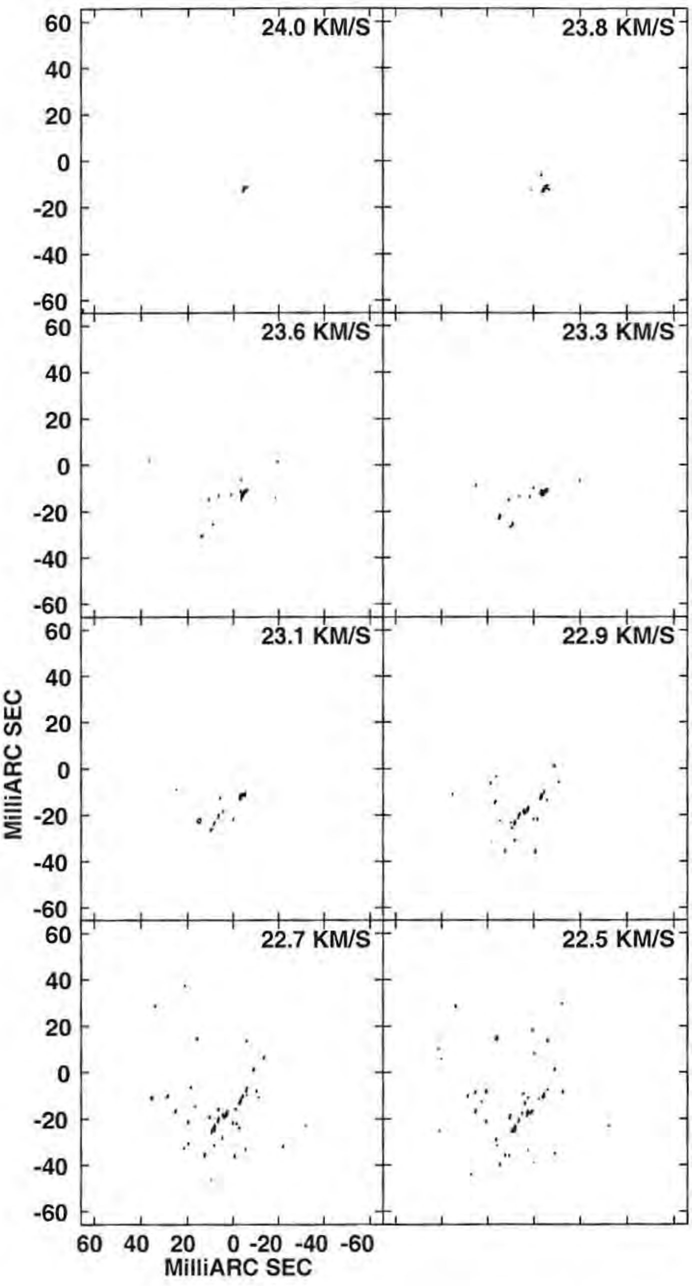

Figure D.5: A contour plot of the Stokes U maser emission for channel maps 22.5 - 24.0 km.s^{-1}, as for Figure D.1.

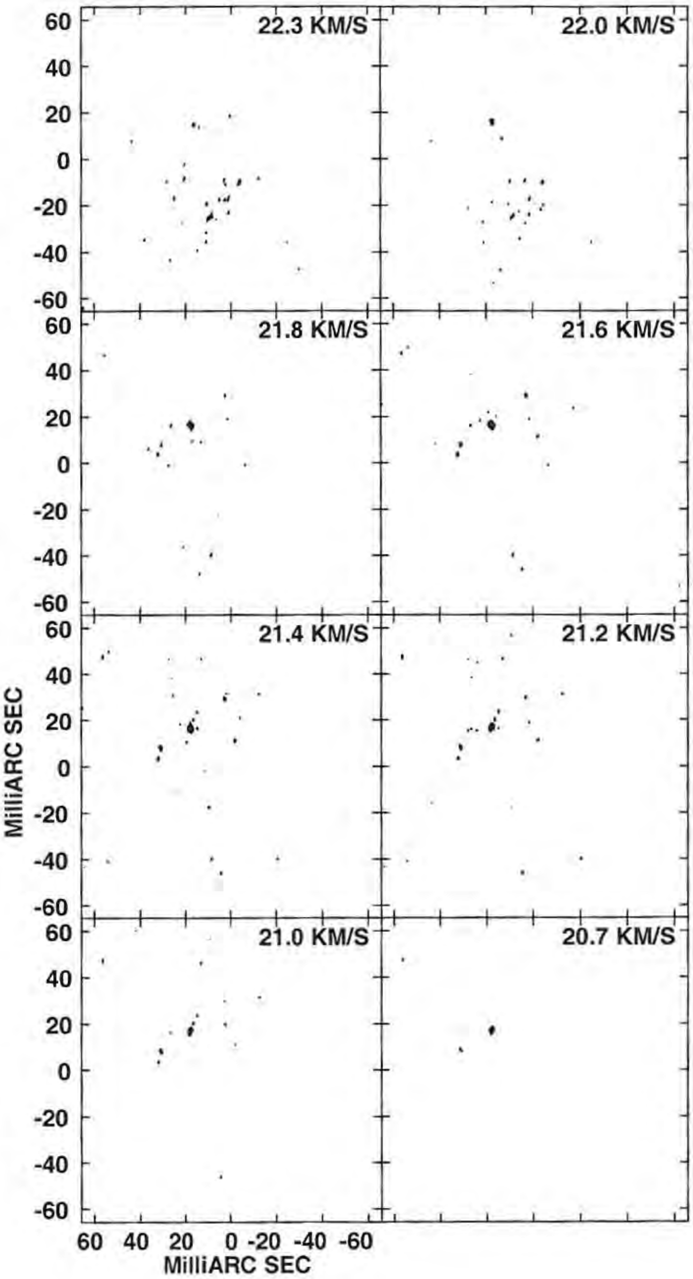

Figure D.6: A contour plot of the Stokes U maser emission for channel maps 20.7 - 22.3 km.s^{-1}, as for Figure D.1.

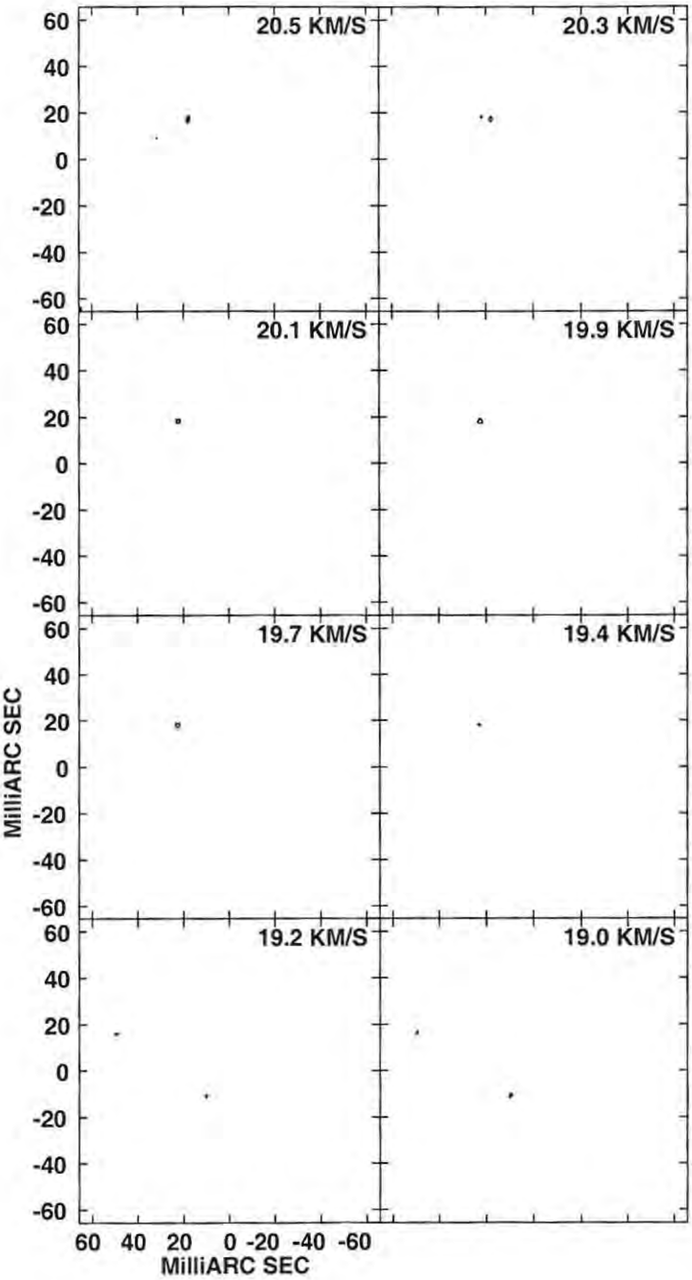

Figure D.7: A contour plot of the Stokes U maser emission for channel maps 19.0 - 20.5 km.s^{-1}, as for Figure D.1.

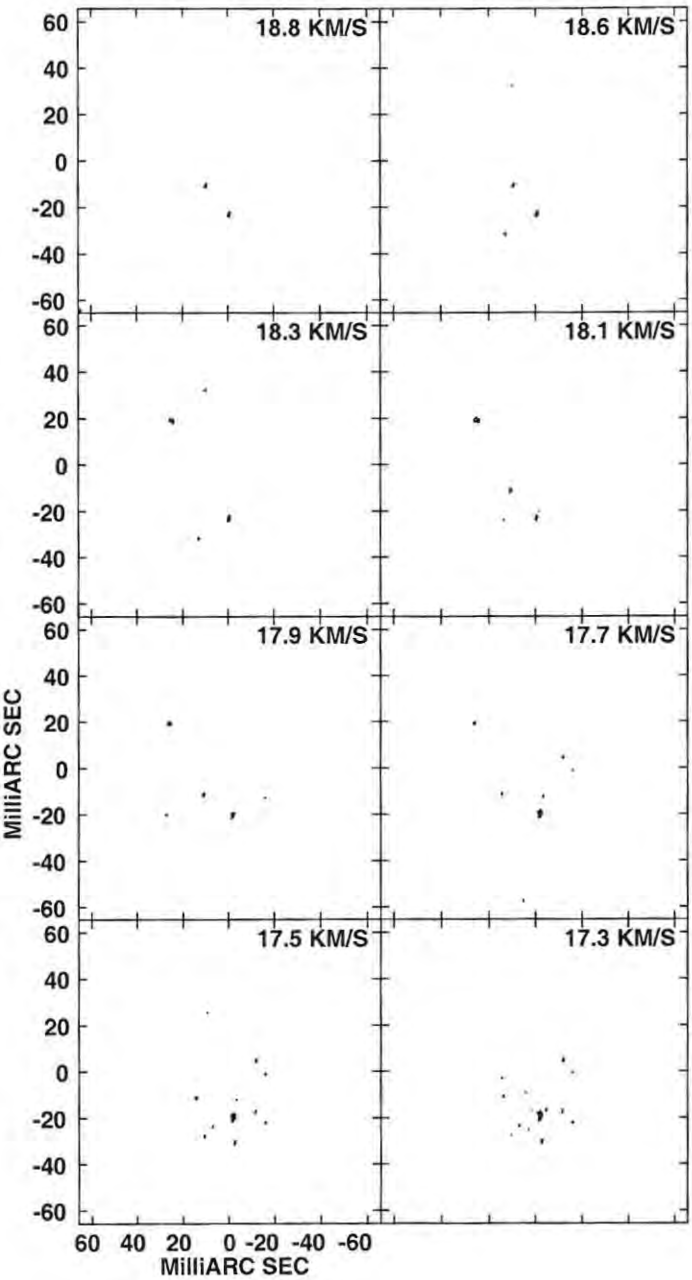

Figure D.8: A contour plot of the Stokes U maser emission for channel maps 17.3 - 18.8 km.s^{-1}, as for Figure D.1.

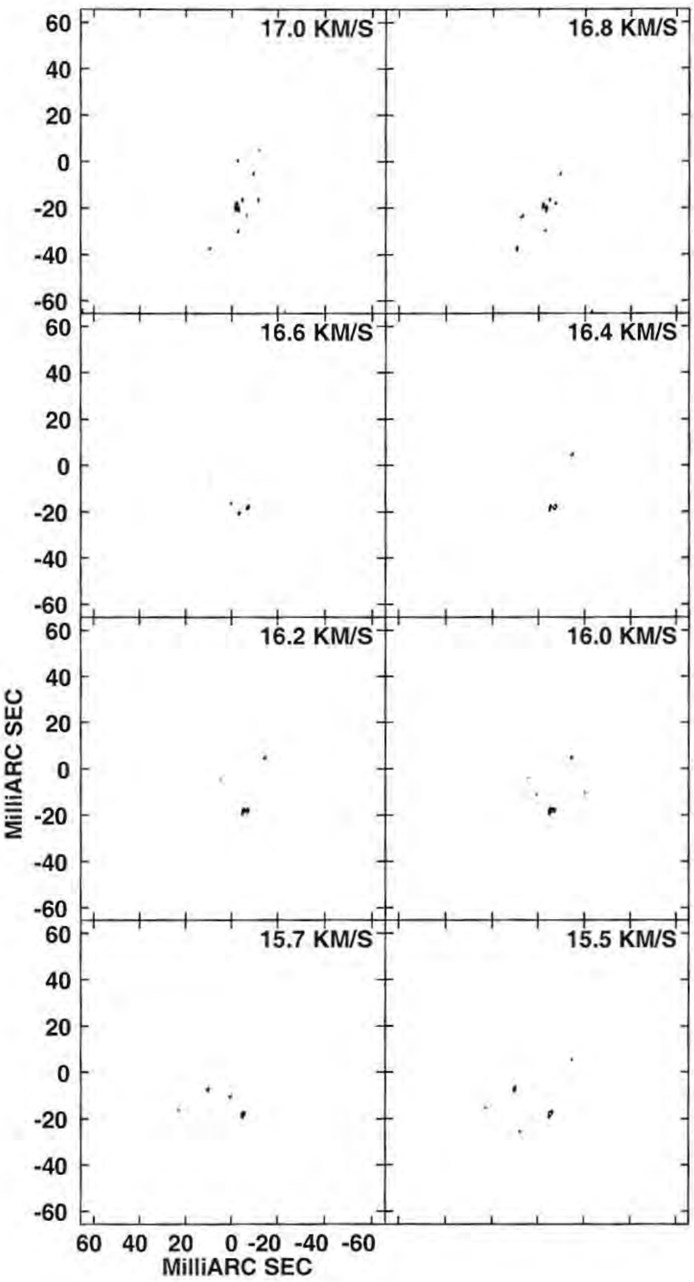

Figure D.9: A contour plot of the Stokes U maser emission for channel maps 15.5 - 17.0 km.s^{-1}, as for Figure D.1.

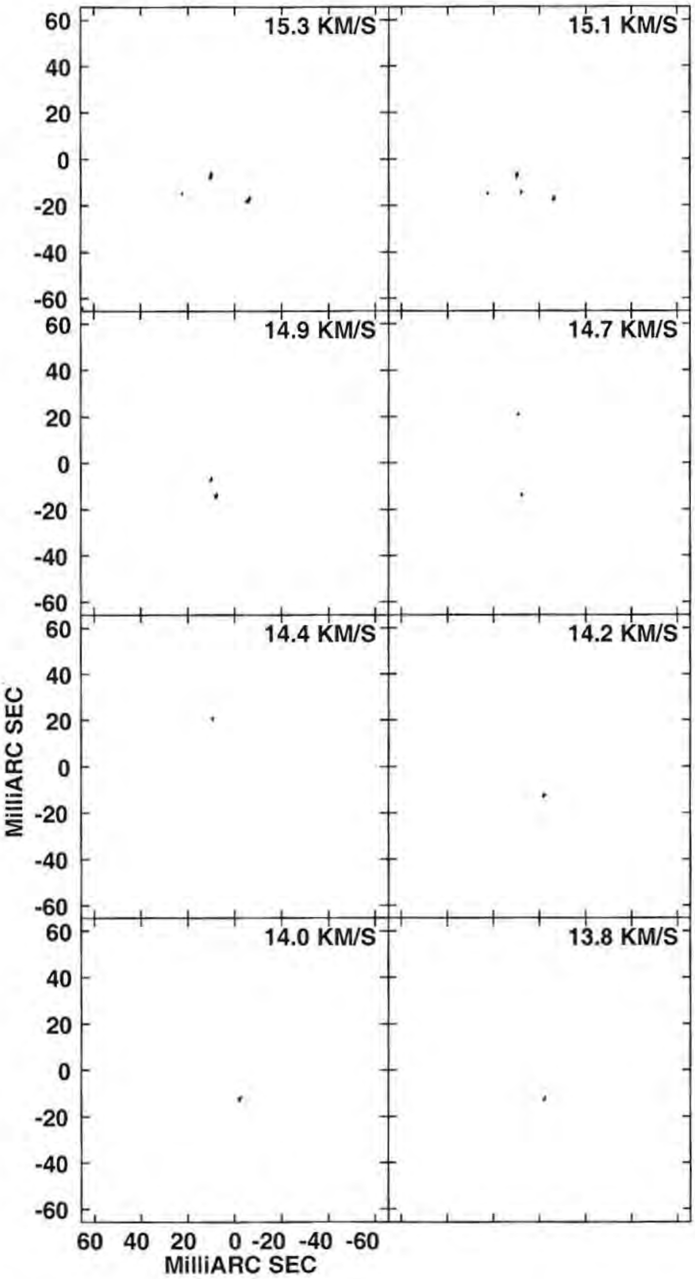

Figure D.10: A contour plot of the Stokes U maser emission for channel maps 13.8 - 15.3 km.s^{-1}, as for Figure D.1.

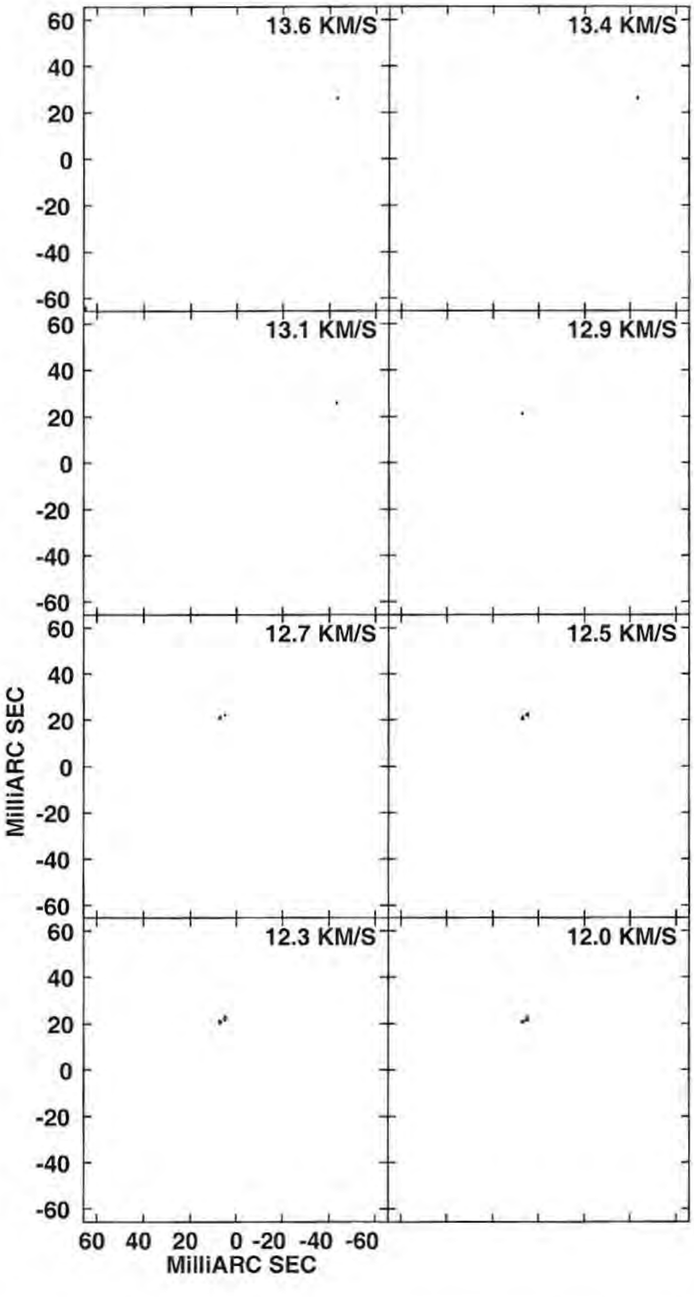

Figure D.11: A contour plot of the Stokes U maser emission for channel maps 12.0 - 13.6 km.s^{-1}, as for Figure D.1.

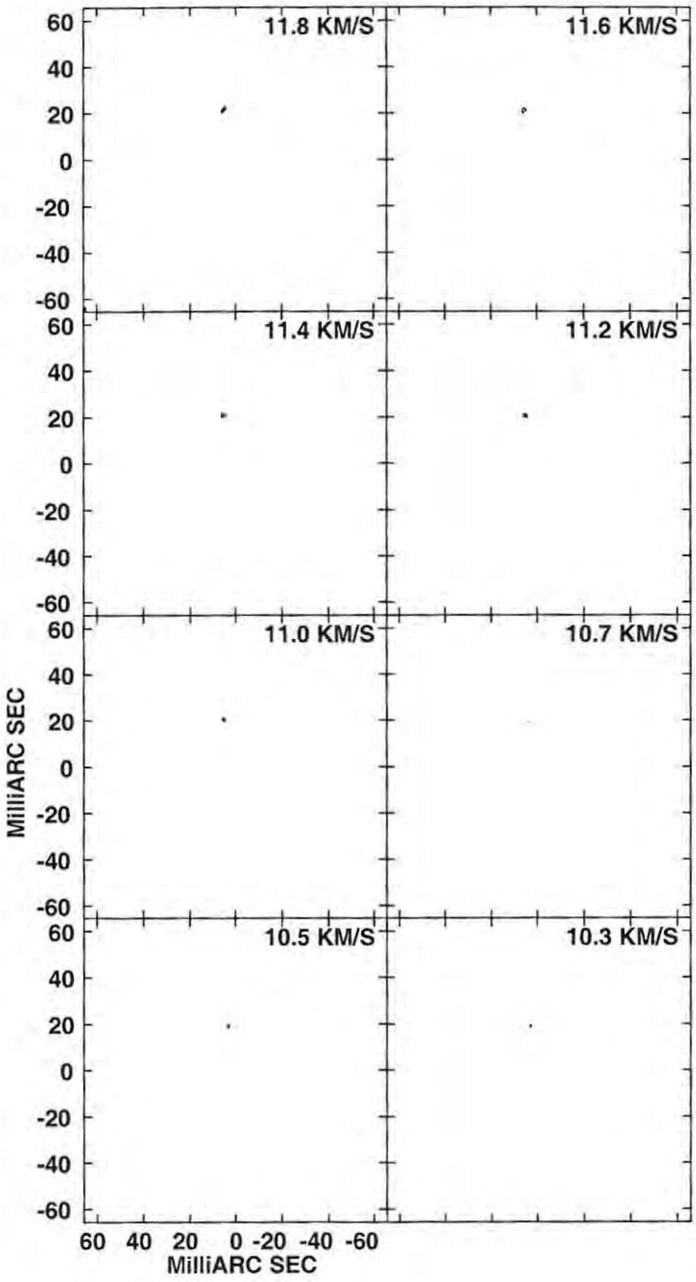

Figure D.12: A contour plot of the Stokes U maser emission for channel maps 10.3 - 11.8 km.s^{-1}, as for Figure D.1.

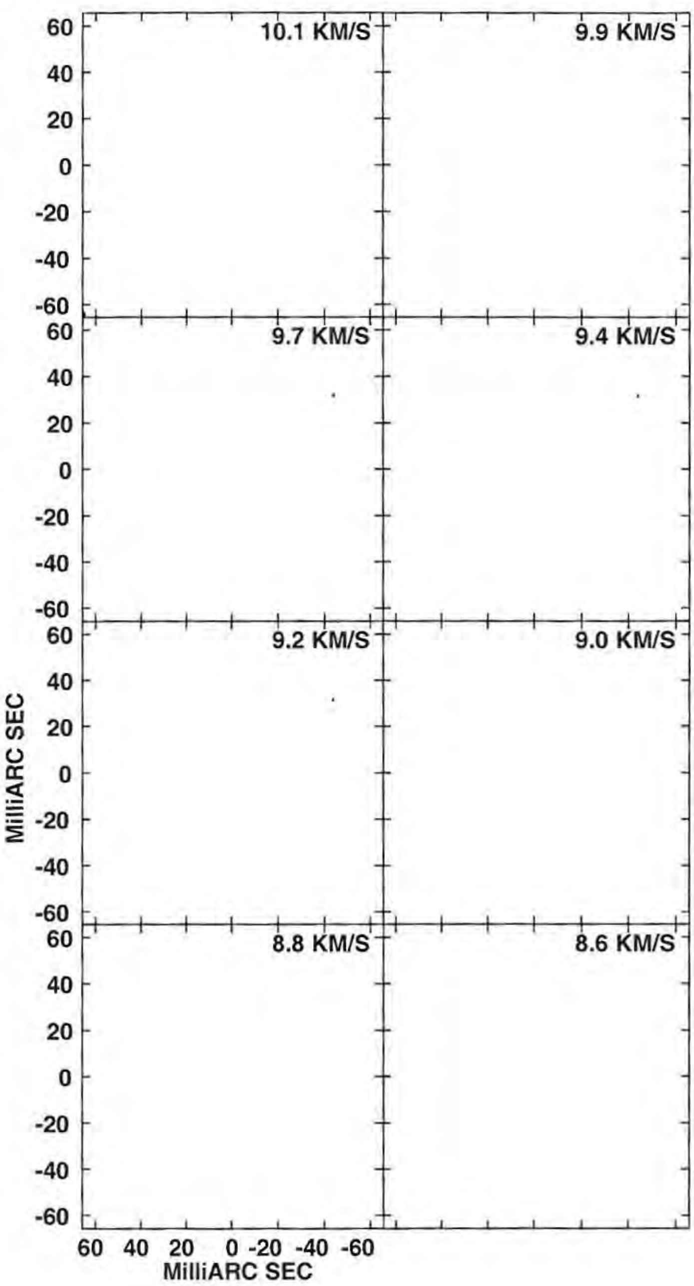

Figure D.13: A contour plot of the Stokes U maser emission for channel maps 8.6 - 10.1 km.s^{-1}, as for Figure D.1.

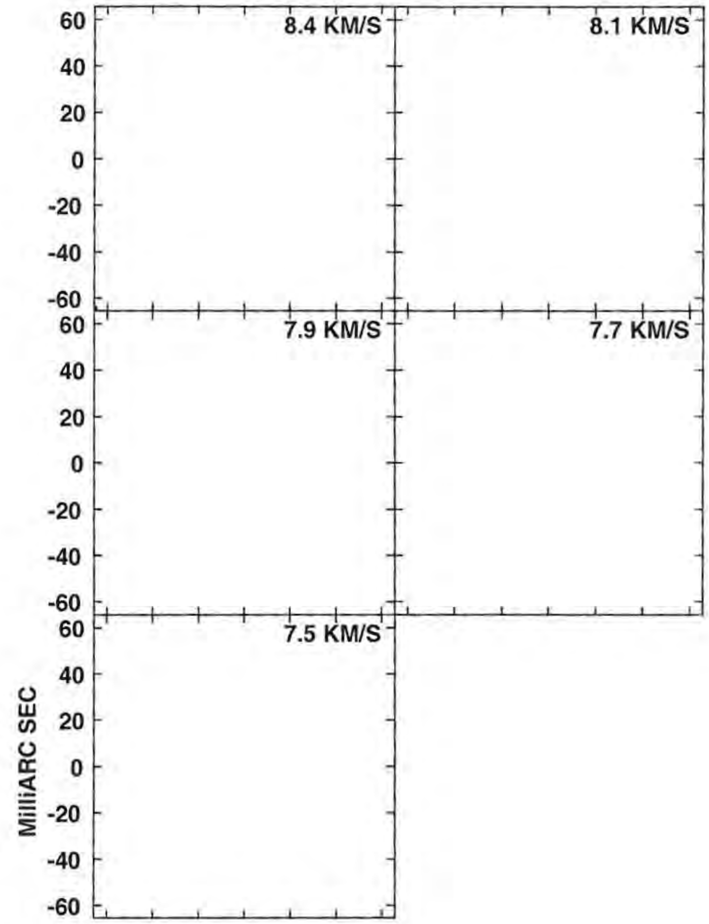

Figure D.14: A contour plot of the Stokes U maser emission for channel maps 7.5 - 8.4 km.s^{-1}, as for Figure D.1.

Appendix E

Stokes V channel maps

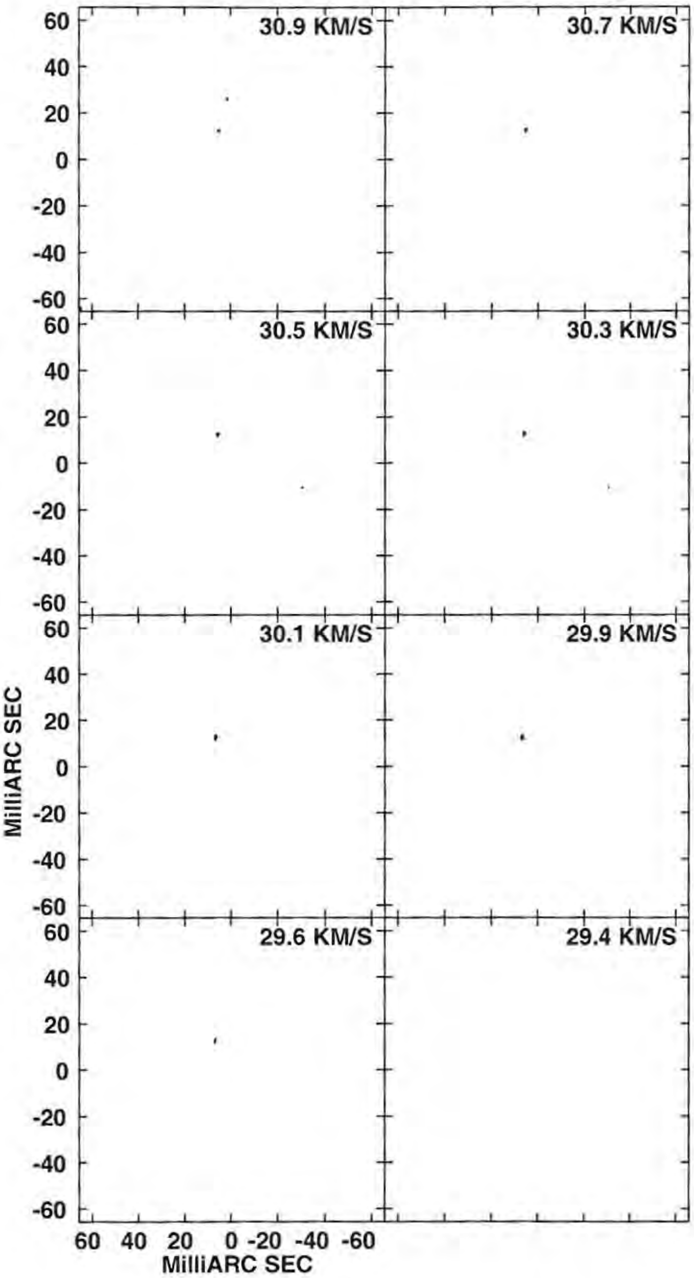

Figure E.1: A contour plot of the Stokes V maser emission for channel maps 29.4 - 30.9 km.s^{-1}. The contour levels are -100, -80, -60, -40, -15, -6, 6, 15, 40, 60, 80 and 100% of the absolute value of the peak flux density in the Stokes V cube, 10.694 Jy/beam.

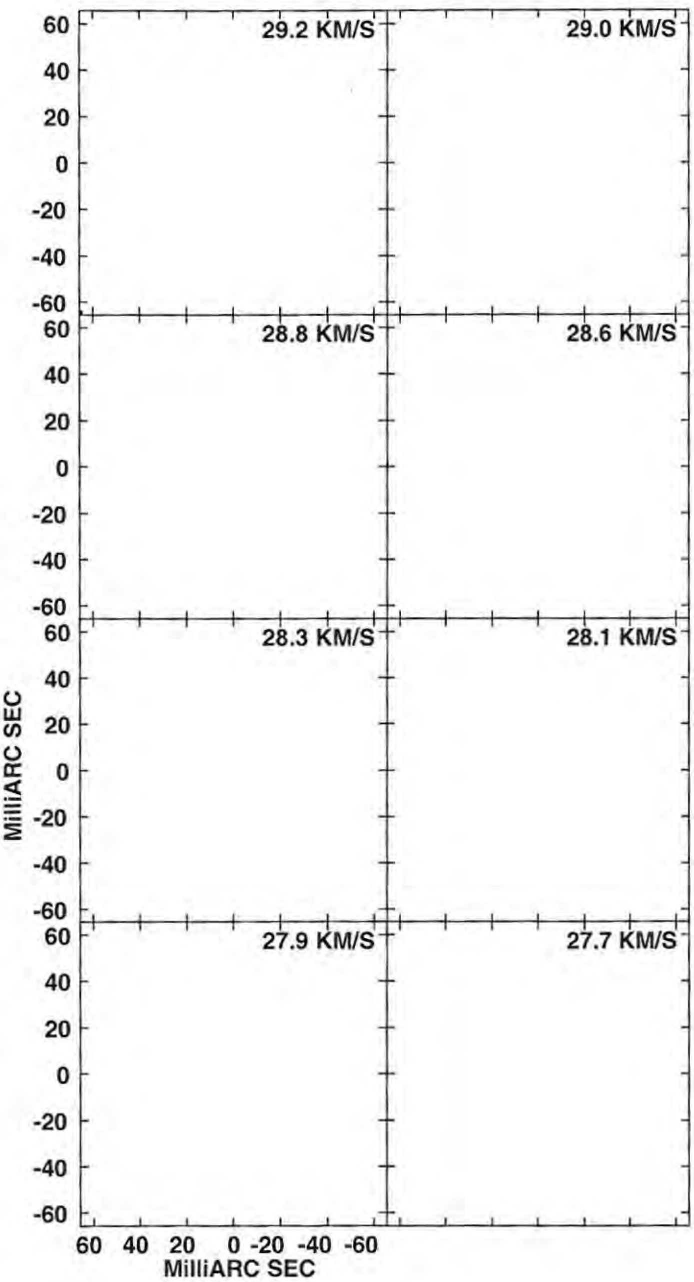

Figure E.2: A contour plot of the Stokes V maser emission for channel maps 27.7 - 29.2 km.s^{-1}, as for Figure E.1.

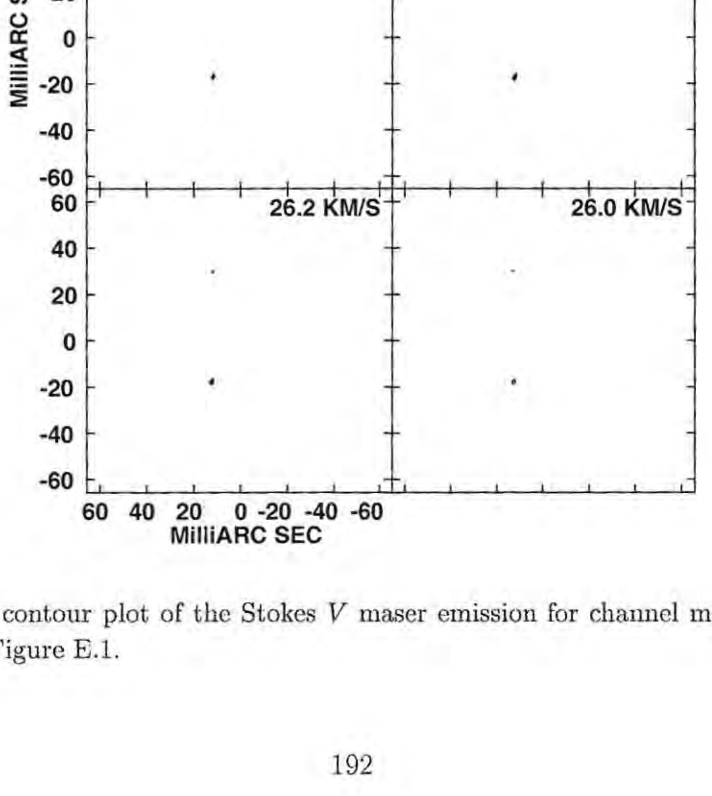

Figure E.3: A contour plot of the Stokes V maser emission for channel maps 26.0 - 27.5 km.s^{-1}, as for Figure E.1.

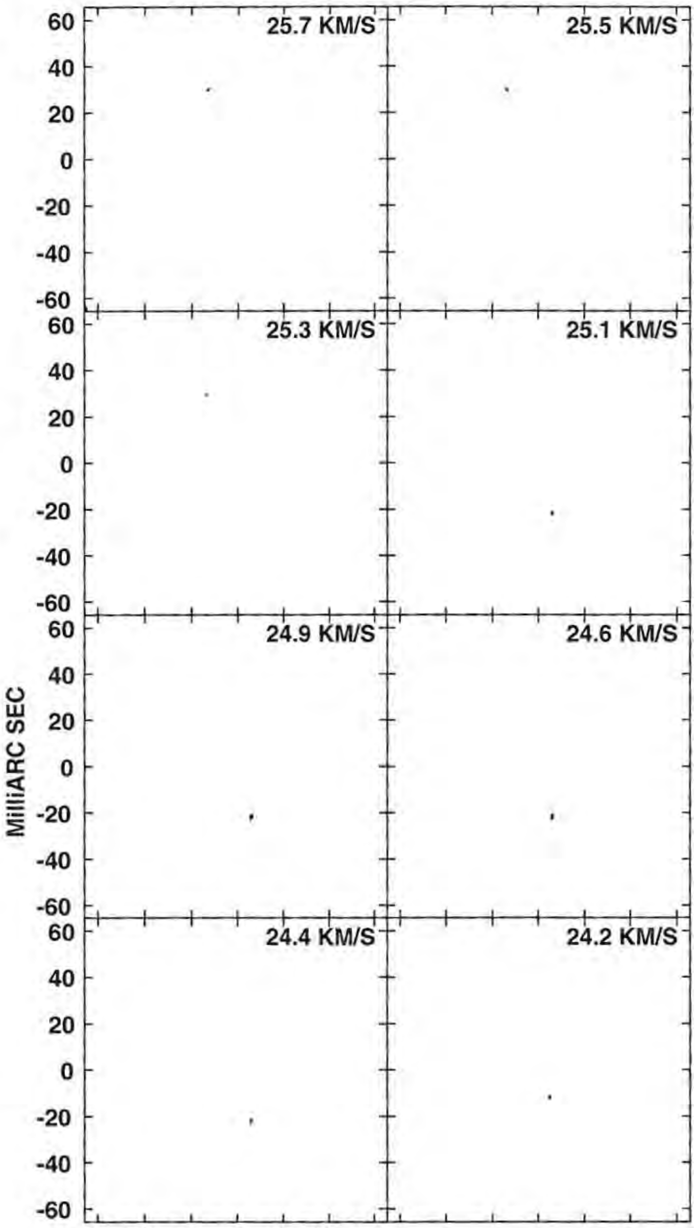

Figure E.4: A contour plot of the Stokes V maser emission for channel maps 24.2 - 25.7 km.s^{-1}, as for Figure E.1.

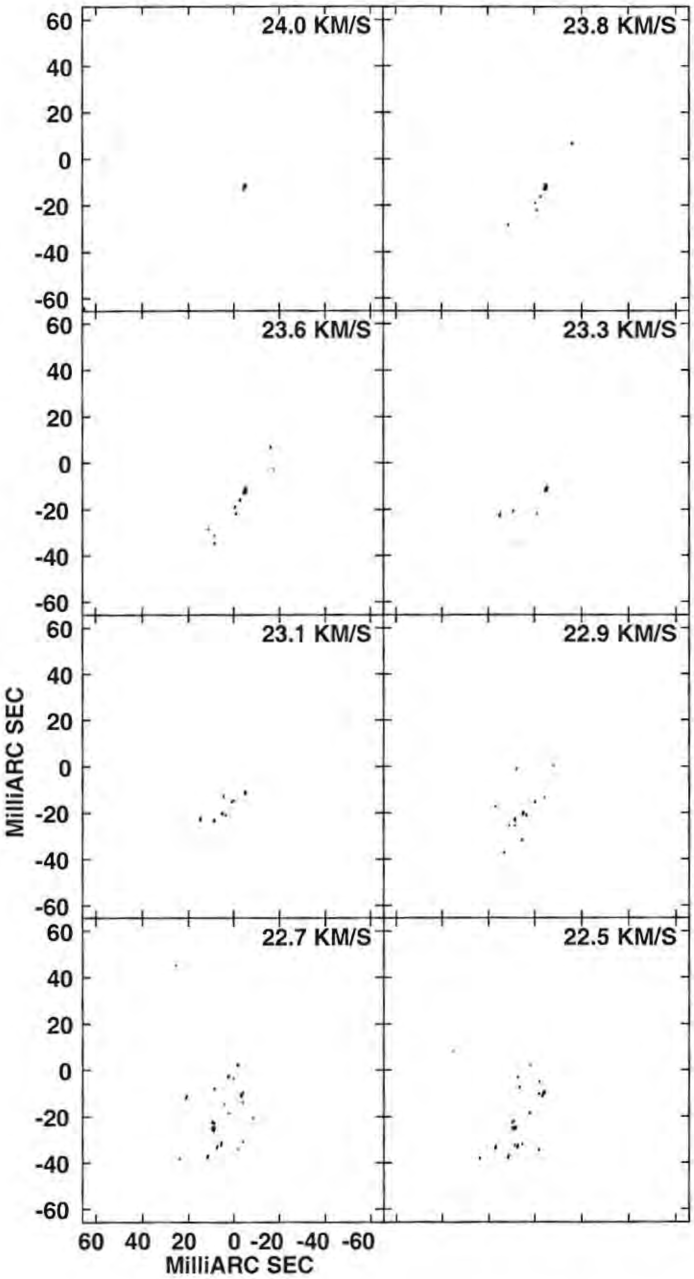

Figure E.5: A contour plot of the Stokes V maser emission for channel maps 22.5 - 24.0 km.s^{-1}, as for Figure E.1.

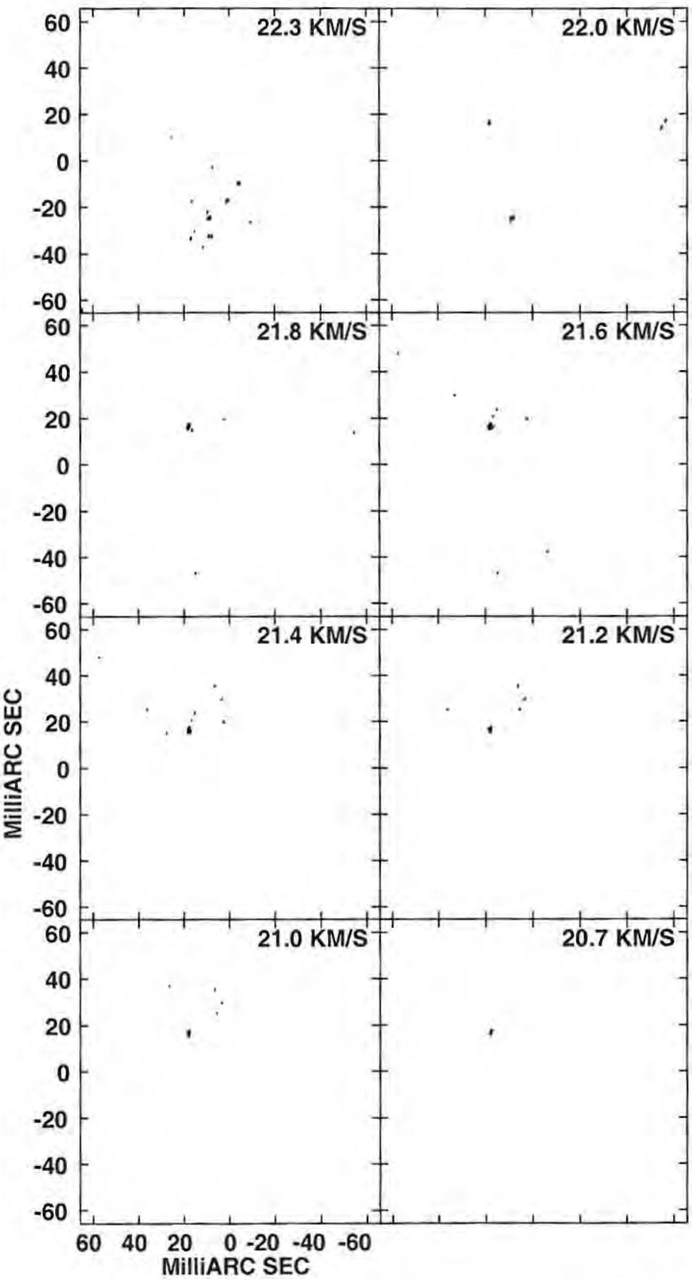

Figure E.6: A contour plot of the Stokes V maser emission for channel maps 20.7 - 22.3 km.s^{-1}, as for Figure E.1.

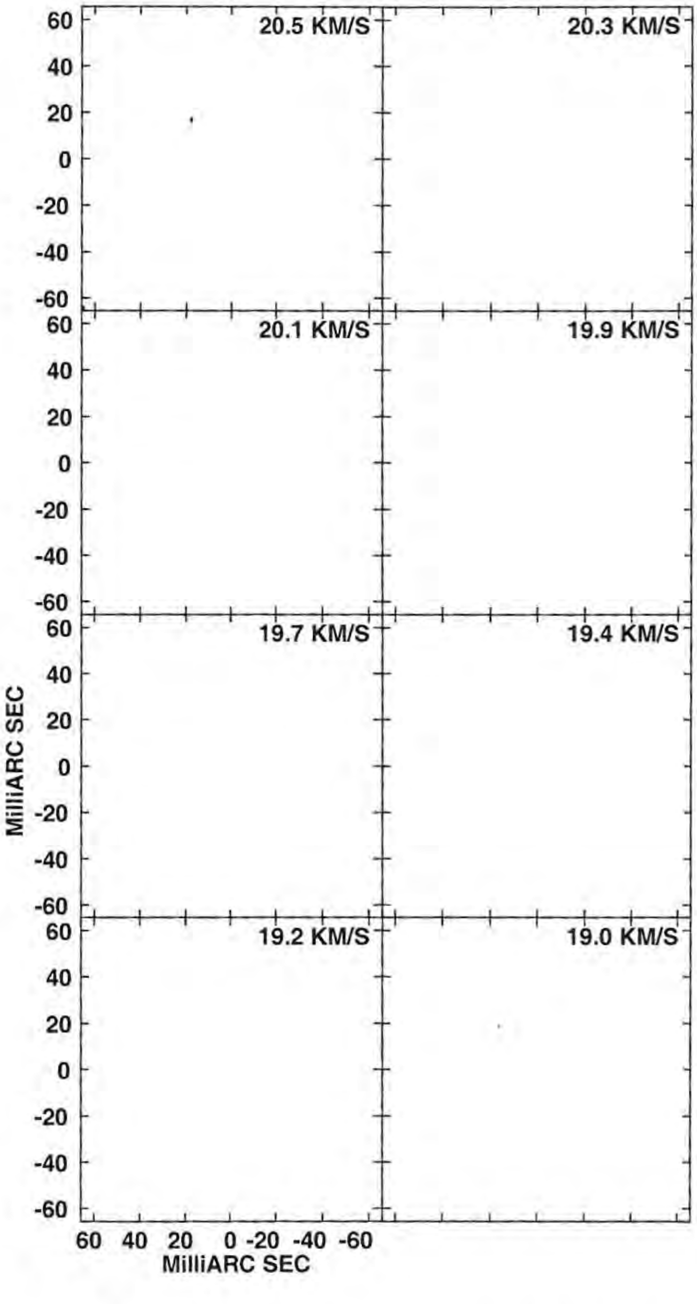

Figure E.7: A contour plot of the Stokes V maser emission for channel maps 19.0 - 20.5 km.s^{-1}, as for Figure E.1.

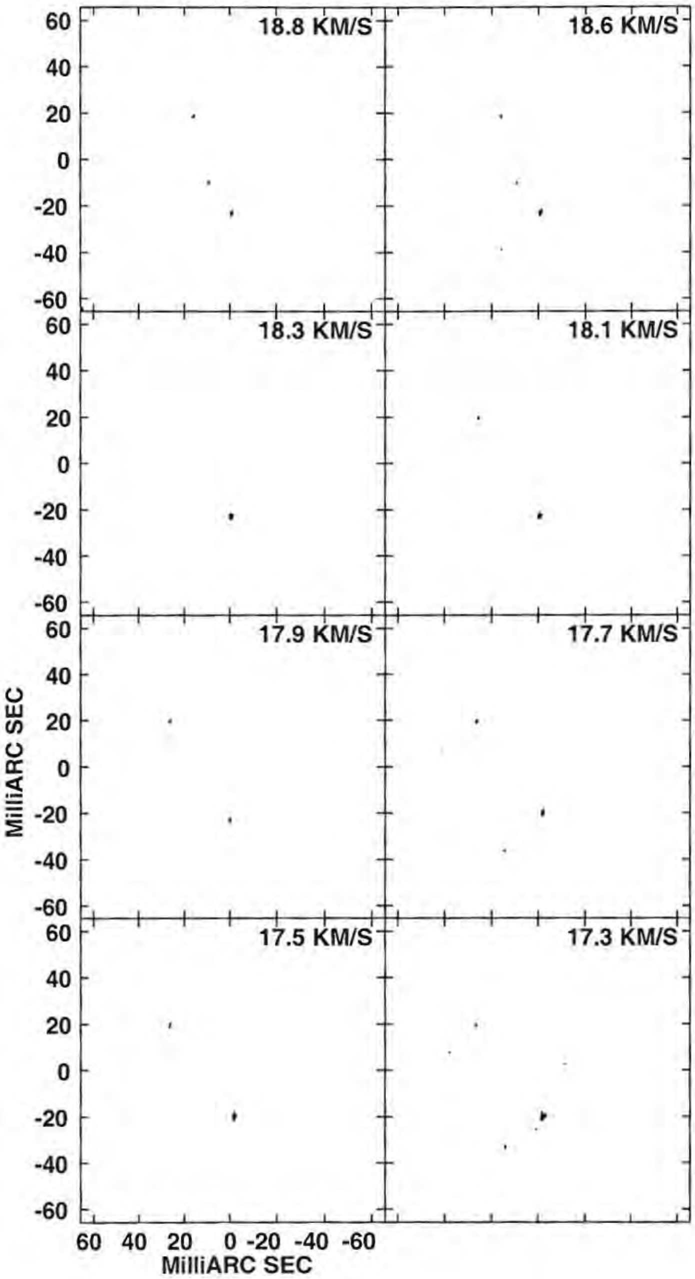

Figure E.8: A contour plot of the Stokes V maser emission for channel maps 17.3 - 18.8 km.s^{-1}, as for Figure E.1.

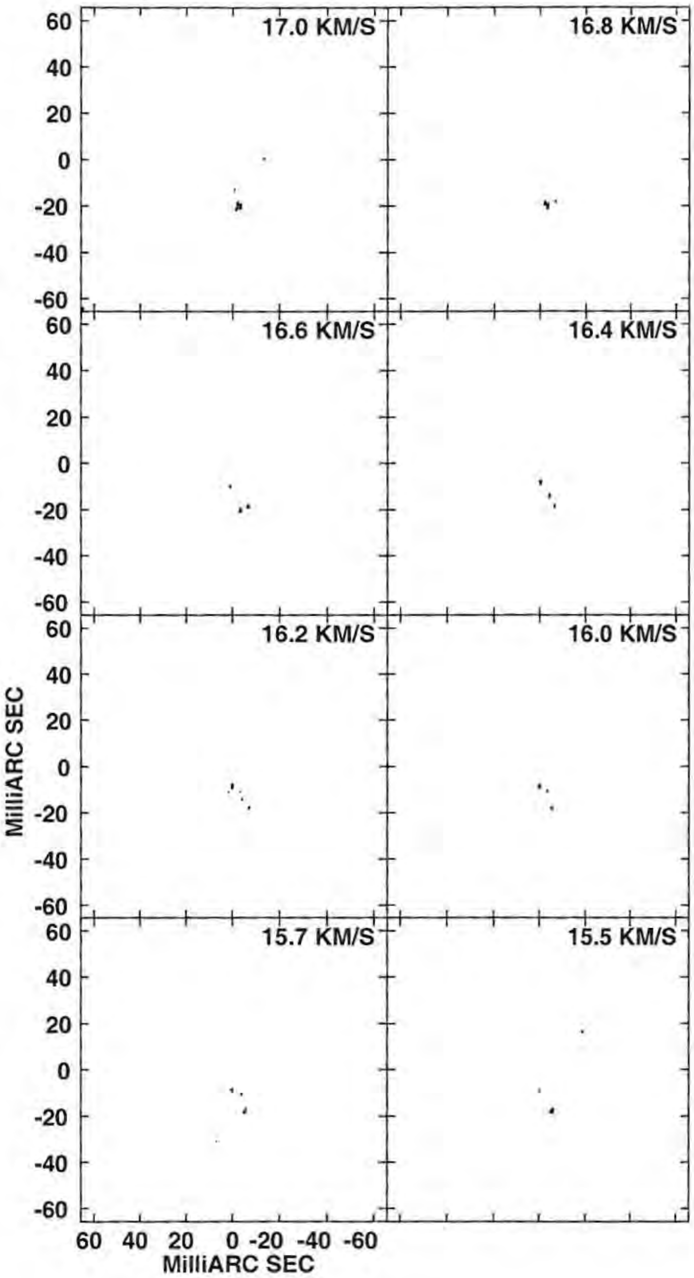

Figure E.9: A contour plot of the Stokes V maser emission for channel maps 15.5 - 17.0 km.s^{-1}, as for Figure E.1.

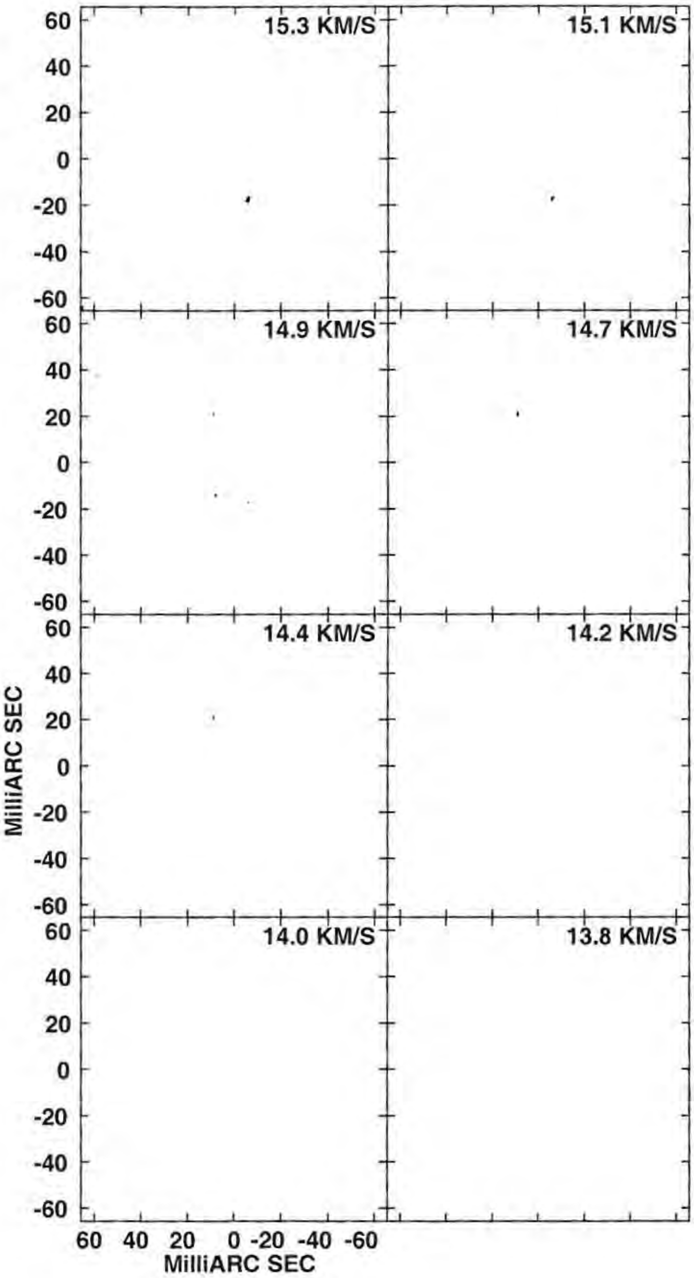

Figure E.10: A contour plot of the Stokes V maser emission for channel maps 13.8 - 15.3 km.s^{-1}, as for Figure E.1.

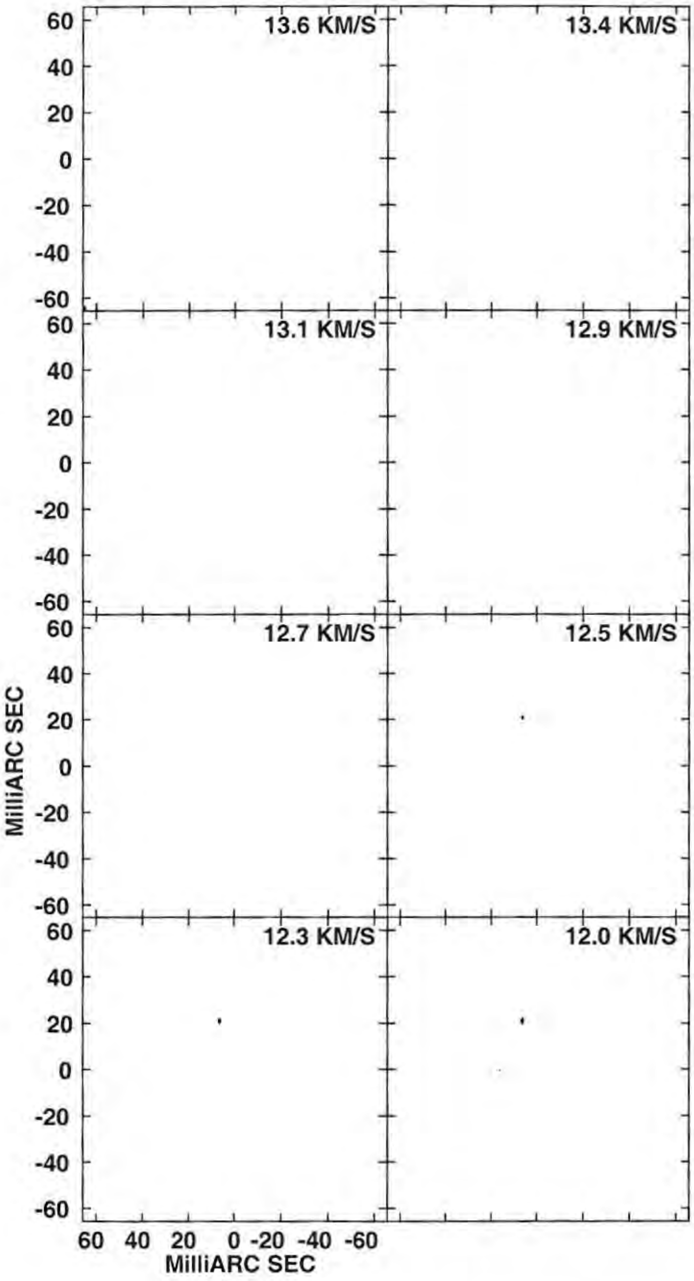

Figure E.11: A contour plot of the Stokes V maser emission for channel maps 12.0 - 13.6 km.s^{-1}, as for Figure E.1.

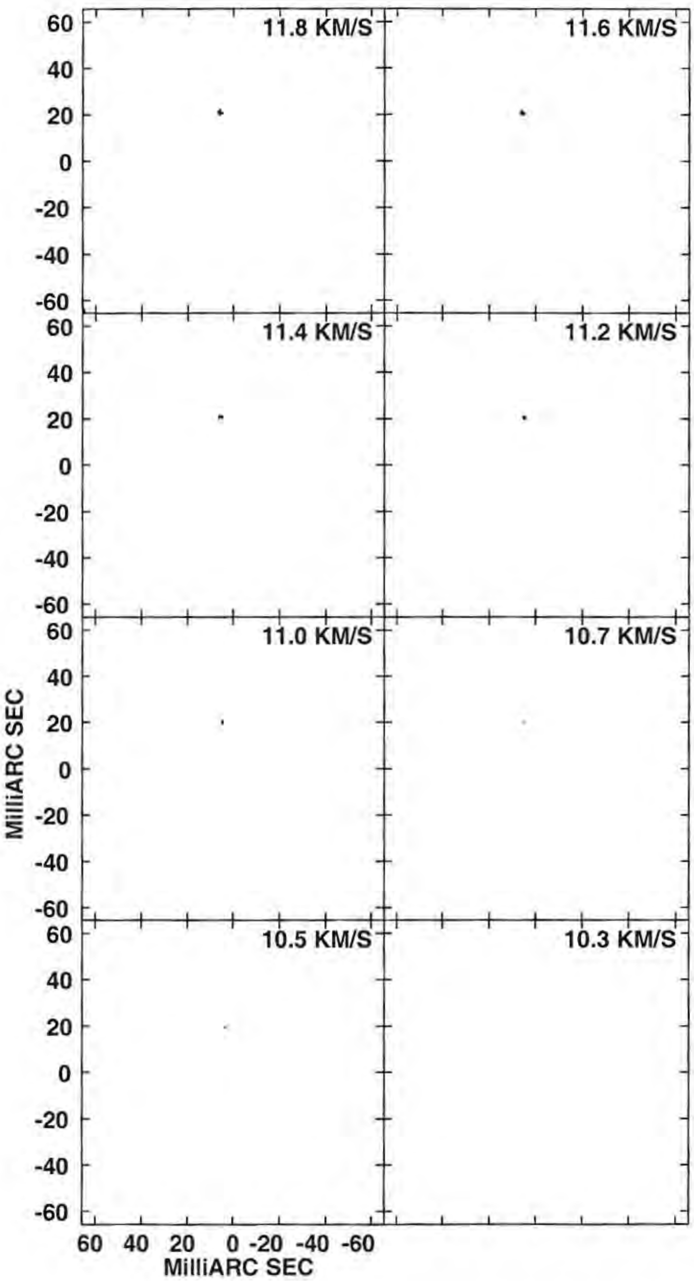

Figure E.12: A contour plot of the Stokes V maser emission for channel maps 10.3 - 11.8 $\mathrm{km.s}^{-1}$, as for Figure E.1.

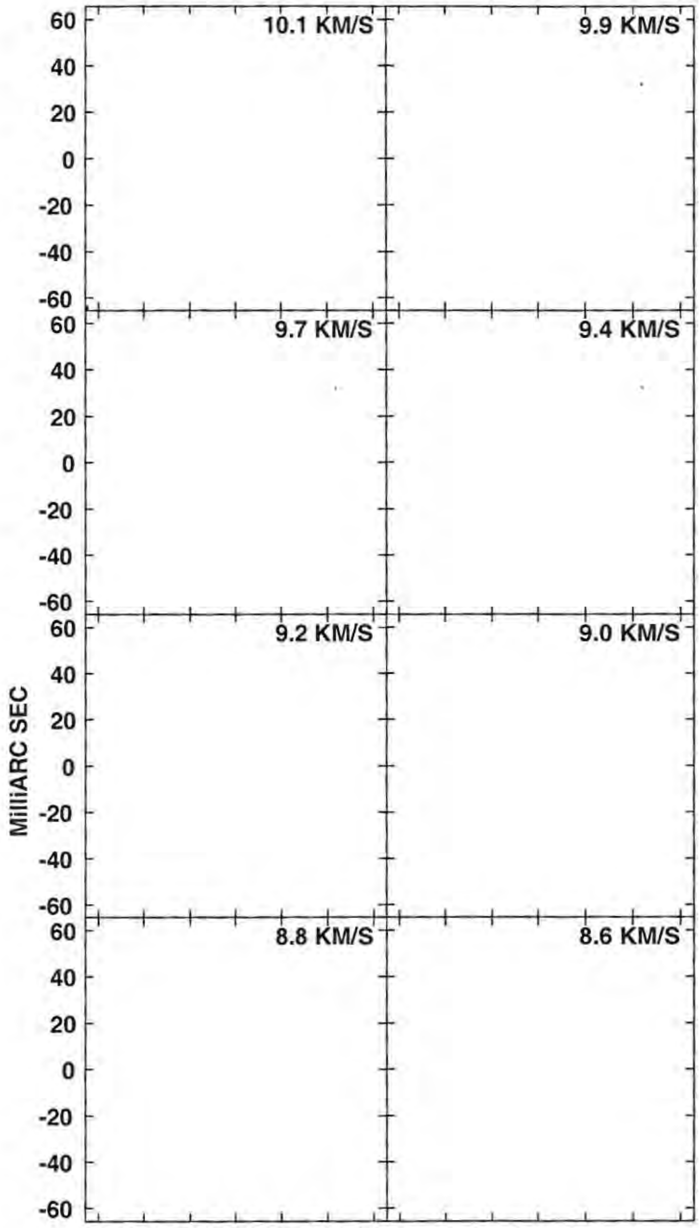

Figure E.13: A contour plot of the Stokes V maser emission for channel maps 8.6 - 10.1 km.s^{-1}, as for Figure E.1.

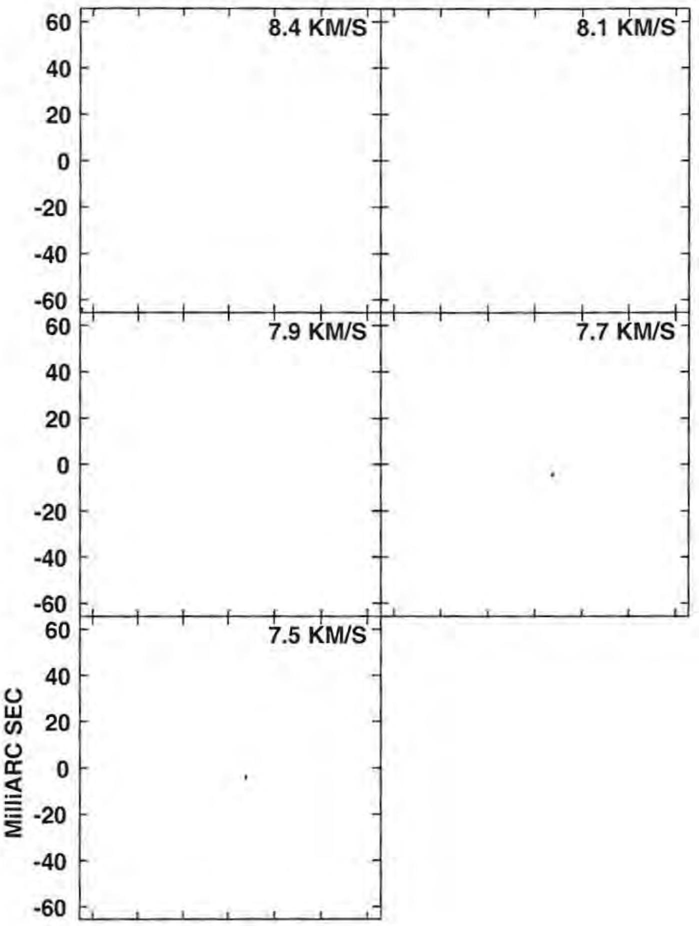

Figure E.14: A contour plot of the Stokes V maser emission for channel maps 7.5 - 8.4 km.s^{-1}, as for Figure E.1.

References

Alcolea, J., Bujarrabal, V., 1992, A&A, 253, 475

Alcolea, J., Bujarrabal, V., Gallego, J. D., 1989, A&A, 211, 187

Armandroff, T. E., Herbst, W., 1981, AJ, 86, 1923

Bachiller, R., Fuente, A., Bujarrabal, V., Colomer, F., Loup, C., Omont, A., de Jong, T., 1997, A&A, 319, 235

Barcia, A., Alcolea, J., Bujarrabal, V., 1989, A&A, 215, L9

Barvainis, R., 1984, ApJ, 279, 358

Barvainis, R., Deguchi, S., 1989, AJ, 97, 1089

Barvainis, R., Predmore, C. R., 1985, ApJ, 288, 694

Benson, J. M., Mutel, R. L., 1982, ApJ, 253, 199

Bieniek, R. J., Green, S., 1983, ApJ, 265, L29

Blackman, E. G., Frank, A., Markiel, J. A., Thomas, J. H., Van Horn, H. M., 2001, Nature, 409, 485

Boboltz, D. A., Diamond, P. J., Kemball, A. J., 1997, ApJ, 487, L147

Boboltz, D. A., Marvel, K. B., 2000, ApJ, 545, L149

Boboltz, D. A. J., 1997, Ph.D. Thesis

Born, M., Wolf, E., 1999, *Principles of Optics*, Cambridge University Press, seventh edition

Bowers, P. F., Claussen, M. J., Johnston, K. J., 1993, AJ, 105, 284

Bowers, P. F., Johnston, K. J., Spencer, J. H., 1981, Nature, 291, 382

Bowers, P. F., Johnston, K. J., Spencer, J. H., 1983, ApJ, 274, 733

Brown, L. F., Roberts, D. H., Wardle, J. F. C., 1989, AJ, 97, 1522

Bucher, I., 1991, `http://www.mathworks.com/matlabcentral/fileexchange/`

Buhl, D., Snyder, L. E., Lovas, F. J., Johnson, D. R., 1974, ApJ, 192, L97

Buhl, D., Snyder, L. E., Lovas, F. J., Johnson, D. R., 1975, ApJ, 201, L29

Bujarrabal, V., 1994, A&A, 285, 953

Bujarrabal, V., Alcolea, J., Sanchez Contreras, C., Colomer, F., 1996, A&A, 314, 883

Bujarrabal, V., Fuente, A., Omont, A., 1994, A&A, 285, 247

Bujarrabal, V., Nguyen-Q-Rieu, M., 1981, A&A, 102, 65

Cernicharo, J., Bujarrabal, V., 1992, ApJ, 401, L109

Cernicharo, J., Bujarrabal, V., Lucas, R., 1991, A&A, 249, L27

Cernicharo, J., Bujarrabal, V., Santaren, J. L., 1993, ApJ, 407, L33

Chapman, J. M., Cohen, R. J., 1986, MNRAS, 220, 513

Chiosi, C., Maeder, A., 1986, ARA&A, 24, 329

Cho, S., Chung, H., Kim, H., Oh, B., Lee, C., Han, S., 1998, ApJS, 115, 277

Cho, S., Ukita, N., 1998, AJ, 116, 2495

Cho, S.-H., Kaifu, N., Ukita, N., 1996, A&AS, 115, 117

Clark, B. G., 1980, A&A, 89, 377

Cohen, R. J., 1987, in I. Appenzeller and C. Jordan (eds.), *IAU Symp. 122: Circumstellar Matter*, p. 229, Kluwer

Condon, J. J., 1997, PASP, 109, 166

Conway, R. G., Kronberg, P. P., 1969, MNRAS, 142, 11

Cooke, B., Elitzur, M., 1985, ApJ, 295, 175

Cornwell, T., 1995, in J. A. Zensus, P. J. Diamond, and P. J. Napier (eds.), *ASP Conf. Ser. 82: Very Long Baseline Interferometry and the VLBA*, p. 39, Astronomical Society of the Pacific

Cotton, W. D., 1993, AJ, 106, 1241

Cotton, W. D., Geldzahler, B. J., Marcaide, J. M., Shapiro, I. I., Sanroma, M., Rius, A., 1984, ApJ, 286, 503

Cotton, W. D., Mennesson, B., Diamond, P. J., Perrin, G., Coudé du Foresto, V., Chagnon, G., van Langevelde, H. J., Ridgway, S., Waters, R., Vlemmings, W., Morel, S., Traub, W., Carleton, N., Lacasse, M., 2004, A&A, 414, 275

Cox, G. G., Parker, E. A., 1979, MNRAS, 186, 197

Cruzalebes, P., Lopez, B., Bester, M., Gendron, E., Sams, B., 1998, A&A, 338, 132

D'Addario, L. R., 1986, in R. A. Perley, F. R. Schwab, and A. H. Bridle (eds.), *Synthesis Imaging*, p. 31, NRAO

Danchi, W. C., Bester, M., Degiacomi, C. G., Greenhill, L. J., Townes, C. H., 1994, AJ, 107, 1469

de Jager, C., 1980, *The Brightest Stars*, D. Reidel Publishing Company

Deguchi, S., 1977, PASJ, 29, 669

Deguchi, S., Good, J., Fan, Y., Mao, X., Wang, D., Ukita, N., 1983, ApJ, 264, L65

Deguchi, S., Iguchi, T., 1976, PASJ, 28, 307

Desmurs, J. F., Bujarrabal, V., Colomer, F., Alcolea, J., 2000, A&A, 360, 189

Desmurs, J.-F., Soria-Ruiz, R., Colomer, F., Marvel, K. B., Bujarrabal, V., Alcolea, J., Diamond, P. J., Boboltz, D., Kemball, A. J., 2002, in E. Ros, R. W. Porcas, A. P. Lobanov, and J. A. Zensus (eds.), *Proceedings of the 6th EVN Symposium*, p. 221, Max-Planck-Institut fuer Radioastronomie (Bonn)

Diamond, P. J., 1995, in J. A. Zensus, P. J. Diamond, and P. J. Napier (eds.), *ASP Conf. Ser. 82: Very Long Baseline Interferometry and the VLBA*, p. 227, Astronomical Society of the Pacific

Diamond, P. J., Johnston, K. J., Chapman, J. M., Lane, A. P., Bowers, P. F., Spencer, J. H., Booth, R. S., 1987, A&A, 174, 95

Diamond, P. J., Kemball, A. J., 2003, ApJ, 599, 1372

Diamond, P. J., Kemball, A. J., Junor, W., Zensus, A., Benson, J., Dhawan, V., 1994, ApJ, 430, L61

Doel, R. C., Gray, M. D., Humphreys, E. M. L., Braithwaite, M. F., Field, D., 1995, A&A, 302, 797

Doeleman, S. S., Lonsdale, C. J., Greenhill, L. J., 1998, ApJ, 494, 400

Dorch, S. B. F., 2004, A&A, 423, 1101

Dyck, H. M., Forrest, W. J., Gillett, F. C., Stein, W. A., Gehrz, R. D., Woolf, N. J., Shawl, S. J., 1971, ApJ, 165, 57

Efstathiou, A., Rowan-Robinson, M., 1990, MNRAS, 245, 275

Elitzur, M., 1980, ApJ, 240, 553

Elitzur, M., 1991, ApJ, 370, 407

Elitzur, M., 1992, *Astronomical Masers*, Kluwer Academic Publishers

Elitzur, M., 1993, ApJ, 416, 256

Elitzur, M., 1996, ApJ, 457, 415

Elitzur, M., 1998, ApJ, 504, 390

Feast, M. W., 1970, The Observatory, 90, 24

Fomalont, E. B., Perley, R. A., 1989, in R. A. Perley, F. R. Schwab, and A. H. Bridle (eds.), *ASP Conf. Ser. 6: Synthesis Imaging in Radio Astronomy*, p. 83, Astronomical Society of the Pacific

Forbes, F. F., 1971, ApJ, 165, L83

Fransson, C., Chevalier, R. A., Filippenko, A. V., Leibundgut, B., Barth, A. J., Fesen, R. A., Kirshner, R. P., Leonard, D. C., Li, W., Lundqvist, P., Sollerman, J., Van Dyk, S. D., 2002, ApJ, 572, 350

Garcia-Barreto, J. A., Burke, B. F., Reid, M. J., Moran, J. M., Haschick, A. D., Schilizzi, R. T., 1988, ApJ, 326, 954

García-Segura, G., López, J. A., Franco, J., 2003, in S. J. Arthur and W. J. Henney (eds.), *Revista Mexicana de Astronomia y Astrofisica Conference Series*, p. 12

Geballe, T. R., Lacy, J. H., Beck, S. C., 1979, ApJ, 230, L47

Geballe, T. R., Townes, C. H., 1974, ApJ, 191, L37

Gehrels, T., 1972, ApJ, 173, L23

Gehrz, R. D., 1972, ApJ, 178, 715

Gillett, F. C., Stein, W. A., Solomon, P. M., 1970, ApJ, 160, L173

Glenn, J., Jewell, P. R., Fourre, R., Miaja, L., 2003, ApJ, 588, 478

Gomez Balboa, A. M., Lepine, J. R. D., 1986, A&A, 159, 166

Gonzalez-Alfonso, E., Alcolea, J., Cernicharo, J., 1996, A&A, 313, L13

Gonzalez-Alfonso, E., Cernicharo, J., 1997, A&A, 322, 938

Gray, M. D., Humphreys, E. M. L., Yates, J. A., 1999, MNRAS, 304, 906

Greenhill, L. J., Colomer, F., Moran, J. M., Backer, D. C., Danchi, W. C., Bester, M., 1995, ApJ, 449, 365

Greisen, E. (ed.), 2004, *AIPS Cookbook*

Högbom, J. A., 1974, A&AS, 15, 417

Habing, H. J., 1996, A&A Rev., 7, 97

Harwit, M., Bergin, E. A., 2002, ApJ, 565, L105

Harwit, M., Malfait, K., Decin, L., Waelkens, C., Feuchtgruber, H., Melnick, G. J., 2001, ApJ, 557, 844

Hashimoto, J., Maihara, T., Okuda, H., Sato, S., 1970, PASJ, 22, 335

Herbig, G. H., 1972, ApJ, 172, 375

Herbig, G. H., Zappala, R. R., 1970, ApJ, 162, L15

Herman, J., Habing, H. J., 1985, A&AS, 59, 523

Hollis, J. M., Pedelty, J. A., Forster, J. R., White, S. M., Boboltz, D. A., Alcolea, J., 2000, ApJ, 543, L81

Humphreys, E. M. L., Gray, M. D., Yates, J. A., Field, D., 1997, MNRAS, 287, 663

Humphreys, E. M. L., Gray, M. D., Yates, J. A., Field, D., Bowen, G., Diamond, P. J., 1996, MNRAS, 282, 1359

Humphreys, E. M. L., Gray, M. D., Yates, J. A., Field, D., Bowen, G. H., Diamond, P. J., 2002, A&A, 386, 256

Humphreys, R. M., 1974, ApJ, 188, 75

Humphreys, R. M., Davidson, K., Ruch, G., Wallerstein, G., 2005, AJ, 129, 492

Hyland, A. R., Becklin, E. E., Frogel, J. A., Neugebauer, G., 1972, A&A, 16, 204

Hyland, A. R., Becklin, E. E., Neugebauer, G., Wallerstein, G., 1969, ApJ, 158, 619

Iben, I., Renzini, A., 1983, ARA&A, 21, 271

Imai, H., Sasao, T., Kameya, O., Miyoshi, M., Shibata, K. M., Asaki, Y., Omodaka, T., Morimoto, M., Mochizuki, N., Suzuyama, T., Iguchi, S., Kameno, S., Jike, T., Iwadate, K., Sakai, S., Miyaji, T., Kawaguchi, N., Miyazawa, K., 1997, A&A, 317, L67

Jewell, P. R., Dickinson, D. F., Snyder, L. E., Clemens, D. P., 1987, ApJ, 323, 749

Joy, A. H., 1942, ApJ, 96, 344

Jura, M., Kleinmann, S. G., 1990, ApJS, 73, 769

Kastner, J. H., Weintraub, D. A., 1998, AJ, 115, 1592

Kemball, A. J., 1992, Ph.D. Thesis

Kemball, A. J., 1999, in G. B. Taylor, C. L. Carilli, and R. A. Perley (eds.), *ASP Conf. Ser. 180: Synthesis Imaging in Radio Astronomy II*, p. 499, Astronomical Society of the Pacific

Kemball, A. J., Diamond, P. J., 1997, ApJ, 481, L111

Kemball, A. J., Diamond, P. J., Cotton, W. D., 1995, A&AS, 110, 383

Kemball, A. J., Diamond, P. J., Pauliny-Toth, I. I. K., 1996, ApJ, 464, L55

Kemper, F., Stark, R., Justtanont, K., de Koter, A., Tielens, A. G. G. M., Waters, L. B. F. M., Cami, J., Dijkstra, C., 2003, A&A, 407, 609

Knapp, G. R., Bowers, P. F., Young, K., Phillips, T. G., 1995, ApJ, 455, 293

Knapp, G. R., Morris, M., 1985, ApJ, 292, 640

Knowles, S. H., Batchelor, R. A., 1978, MNRAS, 184, 107

Knowles, S. H., Mayer, C. H., Cheung, A. C., Rank, D. M., Townes, C. H., 1969, Science, 163, 1055

Kogan, L., 1996, AIPS Memo Series, 92

Kukarkin, B. V., Kholopov, P. N., Pskovsky, Y. P., Efremov, Y. N., Kukarkina, N. P., Kurochkin, N. E., Medvedeva, G. I., 1971, in *General Catalogue of Variable Stars, 3rd ed.*, p. 0

Kwan, J., Scoville, N., 1974, ApJ, 194, L97

Lada, C. J., Reid, M. J., 1978, ApJ, 219, 95

Le Sidaner, P., Le Bertre, T., 1996, A&A, 314, 896

Lockett, P., Elitzur, M., 1992, ApJ, 399, 704

Loup, C., Forveille, T., Omont, A., Paul, J. F., 1993, A&AS, 99, 291

Lovas, F. J., 2004, `http://physics.nist.gov/PhysRefData/Micro/Html/contents.html`

Lucas, R., Bujarrabal, V., Guilloteau, S., Bachiller, R., Baudry, A., Cernicharo, J., Delannoy, J., Forveille, T., Guelin, M., Radford, S. J. E., 1992, A&A, 262, 491

Marshall, C. R., Leahy, D. A., Kwok, S., 1992, PASP, 104, 397

Martinez, A., Bujarrabal, V., Alcolea, J., 1988, A&AS, 74, 273

Marvel, K. B., 1996, Ph.D. Thesis

Masheder, M. R. W., Booth, R. S., Davies, R. D., 1974, MNRAS, 166, 561

McIntosh, G. C., Predmore, C. R., Patel, N. A., 1994, ApJ, 428, L29

McLaren, R. A., Betz, A. L., 1980, ApJ, 240, L159

Menten, K. M., Melnick, G. J., 1989, ApJ, 341, L91

Menten, K. M., Melnick, G. J., 1991, ApJ, 377, 647

Menten, K. M., Young, K., 1995, ApJ, 450, L67

Merrill, K. M., Stein, W. A., 1976, PASP, 88, 285

Miyoshi, M., 2003, in Y. Nakada, M. Honma, and M. Seki (eds.), *ASSL Vol. 283: Mass-Losing Pulsating Stars and their Circumstellar Matter*, p. 303, Dordrecht: Kluwer Academic Publishers

Miyoshi, M., Matsumoto, K., Kameno, S., Takaba, H., Iwata, T., 1994, Nature, 371, 395

Monnier, J. D., Danchi, W. C., Hale, D. S., Lipman, E. A., Tuthill, P. G., Townes, C. H., 2000a, ApJ, 543, 861

Monnier, J. D., Danchi, W. C., Hale, D. S., Tuthill, P. G., Townes, C. H., 2000b, ApJ, 543, 868

Monnier, J. D., Geballe, T. R., Danchi, W. C., 1998, ApJ, 502, 833

Monnier, J. D., Geballe, T. R., Danchi, W. C., 1999a, ApJ, 521, 261

Monnier, J. D., Traub, W. A., Schloerb, F. P., Millan-Gabet, R., Berger, J.-P., Pedretti, E., Carleton, N. P., Kraus, S., Lacasse, M. G., Brewer, M., Ragland, S., Ahearn, A., Coldwell, C., Haguenauer, P., Kern, P., Labeye, P., Lagny, L., Malbet, F., Malin, D., Maymounkov, P., Morel, S., Papaliolios, C., Perraut, K., Pearlman, M., Porro, I. L., Schanen, I., Souccar, K., Torres, G., Wallace, G., 2004, ApJ, 602, L57

Monnier, J. D., Tuthill, P. G., Lopez, B., Cruzalebes, P., Danchi, W. C., Haniff, C. A., 1999b, ApJ, 512, 351

Moran, J. M., Ball, J. A., Predmore, C. R., Lane, A. P., Huguenin, G. R., Reid, M. J., Hansen, S. S., 1979, ApJ, 231, L67

Moran, J. M., Ball, J. A., Yen, J. L., Schwartz, P. R., Johnston, K. J., Knowles, S. H., 1977, ApJ, 211, 160

Moran, J. M., Dhawan, V., 1995, in J. A. Zensus, P. J. Diamond, and P. J. Napier (eds.), *ASP Conf. Ser. 82: Very Long Baseline Interferometry and the VLBA*, p. 161, Astronomical Society of the Pacific

Moran, J. M., Papadopoulos, G. D., Burke, B. F., Lo, K. Y., Schwartz, P. R., Thacker, D. L., 1973, ApJ, 185, 535

Morris, D., Radhakrishnan, V., Seielstad, G. A., 1964, ApJ, 139, 551

Morris, M., Bowers, P. F., 1980, AJ, 85, 724

Nedoluha, G. E., Watson, W. D., 1994, ApJ, 423, 394

Nercessian, E., Omont, A., Benayoun, J. J., Guilloteau, S., 1989, A&A, 210, 225

Neufeld, D. A., Feuchtgruber, H., Harwit, M., Melnick, G. J., 1999, ApJ, 517, L147

Neugebauer, G., Leighton, R. B., 1969, *Two-micron sky survey. A preliminary catalogue*, NASA SP, Washington: NASA, 1969

Nyman, L.-A., Booth, R. S., Carlstrom, U., Habing, H. J., Heske, A., Sahai, R., Stark, R., van der Veen, W. E. J. C., Winnberg, A., 1992, A&AS, 93, 121

Olofsson, H., Rydbeck, O. E. H., Lane, A. P., Predmore, C. R., 1981, ApJ, 247, L81

Olofsson, H., Rydbeck, O. E. H., Nyman, L.-A., 1985, A&A, 150, 169

Omont, A., Lucas, R., Morris, M., Guilloteau, S., 1993, A&A, 267, 490

Pardo, J. R., Alcolea, J., Bujarrabal, V., Colomer, F., del Romero, A., de Vicente, P., 2004, A&A, 424, 145

Pearson, T. J., Readhead, A. C. S., 1984, ARA&A, 22, 97

Perrine, C. D., 1923, PASP, 35, 229

Perryman, M. A. C., Lindegren, L., Kovalevsky, J., Hoeg, E., Bastian, U., Bernacca, P. L., Crézé, M., Donati, F., Grenon, M., van Leeuwen, F., van der Marel, H., Mignard, F., Murray, C. A., Le Poole, R. S., Schrijver, H., Turon, C., Arenou, F., Froeschlé, M., Petersen, C. S., 1997, A&A, 323, L49

Phillips, R. B., Boboltz, D. A., 2000, AJ, 119, 3015

Phillips, T. G., van Dishoeck, E. F., Keene, J., 1992, ApJ, 399, 533

Pijpers, F. P., Pardo, J. R., Bujarrabal, V., 1994, A&A, 286, 501

Rausch, E., Kegel, W. H., Tsuji, T., Piehler, G., 1996, A&A, 315, 533

Reid, M. J., 1995, in J. A. Zensus, P. J. Diamond, and P. J. Napier (eds.), *ASP Conf. Ser. 82: Very Long Baseline Interferometry and the VLBA*, p. 209, Astronomical Society of the Pacific

Reid, M. J., Dickinson, D. F., 1976, ApJ, 209, 505

Reid, M. J., Haschick, A. D., Burke, B. F., Moran, J. M., Johnston, K. J., Swenson, G. W., 1980, ApJ, 239, 89

Reid, M. J., Moran, J. M., Johnston, K. J., 1981, AJ, 86, 897

Reid, M. J., Muhleman, D. O., 1978, ApJ, 220, 229

Reid, M. J., Muhleman, D. O., Moran, J. M., Johnston, K. J., Schwartz, P. R., 1977, ApJ, 214, 60

Richards, A. M. S., Yates, J. A., Cohen, R. J., 1998, MNRAS, 299, 319

Roberts, D. H., Potash, R. I., Wardle, J. F. C., Rogers, A. E. E., Burke, B. F., 1984, in R. Fanti, K. Kellermann, and G. Setti (eds.), *IAU Symp. 110: VLBI and Compact Radio Sources*, p. 35, D. Reidel

Roberts, D. H., Wardle, J. F. C., Brown, L. F., 1994, ApJ, 427, 718

Rosen, B. R., Moran, J. M., Reid, M. J., Walker, R. C., Burke, B. F., Johnston, K. J., Spencer, J. H., 1978, ApJ, 222, 132

Sahai, R., Wannier, P. G., 1992, ApJ, 394, 320

Samus, N. N., Durlevich, O. V., et al., 2004, VizieR Online Data Catalog, 2250, 0

Schwab, F. R., Cotton, W. D., 1983, AJ, 88, 688

Serkowski, K., 1969, ApJ, 156, L139

Shawl, S. J., 1969, ApJ, 157, L57

Shibata, K. M., Chung, H., Kameno, S., Roh, D., Umemoto, T., Kim, K., Asada, K., Han, S., Mochizuki, N., Cho, S., Sawada-Satoh, S., Kim, H., Bushimata, T., Minh, Y. C., Miyaji, T., Kuno, N., Mikoshiba, H., Sunada, K., Inoue, M., Kobayashi, H., 2004, PASJ, 56, 475

Shinnaga, H., Claussen, M. J., Lim, J., Dinh-van-Trung, Tsuboi, M., 2003, in Y. Nakada, M. Honma, and M. Seki (eds.), *ASSL Vol. 283: Mass-Losing Pulsating Stars and their Circumstellar Matter*, p. 393, Dordrecht: Kluwer Academic Publishers

Shinnaga, H., Moran, J. M., Young, K. H., Ho, P. T. P., 2004, ApJ, 616, L47

Shinnaga, H., Tsuboi, M., Kasuga, T., 1999, PASJ, 51, 175

Smith, N., 2004, MNRAS, 349, L31

Smith, N., Humphreys, R. M., Davidson, K., Gehrz, R. D., Schuster, M. T., Krautter, J., 2001, AJ, 121, 1111

Snyder, L. E., Buhl, D., 1974, ApJ, 189, L31

Snyder, L. E., Jewell, P. R., Dinger, A. S., Dickinson, D. F., Buhl, D., 1986, AJ, 92, 416

Soker, N., 1998, MNRAS, 299, 1242

Soker, N., 2000, MNRAS, 312, 217

Soker, N., Clayton, G. C., 1999, MNRAS, 307, 993

Soker, N., Harpaz, A., 1999, MNRAS, 310, 1158

Soria-Ruiz, R., Alcolea, J., Colomer, F., Bujarrabal, V., Desmurs, J.-F., Marvel, K. B., Diamond, P. J., 2004, A&A, 426, 131

Spencer, J. H., Schwartz, P. R., Winnberg, A., Olnon, F. M., Matthews, H. E., Downes, D., 1981, AJ, 86, 392

Stanek, K. Z., Knapp, G. R., Young, K., Phillips, T. G., 1995, ApJS, 100, 169

Sudol, J. J., Dyck, H. M., Stencel, R. E., Klebe, D. I., Creech-Eakman, M. J., 1999, AJ, 117, 1609

Sutton, E. C., Storey, J. W. V., Betz, A. L., Townes, C. H., Spears, D. L., 1977, ApJ, 217, L97

Tevousjan, S., Abdeli, K.-S., Weiner, J., Hale, D. D. S., Townes, C. H., 2004, ApJ, 611, 466

Thompson, A. R., 1989, in R. A. Perley, F. R. Schwab, and A. H. Bridle (eds.), *ASP Conf. Ser. 6: Synthesis Imaging in Radio Astronomy*, p. 11, Astronomical Society of the Pacific

Thomson, A., Moran, J., Swenson, G. J., 2001, *Interferometry and Synthesis in Radio Astronomy*, John Wiley and Sons, Inc., second edition

Turner, B. E., 1970, PASP, 82, 996

Van Blerkom, D., Auer, L., 1976, ApJ, 204, 775

Vlemmings, W. H. T., Diamond, P. J., van Langevelde, H. J., 2002a, A&A, 394, 589

Vlemmings, W. H. T., van Langevelde, H. J., Diamond, P. J., 2002b, A&A, 393, L33

Wallerstein, G., 1958, PASP, 70, 479

Wallerstein, G., 1978, The Observatory, 98, 224

Wallerstein, G., 1986, A&A, 164, 101

Wardle, J. F. C., Kronberg, P. P., 1974, ApJ, 194, 249

Watson, W. D., Elitzur, M., Bieniek, R. J., 1980, ApJ, 240, 547

Weaver, H., Williams, D. R. W., Dieter, N. H., Lum, W. T., 1965, Nature, 208, 29

Wendker, H. J., 1995, A&AS, 109, 177

Western, L. R., Watson, W. D., 1983, ApJ, 275, 195

Wiebe, D. S., Watson, W. D., 1998, ApJ, 503, L71

Wittkowski, M., Langer, N., Weigelt, G., 1998, A&A, 340, L39

Wolff, R. S., Carlson, E. R., 1982, ApJ, 257, 161

Worley, C. E., 1972, ApJ, 175, L93

Wright, M. C. H., Carlstrom, J. E., Plambeck, R. L., Welch, W. J., 1990, AJ, 99, 1299

Wrobel, J., Ulvestad, J., 2004, *Very Long Baseline Array Observational Status Summary*, Technical report

Wu Zheng, X., Scalise, E. J., Han, F., 1998, ApJ, 507, 384

Yates, J. A., Cohen, R. J., 1994, MNRAS, 270, 958

Yates, J. A., Cohen, R. J., Hills, R. E., 1995, MNRAS, 273, 529

Yates, J. A., Field, D., Gray, M. D., 1997, MNRAS, 285, 303

Yuasa, M., Unno, W., Magono, S., 1999, PASJ, 51, 197

Zhou, Z.-P., Kaifu, N., 1984, A&A, 138, 359

Zijlstra, A. A., Chapman, J. M., te Lintel Hekkert, P., Likkel, L., Comeron, F., Norris, R. P., Molster, F. J., Cohen, R. J., 2001, MNRAS, 322, 280

Zuckerman, B., Dyck, H. M., 1986, ApJ, 304, 394